

Self-assembly of Organic Semiconductors through Non-Contact Vapour-guided Deposition

Zach Edwards

Submitted in partial fulfilment of the requirements for the degree of Master of Philosophy in Chemistry

University College London

November 2024

Declaration

I, Zacharie Edwards, confirm that the work presented in this thesis is my own. Where information has been derived from other sources, I confirm that this has been indicated in the thesis.

Abstract

Crystallisation is a critical factor in the performance of organic semiconductors, as it directly influences charge transport properties and overall device efficiency. Achieving high crystallinity and uniform molecular alignment within organic semiconductor crystals and films is essential for optimising their functionality in electronic devices. However, traditional deposition methods often struggle with controlling crystallisation, leading to defects and inconsistencies that hinder the performance of organic field-effect transistors and other devices. Addressing these challenges, this thesis introduces a novel non-contact vapour-guided deposition technique designed to enhance crystallisation control and improve the performance of organic semiconductors.

This research focuses on the synthesis and characterisation of water-soluble and fluorinated naphthalene diimide and perylene diimide derivatives. The vapour-guided deposition technique developed in this work manipulates the self-assembly processes of these compounds, leading to the formation of highly ordered single crystals. These crystals are compared against those produced by traditional methods.

Furthermore, the thesis studies the effects of various deposition parameters, such as droplet movement speeds, on the crystallisation process. The results show that the non-contact vapour-guided deposition technique provides additional control over crystal growth which may lead to scalable and reproducible methods for fabricating high-performance organic semiconductor crystals and films.

The findings of this research advance the understanding of the fundamental principles of organic semiconductor crystallisation and offer practical solutions to existing challenges in the field. The novel techniques and insights developed here have the potential to drive future innovations in organic electronics.

Statement of Impact

The research presented in this thesis was conducted with the goal of developing novel organic semiconductors and implementing an innovative non-contact vapor-guided deposition technique. While crystallisation control has been extensively studied, many existing techniques still face challenges in synthesising independent OSC crystals with sufficient control and precision. The non-contact vapor-guided deposition method offers a promising solution to these challenges by addressing the issues of crystallisation control and charge transport efficiency, which have historically limited the performance of organic semiconductors in electronic devices.

This technique capitalises on the precise manipulation of molecular self-assembly, enabling the formation of highly ordered single crystals. These ordered structures are critical for maximising charge carrier mobility and reducing dynamic disorder, both of which are essential for improving the performance of organic semiconductors. The method also shows potential for producing highly ordered OSC films, further enhancing device performance.

By synthesising water-soluble and fluorinated derivatives of naphthalene diimide and perylene diimide, this research explores the synergy between advanced molecular design and cutting-edge deposition methods. This work aims to deepen our understanding of the relationship between molecular interactions, self-assembly, and crystallisation in organic semiconductors, but also provides a scalable and cost-effective approach to fabricating high-performance, flexible, and environmentally friendly electronics.

Furthermore, the insights gained from the systematic investigation of deposition techniques could revolutionise the production molecular crystals and films further improving the production of organic electronics. Additionally, these advancements add significant insight into molecular design further realising the potential for fluorinated organic semiconductors. In this context, the research presented in this thesis serves as a key contribution to both the academic study and practical application of organic semiconductors.

Contributions

I would like to thank some contributions who took the time to dedicate so much time and work to this thesis. If not for their efforts this work would never have been possible.

Single crystals x-ray diffraction data for Chapter 3 was collected by Dr Laura J. McCormick at the National Crystallography Service and Dr Kreso Bucar from University College London.

The infrared and OECT measurements for Chapter 3 and 4 were performed by Dr. Peter Gilhooly-Finn at University College London.

Dr Lewis Cowen at University College London resynthesised compound **7** in Chapter 4 to allow for some additional measurements to be carried out.

Big thank you toAdibah and Aisha for helping me obtain some final CV and UV measurements

I would finally like to thank Dr. Abil Aliev and Dr. Kersti Karu for their knowledge and excellent running of the University College London Chemistry NMR and Mass spectrum facilities.

Acknowledgements

First of all, I would like to thank my supervisors Prof Bob Schroeder and Prof Giorgio Volpe for allowing me to join their groups and take part in this project. Thank you for allowing me to grow as a person and as a professional and for your undying patience and enthusiasm. I could not have asked for better supervisors.

A huge thank you to Dr. Lewis Cowen and Dr. Peter Gilhooly-Finn. Lewis, thank you for always being there, ever since day one to lend a hand and always allowing me to pick your brain. Don't think I would have got this far without you, thank you. Pete, I appreciate you always encouraging me to think differently and always being enthusiastic about any project. Without your insightful words and encouragement, I would have never finished.

I would like to extend a massive thank you to Dr Robert Malinowski for pioneering the systems I worked on. Also, for always having the answers and always being willing to help.

I am very lucky to have been a member of both the Schroeder group and Soft Active Mater Lab filled with amazing teams of scientists. I would like to thank all the members of each group for lending an ear when times are tough and for the advice given over the years. Also, I am privileged to have built so many friendships with these people over the years.

A special thank you goes to Dr Megan Westwood and Dr Ryan Trueman for never giving up on me even after the relentless quotes in the lab. You both made things bearable when they were tough and never failed to make me smile. Working with you has been a pleasure and you both made me work harder because of how good you were.

Thank you to my mum, Sarah. Thank you for always encouraging me to do whatever made me happy. For always being there whenever I needed someone to talk to and for supporting my passion even if you had no idea what I was on about.

To my fiancé, Charlotte. Thank you for putting up with me over the years and allowing me to be able to pursue my passion. Thank you for reading through my dyslexia and trying to understand what I mean. You made this all possible.

Contents

Declaration	2
Abstract	3
Statement of Impact	4
Contributions	5
Acknowledgements	
Publications	
Abbreviations	
1. Introduction	
1.2 Organic Semiconductors (OSCs)	14
1.2.1 Charge Transport	15
1.3 Molecular Design	21
1.3.1 π-Conjugated Molecular Core	21
1.3.2 Molecular Orbital Design	22
1.4 Molecular Semiconductors	24
1.4.1 Functional Naphthalene Diimides and Perylenediimide	24
1.4.2 Solubility of Naphthalene Diimides and Perylenediimide	26
1.5.1 Carbon-Fluorine Bond	28
1.5.2 Organoflourine Compounds	29
1.5.3 Fluorine Applications	30
1.5.4 Organic Electronics with Florine	31
1.5.5 Fluorine in Organic Field-Effect Transistors	31
1.6 Deposition Methods	33
1.6.1 Drop-casting	33
1.6.2 Spin Coating	34
1.6.3 Meniscus-guided Coating	35
1.6.4 Printing	40
1.7 Droplets	42
1.7.1 Contact Angle and Wetting	43

	1.7.2 Coffee-Ring Effect	43
	1.7.3 Marangoni Flows	44
	1.8 Mobile Droplets	46
	1.8.1 Methods of motion	47
	1.9 Binary Droplets	49
	1.9.1 Surface Tension and Compositional Gradients	50
	1.9.2 Motion	50
	1.10 Scope & Aim	51
2	. Methodology	
	2.2 Optical Microscopy	53
	2.3 Vapour Source and Droplet Composition	55
3 th	neir Deposition	57
	3.1 Introduction	
	3.2 Synthesis of water-soluble PDIs	59
	3.3 Sulphur end groups for gold electrode functionalisation	64
	3.4 PDI Deposition	67
	3.5 Deposition of Dicarboxylic NDI	69
	3.6 Synthesis and Characterisation of Glycol Terminated NDIs	73
	3.7 Droplet Manipulation	92
	3.8 Conclusion & Outlook	113
4	Synthesis and Characterisation of Fluorinated Naphthalenediimide	
	4.2 Synthesis of Linear Fluorinated Naphthalenediimide	116
	4.3 Synthesis of Branched Fluorinated Naphthalenediimide	120
	4.4 Conclusion & Outlook	137
5		
R	Experimental Procedures	141

	6.1 General Experimental	141
	6.2 Experimental Procedure for Chapter 3	142
	6.3 Experimental Procedure for Chapter 4	149
7	7.0 References	155

Publications

Degousée, T.; Neal, W. G.; Edwards, Z.; Singh, S.; Selvarajah, J.; Talha-Dean, T.; Palma, M.; Schroeder, B. C.; Mol, J. A., One hour road to high-quality arrays of gold nanoparticles coated with organic ligands. Journal of Materials Chemistry C 2023, 11 (47), 16518-16526.

Abbreviations

COSY - Correlation Spectroscopy

CRE - Coffee-Ring Effect

CV - Cyclic Voltammetry

DMF - Dimethylformamide

DMSO - Dimethyl Sulfoxide

DSC - Differential Scanning Calorimetry

FLUENCE - Fluid-Enhanced Crystal Engineering

FTIR - Fourier-transform infrared

HMBC - Heteronuclear Multiple Bond Correlation

HOMO - Highest Occupied Molecular Orbital

HSQC - Heteronuclear Single Quantum Coherence

IPA - Isopropanol

IR - Infrared

LUMO - Lowest Unoccupied Molecular Orbital

MS – Mass spectrometry

NDA - Naphthalene dianhydride

NDI - Naphthalenediimide

NMR - Nuclear Magnetic Resonance

OECT - Organic Electrochemical Transistor

OFET - Organic Field-Effect Transistor

OLED - Organic light emitting diode

OPV - Organic Photovoltaics

OSC - Organic Semiconductor

PDA – Perylene dianhydride

PDI – Perylenediimide

PDMS - Polydimethylsiloxane

PG - Propylene Glycol

PTFE - Polytetrafluoroethylene (Teflon)

RPM - revolutions per minute

SAM - Self-Assembled Monolayer

TEA - Triethylamine

TFA - Trifluoroacetic Acid

TGA - Thermogravimetric analysis

TIPS - Triisopropylsilylethynyl

TL - transient localisation

UV-Vis – Ultraviolet visible near IR spectroscopy

VG - Vapor-Guided

1. Introduction

1.1 Plastic electronic and Organic-Semiconductors

Plastic electronics and organic semiconductors have revolutionised the field of electronic devices by offering a host of unique advantages over traditional inorganic semiconductor materials. These innovative materials have opened up exciting possibilities for flexible, low-cost, and environmentally friendly electronics.

By harnessing the properties of organic semiconductors, researchers and engineers have paved the way for the development of a new generation of electronics that are lightweight, versatile, and energy-efficient. Plastic electronics offer significant advantages in terms of manufacturing cost. Traditional inorganic semiconductor fabrication processes are complex and expensive, involving high-temperature deposition techniques and stringent cleanroom conditions. In contrast, organic semiconductors can be produced using low-cost manufacturing techniques such as solution processing, printing, or roll-to-roll processing. These methods make largescale production more accessible, leading to cost-effective electronic devices with wide-scale applications. Another noteworthy advantage of organic semiconductors is their ability to cover large areas. Inkjet printing and vapor deposition techniques can be employed to deposit organic semiconductors over large areas, facilitating the production of expansive electronic components like large-area displays or solar panels. This capability, combined with the low-cost manufacturing methods, further enhances the scalability and commercial viability of plastic electronics. Energy efficiency is a critical consideration in the development of electronic devices. Organic semiconductors have demonstrated high energy conversion efficiencies²⁻⁵ and lowpower operation⁶⁻⁸. These properties make them ideal for applications requiring energy-efficient solutions, such as photovoltaics.

In summary, plastic electronics and organic semiconductors have revolutionised electronic device design, offering flexibility, low-cost manufacturing, large-area coverage, energy efficiency, and environmental benefits. These innovative materials hold great promise for the development of next-generation electronics, and ongoing advancements continue to push the boundaries of what is possible in the field of electronic devices.

1.2 Organic Semiconductors (OSCs)

Organic semiconductors (OSCs) consist of mainly π -conjugated systems, which can be split into two main groups, π -conjugated small molecules and polymers. Both rely on the same phenomenon to allow for the conduction of charges. Organic materials conduct charges through conjugation which occurs through sp²-hybridisaiton where the carbon-carbon bonds consist of three σ -bonds and one π -bond. The sp²-orbitals form a triangle within a plane and the remaining p_z -orbitals are in a perpendicular plane⁹. Each carbon atom donates an electron remaining in the p_z -orbital to produce an overlapping π -bond. This π -bond is what allows for electrons to become delocalised across conjugated systems with the extent of π -conjugation varying hugely in organic semiconducting systems. Both small molecules and polymers can be semiconducting where these small molecules can have a few π -bonds per molecule and polymers can have alternating π -bonds that extend over numerous monomers throughout the system. When observing the simplest conjugated system (ethylene, Figure 1) there are two sp²-hybridsed carbon atoms, each containing one

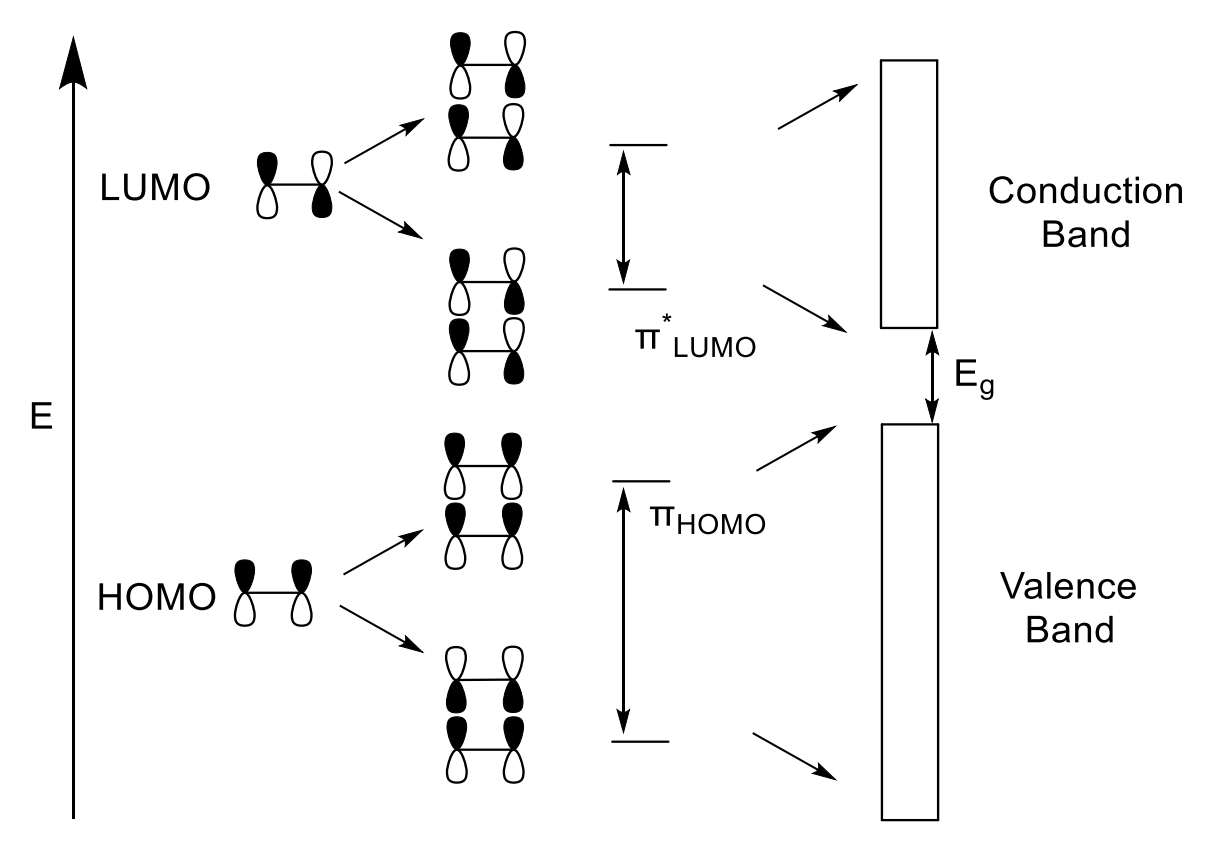


Figure 1: Molecular orbital diagrams of gas phase bonding and antibonding interactions between the HOMO/LUMO levels of two ethylene molecules in a co-facial configuration, with the formation of valence and conduction bands when a large number of interacting molecules stack.

electron in its p_z-orbital. When these two orbitals overlap both a π -bonding and π *antibonding orbital are produced. With the formation of the π -bonding orbital electron density increases in the plane between the carbon nuclei. Electrons that occupy this orbital will have the effect of lowering the potential energy of the combination. Electrons that occupy the π^* -antibonding orbital will lie outside of the internuclear region which has a nodal plane perpendicular to the internuclear axis pushing the nuclei apart. Due to ethylene only having a single electron in the 2pz-orbitals there are only two electrons which occupy the π -bonding orbital leaving the π *-antibonding orbital empty giving rise to shorter (133.9 pm vs. 153.5 pm)¹⁰ and stronger (600 kJ mol⁻¹ vs. 346 kJ mol⁻¹ (ethane)¹⁰) double bonds. Using molecular orbital theory each orbital is split into a discrete energy level. First there is the Highest Occupied Molecular Orbital (HOMO) with the second being the Lowest Unoccupied Molecular Orbital (LUMO) which are separated by what is known as the band gap energy. To reduce the energy of the band gap and bring the orbitals closer together the number of aligned small molecules can be increased or the polymer chain length can be increased. The effect this has is to increase the number of molecular orbitals to a theoretical infinite amount where the π -bonding orbitals begin to form a valence band and the π^* antibonding orbitals will form the opposing conduction band. This leads to a model that is comparable to band theory which is used to describe the conduction of many inorganic semiconductors.

1.2.1 Charge Transport

For many OSCs high levels of electrical conductivity can be achieved with high levels of extrinsic doping, which is associated with high density of charge carriers. The electrical conductivity (σ) can be expressed in a material by¹¹:

$$\sigma = n \cdot e \cdot \mu \tag{1}$$

where n is the number of charge carriers, e is the elementary charge, and μ identifies the charge carrier mobility, this can be defined as:

$$\mu = \frac{v}{E} \tag{2}$$

where v is the charge carriers drift velocity and E is an applied electric field¹².

Mobility is the measure of the ability for charges to move and thus is it important to understand their dynamics within a material. Electrons can travel in a wave-like matter through the quantum world. For strongly coupled systems that maintain high levels of transitional lattice symmetry the solid-state electronic band structure is observed. When a field induces momentum, the delocalised electron wave-packets move coherently between Bloch states. This allows for charges to move though a material as described by band theory, where charges move through the two different bands over a delocalised area. An electron can be either introduced or excited into the conduction band allowing for delocalisation. Alternatively, an electron can be removed from the valence band leaving a hole in its place which can then move across the band via overlapping wavefunctions.

Band transport is commonly observed in highly ordered large organic crystals and inorganic semiconductors when the electron-phonon coupling is weak, and the charge carriers span over a delocalised area as illustrated in Figure 2¹³. There are many proposed models, but they are mainly based on the mobility expression:

$$\mu = \frac{e}{m^*} \tau \tag{3}$$

where, τ is the mean relaxation time between collisions, m^* is the effective mass¹⁴. When band transport is present lattice vibrations (phonons) can disrupt the transport. This in turn can lead to the formation of polarons that can become more detrimental with the increase in temperature due to an increase in scattering frequency¹⁴. This, coupled with the fact that most OSCs are more likely to form amorphous morphologies causes the overlapping of wave functions is significantly decreased. This can lead to the formation of more frequent electron-phonon coupling which can be comparable to

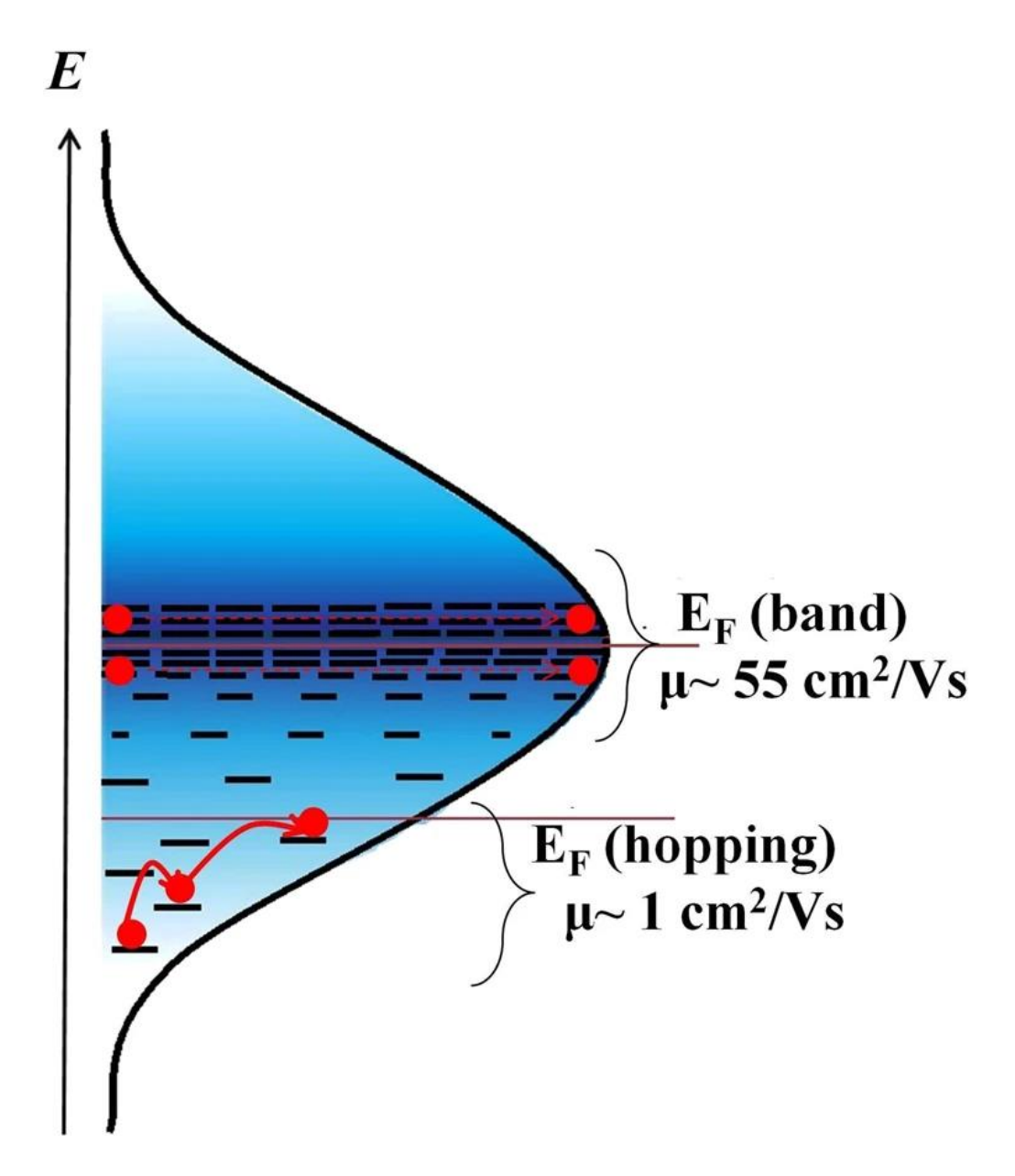


Figure 2: Schematic representation of charge transport: Schematic illustration of charge transport governed by two different transport motifs. When the Fermi level lies the bottom of the curve, transport is described by thermally activated hopping. As the Fermi level moves towards the central region, band-like transport becomes possible¹³.

or even higher than the inter-lattice coupling. As the electron-phonon coupling becomes more local, the mean free-path of electrons in turn become comparable to adjacent lattice distances. This then leads to transport that no longer follow a band transport but incoherent hopping. When there are significant weak intermolecular couplings then the time scale of charge transfer can become so small that an electron will relax down to ground state. Knowing this, the assumption can be made that the charge will be localised to molecular sites, meaning that for charge transport to occur

it will need to travel via "occasional" leaps. This is hopping transport and scales with temperature which the opposite of band transport. It can be written as:

$$k = \frac{2\pi}{\hbar} \frac{J^2}{\sqrt{4\pi\lambda k_{\rm B}T}} e^{-\frac{\lambda}{4k_{\rm B}T}} \tag{4}$$

where \hbar is the reduced Planck constant, J is the transfer integral, λ is the reorganisation energy, $k_{\rm B}$ the Boltzmann constant and e is the elementary charge^{14,} ¹⁵. If we consider the charge-carrier moving along an array of molecules and apply the Boltzmann equipartition theorem, and then assume the mean free-displacement of the charge carrier is comparable to intermolecular spacing, we can write the one-dimensional mobility as:

$$\mu = \frac{e}{k_{\rm B}T} \frac{ka^2}{2} \tag{5}$$

In OSC systems a charge needs to be able to move freely throughout for improved performance. This charge transport is greatly affected by a molecular systems ability to delocalise its π -conjugated electronic states across multiple units. The charge transfer integral (J) is the ability for a molecule system to transfer a charge between neighbouring molecules greatly affecting the performance of the system. A shorter

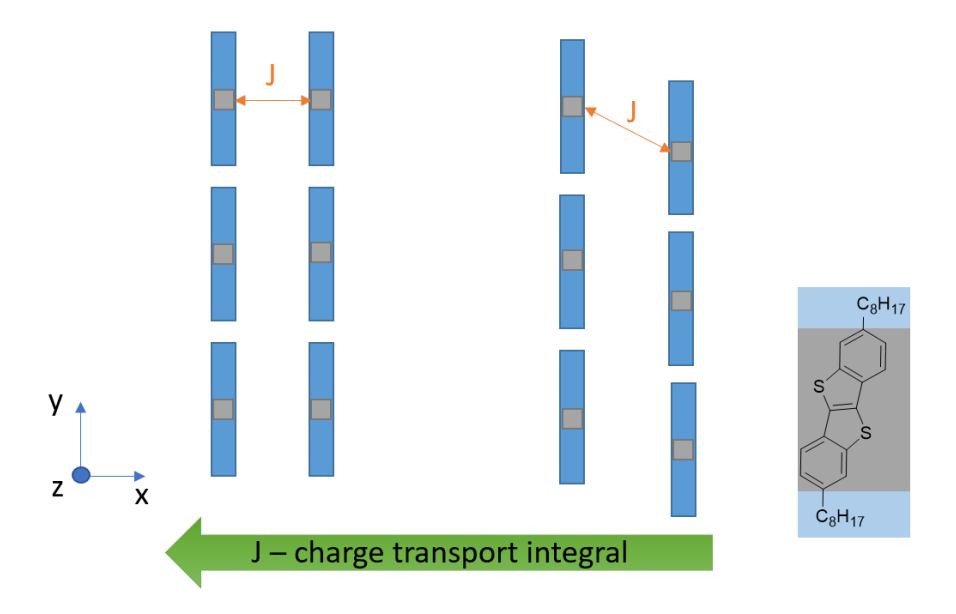


Figure 3: Schematic representation of charge transfer integral (J) between individual molecules with C_8 -BTBT as a reference.

distance between molecules can lead to improved π -orbital overlap in turn causing greater J-coupling thereby increasing the electronic performance. Systems that contain molecules further apart will have comparatively low J values and thus decreased performance. Charge transport is dependent on the molecular geometry and is very sensitive to intermolecular packing illustrated in Figure 3. The most commonly observed packing motifs in benchmark materials are: a) slipped stack, b) slipped π -stack, c) brick wall and d) herringbone¹⁶. These packing motifs all show dominant transfer integrals between adjacent molecules, which can all be observed in Figure 4.

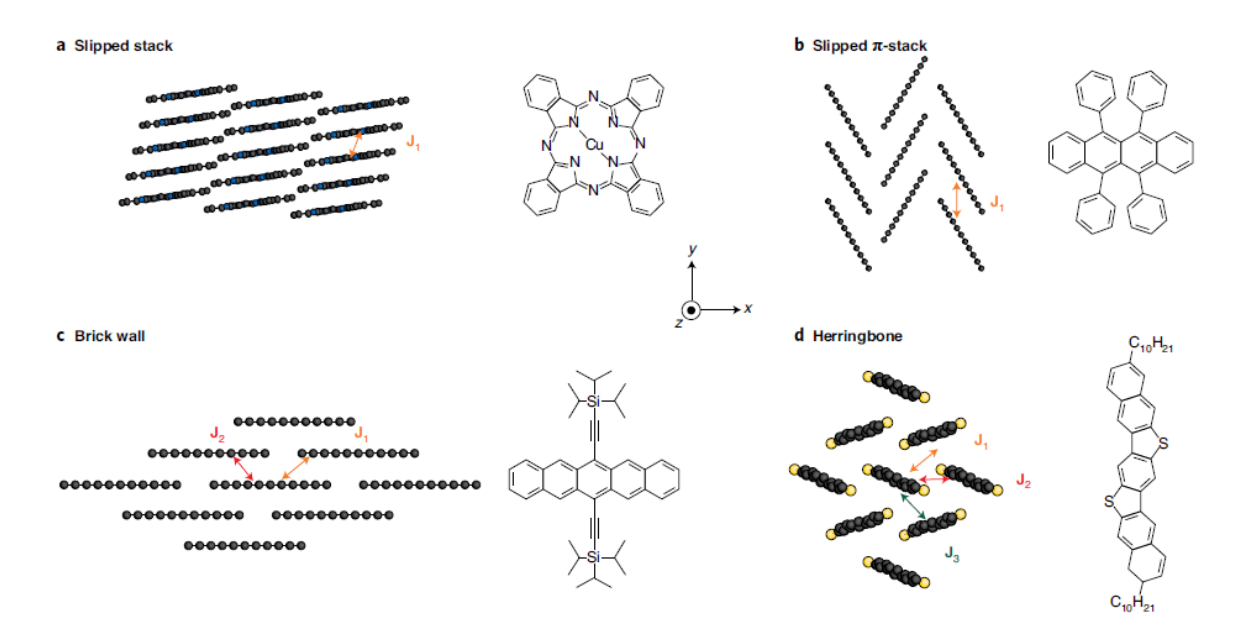


Figure 4: Most observed molecular packings in crystals of molecular OSCs and corresponding benchmark materials. Top view; hydrogen atoms, side chains and rings are omitted for clarity. a) copper phthalocyanine, b) rubrene, c) TIPS-pentacene and d) C10-DNBDT-NW⁴.

With systems that primarily transport in the x-y plane there will be one large J exhibiting strong anisotropic transport. The carrier transport will be at its highest in a specific direction. This phenomenon is expressed in systems that arrange with the slipped stack and slipped π -stack. Systems that pack via the herringbone motif are not affected by the anisotropy of transport, because they contain three large transfer integrals due to the molecular arrangement¹⁷. These systems provide isotropic transport in the x-y planes where the three J values can be very similar or even the same. The brick-wall packing motif can be considered an intermediate regime. One exception is rubrene, with the slipped π -stack packing motif, it remains to have one of the highest reproducible mobilities (>15 cm² V-¹ s-¹) to date.

Charge carriers in molecular crystals are not fully extended Bloch electrons. Instead, the molecular charge character resembles those of radical cations/anions in solution. In this case, it suggests that the electron wave function is delocalised over small clusters of molecules rather than the entire lattice. It has been evidenced in recent studies that there is a correlation between the suppression of thermal lattice fluctuations and improved carrier mobility. Studies showed that an increase in film mobility under compressive strain was too large to be explained by strain induced changes expected within a Bloch electron band structure, but was more consistent with a reduction in dynamic disorder due to the stiffening of the molecular lattice¹⁸. Knowing this, the standard Bloch electron motion can be considered as continuous collisions with scattering centres in a crystalline arrangement. Molecules that have large thermal vibrations cause quantum microscopic processes (electron phononcoupling) that go beyond the semi-classical description. This is due to the presence of strong molecular disorder making the electronic wave function localisations to be extremely short, leading to a large suppression of charge diffusion. Due to this fact, the transient localisation (TL) is used to show mobility using this equation:

$$\mu = \frac{e}{k_{\rm B}T} \frac{L^2}{2\tau_{\rm vib}} \tag{6}$$

where e is the elementary charge, k_B is the Boltzmann constant, T is the temperature, L is the length and τ_{vib} is the timescale of intermolecular motions. Using equation (6), it is clear to see that the parameters governing charge transport, L and τ_{vib} , are different from conventional semiconductors. This is relevant to molecular order because when an OSC has strong disorder the carriers become localised on a single molecule, which leads to the previous equation being invalid. With this realisation the transitions become a thermally activated hopping regime yielding far lower mobilities. This can be avoided by controlling crystallisation moving to a more ordered system and thus, a more favourable transient localisation regime illustrated in Figure 5.

Equation 6 shows that there are two parameters that can be improved to gain better performance. Firstly, there is energetic disorder always present even in perfectly crystalline solids, which mostly originates from thermal fluctuations of intermolecular transfer integrals¹⁹. This dynamic disorder can be optimised by engineering the different intermolecular interactions. Secondly, the degree of anisotropy of the band

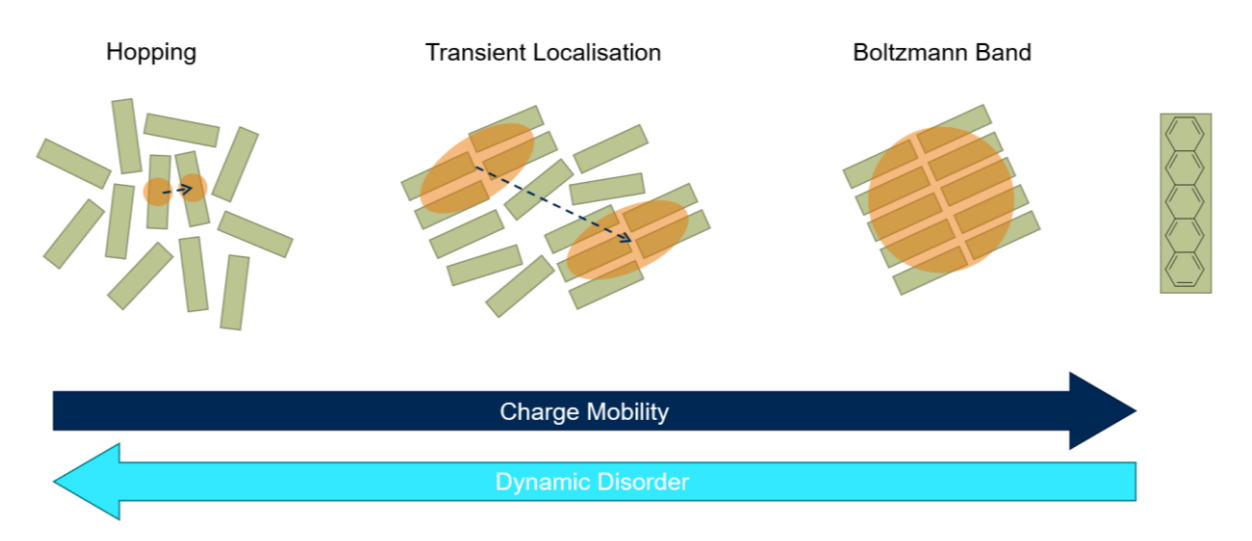


Figure 5: Illustration of three theories of charge transport as the disorder changes affecting mobility and material performance, with pentacene as a reference.

structure. This is determined by the transfer integrals in different bonding directions controlling the sensitivity of carrier motion to disorder. It has been shown that films most resilient to quantum effects have positive isotropic transfer integrals in different directions²⁰. All these factors affect the performance of an OSC and show the need for crystallisation control techniques for the advancement of this field. This leads onto the currently established techniques that are being utilised today as follows.

1.3 Molecular Design

1.3.1 π-Conjugated Molecular Core

When designing OSCs the first step is to establish an aromatic core, this can be taken from the established diverse array of well-performing crystalline OSC molecular materials. Almost all the functionalised organic molecules can be fragmented into molecular backbones mostly consisting of one or more central groups, linkers allowing for central group connections and solubilising side chains. The side chains can be utilised to tune numerous properties such as solubility, molecular packing and band gap manipulation. Looking at these conjugated molecular building blocks retro synthetically, Reuter $et\ a\ell^1$ observed that only 22 simple molecular moping operations needed to be done in order to design the other current best performing back bones when working from benzene seen in Figure 6. With this knowledge there is a blueprint emerging for the design and synthesis of future variations of OSCs. When designing molecules it has been observed that molecular symmetry plays a crucial role; the first reason is that symmetry is beneficial for synthesis and makes the molecule more

accessible. Secondly a reduction in symmetry leads to a decrease in charge localisation which will have a negative effect on the charge mobility of the OSC²². This is because more complex packing can lead to a reduction in charge transfer integrals.

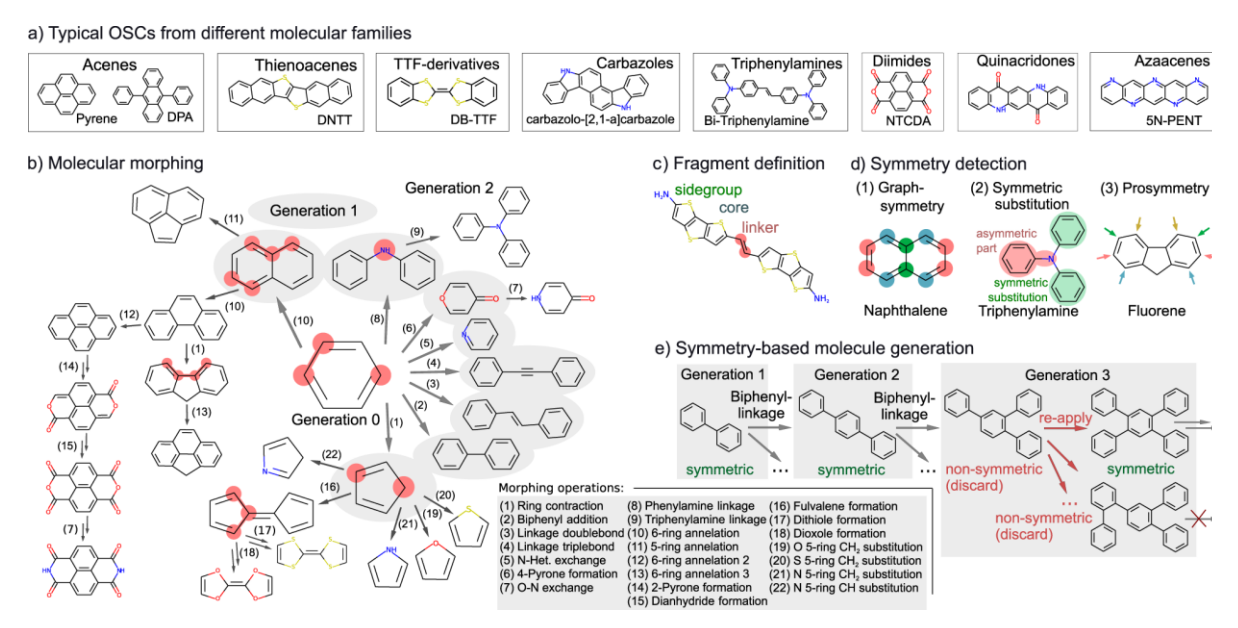


Figure 6: a) Important π -conjugated molecular families and examples of well-performing OSC-molecules therein. b) Schematic overview of the molecular generation process. Starting from benzene, diverse molecules are created by iterative application of up to 22 morphing operations. c) Fragment-definitions used throughout the text exemplified for the molecule BDTTE. d) Concepts for symmetry detection used throughout the molecular generation process. e) Modified molecular morphing step, adapted to the symmetry constraints imposed on candidate molecules¹⁰.

1.3.2 Molecular Orbital Design

For the materials being synthesised to maintain their semiconducting properties the band gap must be kept small enough, this remains true for both small molecules and polymers. Due to this factor a range of aromatic, olefin and alkyne building blocks have been employed. To precisely tune the electronic properties of these materials, a range of heteroatoms, such as nitrogen, sulphur, and fluorine, can be strategically incorporated into the molecular structure. These atoms introduce electron-withdrawing or electron-donating effects, modulating key parameters such as electron affinity and ionisation potential. Furthermore with the addition of solubilising groups such as alkoxy and alkyl chains the processability of these materials can be modified.

For both small molecules and polymers, the distribution of the orbitals and their energies in a π -conjugated system play an important role in many properties such as intramolecular and intermolecular charge transport, light emission/absorption,

electrochemistry and charge extraction/injection/trapping. Components that can be utilised to rase the HOMO level are ones that donate electron density, this can be either inductively through things such as alkyl chains, or mesomerically through lone pair donation from heteroatoms (N, S or O). Alternatively atoms and/or groups that have electron withdrawing properties (-F, -C≡N or -C(O)R) have the opposite effect of lowering the HOMO and LUMO energies²³.

In Figure 7 is an example of a familiar molecule IDFBR where the HOMO wave function is delocalised over the backbone and the LUMO is localised over the electrondeficient 2,1,3-benzothiadiazole (BT) moieties²⁴. In this molecule the LUMO can be tuned by adding substituents to the terminals, while the HOMO can be manipulated by adding substituents to the conjugated core. A decrease in the HOMO energy can be seen when the central indenofluorene core is replaced with a smaller fluorene unit, this reduces the HOMO because the fluorene has less delocalised electrons which in turn also reduces the LUMO energy because there is more electron withdrawing functionality over a larger fraction of the conjugated unit as seen in FBR. Continuing from this molecule the **BT** units can be exchange with phenylene to produce **PH**, due to the phenylenes being less electron-deficient the LUMO energy is much higher, with minimal change of the HOMO. With the addition of groups with electron-withdrawing inductive effects like fluorine both the HOMO and LUMO energy and decreased as seen with the addition of two F atoms to the BT units of FBR producing diFBR. Additionally, **FBR** can be modified by replacing the C=S (thiocarbonyl) groups with a more strongly electron-withdrawing dicyanovinyl group. With this replacement diCN can be produced and has HOMO and LUMO energy levels that are lower compared

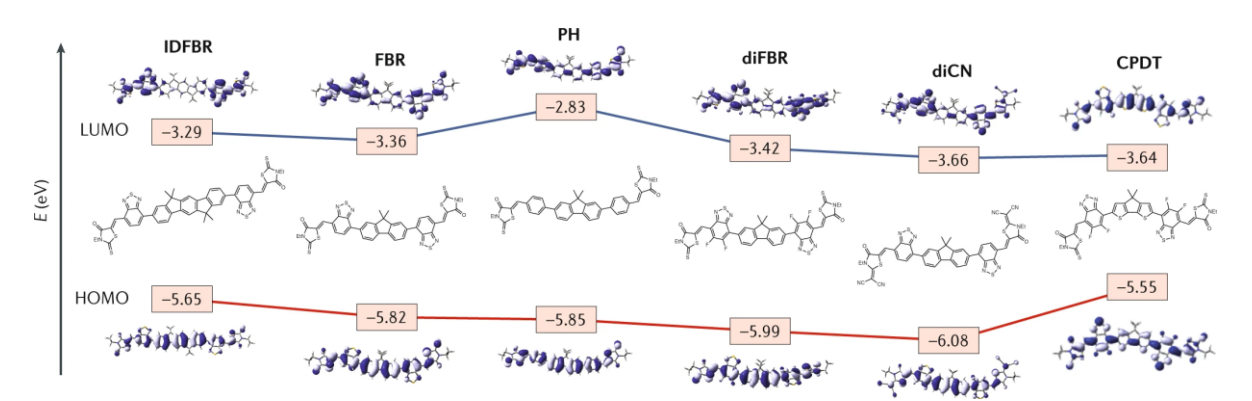


Figure 7: Visual representation of HOMO and LUMO levels of conjugated aryl molecules obtained via density functional theory with the B3LYP method and def2-SVP basis set, using Grimme's D3 dispersion correction and the BJ damping function produced by Bronstein *et al*¹¹.

with **FBR**. All these changes show that electron density distribution and the delocalisation of the π orbitals play an important role in determining their orbital energies. Some of the steric effect that arise from the **BT** and fluorene neighbouring protons in **FBR** can be reduced by replacing fluorene with cyclopentadithiophene to produce **CPDT**. With this molecule the HOMO energy is increased and the LUMO is decrease due to the increase π orbital overlap between the rings. Additionally, the electron-rich thiophene can raise the HOMO energy further. **CPDT** also sees electrostatic interactions between the S and F atoms due to their electropositive and electronegative properties respectively. This effect stabilises the planer backbone which in turn also raises the HOMO and decreases the LUMO energy.

1.4 Molecular Semiconductors

1.4.1 Functional Naphthalene Diimides and Perylenediimide

Two of the commonly employed OSC cores are, naphthalene diimide (NDI) and perylenediimide (PDI) (Figure 8). NDI and PDI molecules have emerged as promising candidates for OSCs due to a combination of advantageous properties. One key

Figure 8: Aromatic diimide structures with potential self-assembly and functional properties. R groups for this work re substituted for various amino acids.

characteristic is their π -conjugated structure, which consists of an extended system of π -electrons. This feature enables efficient electronic delocalisation and facilitates the transport of charges within the material. Additionally, these molecules typically possess a high electron affinity, making them effective at accepting electrons and promoting efficient charge injection and transport in organic semiconductor devices.

NDI-based materials also exhibit good stability, both thermally and chemically, ensuring reliable performance and durability in practical applications^{25, 26}. Moreover, these materials often demonstrate high charge carrier mobilities, allowing for efficient conduction of electrons or holes in organic electronic devices²⁷. This property is crucial for achieving high-performance organic transistors, photovoltaics, and other electronic applications. PDI derivatives specifically are known for their excellent thermal²⁸ and chemical stability²⁹, ensuring long-term performance and durability of organic semiconductor devices. This stability is crucial for maintaining device functionality under operating conditions and contributes to their suitability for various applications. Another advantage of these molecules is their versatility. They can be chemically modified and functionalised to tune their electronic properties, solubility, and selfassembly behaviour^{25, 26, 29}. This flexibility enables the design of tailored materials with desired characteristics for specific applications. Furthermore, many NDI and PDI derivatives are soluble in common organic solvents, making them amenable to solution processing techniques such as spin coating, inkjet printing, or roll-to-roll deposition. This solution processability facilitates scalable and cost-effective fabrication of organic semiconductor devices. The combination of π -conjugation, high electron affinity, stability, charge transport properties, versatility, and solution processability makes NDI and PDI a highly promising class of materials for various organic semiconductor applications, including organic transistors, solar cells, lightemitting diodes, and sensors.

Both NDIs and PDI derivatives show varying self-assembly properties with the supramolecular chemistry being widely studied³⁰⁻³². The self-assembly properties play an important role in the formation of thermodynamically stable structures which can heavily affect the charge transfer performance. there are many different supramolecular self-assembly approaches, but some notable ones are:

- Amino acid and peptide derivatised systems; this includes a multitude of research looking into the impact of position of the substitution of the NDI and PDI, aliphatic vs aromatic, chiral vs achiral amino acid and peptides, branched vs straight chain (chain length)^{33, 34}.
- Self-assembly through molecular recognition; this involves the tuning of specific groups in order to change the self-assembly properties through noncovalent

- bonding such as hydrogen bonding, hydrophobic forces, van der Waals and π π stacking³⁵⁻³⁷.
- Chiral self-assembly; studies have shown sophisticated self-assembly through the use of chirality derived self-sorting strategies controlling the supramolecular organisation^{38, 39}.

The ease of use and extensive literature meant NDIs and PDIs became the primary focus molecule of this project allowing for many different molecules to be synthesised to then analyse the effectiveness of the novel deposition method.

1.4.2 Solubility of Naphthalene Diimides and Perylenediimide

The solubility of organic semiconductors (OSCs), such as naphthalene diimides (NDIs) and perylene diimides (PDIs), is critical for their processing and subsequent application. Solubility is inherently influenced by the molecular structure of these compounds, as well as the nature and positioning of substituents attached to their core. NDIs, characterized by a naphthalene core with two imide groups positioned at the 1,4-positions (Figure 7), typically exhibit poor solubility in non-polar solvents. This limited solubility is primarily attributed to the rigid naphthalene core and the strong intermolecular interactions, notably π - π stacking, which lead to the formation of NDI aggregates²⁶. These interactions hinder dissolution and reduce solubility in conventional solvents. However, the solubility of NDIs can be significantly enhanced by introducing various substituents at either the core or imide positions^{25, 26}. For example, the attachment of alkyl chains at the imide positions improves solubility in non-polar solvents, while the incorporation of polar functional groups, such as carboxylic acids, amines, or sulfonates, increases solubility in polar solvents.

Similarly, PDIs, which possess an extended structure over two naphthalene cores with imide groups located at the 3,4,9,10-positions (Figure 8), also display low solubility in non-polar solvents. This is largely due to their planar and rigid structure, which results in strong π - π interactions over the larger perylene core⁴⁰. As with NDIs, the solubility of PDIs can be enhanced by modifying the structure with various substituents. For instance, alkyl chains or bulky groups attached to the perylene core or imide nitrogen can increase solubility by disrupting π - π stacking and introducing steric hindrance, thereby enhancing solubility in both polar and non-polar solvents^{41, 42}.

A more unique strategy for tuning the solubility of NDIs and PDIs involves the incorporation of fluorine-containing substituents. Fluorine possesses unique chemical and physical properties, which can be exploited to finely adjust the solubility of these compounds. The specific influence of fluorine on solubility, along with its broader implications for molecular design, is discussed in greater detail in the subsequent section.

1.5 Organofluorine Chemistry

The study of organofluorine chemistry is an interesting field in crystal engineering, as the distinct characteristics of fluorine, like its strong carbon-fluorine bond, high electronegativity, and small atomic radius, can have a considerable impact on crystal structure. Despite the intriguing features, many aspects of how fluorine affects the arrangement of crystals, interactions between molecules, and structural organization are not thoroughly investigated. This section examines the characteristics and structural response of organofluorine compounds, exploring their possible uses and impacts on advanced crystal engineering.

Organofluorine chemistry is described as the chemistry focused on organic compounds that contain the carbon-fluorine bond. Organofluorine compounds have been utilised in many diverse applications, commonly seen in water and oil repellents, pharmaceuticals, refrigerants, catalysis chemistry and organic semiconductors. Pure fluorine is a greenish-yellowish gas it is highly toxic and extremely corrosive, where most organic compounds spontaneously combust or explode when in contact with dilute fluorine in ambient pressure. Fluorine's reactivity is in part due to the ease of its homolytic dissociation into radicals (37.8 kcal mol⁻¹) whilst also its high redox potentials of +3.06 V and +2.87 V, respectively, in acidic and basic aqueous media⁴³. Similar to its counterpart in group 7 fluorine is very electronegative and being the smallest of the halogens it is the most electronegative element (electronegativity 3.98⁴⁴). Fluorine exclusively maintains an oxidation state of -1, has a high electron affinity (3.448 eV⁴⁵), extreme ionization energy (17.418 eV⁴⁵), and retains a unique position in the periodic table being the first element with p orbitals which has the ability to achieve a noble gas electron configuration with the addition of one electron.

1.5.1 Carbon-Fluorine Bond

Fluorine has many differences when compared to other substituents including other halogens that occupy group 7. Due to this organofluorides have characteristic physical and chemical properties. The C-F bond is one of the strongest bonds in organic chemistry with an average energy of 480 kJ mol⁻¹ ⁴⁵. On average a C-Cl bond is around 320 kJ mol⁻¹ ⁴⁵ much less than comparable C-F bonds, these significantly stronger bonds mean fluororganic compounds have high thermal and chemical stability. As mentioned previously fluorine is highly electronegative making the C-F bond significantly polarised. Electron density will be concentrated around the fluorine which in turn leaves the carbon very electron poor. Ionic character is then introduced where each atom has partial charges (C⁵⁺-F⁵⁻), these charges are attractive leading to the large bond strength mentioned. The C-F bond is shorter than other halogen carbon bonds with an average length of 1.35 Å⁴⁵ which can be attributed to the ionic character. Polyfluorinated compounds experience almost no steric strain this is due to the low Van der Waals radius of fluorine being 1.47 Å⁴⁵ shorter the other substituents other than hydrogen. This aids in the high thermal stability and the efficient shielding of the carbon skeleton from attacking reagents giving additional chemical stability in polyfluorinated compounds. Fluorine also has the lowest polarizability of all atoms 0.56x10⁻²⁴ cm^{3 45} which causes very weak dispersion forces to be produced between polyfluorinated molecules. Often this can cause a reduction in the boiling point of these compounds when compared with protonated counterparts.

As mentioned, fluorine's high electronegativity allows for hydrogen bonding. This can be utilised when fluorine is a hydrogen bond acceptor where it can stabilise specific conformations by acting as a hydrogen bonding intermolecular bridge. 2-fluoroethanol is an example of the simplest form of this, this molecule is fixed in a *gauche* conformation in both the vapour phase and the liquid state. The internal hydrogen bonding contributes ~2 kcal mol⁻¹ to the conformational stabilisation⁴⁶, with the rest of the stabilisation being attributed to stereoelectronic effects. Quantitatively it is difficult to predict the strength of these hydrogen bonds because they depend on the specific interactions of the chemical environment. The strength of a typical C-F - - - H-O hydrogen bond is about half that of a normal O-H hydrogen bond⁴⁷ ~2.4 kcal mol⁻¹. As mentioned, fluorinated compounds, often prefer the *gauche* conformation over other conformations. A comparison between the *anti* and *gauche* conformation of 1,2-

fluoroethene⁴⁸ and butane⁴⁹ can be seen in Figure 9. The difference in Gibbs free energy shows how most organic materials will have the lowest energies in the anticonformation but organofluorine compounds prefer the *gauche* conformation. This phenomenon is due to hyperconjugation formation where electron density from the C-H σ bonding orbital is donated to the C-F σ * antibonding, stabilising the *gauche* effect. With fluorine's greater electronegativity, the C-H σ orbital is a better electron donor than the C-F σ orbital. Additionally, the C-F σ * orbital is a far better electron acceptor than the C-H σ * orbital. This concludes that the *gauche* conformation allows the best donor and the best acceptor to have the preferred overlap.

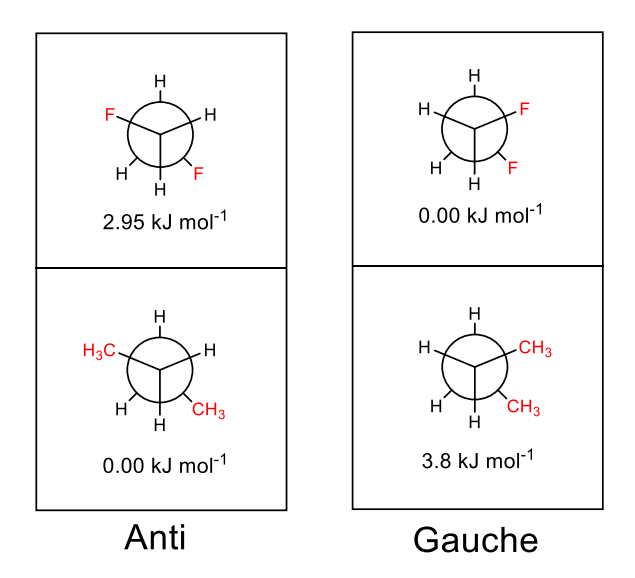


Figure 9: Anti and gauche conformations of butane and 1,2-diffuoroethane with the relative Gibbs free energies.

1.5.2 Organoflourine Compounds

Traditionally fluorocarbons are compounds that are comprised of only carbon and fluorine, sometimes referred to as perfluorocarbons. Perfluoroalkanes are very stable due to the strength of the C-F bond, the stability increases with the number of C-F bonds with each adjacent bond strengthening the skeletal C-C bonds through inductive effects. Fluorocarbons are colourless and highly dense they have low solubility in most organic solvents with some exceptions and are not miscible with water, the very low polarizability that arises due to the highly electronegative fluorine means they're not susceptible to fleeting dipoles that form dispersion forces. Fluorocarbons are among some of the most non-polar solvents in existence even though the C-F bond itself is highly polarised. This can be explained by the fact that

each local dipole that is produced by the C-F bond cancels out within the same molecule, this in turn will lead to the overall molecule being non-polar which can explain its lack of miscibility in water. Fluorine also maintains a slightly larger size when compared with hydrogen (23% larger Van der Waals radius)⁴⁵, which has a consequence for fluorocarbons structure and molecular dynamics. Traditional linear hydrocarbons will form a linear zigzag conformation, in contrast, fluorocarbons form helical structures seen in Figure 10. These structures are formed because of the steric repulsion of the electronically "hard" fluorine's bound to the carbons in a relative 1,3position. Another contrast is that linear hydrocarbon maintains some flexibility in their fluorocarbons rigid, rod-like backbone where are molecules. difluoromethylene groups will repulsively stretch causing the rigidity of the molecule.

A characteristic of fluorocarbons often observed is the extremely low surface tension that arises due to the weak intermolecular interactions. Fluorocarbons have the lowest surface tension of any organic liquids meaning they will wet almost any surface. This low surface energy is seen predominantly with poly(tetrafluoroethylene) (PTFE, Teflon) which is commonly used for anti-stick and low friction surfaces and other applications.

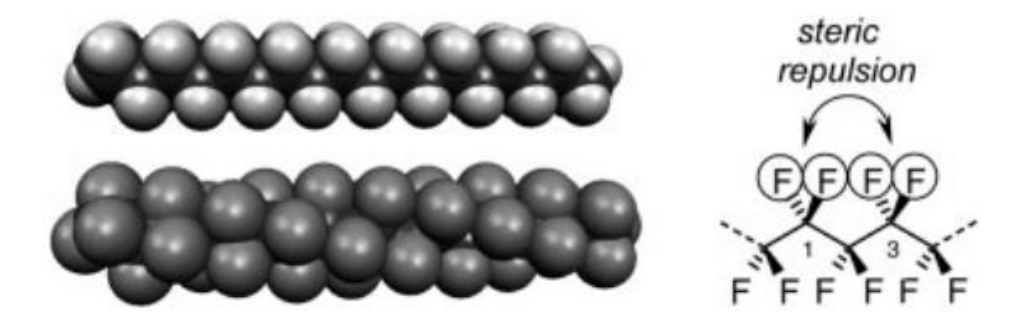


Figure 10: The zigzag conformation of octadecane (left above) compared with the helical perfluorooctadecane (left below)²⁷.

1.5.3 Fluorine Applications

Fluorine compounds have been extensively researched and utilised in many different industries. One of the first large scale uses of organofluorine compounds is infamously the use of chlorofluorocarbons (CFCs) as refrigerants in cooling applications⁵⁰. Another prominent application are polymers and lubricants with popular examples such as polytetrafluoroethylene (PTFE) (Teflon) discovered by R.J. Plunkett at DuPont in 1938. Another functional material that was discovered at DuPont is Nafion which is

a sulfonic acid derivative of a perfluorinated polyether. Nafion has been used for years as an ionic polymer membrane allowing for ion transport in chloralkali electrolysis cells.

1.5.4 Organic Electronics with Florine

As mentioned before fluoro-organic compounds have been used in many different applications, but most were developed many years ago, an emerging field that utilises these compounds is organic electronics. Fluoro-organic are being developed for a range of applications such as organic light emitting diodes (OLEDs)⁵¹, organic field effect transistors (OFETs)⁵² and organic photovoltaics (OPV)⁵³. Fluorine has not only been used as functional part of the organic semiconductor⁵⁴ itself but also as components for, self-assembled monolayers (SAMs)⁵⁵, dielectrics and even electroluminescent emitters.

1.5.5 Fluorine in Organic Field-Effect Transistors

In order for a device that has either holes or electrons injected through the source and the drain electrode to function efficiently the energetic barrier that can imped charge injection much be avoided. This means that depending on the semiconductor (p or n type) the energies of both the ionisation potential and electron affinity must match the work function of the contacting materials. With the addition of fluorination this issue can be alleviated because fluorine substituents in general maintain lower ionisation potential and electron affinity energies due to the inductive effects. With the addition of aromatic fluorination both the band gap and the absolute ionisation potential and electron affinity/ can be altered via the mesomeric effects of the additional fluorine. Another benefit if the addition of fluorine to organic semiconductors that by is lowering the orbital energy if the compound can increase its overall stability due to the lower work function that can be utilised for electron injection. Also, the interplanar distance of a π system can be influenced by aromatic fluorination⁵⁶, which can in turn cause the modification of the transfer integral through the overlapping of frontier molecular orbital overlap. When the extended π system contains fluorinated sections, they tend to have an affinity for electron-rich sections through quadrupolar interactions allowing for them to "stick". Not only is the molecular orientation effect but it also may lower the interplanar or aromatic edge to edge distances which also can significantly increase the transfer integrals. Favourable electron transfer can be increased because fluorination can change the supramolecular organisation, where examples go from a herringbone packing motif to an untitled π -stack⁵⁷. This has not only been utilised for small molecules but also for polymers, by alternating electron-poor and electron-rich regions a smaller band gap can be achieved whilst also allowing for closer stacking. This produced more crystalline polymers with subsequent higher charge carrier mobilities⁵⁸. To reduce the more anisotropic nature of small aromatic π -stacking molecules bulky substituents are introduced⁵⁹, then to stabilise the structure aromatic fluorination influences the stacking by interplanar interactions. Additionally weak bonds can occur between the highly electronegative fluorine and electropositive hydrogen⁶⁰, sulphur⁵⁹ (Figure 11), and halogens⁶¹ to further shape the final crystal structure by these weak electrostatic interactions.

Figure 11: The crystal structure of the dithienoanthracene derivative is controlled by the steric repulsion between the bulky triethylsilylethinyl substituents. The structure is stabilised by directed sulphur-fluorine and, presumably, fluorine–fluorine interactions³⁹.

OFETs require a dielectric to be used as the gate, fluorination can provide some advantages here. Firstly, majority of fluoropolymers have a very low dielectric constant, this can allow for the field induced charge carrier mobilities to be much higher most commonly seen in amorphous organic semiconductors. Secondly, due to the lower surface energy seen in these fluorinated compounds the morphology of the neighbouring semiconductor layer to be controlled larger distance compared with alternatives, this can benefit the charge carrier mobility and thus the overall performance of the OFET. Thirdly, many fluorinated polymers are soluble in fluorinated solvents where the other organic semiconductors are only solvent on hydrocarbon solvents. This allows printing of multi-layered devices with the reduction of any functional layers being dissolved or contaminated during the printing process.

1.6 Deposition Methods

The section on deposition methods offers a comprehensive examination of the various techniques employed in the deposition of organic semiconductors, a fundamental step in the fabrication of high-performance electronic devices. Accurate and controlled deposition is crucial for organic semiconductors to achieve optimal crystallinity, uniformity, and charge transport properties.

Improving the deposition conditions and methods for solution-based processes can improve charge transport in organic semiconductor films. This involves managing variables like concentration of solution, rate of solvent evaporation, temperature of substrate, and post-deposition processes (such as thermal annealing) to promote the creation of well-structured formations and enhance mobility of charge carriers. In order to achieve high charge carrier mobility and efficient charge transport in organic semiconductor devices, it is essential to carefully consider both the deposition technique and the resulting film morphology and crystallinity.

This section provides an in-depth analysis of a range of deposition techniques, including spin coating, meniscus-guided coating, and other non-contact methods. It critically evaluates the advantages, limitations, and potential implications of each technique on the scalability and performance of organic semiconductor devices, emphasising the pivotal role of deposition control in advancing the field of organic electronics.

1.6.1 Drop-casting

Drop-casting is a widely utilized technique for producing organic semiconductor (OSC) films. It is a simple, quasi-equilibrium process that relies on the evaporation of a

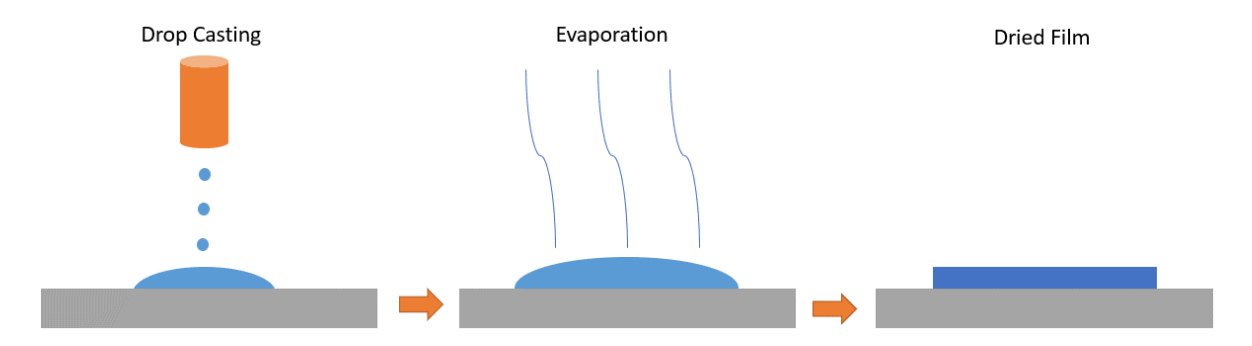


Figure 12: Sketch of the drop-casting method.

solvent to facilitate the deposition of the OSC as a thin film (Figure 12). OSCs with self-assembly properties can form crystalline films either directly during the drop-casting process or through additional steps. Over time, various modifications to this technique have been developed to enhance the quality of the resulting films.

One such modification involves the application of unidirectional sound waves that vibrate the sample during solvent evaporation. This approach has been shown to improve the electrical performance of the films by enhancing their crystalline quality 62. Other advancements in the drop-casting method focus on controlling the evaporation rate of the solvent, which can significantly impact the structure and performance of the resulting film. Solvent evaporation control can be achieved through several strategies, such as: surface treatments⁶³, inert gas purging⁶⁴, sealed chambers⁶⁵ and azeotropic mixtures⁶⁶. Drop-casting is a simple, cost-effective, and rapid technique for producing organic semiconductor films. However, despite its ease of use and low cost, it has a significant limitation. Even under optimal conditions, dropcasting often suffers from variations in evaporation rates, leading to the formation of the well-known "coffee-ring effect" commonly observed in droplet-based deposition methods^{67, 68}. This effect results in films and crystals with uneven thickness and nonuniform crystal structures, which can substantially impair the overall performance of the organic semiconductor. Additionally, the confined size of sessile droplets restricts the scalability of this technique, making it challenging to produce films on a larger scale, thereby limiting its application in industrial processes.

1.6.2 Spin Coating

An alternative technique frequently employed for the production of OSC films is spin coating. In this process, a solution containing the OSC is deposited onto a substrate, which is then rotated at high revolutions per minute (RPM). The centrifugal force generated by the spinning causes the solution to spread uniformly across the surface, followed by the evaporation of the solvent, resulting in the formation of a thin, uniform film⁶⁹. The thickness of the film depends on various properties of the solution, including viscosity and concentration, but spin coating is generally effective in producing larger, more uniform films compared to other methods like drop-casting.

Yuan *et al.* introduced a modification to the standard spin coating technique to create ultra-high mobility transparent films^{70, 71}. Their approach, referred to as the "off-centre"

method (Figure 13), involved placing the substrate 20 to 40 mm away from the central axis of rotation. This adjustment leveraged the centrifugal force to promote unidirectional alignment, improving the crystallisation of the film and significantly enhancing its performance. Their method resulted in devices with exceptional average charge carrier mobilities exceeding 20 cm² V⁻¹ s⁻¹ ⁷¹.

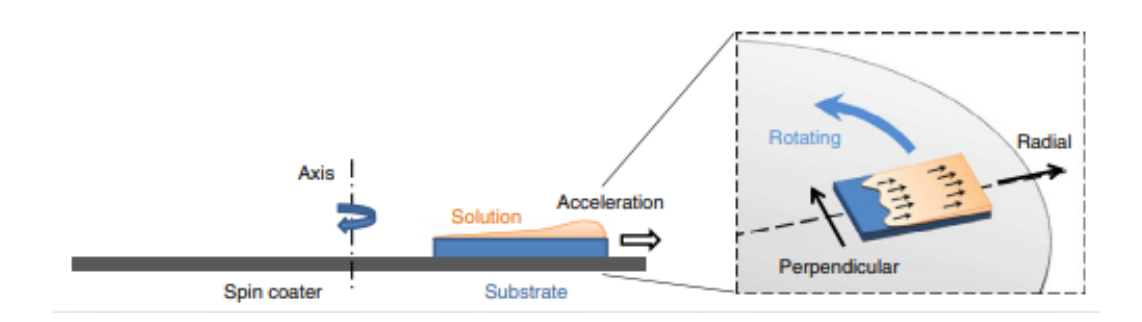


Figure 13: Schematic illustration of the OSC process, in which the substrates are located away from the axis of the spin-coater⁴⁷.

While spin coating is commonly employed to deposit the active layer in organic semiconductor devices, a recent study demonstrated a promising one-step approach that can simultaneously deposit both the semiconducting and dielectric layers. This method utilised vertical phase segregation, coupled with the self-assembly properties of the OSC, to achieve an enhanced film morphology. The improved morphology contributed to better device performance and reduced manufacturing costs.⁷². Despite these advancements, challenges remain, including the relatively poor thermal stability of these devices and inherent difficulties associated with fabricating multilayer structures using spin coating⁷³.

1.6.3 Meniscus-guided Coating

Several types of meniscus-guided coating techniques are commonly employed in the deposition of organic semiconductor films, all of which operate on a similar underlying principle. These methods utilize a solution meniscus, which serves as an air-liquid interface, playing a critical role in directing solvent evaporation. The process typically involves the linear motion of either the coating tool or the substrate, which induces the alignment of the crystal structure in the deposited film. As the solvent evaporates, the solution becomes progressively more concentrated, eventually reaching a point of supersaturation. At this stage, the solutes are deposited onto the substrate as a thin film.

The linear movement in these techniques plays a crucial role in guiding the alignment of the growing film, effectively controlling the crystallisation process. This ability to manage crystallisation is particularly valuable for achieving films with high structural order, which is essential for optimal electronic properties in organic semiconductor devices. By influencing the orientation and arrangement of molecules within the film, meniscus-guided coating techniques offer a precise method for enhancing film morphology and improving device performance⁷⁴.

1.6.3.1 Dip Coating

Dip coating is a widely used alternative deposition technique for processing OSC films. This technique involves immersing a substrate into a container filled with an OSC solution, followed by the gradual withdrawal of the substrate. As the substrate is removed from the solution, the solvent evaporates, leaving behind a thin OSC film. Key parameters, such as the withdrawal velocity and the temperature of the solution, significantly influence the development of concentration gradients and fluid flow within the meniscus, which in turn affect the quality of the resulting film.

Controlling these parameters precisely can be challenging, making it difficult to consistently achieve homogeneous films. However, research by Kim et al. demonstrated the significant impact of optimizing process timing on film production⁷⁴. Their study revealed that improved film morphology could be achieved by leaving the substrate at the edge of the solvent chamber for a period of "residual time" before fully removing it (Figure 14)⁷⁴. This adjustment allowed for more controlled solvent evaporation and enhanced crystallinity in the final film, thus contributing to better overall device performance.

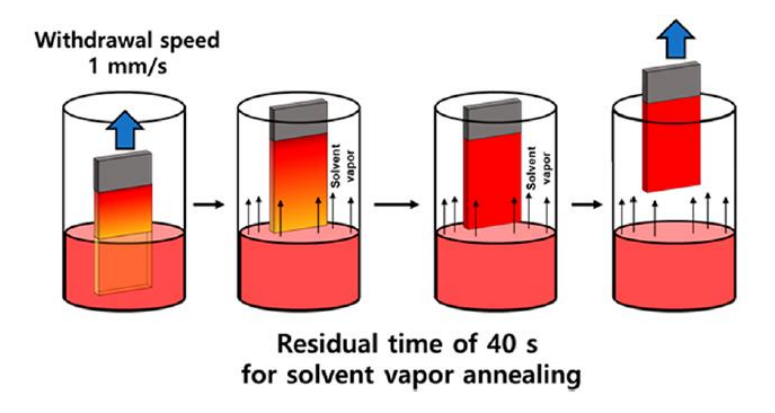


Figure 14: Schematic illustrating how the dip-coating method⁷².

Another effective approach to enhancing film performance is through the careful selection of solvents. The use of azeotropic solvent mixtures, in particular, has been shown to significantly improve film morphology and, consequently, device performance. A notable example of this was demonstrated by Rogowski et al., who synthesized high-performance 6,13-bis(triisopropylsilylethynyl)pentacene (TIPS-PEN) ribbons using a combination of controlled dip-coating speed and azeotropic binary solvent mixtures⁷⁵.

1.6.3.2 Zone Casting

Zone casting is a deposition technique adapted from the zone refining process, historically used for producing high-purity single crystals inorganic of semiconductors⁷⁶. This method has been successfully applied to OSCs by utilising a heated tip or wire to melt a pre-formed solid. The molten solution is then deposited onto a moving substrate, where the solvent evaporates, leaving behind a thin, ordered solid film. Key parameters such as substrate velocity, the volume of solution deposited, and the rate of solvent evaporation play crucial roles in determining the film's thickness, crystallinity, and molecular alignment, as illustrated in Figure 15⁷⁷. While zone casting offers potential for creating highly ordered films, it also presents significant challenges. Achieving uniformity across the entire film is difficult due to the complex interplay of process variables, often resulting in films with defects.

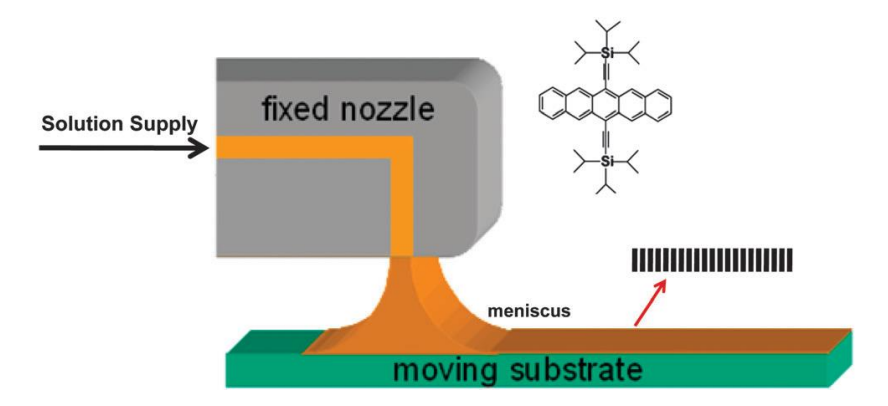


Figure 15: Schematic representation of the zone-casting technique⁷⁵.

1.6.3.3 Hollow-pen Writing

A recently developed deposition technique, known as hollow-pen writing or capillary pen writing, operates on a principle similar to that of a conventional ballpoint pen. As illustrated in Figure 16, the "pen" is typically mounted on an XYZ controller, which can be programmed to create complex film patterns⁷⁸. The movement of the "pen" across the substrate induces alignment in the organic semiconductor (OSC) film, with the substrate often heated to promote faster solvent evaporation and to maintain proper film alignment. This technique's effectiveness is highly dependent on the dimensions of the "pen," as they directly influence the precision of film deposition and alignment. However, a notable limitation of hollow-pen writing is that the film thickness may vary when the pen changes direction. This variation can introduce inconsistencies in the film's morphology, potentially affecting the uniformity and performance of the resulting OSC films.

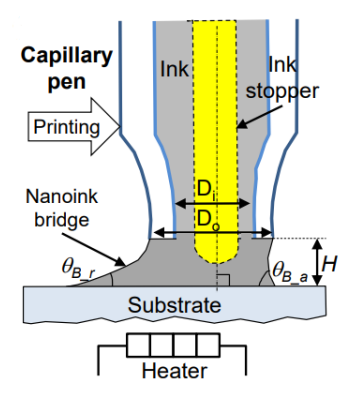


Figure 16: Nanoink bridge induced capillary printing concept⁷⁶.

1.6.3.4 Solution Shearing and Blade Coating

Solution shearing and blade coating are highly versatile techniques widely used for depositing OSC) films. Blade coating involves a solid blade that passes over a reservoir containing the OSC solution, leaving a uniform layer of material behind as the solvent evaporates. In contrast, solution shearing utilises a shearing blade that holds the OSC solution over a temperature-controlled substrate. As the blade moves at a fixed velocity, a portion of the solution meniscus is exposed, allowing solvent evaporation and film deposition to occur. The key difference between the two methods lies in the angle of the blade, which, in solution shearing, limits solvent evaporation to the edges of the film while the bulk solution remains largely unaffected.

The kinetic nature of solution shearing allows for the formation of metastable structures, which can influence the crystallinity and morphology of the deposited film. Giri et al. demonstrated the potential of this technique by synthesizing "lattice-strained" crystal structures. By simply increasing the shearing speed, they were able to reduce the π - π stacking distance in TIPS-pentacene from 3.33 Å to 3.08 Å, significantly altering the material's properties and demonstrating the fine control this method offers over molecular arrangement. Solution shearing, therefore, provides an efficient means of producing highly ordered films with tailored structural properties, making it a valuable technique for improving the performance of OSC devices⁷⁹.

This method has been modified by Diao *et al* and was named "fluid-enhance crystal engineering", or FLUENCE. To enhance the polymer crystallinity without increase domain size flow induced nucleation was utilised. This was achieved by using a shearing blade that was patterned with pillars, which induced molecular alignment as the polymer chains elongated under the shear forces as shown in Figure 17⁸⁰.

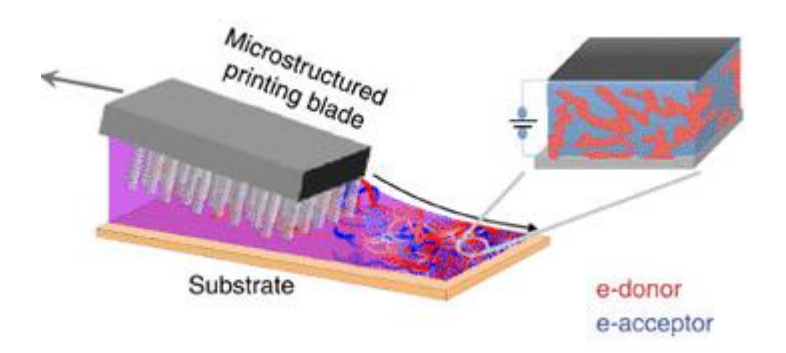


Figure 17: Schematic of the FLUENCE method implemented on the solution shearing platform⁷⁸.

Another approach to solution shearing used an electrified blade to aid in molecular alignment. The electrified blade (Figure 18) and the substrate have a maintained electrical potential difference, as the blade is moved at a constant velocity⁸¹. This

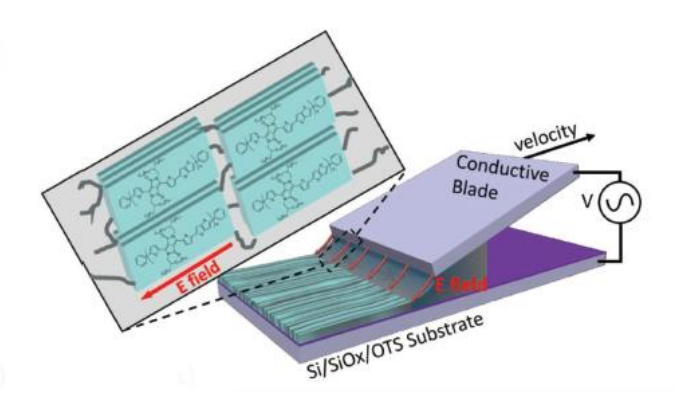


Figure 18: Sketch of the E-blade setup⁷⁶.

showed improved backbone alignment in the direction of the electrical field, adding more control over the searing method. Solution shearing shows improved molecular alignment control over the previous techniques, but also increases the complexity.

1.6.4 Printing

In this context, printing refers to a crystallisation control method that prioritises largearea deposition with precise spatial control, while not relying on meniscus-driven coating as the primary mechanism for regulating film formation. Instead, printing techniques focus on controlled material deposition patterns and the management of solvent evaporation to influence crystallisation, allowing for tailored film morphology across large surfaces.

1.6.4.1 Inkjet Printing

One area of significant research focus is inkjet printing, a technique that involves the precise ejection of ink droplets from a reservoir using either a thermal or piezoelectric process. Each droplet, containing the OSC material, is deposited onto a substrate, where it subsequently dries, akin to the previously discussed drop-casting method. To ensure effective droplet formation and deposition, several parameters must be carefully optimised, including ink surface tension, substrate surface energy, ink viscosity, and droplet deposition dynamics. When executed with precision, inkjet printing can offer substantial control over droplet spreading and fluid momentum, allowing for fine-tuned crystallisation and film formation.

However, like drop-casting, inkjet printing is susceptible to issues such as inhomogeneities in the dried film. These inconsistencies can result from variations in solvent evaporation rates or from surface tension gradients in mixed solvent systems. To address these challenges, Minemawari et al. introduced a novel approach, using a multi-solvent process in which an antisolvent is first deposited, followed by the OSC solution on top to form a controlled mixture (Figure 19)⁸². This method significantly improved the uniformity of film thickness and promoted the growth of highly ordered

crystals, demonstrating the potential of inkjet printing for producing high-quality OSC films with enhanced performance.

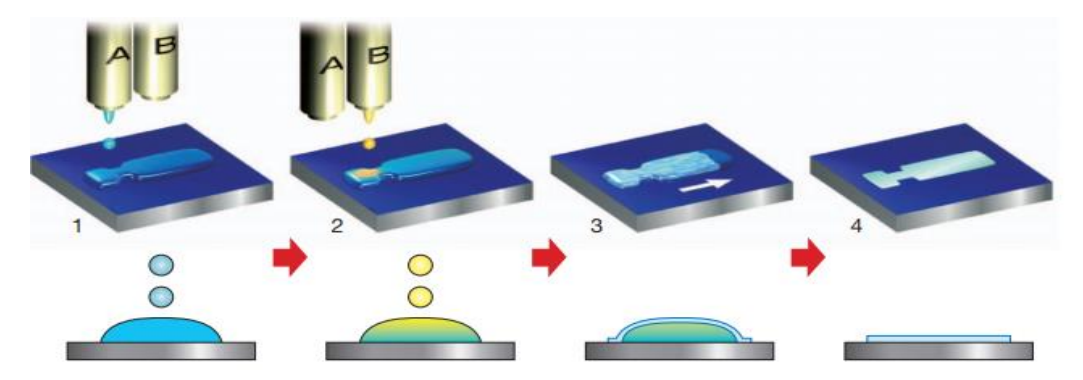


Figure 19: Schematic of the process. Antisolvent ink (A) is first inkjet-printed (step 1), and then solution ink (B) is overprinted sequentially to form intermixed droplets confined to a predefined area (step 2). Semiconducting thin films grow at liquid—air interfaces of the droplet (step 3), before the solvent fully evaporates (step 4)⁸⁰.

1.6.4.2 Spray Coating

Spray coating, similar to inkjet printing, involves the ejection of a solution to produce droplets that are deposited onto a substrate. However, a key distinction between the two methods is that spray coating forms small droplets through aerosolization, using an inert gas carrier to disperse the solution. This technique is governed by several critical parameters, such as surface tension, viscosity, temperature, and concentration, in addition to the spray nozzle's size and shape and the atomization gas pressure. As the aerosolized droplets reach the substrate, they dry quickly, forming thin, continuous films. To enhance the performance of spray-coated devices, Pitsalidis et al. employed electrostatic spray deposition. This method utilizes electrohydrodynamic atomization, in which the liquid is ejected through the nozzle under the influence of an electric field (illustrated in Figure 20)83. By using a solution mixture of conducting polymers and small molecules, this technique produced highperformance films with continuous, well-ordered crystalline structures and reduced device-to-device variation. Despite these advancements, one of the persistent challenges with spray coating is the variability in film thickness, which can result in decreased device performance due to poor electrical contacts. Achieving uniformity in film thickness remains a critical area for further refinement.

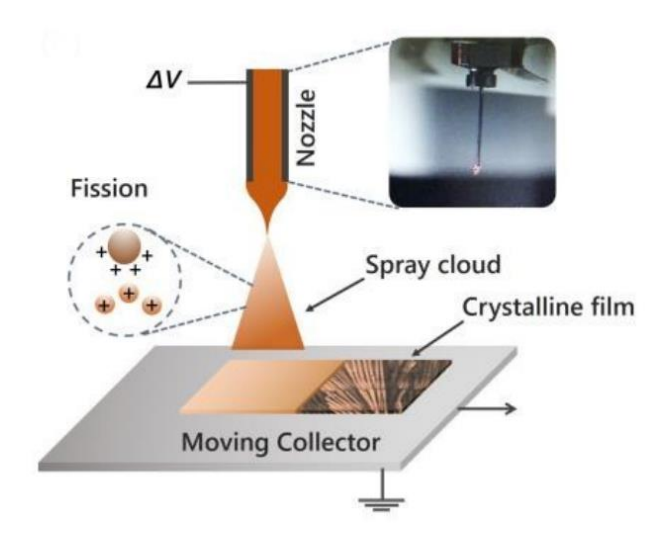


Figure 20: Illustration of the electrospray printing method. The inset photograph shows a magnified view of the nozzle during spraying⁸¹.

The study of deposition methods provides a foundation for understanding how organic semiconductor films are formed, emphasising the importance of crystallisation control, film uniformity, and charge transport properties. However, a deeper understanding of the dynamics at play within the deposition process, particularly the behaviour of liquid droplets, is essential for further optimising film morphology and performance. The subsequent section focuses on the critical role that droplet behaviour plays in determining the quality and uniformity of organic semiconductor films.

1.7 Droplets

The behaviour of droplets is a critical factor that significantly influences film uniformity, crystallinity, and overall electronic performance. This section offers an in-depth analysis of the fundamental principles governing droplet dynamics, including key concepts such as contact angles, wetting phenomena, and the coffee-ring effect. These principles are essential for achieving precise control over the deposition process, particularly when striving for reproducibility and high-quality outcomes. Furthermore, this section examines the influence of Marangoni flows—both thermal and solutal—on droplet motion and evaporation patterns, providing insights into how these mechanisms can be harnessed to optimize droplet behaviour during semiconductor deposition. A comprehensive understanding of these processes is crucial for the development of innovative deposition techniques that can enhance the uniformity, and overall quality of organic electronic devices.

1.7.1 Contact Angle and Wetting

Wetting refers to the process where a liquid droplet comes into contact with a solid surface without obstruction, achieving a balanced state determined by the interactions between the liquid, solid, and surrounding vapor. The degree of wetting depends on the energy interactions involved: high-energy interactions promote wetting, while low-energy interactions inhibit it⁸⁴. In the absence of external factors, a droplet typically assumes a spherical cap shape to maximize surface area, a behaviour explained by the Young-Dupré equation (Equation 7):

$$\gamma_{\rm sv} = \gamma_{\rm sl} + \gamma_{\rm lv} \cos \theta_{\rm c} \tag{7}$$

In this equation θ_c represents the contact angle formed between the liquid and the solid surface, while γ_{sv} , γ_{sl} and γ_{lv} represent the surface tensions between the solid-vapor, solid-liquid, and liquid-vapor phases, respectively (Figure 21). For a stable contact angle, these three tensions must be in balance at the droplet contact line, similar to mechanical tension forces acting to minimize the liquid surface area and bring the system to equilibrium.



Figure 21: Differing wettability's of droplets on different surfaces. A droplet on (a) a high energy surface and (b) a low energy surface.

1.7.2 Coffee-Ring Effect

Many may have noticed, although perhaps not reflected upon, that when a drop of coffee dries, most of its residue accumulates along the outer edge of its original shape. This phenomenon, known as the coffee-ring effect (CRE), results in the formation of a ring-like pattern, as illustrated in Figure 22. When the vapor surrounding a droplet is not fully saturated, evaporation occurs, affecting the droplet's physical properties due to its small size. As the droplet evaporates, capillary-driven flow emerges, liquid from the centre of the droplet moves outward to replace the liquid evaporating at the edges. This outward flow carries the non-volatile components that are dispersed in the droplet toward the edge, where they are deposited, forming the characteristic CRE pattern⁸⁵.

⁸⁶. For CRE to occur, three conditions must be met: the droplet must evaporate, it must have a non-zero contact angle, giving it a spherical cap shape, and the contact line must be pinned.

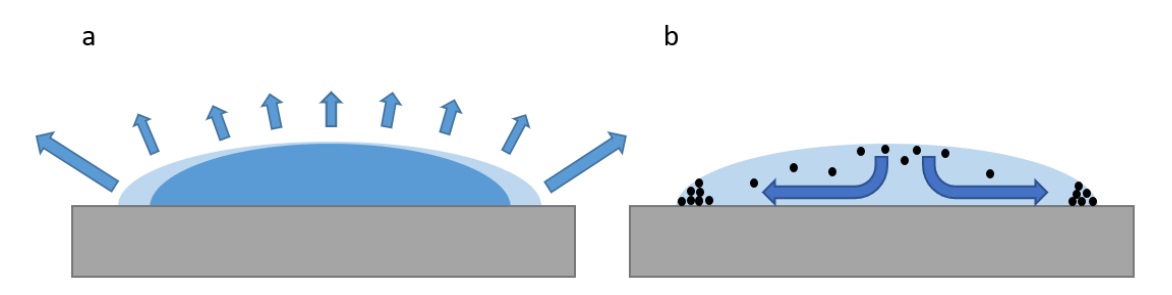


Figure 22: visual representation of the CRE a) The rate of evaporation happens faster at the droplets edges. b) Solids being deposited at the edges due to flows produced form the CRE.

Controlling the CRE has been the focus of considerable research^{67, 68, 87-89}, as it often hinders the uniform distribution of materials, which can be detrimental in various applications. The next section discusses the use of Marangoni flows to disrupt the CRE and how these can be induced in a droplet.

1.7.3 Marangoni Flows

Understanding Marangoni flows is crucial for comprehending droplet behaviour during evaporation and for effectively managing how suspended particles are deposited, while simultaneously suppressing the CRE. Marangoni flows are characterized by fluid movement driven by variations in surface tension at the interface between two phases, typically liquid/gas or liquid/liquid. These surface tension differences can arise from either temperature changes (thermal Marangoni effect) or concentration changes (solutal Marangoni effect). In simple terms, Marangoni flows occur when surface tension gradients are created due to temperature or concentration differences, causing liquid to flow from regions of lower surface tension to regions of higher surface tension.

As shown in Figure 23, these liquid flows can effectively counteract the typical capillary-driven outward flow responsible for CRE, leading to more uniform deposition of suspended particles⁹⁰.

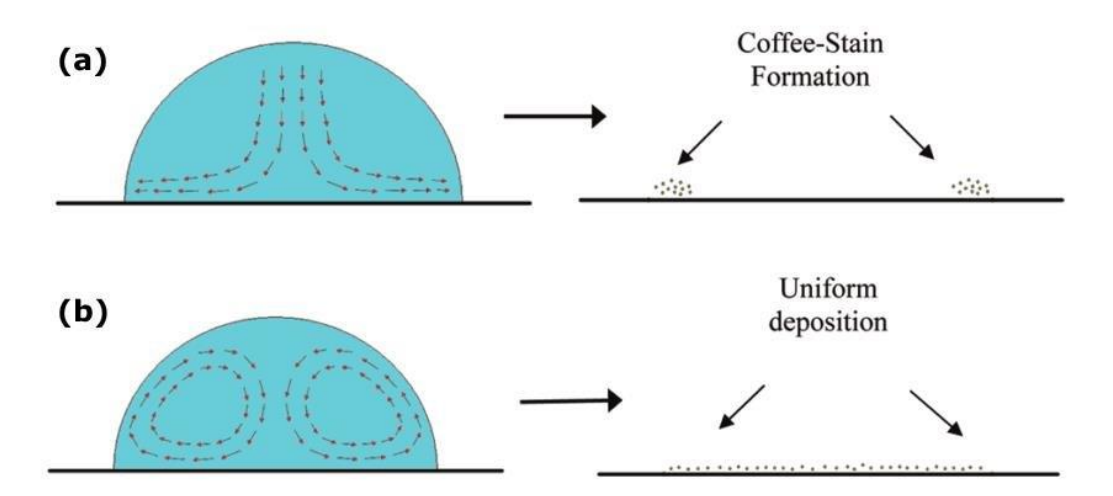


Figure 23: Evaporation of a colloidal drop under standard ambient conditions: (a) outward flow in a droplet creates a coffee-ring stain; (b) recirculating Marangoni flow creates a uniform pattern⁸⁵.

1.7.3.1 Thermal Marangoni Flows

One method to manipulate Marangoni flows is by introducing thermal gradients to droplets. This can be achieved by heating the substrate beneath the droplet, which raises the temperature at the base and lowers the surface tension at the edges, thereby generating cyclic flows within the droplet^{91, 92}. Research has shown that these thermal-induced flows can be complex, with some studies reporting either an increase⁸⁷ or decrease⁹³ in the CRE depending on the system. For instance, smaller particles may experience an increased CRE, while larger particles or fully dissolved substances may exhibit a reduction in the effect.

Non-uniform heating can further create asymmetrical flows, particularly when only one side of the substrate is heated. This results in solid deposition occurring on the cooler side of the droplet due to the induced flow patterns⁹⁴. A more refined approach involves using lasers to apply localized heating, enabling temperature changes and providing enhanced control over the deposition process. The rapid response time of lasers allows for real-time adjustments to droplet deposition, leading to greater precision in controlling particle distribution⁹⁵. While temperature regulation offers several benefits, it can also introduce challenges. Techniques that rely on thermal manipulation can be difficult to control, and non-uniform heating may lead to

unintended effects. Methods such as laser heating offer more precision but also require more complex arrangements, motivating the exploration of alternative techniques for more efficient and controllable deposition processes.

1.7.3.2 Solutal Marangoni Flows

The physics of droplets is highly sensitive to variations in their chemical composition, particularly due to their small size. Even minor changes can lead to significant alterations in surface tension. When two pure liquids are mixed, the surface tension of the resulting droplet typically varies within the range of the original surface tensions of the two liquids. For instance, in a mixture of ethanol and water, the surface tension of water is approximately three times greater than that of ethanol. As a result, a droplet formed from such a mixture can exhibit a wide range of surface tensions.

This variation in surface tension can be dynamically induced and maintained, particularly by employing solvent mixtures with differing boiling points and evaporation rates. As these solvents evaporate at different rates across the droplet's surface, Marangoni stresses arise, driving flows within the droplet. However, these flows can sometimes become chaotic, especially when volatile solvents are used, making it difficult to maintain precise control⁹⁶. To mitigate this issue, non-volatile solvents are often preferred, as they offer better control over droplet behaviour while still allowing for reasonable evaporation timescales in smaller droplets. This balance between solvent volatility and control is critical for optimising droplet dynamics in various applications^{97, 98}.

1.8 Mobile Droplets

A simple and commonly observed method for droplet movement is gravity-driven motion, where a droplet on an inclined surface will roll or slide downward. However, droplets can move through a variety of other mechanisms, many of which offer greater control and enable more complex functions. Since droplets are self-contained systems, controlling their motion can facilitate tasks such as stirring, mixing, or dividing, which are essential for a range of applications. The following sections will explore several of these advanced techniques, highlighting how droplet motion can be harnessed for more intricate operations in various scientific and technological contexts.

1.8.1 Methods of motion

One of the key challenges in inducing droplet motion is overcoming contact angle hysteresis. Contact angle hysteresis refers to the difference in the contact angle of a liquid droplet on a solid surface when it is either advancing (spreading) or receding (contracting) on the surface. In simpler terms, it describes the variance between the advancing and receding contact angles, which can impede droplet movement. This concept implies that effective droplet motion can either be achieved by overcoming or minimizing the effects of contact angle hysteresis.

There are several mechanisms that can induce droplet motion by addressing this barrier. Some examples include motion driven by thermal gradients, surface gradients in wettability, the use of gravity on inclined surfaces, and gradients in chemical surface tension (as discussed in the *Solutal Marangoni Flows* section). Each of these methods leverages different physical principles to either overcome or reduce contact angle hysteresis, allowing for controlled droplet motion across surfaces.

1.8.1.1 Surface Wettability

In the *Contact Angle and Wetting section*, it was discussed that a droplet on a uniform surface adheres to the Young-Dupré equation, resulting in consistent wetting in all directions. However, when a droplet is placed on a surface with uneven adhesion, it will be energetically driven to move toward areas of greater wettability. This behavior can be exploited to control droplet movement by directing it toward regions with higher surface energy, which may be achieved through gradients in roughness⁹⁹ or hydrophobicity¹⁰⁰. To optimise this technique, it is essential to have precise control over the droplet's motion, which can be accomplished by manipulating the surface's wetting properties.

One approach to achieve this control is by chemically modifying the surface to switch between different states. For instance, surfaces coated with compounds containing photoisomerisable groups can become more hydrophobic under UV light and return to their original state under blue light, as shown in Figure 24¹⁰¹. Another method involves molecular motors that display hydrophobic groups on a functionalized surface, producing a similar effect to the photoresponsive technique¹⁰². Additionally, electrochemical methods can alter surface wettability by adjusting the voltage applied to the substrate, though this approach requires the entire system (substrate and

droplet) to be immersed in an electrolyte, as the mechanism relies on an electrochemical reaction 103.

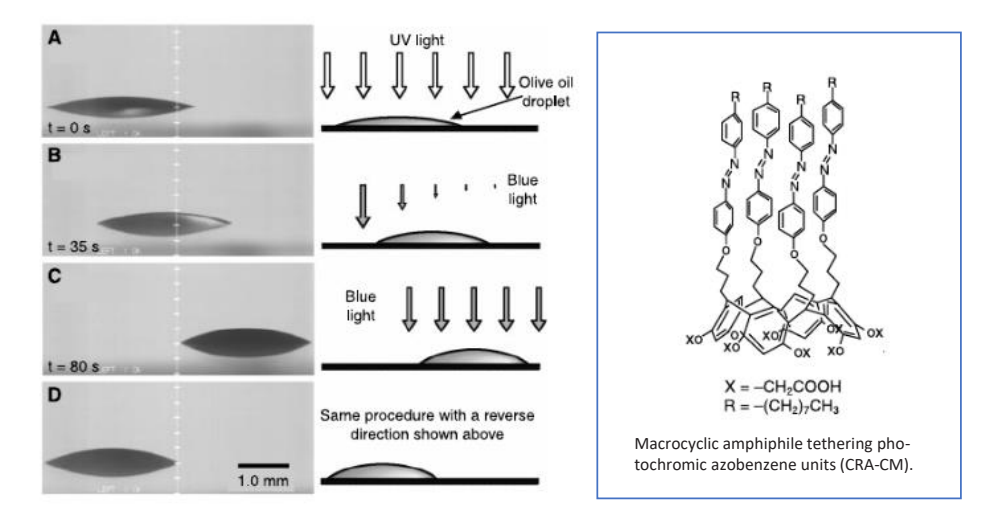


Figure 24: Lateral photographs of light-driven motion of an olive oil droplet on a silica plate modified with CRA-CM. The olive oil dropleton a cis-rich surface moved in a direction of higher surface energy by asymmetrical irradiation with 436-nm light perpendicular to the sur-face. (A to C) The sessile contact angles were changed from 18° (A) to 25° (C). (D) The moving direction of the droplet was controllable by varying the direction of the photoirradiation⁹⁷.

Electrowetting is another technique used to modify surface wettability. In this method, a voltage is applied to a specific solid-liquid interface, reducing the contact angle by redistributing dipoles and altering the surface tension¹⁰⁴. However, electrowetting is limited to certain types of surfaces and requires a fully connected circuit, meaning a conductive cable must be applied to the droplet.

1.8.1.2 Thermally Driven Motion

One of the most well-known and striking examples of unconstrained droplet motion is the Leidenfrost effect, where a droplet of water placed on a surface much hotter than the boiling point of the liquid can move freely. In this phenomenon, the droplet hovers on a cushion of its own vapor, with no contact angle between the liquid and the surface, allowing for nearly frictionless motion in any direction.

A different approach to inducing droplet motion at cooler temperatures involves utilizing surfaces with low contact angle hysteresis in combination with thermal gradients. In this method, as the surface heats up, it alters the surface tension around the droplet's edges, generating Marangoni flows. These flows, particularly when uneven heating is applied to one side of the droplet, can overcome contact angle

hysteresis, causing the droplet to move from the hotter to the cooler side due to viscous drag¹⁰⁵.

Recent studies have explored the use of specialized surfaces with inherently low contact angle hysteresis, which respond dynamically to external heating sources such as lasers¹⁰⁶ and hot objects¹⁰⁷. This technique allows for precise control of 2D droplet movement via the management of Marangoni flows induced by the localized heat source. While this method offers excellent control over droplet motion, it presents a limitation when scaled up due to the specificity and complexity of the surface required, thus restricting its broader applicability.

1.9 Binary Droplets

The majority of methods discussed in Section 1.6 rely on the substrate to control and manipulate droplet behaviour, offering minimal to no direct control over the droplet itself. However, as outlined in Section 1.8.1, droplets can also be manipulated using more indirect techniques. For instance, binary droplet systems, which consist of two compatible liquids, have the potential to generate powerful internal Marangoni flows, enabling internal droplet motion. Only recently have researchers begun to explore the full impact of these flows for use in advanced systems. Sections 1.9.1 and 1.9.2 discuss how surface tension and compositional gradients within these binary systems can create motion in droplets, revealing new avenues for controlling and harnessing droplet dynamics in innovative applications.

1.9.1 Surface Tension and Compositional Gradients

As discussed in the section on the Coffee Ring Effect, droplets tend to evaporate more rapidly at the edges while evaporation within the bulk is slower. In the case of binary droplets, composed of two solvents with different vapor pressures, this leads to a disparity in evaporation rates and subsequently creates a compositional gradient along the droplet's interface. As evaporation continues, this compositional gradient is sustained. The direction of internal flows within the droplet is determined by the vapor pressures of the two solvents and their respective surface tensions, as illustrated in Figure 25. If the more volatile solvent has a higher surface tension than the less volatile one, the droplet will shrink, indicating that it remains under continuous tension, which can enable the droplet to move. Conversely, if the more volatile solvent has a lower surface tension, the droplet will spread outward across the substrate. This interplay between evaporation rates, surface tension, and solvent volatility defines the droplet's behaviour and can be leveraged for precise control of droplet movement and deposition in various applications.

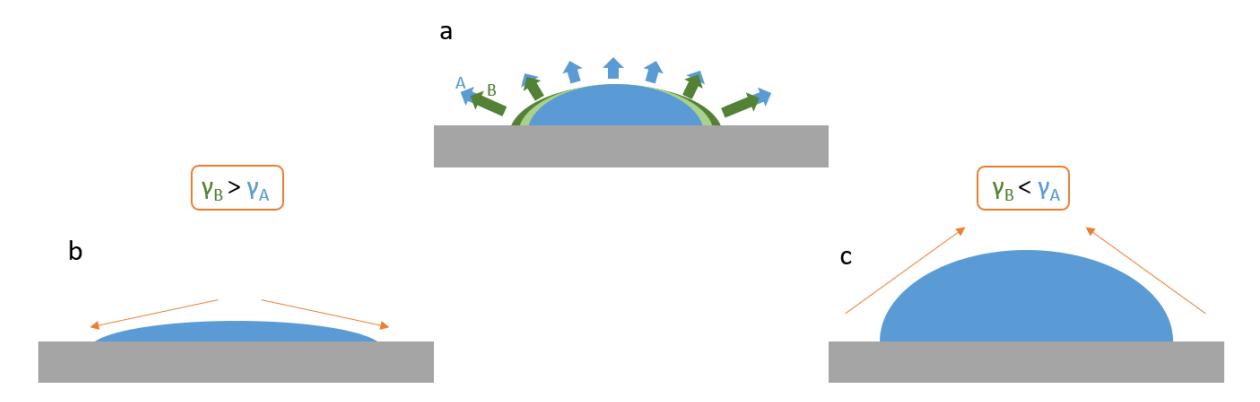


Figure 25: a) droplets have higher evaporation at the edges, if the droplet consists of two components with different vapour pressures, A and B, there will be a natural composition gradient produced. b) If the more volatile component, A, has a lower surface tension than B, there will be an increased surface tension puling the droplet outwards. (c) If the more volatile component, A, has a higher surface tension, the droplet contacts pulling it inwards.

1.9.2 Motion

When droplets are in a contracted state, as described in the previous section, they can exhibit motility. This is primarily due to their extremely low or even zero contact angle hysteresis¹⁰⁸. The Marangoni forces generated by compositional gradients in binary droplets further reduce the influence of surface roughness on contact angle, unlike in single-component droplets. This reduction in contact angle hysteresis makes it much

easier to induce motion in binary droplets. These droplets become highly sensitive to small external forces, such as minor inclines, and, more importantly, to internal Marangoni stresses driven by imbalanced evaporation.

As the droplets evaporate, they create their own vapor gradients, enabling them to interact with nearby droplets. This leads to a sensing mechanism where droplets in close proximity can exert forces on one another, as observed by Cira *et al.* in experiments with water/propylene glycol droplets of varying concentrations¹⁰⁹. In these cases, droplets were seen to move toward each other over distances several times their diameter, driven by the evaporation of water vapor. When droplets with similar concentrations meet, they coalesce, but if their concentrations differ, they do not immediately merge. Instead, due to differences in surface tension, the droplet with higher propylene glycol content will trail the one with a lower concentration¹¹⁰.

This section provides critical insights into the behaviour of droplets on different surfaces and under various conditions by examining the roles of contact angles, wetting, and Marangoni flows. This knowledge is instrumental in enhancing non-contact vapor-guided deposition techniques discussed later in the thesis. By understanding how internal flows within droplets can be manipulated, these behaviours can be harnessed to improve the crystallisation process of organic semiconductor materials, potentially leading to improved crystallinity and uniformity in organic semiconductor crystals and films.

1.10 Scope & Aim

The aims of this thesis are sorted into two categories: The synthesis of water soluble and fluorinated OSCs, and the deposition of these OSCs using a novel non-contact vapour guided deposition technique. As discussed in the literature by developing deposition techniques the performance of OSCs can be significantly improved. The chapter are presented as follows:

Chapter 3 – Synthesis of Water-Soluble Perylene diimides and Naphthalene diimides and their Deposition

Chapter 3 initially investigates the synthesis of carbocyclic acid terminated PDIs as a proposed method for water solubility. These can then be deposited using the novel non-contact deposition technique to produce OSC films. With the use of varying amino

acids PDIs can be terminated with carboxylic acids and additional functional groups to produce OSC for different functionalities. This chapter then transitions onto the synthesis of water soluble OSC centred around NDIs with glycol terminated end groups. Single crystals are then formed through a novel non-contact vapour guided deposition technique utilising surface tension gradients to move droplets with dissolved OSC that then crystallise in-situ. The crystal structures that are formed during the novel deposition and through solution evaporation are then compared. Additionally, the novel deposition is then used to deposit NDIs with shorter and longer glycol chains to assess the performance of other OSCs.

Chapter 4 – Synthesis and Characterisation of Fluorinated Naphthalenediimide

Chapter 4 explores the synthesis of fluorinated linear and branched NDIs. The crystallisation potential of these compounds is compared against the changes that occur due to the additional fluorination. The electrical properties of these compounds are compared against both linear alkylated and glycol terminated NDIs to identify the effects fluorination has on their performance.

2. Methodology

The methodology section of this thesis outlines the experimental procedures and techniques used to investigate the deposition of organic semiconductors, with a particular focus on the innovative non-contact vapor-guided deposition technique. This technique utilises surface tension gradients to precisely control droplet movement and crystallisation processes, enabling the formation of highly ordered organic semiconductor films and crystals. The section provides a comprehensive account of the preparation of substrates, including surface treatments and chemical modifications, as well as the manipulation of droplets using a custom microscope setup.

2.1 Slide Preparation

Slide preparation is critical to ensuring that the droplet movement is unhindered and reproducible. Glass microscopy slides (Thermo Fischer) 25×75 mm must be cleaned to remove any impurities present and allow for a smooth surface for droplet movement. By removing as many contaminants as possible the form the substrate this reduces the pinning observed when droplets encounter any foreign objects.

The slides are sonicated in acetone in a glass Coplin jar for 5 minutes. They are then sonicated again in water for another 5 minutes, after which the water is removed, and water with teepol detergent is added and sonicated for 15 minutes. Another water wash is performed to remove any residual detergent, and the slides are dried using pressurised nitrogen gas. These slides are then placed in an ozone cleaner for 10 minutes and put in a clean glass Coplin jar until used in the microscope set-up. The ozone cleaner effectively removes any remaining organic contaminants left on the substrate after the initially cleaning in the effort to make a contaminate free surface. All slides were used within one day or discarded, this was done to ensure consistency in the removal of any contaminants. All the water used is deionised to the same standard ($\geq 18 \text{ M}\Omega.\text{cm}$).

2.2 Optical Microscopy

All deposition experiments were performed using a custom inverted optical microscope. The schematic of the optical components can be seen in Figure 26. All

experiments were performed in bright filed using a white LED to illuminate the subject. These colour images and videos were recorded with a camera (Thorlabs, Zelux CS165CU, resolution: 1440 x 1080 px) positioned at the bottom of the microscope to observed and record the experiments in situ. The objective lens was on an adjustable rail allowing for precise adjustments while also providing the ability to add different focal length lenses, which could enable the use of different magnifications if required. A side view of the droplets and vapour source could be achieved using the second monochromatic camera (Thor labs, CS165M, resolution: 1440 x 1080 px), this allowed for the measuring of the distance of the vapour source from the droplet. These images were illuminated by the green LED in parallel with the camera. The droplets could be manipulated without direct contact using the capillary as the vapour source discussed further in the section 2.3. The vapour source remained stationary as the substate (glass slide) is moved via the stage it rests upon. This stage can be moved in the x and y directions at different speeds using controllable motors. The speed can be change in situ depending on the experiment's requirements. Additionally, all experiments were performed in a lab where the room temperature was controlled at 21+/-1 °C and a humidity of 40-50%.

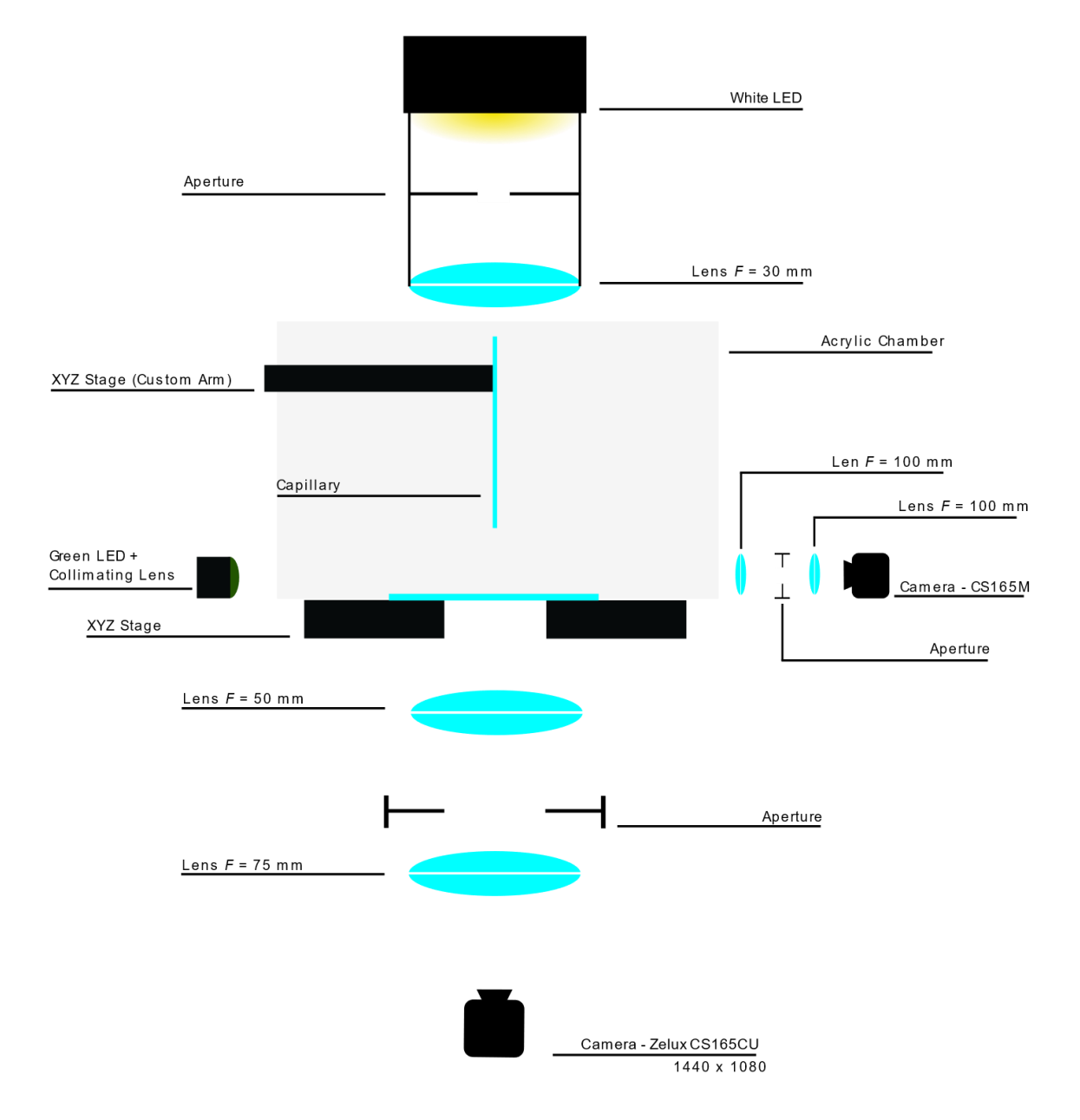


Figure 26: Optical microscope scheme. Diagram shows the custom optical microscope arrangement used in this thesis. This configuration was used to record images and videos in colour. An additional camera and LED are positioned parallel with the substates to measure the height of the capillary before depositions. Two stages where used, the first is for sample substate (XYZ) and the second is for the capillary.

2.3 Vapour Source and Droplet Composition

The vapour source was constructed of a glass capillary with an internal diameter of 1 mm and was used throughout the experiments illustrated in Figure 27. This contained a source of deionised water (10 μ L) that was suspended at the base of the capillary tube, allowing for a strong vapour field to facilitate droplet movement. This source was placed using an XYZ stage in the environmental chamber, which can be moved

independently of the sample stage. The environmental chamber consists of an acrylic box cemented together with sections removed to allow for vital components to move. The bottom of the chamber is place on the XYZ stage so that it moves with the stage. The vapour source side is open to allow the vapour source to move freely. The front is also open to allow the positioning of substates and droplets. The intended use of the acyclic box is to reduce the air flows that are produce in the lab due to people's movement and the air conditioning. Additionally if reduced the amount of particles that accumulate in the microscope and the substrate during a deposition. The capillary was stationary, whilst the microscopy slide was driven via a motor that the computer could control or, alternatively, could be positioned by hand. Initial droplet composition based on previous work89 is a 5 mol% propylene glycol (PG): 95 mol% deionised water mixture, which was later changed to 95 mol% deionised water:5 mol% DMF.

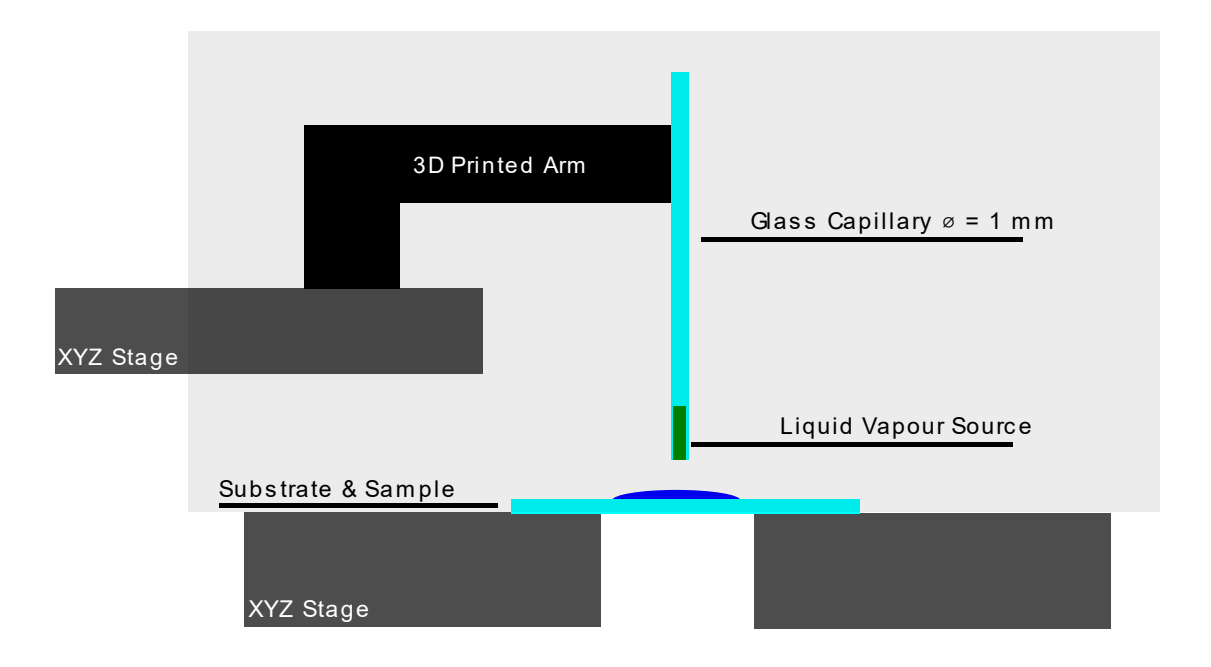


Figure 27: Experimental configuration of vapour source. With individual XYZ stages, one could control the moment of the suspended capillary and the second was where the glass substrate was positioned. The second stage has a hole to allow for observations of the droplet as it was manipulated.

3. Synthesis of Water-Soluble Perylene diimides and Naphthalene diimides and their Deposition

3.1 Introduction

The first chapter outlined the importance for understanding charge transport in organic semiconductors, emphasising the critical role of molecular design in enhancing charge transport. Through molecular design, the charge transport can be significantly improved by designing organic semiconductors that can align through favourable intra-and inter-molecular interactions²³. However there is still a lack of techniques that allow for the controlled deposition of single crystals and this chapter explores a novel deposition technique with the aim of improving the controllability of crystallisation.

Through the use of advanced deposition techniques, the semiconductor solid state order and crystallinity can be controlled and as a result the charge transport improved further. Examples of such techniques include spin coating^{69, 71, 73}, dip coating^{74, 111}, bar coating¹¹² and many more are discussed in Chapter 1. The problems encountered with these techniques are the lack of control and the focus on polymer films rather then small molecules. Each technique has specific factors that affect the level of control they possess. While non-contact techniques such as inkjet printing⁸², drop casting⁶²⁻⁶⁴, zone casting⁷⁷ and spray coating⁸³ suffer from uniformity issues, the contact techniques suffer from contamination due to the requirements for direct contact with the organic semiconductor solution.

Additionally, none of these techniques are designed explicitly for the deposition of single crystals, which are crucial for optimal charge transport due to their high degree of molecular order and reduced dynamic disorder.

Single crystals have superior charge transport compared to amorphous and semi-amorphous solids. To continue to synthesise high-mobility OSCs, highly ordered crystals need to be synthesised. There are considerable challenges that impact single-crystal synthesis, such as nucleation control^{113, 114}, supersaturation^{115, 116}, size limitations¹¹⁷, air and moisture sensitivity¹¹⁸ and solvent manipulation¹¹⁹. The development of new techniques that reduce or remove these challenges can enable more control over crystal growth.

This research attempts to synthesise single-crystal organic semiconductors which are then deposited using a novel non-contact vapour-guided deposition technique. This technique was pioneered by a previous PhD student, Dr Robert Malinowski¹¹⁰. The initial phase of this study focuses on the synthesis and characterization of water-soluble OSCs based on a perylene diimide (PDI) core. The methodology involves incorporating carboxylic acid-terminated end groups derived from amino acids, providing additional functional groups to facilitate hydrogen bonding, thereby enhancing water solubility. These OSCs can then be deposited using the water-based non-contact vapour-guided deposition technique that uses a water vapour source to move water/DMF based binary droplets. The flows that are induced in these droplets produce independent single crystals with the same crystals features as crystals grown through solvent evaporation.

This chapter investigates the synthesis of water-soluble perylene diimides (PDIs) through functionalisation with amino acid-derived dicarboxylic acid groups. This strategy offers both water solubility and an adaptable structural framework for hydrogen bonding, improving deposition behaviour through more stable and controlled crystallization. Utilising binary solvent systems, such as those based on water and propylene glycol, amplifies the advantages of non-contact deposition by generating compositional gradients that enhance film uniformity.

3.2 Synthesis of water-soluble PDIs

To synthesise water-soluble OSCs there are two components: the OSC core which in this case is PDI and the end groups which allow for water solubility. PDIs where used due to their vibrant colours which was theorised to act as a visual add during depositions.

To increase water solubility there needs to be functional groups that can interact favourably with the water molecules. Water is highly polar so with the addition of more polar functional groups water solubility can be improved. Therefore, it was theorised that the incorporation of carboxylic acids into the PDI structure would add polar groups that can enhance water solubility. The simplest way to achieve this is through the addition of amino acids. This is because they allow for simultaneous formation of the imide bond of the PDI and the introduction of the necessary carboxylic acids. Additionally, they also have a range of different functional groups that may be used to manipulate different packing.

The general procedure is as follows for all the PDIs synthesised: PDA and the desired amino acid were reacted in DMF using imidazole to function as an organic base. Given the enlarged core of the PDI molecule, which has more π - π stacking interaction, a considered alteration in the choice of amino acid was proposed. The initial plan was to use amino acids that contain more functional groups that could facilitate hydrogen bonding. Aspartic acid was chosen for its additional carboxylic acid groups, which was hypothesised to enhance water solubility through more hydrogen bonding candidates or through the generation of the carboxylic salt. The synthesis of compound 1 (Figure 28) utilising aspartic acid successfully introduced the desired additional carboxylic acid groups, resulting in vividly red PDIs that facilitated visually striking depositions.

A thorough literature review revealed that many PDI reactions benefit from using imidazole as a base. Imidazole enhances solubility and promotes condensation reactions without compromising yield through parallel imide bond formation. Which led to imidazole being used in all further reactions. To ensure comprehensive product collection, 2.0 M hydrochloric acid was introduced to precipitate the protonated acids,

resulting in precipitates that were filtered through an acid-resistant nylon 0.45-micron filter.

Figure 28: Structure of the synthesised PDIs using four different amino acids 1) aspartic acid, 2) threonine, 3) L-Serine, 4) β-Alanine and 5) L-Tyrosine.

Additional design iterations were conceptualised to identify the potential effects of different functional groups on how the PDIs would pack during deposition experiments. Additionally the different functional groups could have a varying degree of effects on the solubility of the PDIs. All compounds adhered to uniform reaction conditions but featured varied terminal groups to enhance water solubility. Compound 2 was synthesised using threonine, incorporating a carboxylic acid group and an alcohol to

augment solubility in polar organic solvents. Compound 3 was synthesised using L-Serine, where the only difference to compound 2 was the reduction of a terminal alkyl group positioned next to the alcohol. Compound 4 utilised β -Alanine to test its effectiveness with the large PDI core. The main issue that arose with all the samples was the lack of purity of the products. The hydrogen bonding nature of the carboxylic acid groups caused the functionalised PDIs to aggregate in solution. Once aggregated these compounds are poorly soluble in both organic and polar solvents. Which made these compounds difficult to solubilise to allow for adequate purification via column chromatography. Additionally, conventional silica gel is weakly acidic, this also causes the carboxylic compounds to adhere to the silica and reduce movement through the column.

To address these challenges, reverse-phase silica with C8 and C18 modifications, where long carbon chains replace hydroxy groups, was explored. This substitution facilitated the use of more polar solvents such as methanol, water, and acetonitrile. However, issues persisted during sample loading onto the C18 silica. The highly acidic groups on the PDIs exhibited an excessive affinity for the mobile phase, leading to minimal separation with various solvent systems.

Ultimately dialysis was chosen as an alternative purification method illustrated in Figure 29. Dialysis tubing is an artificial semi-permeable membrane that facilitates the flow of substances in solution through differential diffusion. The pore size of the membrane defines which substances can diffuse through the membrane and which ones are retained.

However, dialysis posed its own set of challenges when applied to PDIs. The limited availability of suitable solvents, often restricted to water, clashed with the need for adjusting pH levels. Acidified PDIs, prone to aggregation in low pH environments, displayed improved solubility at higher pH levels. Membranes with a minimum pore size of 500 Daltons have a very limited range of solvents that they can be submerged in. The solvents that can be used with these membranes cannot be organic and can only have a pH of 7 of they will break down, this means they can only be successful used with pH7 water. To mitigate these issues, samples were stirred in deionised water at pH 8 before insertion into dialysis tubing. The tubing was then placed in 5-litre beakers filled with deionised water, allowing excess water for impurity diffusion.

Despite multiple water replacements, inconsistent results were observed, with some samples showing improved purity while others remained minimally affected.

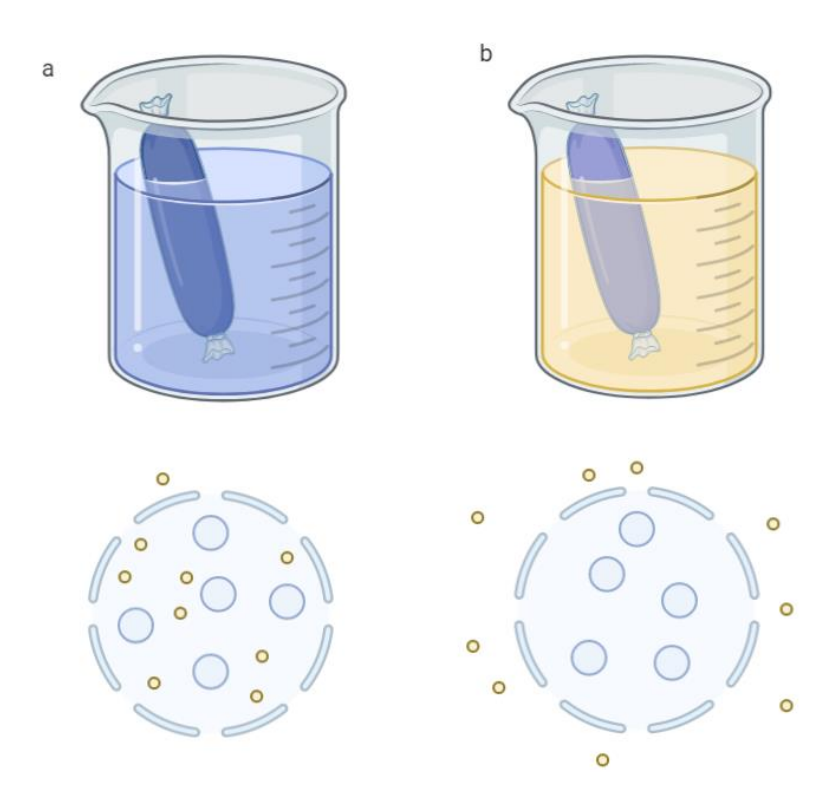


Figure 29: Visual representation of dialysis used for purification of PDI where PDI remain in dialysis tubes with the impurities move into the bulk. a) dialysis tubing containing the crude sample placed into a beaker containing water. b) large molecules have remained inside the tubing whilst smaller molecules have diffused into the bulk water.

The infrared data showed the presence of multiple carbonyl peaks. The first carbonyl peak that is present in all the samples corresponds to the asymmetrical C=O stretching from PDA seen in all samples at 1755 cm⁻¹ confirmed in the literature¹. Further confirming the presence of PDA is the peak seen in all compounds at 1300 cm⁻¹ which is -COOOC- stretching¹ confirming not all the PDA was converted into PDI due to the presence of the anhydride. This additionally validates the lack of purity of each sample. But these are not the only peaks validating the presence of carbonyls, in each sample there are multiple peaks in the carbonyl region. In all samples, there are very similar peaks seen in figure 30 at 1764-1770 cm⁻¹ and peaks at 1729 cm⁻¹ which are C=O asymmetric stretching¹²⁰ seen in Table 3. These peaks are attributed to the presence of carbonyls, these can either be assigned to the imides or the carboxylic acids but remain difficult to assign because they fall in similar regions. In addition to those

carbonyl peaks there are symmetrical C=O stretching for each sample found between 1682-1699 cm⁻¹ which would not normally be found in PDA samples in these regions¹²⁰. These NMR and IR results suggest that **1**, **2** and **4** have been synthesised but due to the lack of purity, they cannot be completely confirmed. With the inclusive NMR results of **2**, the claim it has been synthesised cannot be made. Compound **5** has promising NMR results, but the IR does not show intense peaks for carbonyl stretching which means it may not have been synthesised.

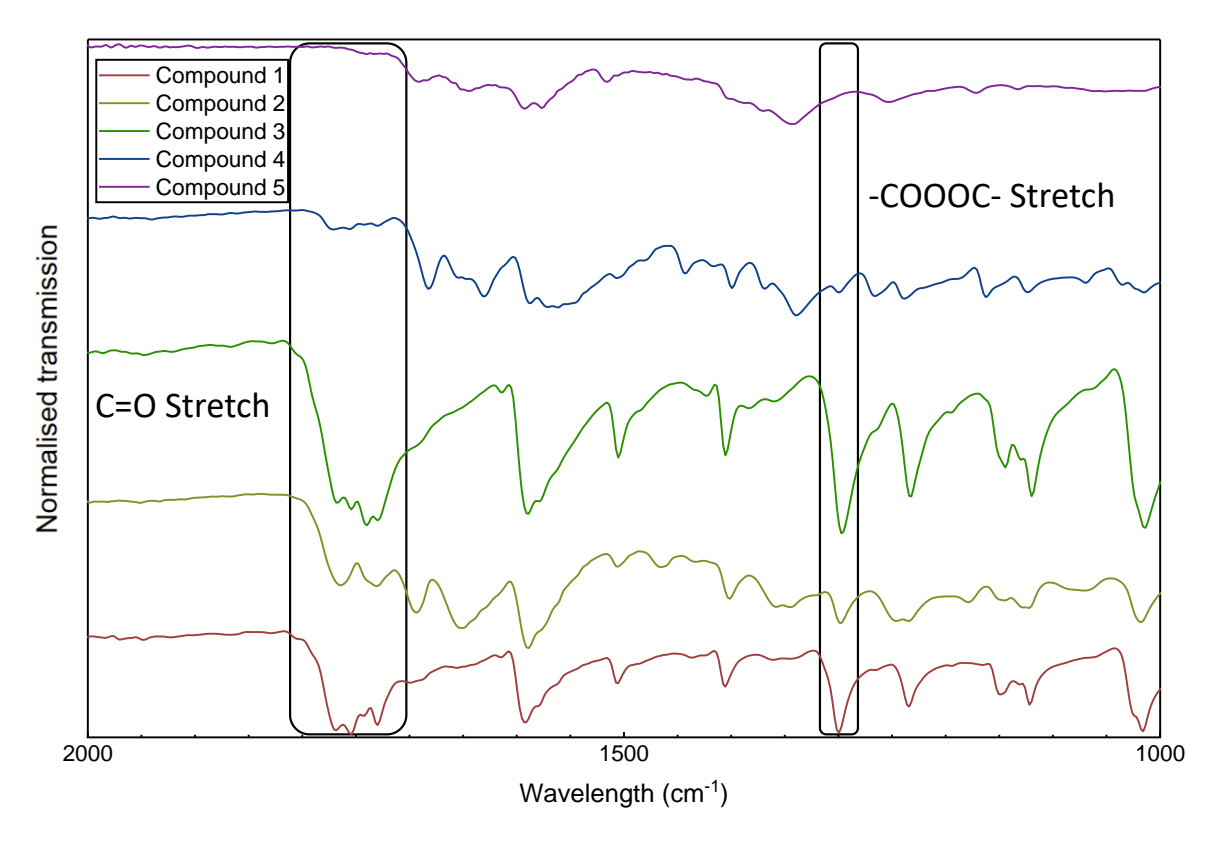


Figure 30: FT-IR spectra of compound 1 (red), 2 (dark green), 3 (light green), 4 (blue) and 5 (purple).

Compound	-COOOC-	C=O asymmetrical	C=O symmetrical
	Strech (cm ⁻¹)	Strech (cm ⁻¹)	Strech (cm ⁻¹)
PDA	1300 ¹	1755 ¹	
1	1299	1766,1729	1699
2	1297	1764,1729	1692
3	1297	1768,1729	1695
4	1299	1770,1729	1682
5	N/A	1741,1729	1690

Table 3.1: FTIR peak assignment of PDA, 1, 2, 3, 4 and 5.

The compounds potentially synthesised show some suggestive IR data but it cannot be definitely decided that these compounds have been synthesised. More unique purification methods would need to be trailed to try and conclusively make pure materials. The aggregation aspect of the compounds hindered their purification. This either needs to be eliminated or utilised in order to use alternative purification methods. The yields also are not a true representation of the product as most samples were not pure. Upon current research it was observed that other synthetic methods have been successful using a combination of acid precipitation and freeze drying 121-123.

3.3 Sulphur end groups for gold electrode functionalisation

As more complex amino acids were being utilised for the analyses of water-soluble NDIs some of the research was shifted. Instead of just functionalising PDIs for solubility and deposition, they could be functionalised for a specific role. It was theorised by functionalising PDIs with thiols they could be used for gold electrode functionalisation.

Gold-sulphur mono layers represent a fascinating area of study within coordination chemistry and nanotechnology due to the unique properties and applications of these compounds¹²⁴⁻¹²⁶. Thiols can form thiolate bonds with gold often utilised in the production of gold-sulphur monolayers, by utilising this phenomenon PDIs could be used to functionalise gold electrode.

Sputtering techniques allow for the deposition of gold layers with excellent thickness control enabling the deposition of layers as thin as 2-3 nm¹²⁷. This thin gold layer maintains the substrate's transparency, which is crucial for observing droplet movement during deposition experiments. Utilising this thin layer of gold the droplets could allow for the analysis of the interactions between gold and the thiol functionalised PDIs.

To leverage the gold-sulphur interaction for gold electrode functionalisation, it is essential to identify amino acids with sulphur-containing end groups. Two primary candidates (Figure 31) were chosen based on their chemical properties and availability: L-Methionine, an essential amino acid characterised by a sulphur-containing thioether (C-S-C) group. The thioether group is able to contribute to its ability to interact with gold surfaces¹²⁶. Cysteine is a non-essential amino acid with a

thiol (-SH) group. The thiol group is particularly effective in forming strong gold-sulphur bonds¹²⁸, making it a valuable component for potential deposition processes. The synthesis for compounds **6** and **7** was identical to the synthesis of to the other PDIs but using the desired amino acid.

Figure 31: Structure of the synthesised PDIs using two different amino acids **6**) L-Methionine and **7**) Cysteine.

Even with the poor purity some preliminary tests were performed on gold-coated glass. To avoid overcoating the glass slide was only exposed to gold sputtering for 30 seconds. This allowed for the thin layer which still allowed for an appropriate level of transparency. After 30 seconds with a sputter rate of 1.56 Ås⁻¹ there was clear deposition of the gold. The substrates then became visibly blue commonly seen with thin layers of gold. When the droplet composition of 95% water and 5% PG with two samples containing 0.33 mg per 1 mL of 6 and 7 were placed on the glass slides there was a low contact angle at around 39 ° as seen in Figure 33. This suggests that the surface of the glass has very little gold and is hydrophilic after the ozone cleaning as with longer sputter time frame will cause the glass to be hydrophobic. Siegel et al have AFM images of different sputtering times with the lowest time of 75 seconds experiencing the highest average surface roughness (Ra) value¹²⁹. This occurs because during the growth stage layers form as islands, but as the deposition continues the islands gain interconnections eventually forming a homogenous and uniform layer. This may have caused increased surface roughness which will decrease the wettability of the substrate surface¹³⁰. Most likely due to pinning the droplets would

not move across the gold-coated glass. This lack of droplet movement and the impurities seen in the semiconductor samples, gold-coated substrates and thiols-terminated PDIs were not researched further.

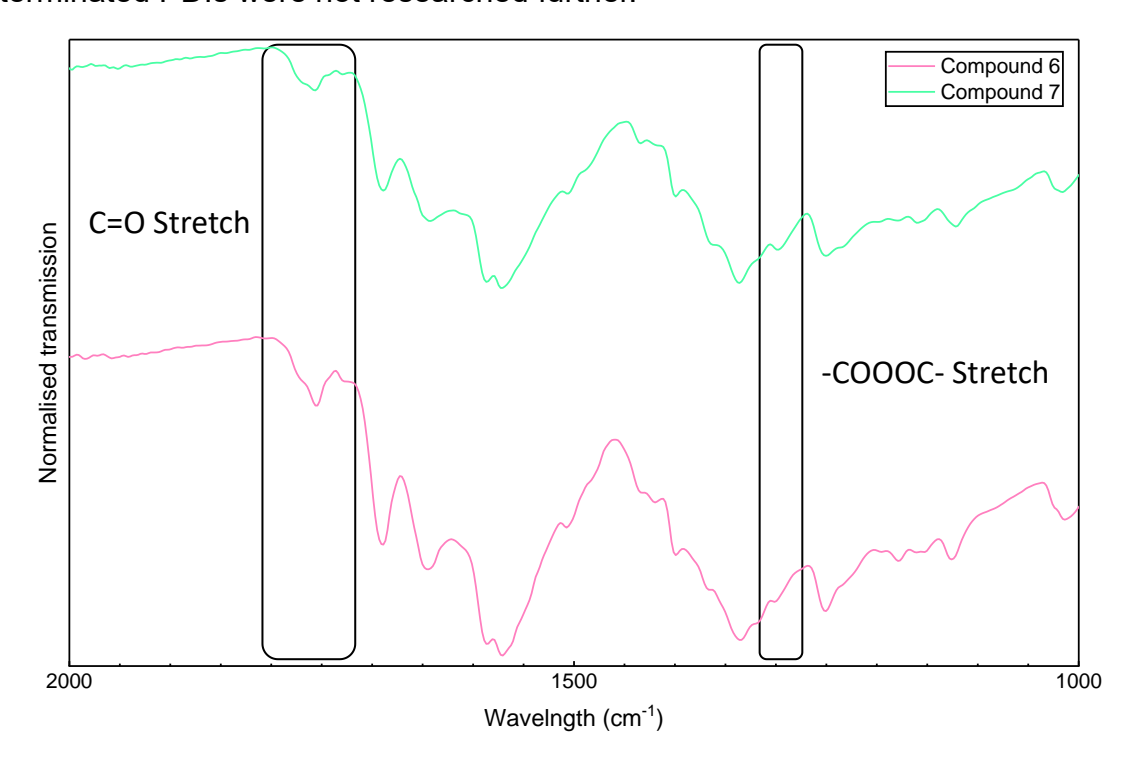


Figure 32: FT-IR spectra of compound 6 (pink) and 7 (green).

Compound	-COOOC-	C=O asymmetrical	C=O symmetrical
	Strech (cm ⁻¹)	Strech (cm ⁻¹)	Strech (cm ⁻¹)
PDA	1300 ¹	1755 ¹	
6	1301	1764,1725	1688
7	1297	1766,1729	1688

Table 3.2: FTIR peak assignment of PDA, 6 and 7.



Figure 33: Contact angle (39 °) measurements for a water droplet on glass that has gold sputtered for 30 seconds after being cleaned using and ozone cleaner.

3.4 PDI Deposition

UV-vis spectrum analysis was performed on drop cast films of compounds 4 and 6 seen in Figure 34. They expressed two main peaks at 500 to 550 nm which were shifted commonly observed with cast films¹³¹. In solution these peaks are commonly observed around 490 and 470 nm for PIDs¹³². The characteristic peaks are almost non-existent, this is due to the large aggregates that form as the solvent evaporates.

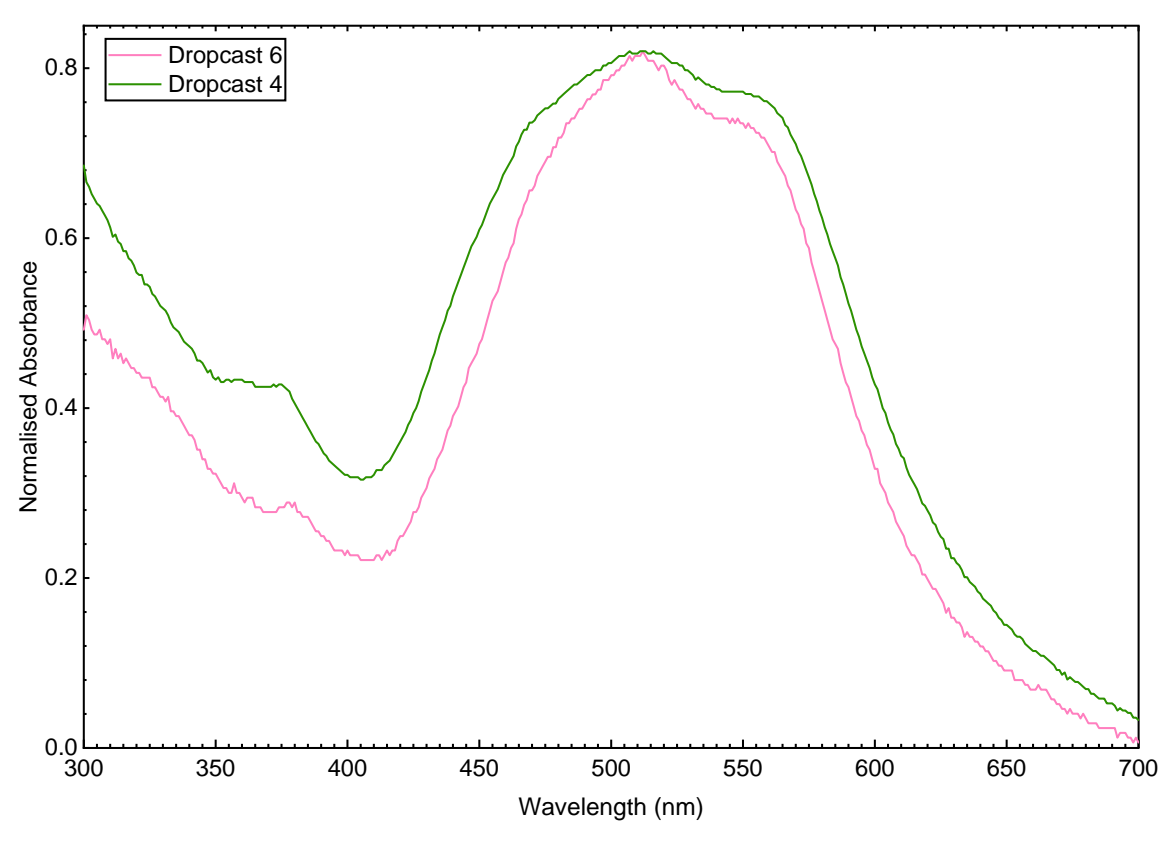


Figure 34: UV-vis. absorption spectrum of compound **4** (green) and compound **6** (pink) drop cast onto a glass substrate.

Due to the issues with purification, none of the samples were confirmed as pure. Nonetheless, the cleanest available samples were selected for deposition tests. The first deposition tests employed the vapour-guided deposition technique. Each sample was prepared with a droplet composition of 95% water and 5% PG. The PDIs were added to the droplet solution at a concentration of 0.33 mg per 1 mL. Two primary factors contributed to this observation: the smaller chains present in the carbocyclic samples had less effect on the π - π stacking compared to longer chains, leading to greater aggregation, reduced solubility, and the presence of impurities.

To prepare the samples for deposition, compound **2** was made up to 0.33 mg in 1 mL of solution, heated to 60°C. Any remaining solids were filtered out using a 5 µm nylon syringe filter, as these solids were likely due to impurities. The initial tests focused on observing droplet movement, which demonstrated that these samples could be effectively manipulated using the existing setup. However, attempts to deposit films of

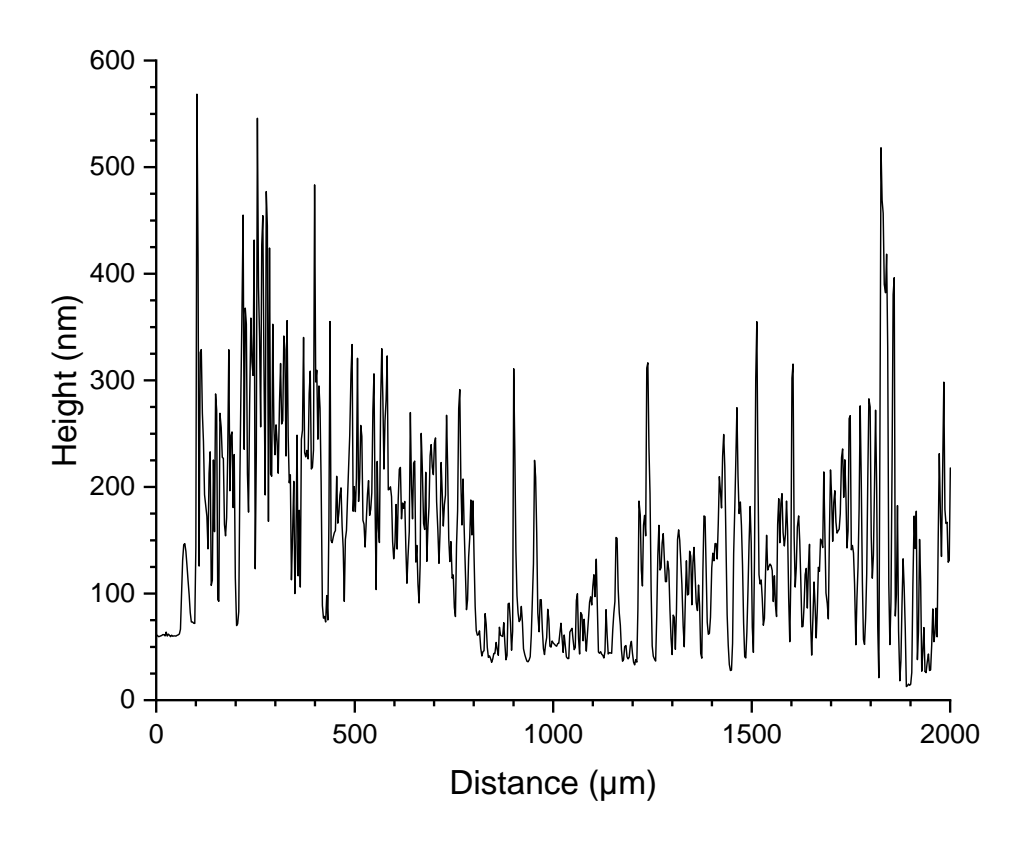


Figure 35: Profilometer data of a thin layer of compound 2 deposited on to glass.

the OSCs were unsuccessful; deposition predominantly occurred at the end of the droplet's lifetime, with most of the material depositing around the edges as the water evaporated. Figure 35 shows the roughness measured using a profilometer of the very thin deposited film, the tallest point was at a height of 568.4 nm with an average thickness of 147.8 nm. The profilometer data shows that there is minimal product being deposited which is most likely due to the compound's poor solubility.

To further investigate the deposition behaviour, drop casting was performed. This method aimed to assess whether uniform films could be produced. As illustrated in Figure 36, the sample formed droplets with scattered clusters. Due to the coffee ring effect, deposits primarily accumulated around the edges, but clusters were also

scattered throughout a thin film between these edges. This pattern emerged towards the end of the droplet's lifetime, causing pinning and ultimately hindering continuous film production.



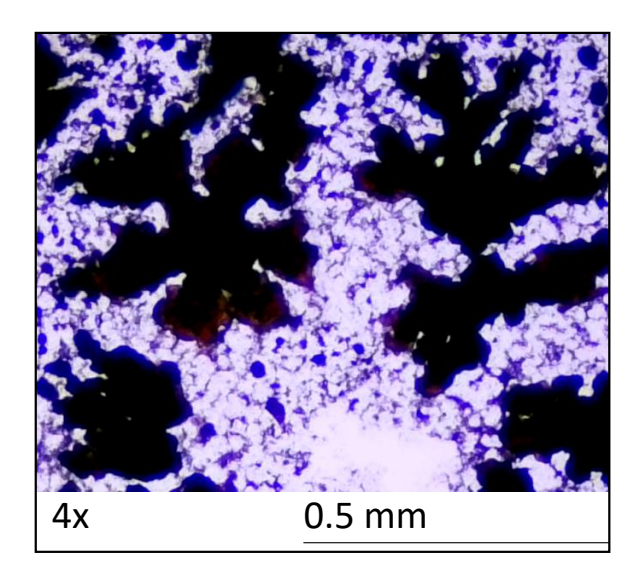


Figure 36: Drop casts of compound **2** at a concentration of 50 mg in 3 mL in deionised water. Top left overview of the drop cast, top right is a microscope image at 4x.

In summary, while the initial objective of creating more vibrant semiconductors was achieved, the reduced solubility and presence of impurities in PDIs and NDIs posed significant challenges for deposition and film formation. These issues necessitate further optimisation to improve solubility and purity, which are crucial for producing uniform and high-quality semiconductor films.

3.5 Deposition of Dicarboxylic NDI

Due to challenges encountered in the synthesis and deposition of PDIs, particularly concerning solubility, purification, and aggregation issues, the research focus was shifted toward NDIs for enhanced crystallisation potential and ease of handling. Initial attempts to modify PDIs with amino acids to introduce carboxylic acid end groups aimed to increase water solubility through hydrogen bonding. However, persistent solubility and aggregation issues, exacerbated by the difficulty of purifying the resulting compounds due to strong intermolecular interactions, significantly limited the efficacy of the deposition process. As a result, the research pivoted toward synthesising and characterising water-soluble NDI derivatives with glycol-based end groups.

To synthesise a water-soluble NDI, a methodology analogous to the synthesis of PDI was employed. The symmetrical naphthalene tetracarboxylic dianhydride (NDA) underwent condensation reaction with β -alanine in DMF at 100°C for 12 hours. Upon completion, the reaction mixture was concentrated under reduced pressure. The resulting concentrate was subsequently introduced into a 2M HCI solution. The precipitated solid was then collected via vacuum filtration, affording the dicarboxylic acid NDI (compound 8) with a 77% yield, as confirmed by H¹ NMR spectroscopy.

Figure 37: Synthetic route used to obtain 8.

The solubility of compound **8** in water is hindered by its tendency to aggregate due to hydrogen bonding. To address this issue, the reversible nature of the carboxylic acid groups was exploited. By manipulating the pH, the solubility of compound **8** can be significantly altered. In acidic conditions, the carboxylic groups are protonated, leading to aggregation and facilitating their isolation during purification. In basic conditions, the carboxylic acids are deprotonated to form carboxylate salts, which are more soluble in water. The formation of these salts enhances solubility due to the interaction of the ionic species with water molecules, which possess permanent dipoles. To achieve this, sodium bicarbonate was used to deprotonate the carboxylic acids, forming the corresponding sodium salts seen in Figure 38. This modification appeared to have improved the solubility of the dicarboxylic NDI in water, allowing for a higher concentration of the OSC in aqueous solutions. This enhanced solubility facilitates the deposition and manipulation of the OSC using vapour sources, thereby improving the overall processability of the material.

Figure 38: Schematic of the formation of compound 8 salt.

The UV-vis data in Figure 39 compares the signal of compound **8** vs compound **5** in water. Compound **8** is at a concentration of 0.01 mg mL⁻¹ whilst compound **5** is at a concentration of 0.001 mg mL⁻¹. The data for compound **8** shows the commonly observed π - π * transitions for NDIs below 400 nm¹³³. Compound **5** expresses two main peaks at 493 and 472 nm, these peaks are commonly observed for PIDs¹³². Normally when PDI is dissolved with sufficient concentration these peaks are more pronounced with a clear split, there is also an additional peak that appears at close to 450 nm¹³².

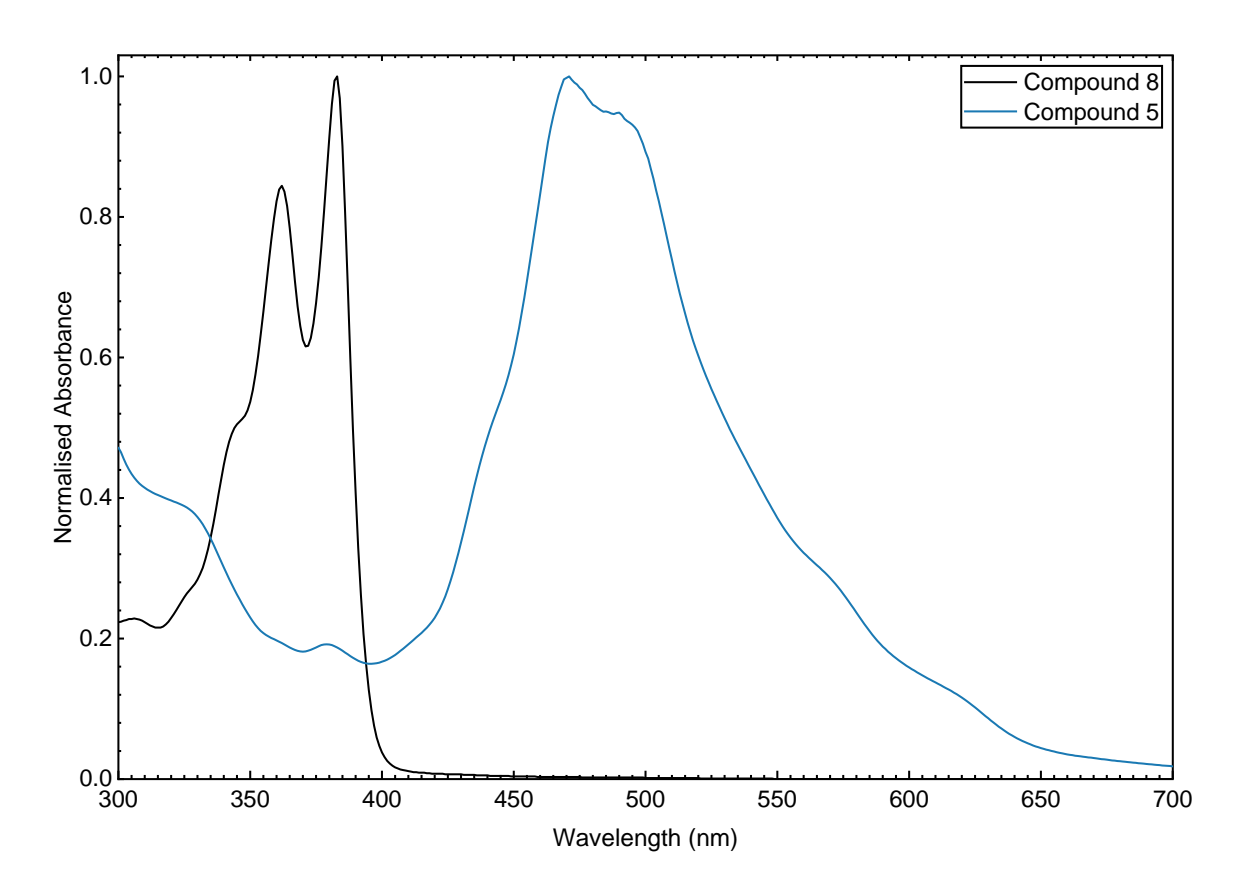


Figure 39: UV-vis. absorption spectrum of compound 8 (black) and compound 5 (blue) in water.

The peaks seen in Figure 39 appear more closely related to the peaks observed by Schill et al. They show aggregated PDIs in water at varying temperatures where the PDIs are not soluble. The comparison of these UV-vis spectra shows that the PDIs were far less soluble compared to the NDI. The enhanced solubility of the NDIs permitted a concentration of 1 mg mL⁻¹ in a solvent mixture comprising 95% water and 5% PG. This marks a substantial improvement; however, the solubility is still constrained by the aromatic core of the NDIs.

The performance of the non-contact vapour-guided deposition technique was unknown for the deposition of OSC films. Compound **8** was a test to assess its performance in film deposition as vapour-guided deposition would then be used for the deposition of water-soluble PDI films. As seen in the method section the non-contact vapour-guided deposition was performed using the set-up described illustrated in section 2.0.

As the solvent droplets with compound **8** move with the vapour source, a brownish film is deposited upon evaporation. However, this deposition results in non-uniform films characterised by areas of varying colour intensity. The most pronounced inconsistencies are observed in regions affected by droplet pinning. Figure 40 illustrates an example of in-situ pinning, which causes offshoots of the main droplet.

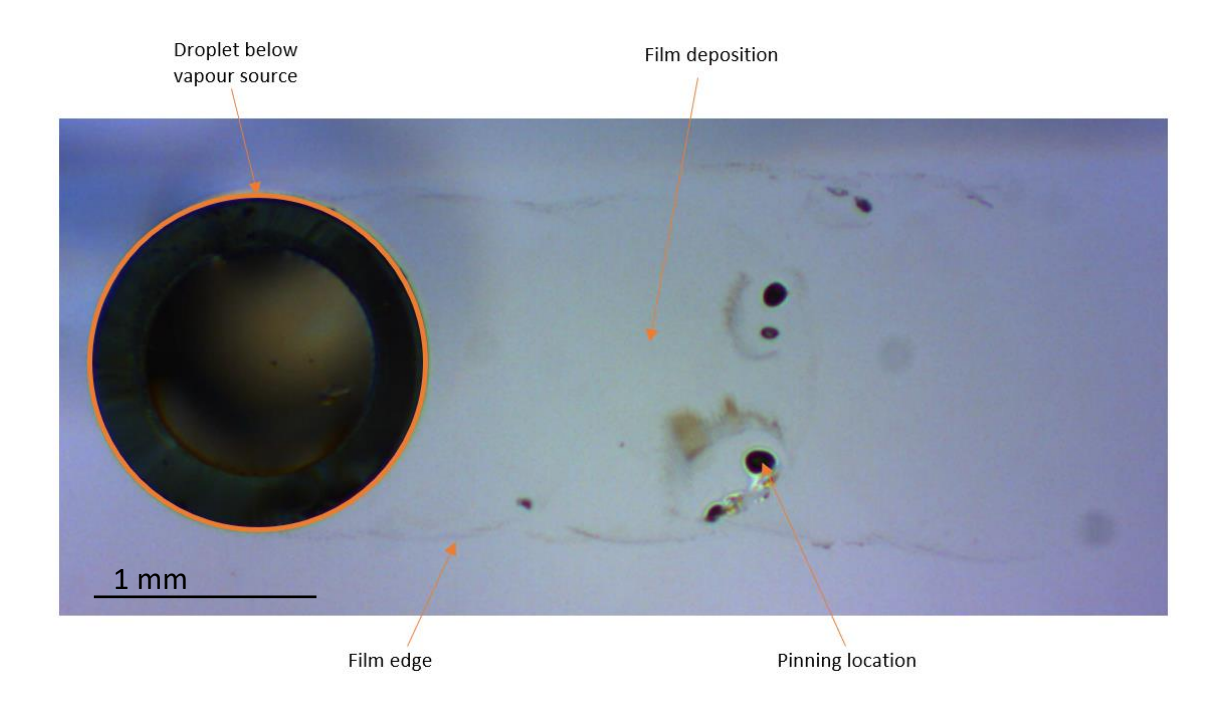


Figure 40: Screenshot of the deposition of compound 8 as a salt.

These smaller, independent droplets remain stationary and evaporate, leading to localised concentrations of the sample at random intervals along the film's path.

This deposition was performed before the changes were made to address pinning issues to substrate contamination. To address these issues the cleaning procedure was changed as stated in section 2.1 Slide Preparation. The most notable change was a switch from base bath washes to an ozone cleaner. With these changes, there was a more consistent substrate surface with fewer pinning occurrences.

Despite these challenges, the results served as a proof of concept, demonstrating the potential for future film deposition of OSCs. The primary issues identified were the insufficient concentration of OSC, which resulted in reduced film thickness, and poor visibility due to the dull appearance of the OSC material. The subsequent section will address these issues and propose solutions for achieving more uniform and visually distinct films.

These NDIs not only demonstrated greater solubility and crystallisation potential but also exhibited enhanced suitability for the non-contact vapour-guided deposition technique. Consequently, the exploration continued with NDI-based single crystals, advancing toward the goal of achieving stable and controlled crystal growth, crucial for the study of charge transport in organic semiconductors.

3.6 Synthesis and Characterisation of Glycol Terminated NDIs

Building on the foundational work by Malinowski¹¹⁰ vapor-guided deposition has shown significant promise as a technique for controlled crystal growth coupled with the work observed earlier in this chapter. This established methodology typically utilises a binary droplet system composed of PG and water. To adapt this approach for the vapor-guided deposition of OSCs, it is essential to identify an OSC candidate that is highly soluble in water. NDIs, a class of small molecule OSCs, have been extensively studied and are known to exhibit a range of highly crystalline forms¹³⁴⁻¹³⁶. NDIs have highly tuneable side chains allowing for manipulation of solubilities in a range of solvents.

To achieve water soluble NDIs, more poplar side chains such as polyethylene glycol (PEG) are commonly utilised, as these moieties provide hydrophilicity and versatility

in chemical design¹³⁷⁻¹⁴⁰. The subsequent section details the synthetic pathway used to introduce glycol-based side chains to produce water-soluble NDIs.

To study the crystallisation behaviour of water-soluble NDIs, three material candidates were identified. The selection criteria for these candidates were based on three key requirements: (1) the OSCs must exhibit good water solubility, as previously outlined; (2) they must retain the NDI core structure to enable direct comparison of the electronic properties; and (3) they should readily crystallise to form high-quality crystals during deposition. To meet these criteria, three NDI derivatives were synthesised, each varying in the length of their glycol side chains to systematically investigate the effect of glycol chain length on crystallinity and solubility.

This approach allowed for a comparative analysis under controlled conditions, testing the hypothesis that decreasing the chain length would enhance crystallinity due to reduced solubility, while increasing the chain length would inversely lead to greater solubility due to the increased length and flexibility of the hydrophilic glycol chains. However, it was hypothesised that the extended glycol chains would also increase conformational disorder, making the compound more challenging to crystallise.

The first NDI derivative synthesised in this study was trimethylene glycol NDI (9). Trimethylene glycol amine was selected as the side chain to assess its impact on solubility, given its availability and known hydrophilic properties. The synthesis of compound 9 was carried out via a condensation reaction between NDA and trimethylene glycol amine, as illustrated in Figure 41. The reaction was allowed to proceed overnight, after which the solvent was completely removed under vacuum.

Figure 41: Synthetic route used to obtain 9.

The crude product was subsequently purified through column chromatography using a mixture of ethyl acetate and methanol as the mobile phase. The concentration of methanol was initially set at 2% and gradually increased to 8%, yielding the final product (9) with an isolated yield of 70%. This yield closely matched the literaturereported value of 78% for similar NDI derivatives¹⁴¹. Given the satisfactory yield, no further optimisation of the synthetic protocol was pursued, as the quantity obtained was deemed sufficient for subsequent droplet manipulation and crystallisation experiments. Initially, the product was analysed via proton NMR, as shown in Figure 42. The singlet peak (Ha) at 8.74ppm corresponding to the four protons on the aromatic core confirmed the molecule's symmetry with identical chemical environments for all aromatic protons. The peak (H_b) at 4.46 ppm is usually observed with NDIs due to the presence of the protons directly next to the imide group and again integrating to four protons due to the molecular symmetry. Protons further away from the imide group show progressively more up field shifts, consistent with the increased shielding effect as the distance from the electron-withdrawing imide group increases. Specifically, the next set of protons (H_c) appears at 3.85 ppm, followed by additional methylene protons at even higher fields, illustrating the expected chemical shift pattern for glycol chains attached to an NDI core. Finally, the terminal methyl group (H_e) is represented as a

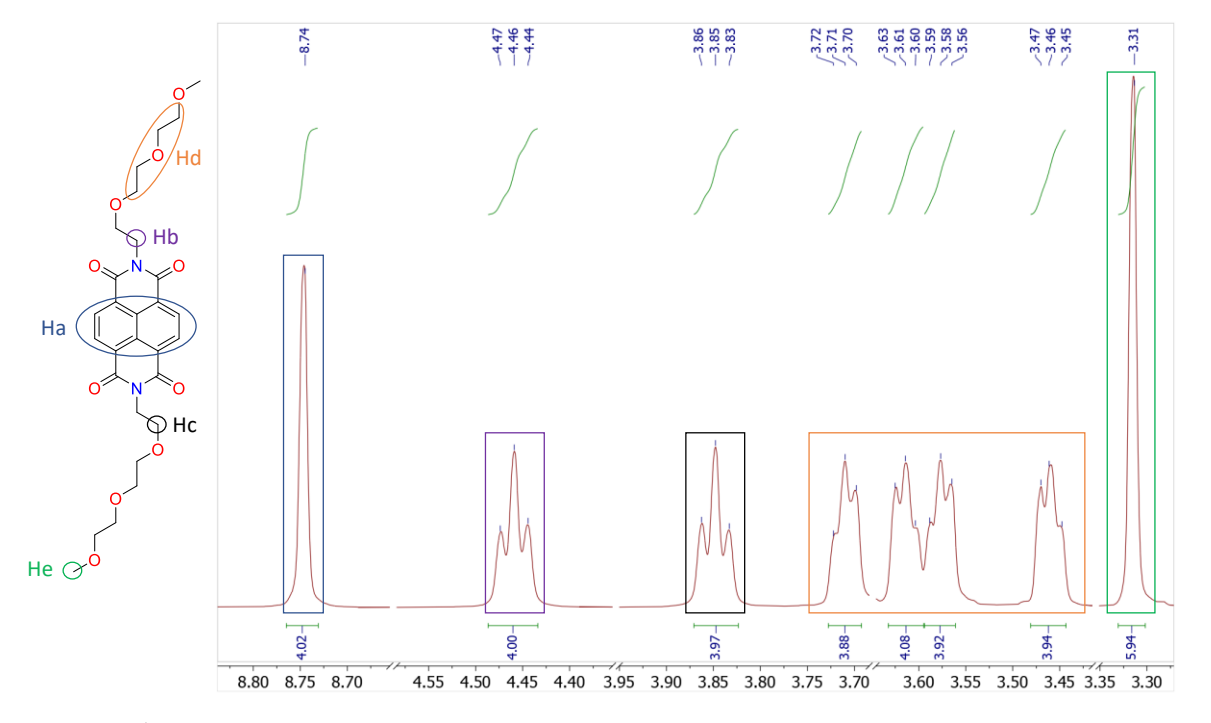


Figure 42: ¹H NMR spectra of **9** with colour coded assignment of peaks where chloroform is the solvent.

singlet at 3.31 ppm, consistent with its position at the end of the triethylene glycol chain. These peaks were confirmed with ¹³C-NMR and the final mass was confirmed by high-resolution electron spray ionisation mass spectrometry.

Compound **9** was successfully crystallised using dimethylformamide (DMF) following its purification. Over the course of several days, yellow needle-like crystals to emerged. The crystals exceeding 5 mm in length and having diameters below 0.2 mm, as depicted in Figure 43. The crystals produced were subsequently characterised using x-ray diffraction discussed later in this chapter.

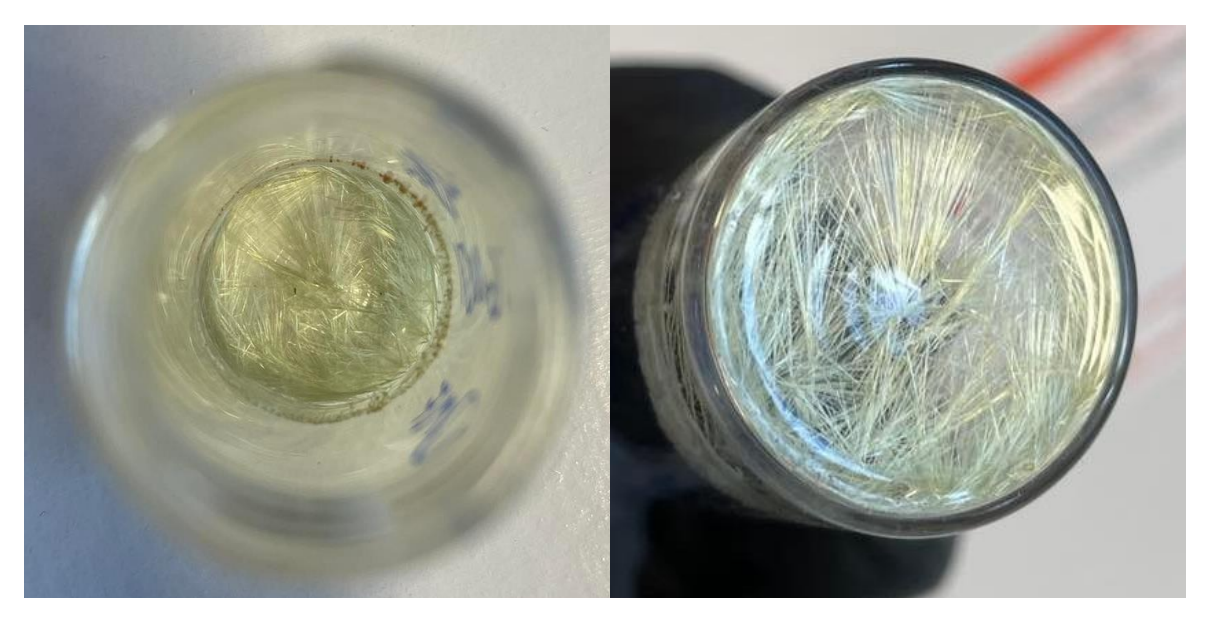


Figure 43: Picture of the crystals that formed after the recrystallisation in DMF.

Next the focus shifted on the synthesis and characterisation of two NDI derivatives that contrast compound **9**: one incorporating two repeating glycol units and the other incorporating four. This comparative study provides insight into how subtle variations in the side chain structure influence the crystallisation behaviour and solubility of NDI-based OSCs.

Diethylene glycol NDI (compound **10**, Figure 44) was synthesised using conditions similar to that employed for compound **9**. NDA and 2-(2-methoxyethoxy)ethan-1-amine were dissolved in DMF and the reaction mixture was heated at 100°C for 24

Figure 44: Synthetic route used to obtain 10.

hours to facilitate condensation. After the reaction was complete, the orange solution was allowed to cool to room temperature before the solvent was removed under vacuum, yielding the crude product. A minimum amount of DMF was used for recrystallisation, producing smaller crystals than obtained for compound **9**, reaching a maximum length of approximately 4 mm. The final product was isolated as compound **10** with a yield of 35% (0.123 g). The structure was confirmed via ¹H NMR (Figure 45).

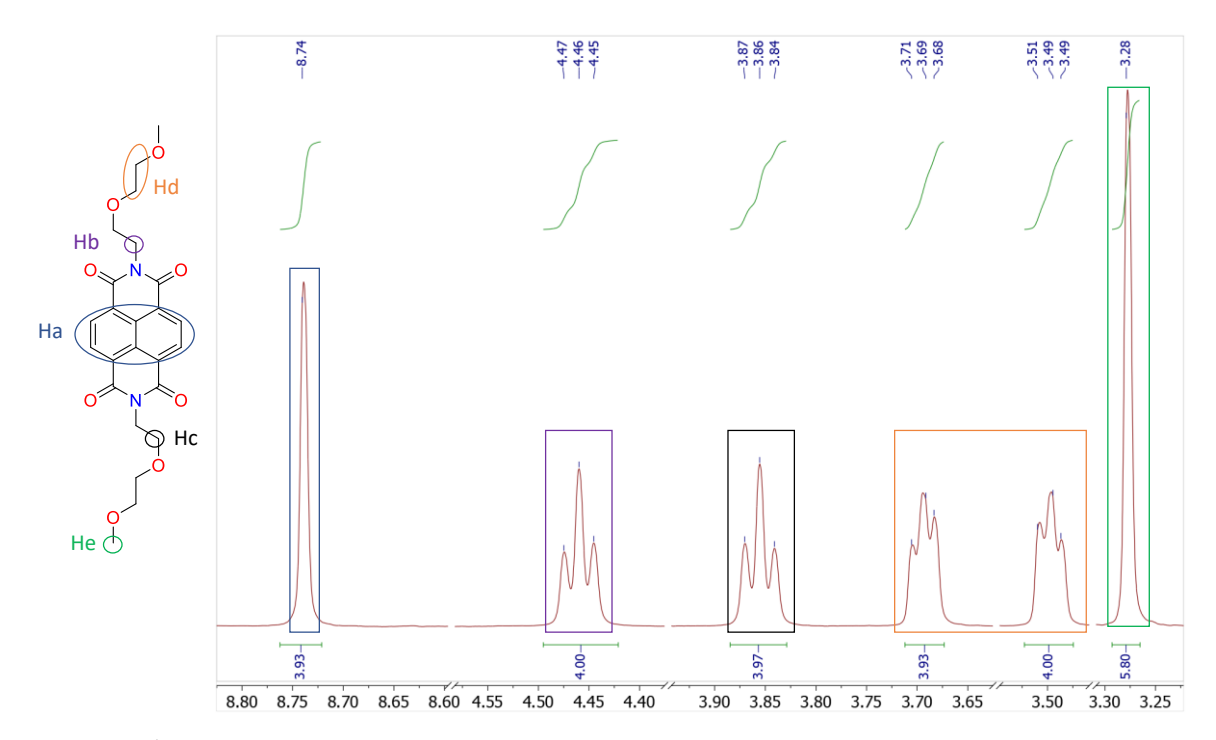


Figure 45: ¹H NMR spectra of **10** with colour coded assignment of peaks where chloroform is the solvent.

The synthesis of compound **11** (Figure 46) followed similar conditions to that used for Compounds **9** and **10**. Specifically, NDA and 2,2,5,8,11-tetraoxatridecan-13-amine were dissolved in DMF and heated at 100°C for 24 hours. After the reaction was

Figure 46: Synthetic route used to obtain 11.

completed, the resulting orange solution was allowed to cool to room temperature before the solvent was removed under vacuum, yielding the crude product. Initial attempts to recrystallise the crude product proved unsuccessful due to the increased solubility of Compound 11. This was in contrast to Compound 10, which exhibited moderate solubility and successfully crystallised in DMF. To overcome this issue, the crude compound 11 was dissolved in a minimal amount of DMF and left much longer to evaporate slowly under controlled conditions. This approach yielded the final product with a yield of 40% (0.482 g). The reduced yield, compared to the 75% yield reported in the literature¹⁴², was likely due to the loss of material during the initial unsuccessful recrystallisation attempt in DMF. The assumption that Compound 11

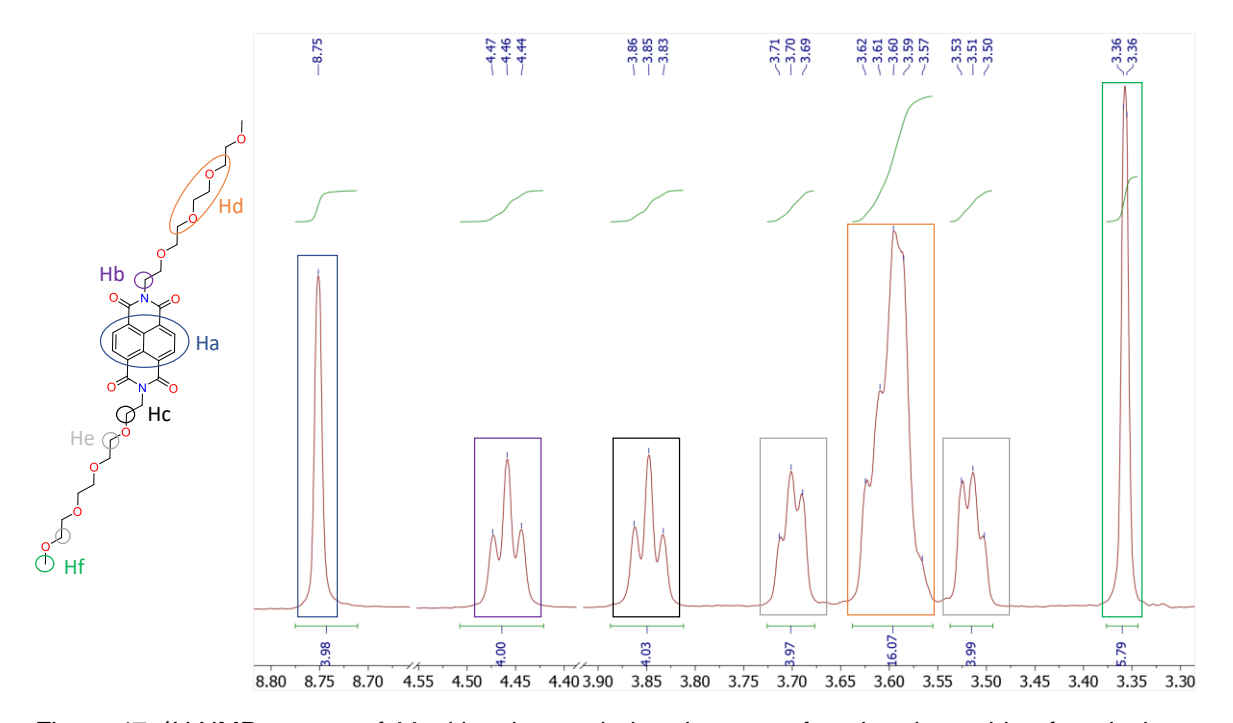


Figure 47: ¹H NMR spectra of **11** with colour coded assignment of peaks where chloroform is the solvent.

would not crystallise as readily as Compounds **9** and **10** was confirmed, indicating that the increased chain length significantly impacted the crystallisation behaviour. The structure of Compound **11** was verified using ¹H NMR spectroscopy, as presented in Figure 47. Additional characterisations such as carbon 13C NMR, COSY, HSQC, HMBC and mass spectrometry were also performed to confirm the molecule's structure.

3.6.1 Evaluation of the Crystal Structures

No structural models have been found for compound **9** and **10**; thus, complete structural diffraction data was collected from single crystal X-ray diffraction. The crystal analysed was from the crystallisation achieved through the evaporation of DMF. The molecular structure and crystal packing of compound **9** crystals have been laid out in Figure 48 at the three different cell lengths (a, b and c).

Crystal **9** crystal was a single pale-yellow lath-shaped crystal. The crystals were orthorhombic, where all three axes were unequal at right angles. The crystal had a cell volume of $5347.4 \, \text{Å}^3$. The crystal structure had low R factors where 1 = 3.89%, representing a good agreement between the observed amplitude and the calculated amplitudes. There was a small level of disorder towards the end of the pegylated end groups. With longer side chains, vacancy rows can form at the chain end if the neighbouring chains remain linear; however, the increase in interchain energy can

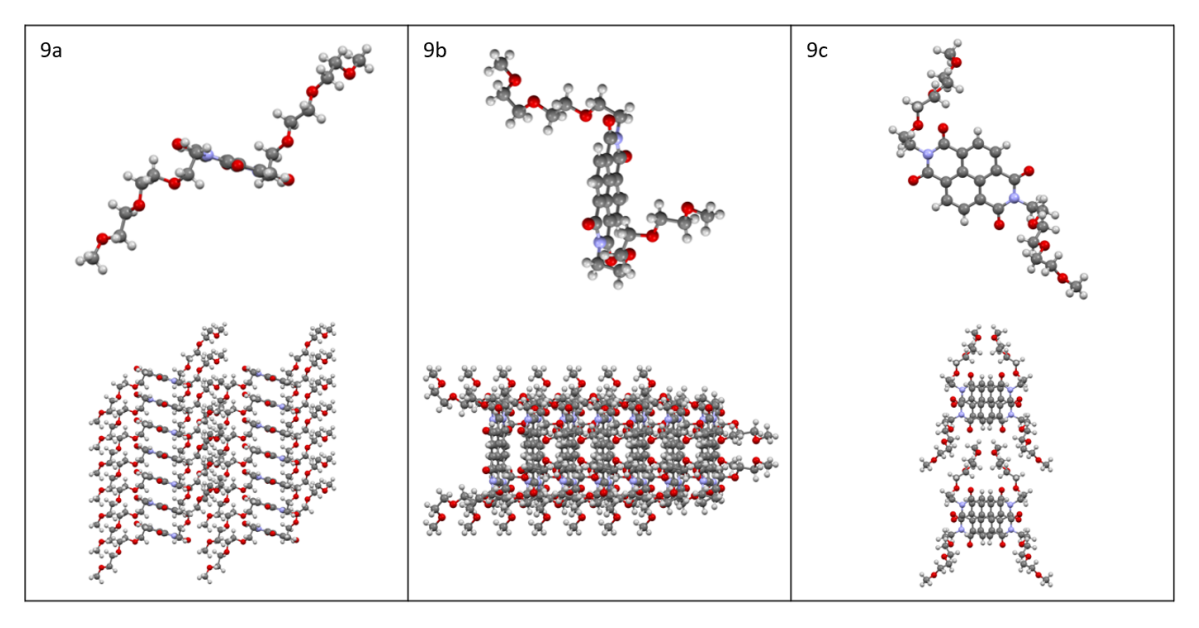


Figure 48: 1a,b,c) illustrations of the molecular geometry of **9** at cell length a, b and c where **9** was dissolved in DMF and left to evaporate over multiple days.

cause this vacancy row to be filled by a neighbour¹⁴³ which can lead to the side chains becoming less ordered as chain length increases.

Crystal Data 9. C₂₈H₃₄N₂O₁₀, M_r = 558.55, orthorhombic, Aea2 (No. 41), a = 26.1972(5) Å, b = 29.2669(4) Å, c = 6.9745(10) Å, $a = b = g = 90^{\circ}$, V = 5347.4(2) Å³, T = 100.00(10) K, Z = 8, Z' = 1, m(Cu K_a) = 0.895 mm⁻¹, 25491 reflections measured, 4376 unique ($R_{int} = 0.0357$) which were used in all calculations. The final wR_2 was 0.1001 (all data) and R_1 was 0.0376 ($I \ge 2$ s($I \ge 2$).

Equally, the crystal analysed for compound **10** was obtained through the crystallisation from DMF. The molecular structure and crystal packing of compound **10** crystals have been laid out in Figure 49 at the three different cell lengths (a, b and c).

The crystals of compound **10** were monoclinic, where all three axes are unequal and a and b are perpendicular, but b and c were not. The crystal had a much smaller cell with a cell volume of 1081.01 Å³. The reduction in repeating glycol units significantly reduced the cell area, which aligned with the reduction in cell lengths where a and b were much lower, and c was more significant when compared to crystals from compound **9**. This is expected because the disorder associated with longer glycol chains was reduced. Even with this reduction, some level of disorder in the crystal structure remained at the end of the glycol groups.

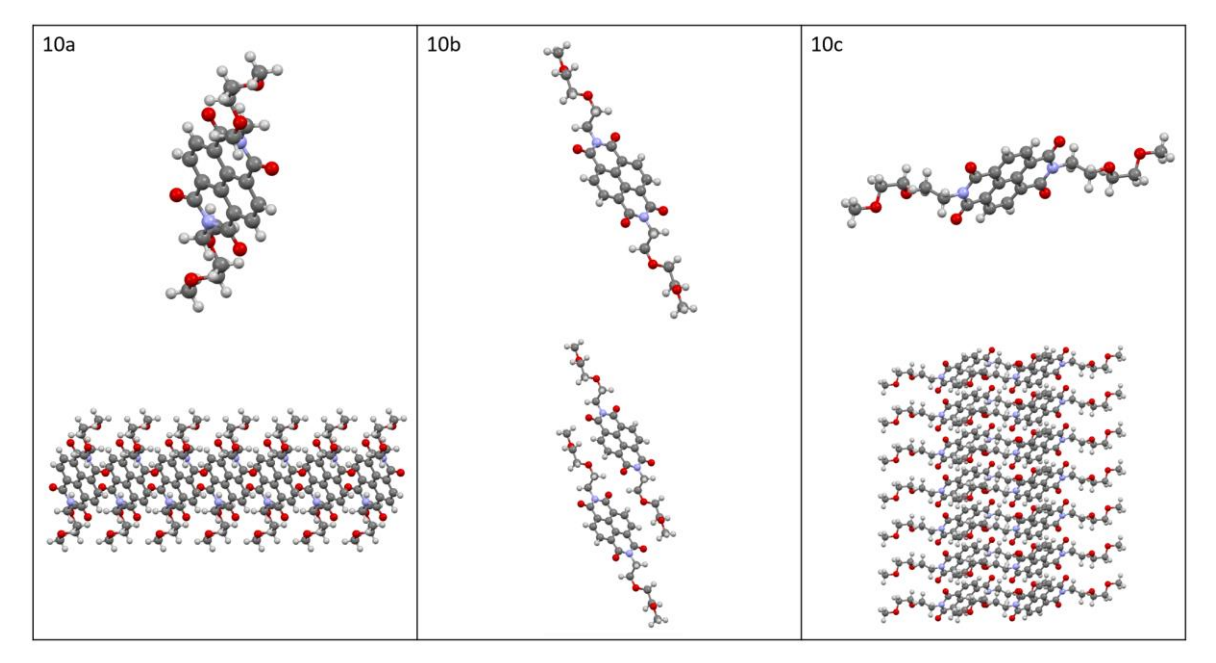


Figure 49: 2 a,b,c) illustrations of the molecular geometry of **10** at cell length a, b and c where **10** was recrystallised for DMF.

Crystal Data 10 C₂₄H₂₆N₂O₈, M_r = 529.56, monoclinic, P2₁/n (No. 14), a = 9.21130(10) Å, b = 4.69340(10) Å, c = 25.1091(3) Å, a = 90° b = 95.2280° g = 90°, V = 1081.01 Å³, T = 100.00(10) K, Z = 2, Z' = 0.5, m(Cu K_a) = 1.54184mm⁻¹, 10630 reflections measured, 4175 unique (R_{int} = 0.0271) which were used in all calculations. The final R_2 was 0.1051 (all data) and R_1 was 0.0389 ($I \ge 2$ s(I)).

3.6.2 Differential Scanning Calorimetry

Differential Scanning Calorimetry (DSC) is a method that analyses the thermal transitions of materials by observing heat flow based on temperature changes during heating and cooling cycles. The technique measures enthalpic changes associated with phase transitions, such as melting, and crystallisation, by comparing the sample's heat flow to that of an empty sample cell. This comparative analysis allows the precise determination of thermal events that occur within the sample. This involves identifying the temperature at which the material shifts from a supercooled liquid to a crystalline solid, offering information about the material's stability and crystallisation kinetics. Additionally, the study of any thermal transitions such as the glass transition temperature and melting temperature are essential for understanding both the amorphous and crystalline phases. DSC also allows for the identification of different crystalline phases, especially in materials that exhibit polymorphism, where multiple endothermic or exothermic peaks may appear. The heat capacity of a material can be calculated using:

$$\frac{dH}{dt} = Cp\frac{dT}{dt} + f(T,t) \tag{8}$$

where $\frac{dH}{dt}$ represents the DSC heat flow signal, $C_{\rm P}$ is the sample heat capacity, $\frac{dT}{dt}$ is the heating rate and f(T,t) is a kinetic term representing heat flow as a function of time and absolute temperature. DSC is particularly valuable for examining the phase behaviour of materials, as it can distinguish between phase transitions based on their distinct thermal responses.

The first heating thermogram showed one distinct melting event for compound **9**; this event is shown in Figure 50 at a peak maximum temperature of 67.8 °C with an enthalpy of fusion of 84.6 J g⁻¹. The first cooling cycle showed a crystallisation event at 15.8 °C with a change of enthalpy of 29.3 J g⁻¹. The crystallisation occurs slowly forming a broad peak, this is repeatable with an identical seen during the second

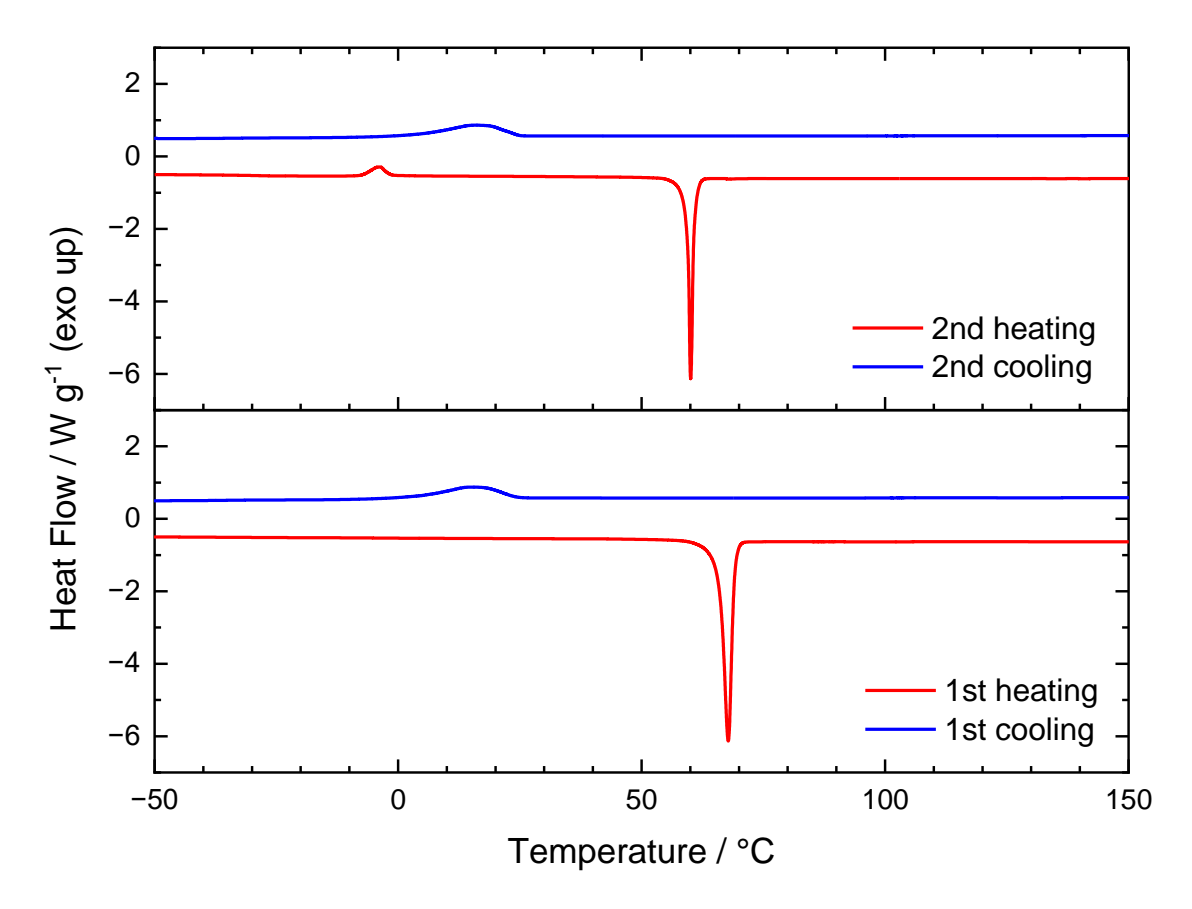


Figure 50: DSC traces measured on a powder of compound **9** with the first heating and cooling cycles below and the second heating and cooling cycles above

cooling cycle. In the second heating cycle a cold crystallisation at -3.8 °C was observed with an enthalpy change of 5.0 J g⁻¹. These can occur when the material is supercooled and crystallises rapidly during the cooling cycle in a less favourable orientation. The "cold crystallisation" occurs via a crystallisation transition during the next heating cycle into a more favourable crystal strctures^{144, 145}. The state in which the compound was before the cold crystallisation was storing excess energy. It is common to see materials that exhibit cold crystallisations also express slow rates of crystallisation from liquid to solid, which is observed for compound 1. Finally, there is a melting event offset from the original temperature and energy at a peak of 60 °C and an enthalpy change of 48.9 J g⁻¹. These results differ heavily when compared to the equivalent alkylated NDI. Milita et al. showed that 2,7-didecylpyrene-1,3,6,8(2H,7H)-tetraone (NDI10, Figure 51) had completely reversible behaviour that was reproduced in the second cycles¹⁴⁶. NDI10 had two exothermic and endothermic transitions as seen in Figure 38. The endothermic transitions are observed at 163 and 183 °C and were confirmed to be due to two different polymorphs. This largely contrasts the

endothermic peaks observed for compound **9** and **NDI10**. **NDI10**s endothermic peaks occurred at a much higher temperature, this can be attributed to their favourable Van der Waals forces that are generated between the alkylated side chains. Additionally, none of the compounds Milita et al. tested exhibited cold crystallisation properties (DSC thermograms seen in figure 52) from 2,7-dibutylpyrene-1,3,6,8(2*H*,7*H*)-tetraone (**NDI4**, Figure 51), 2,7-dibexylpyrene-1,3,6,8(2*H*,7*H*)-tetraone (**NDI6**, Figure 51), 2,7-dioctylpyrene-1,3,6,8(2*H*,7*H*)-tetraone (**NDI8**, Figure 51) and **NDI10**¹⁴⁶. This suggested the cold crystallisation properties are possibly related to the presence of the glycol chains. Glycol and alkyl chain crystalise very differently, this is due to the presence of polar oxygen seen in glycol chains.

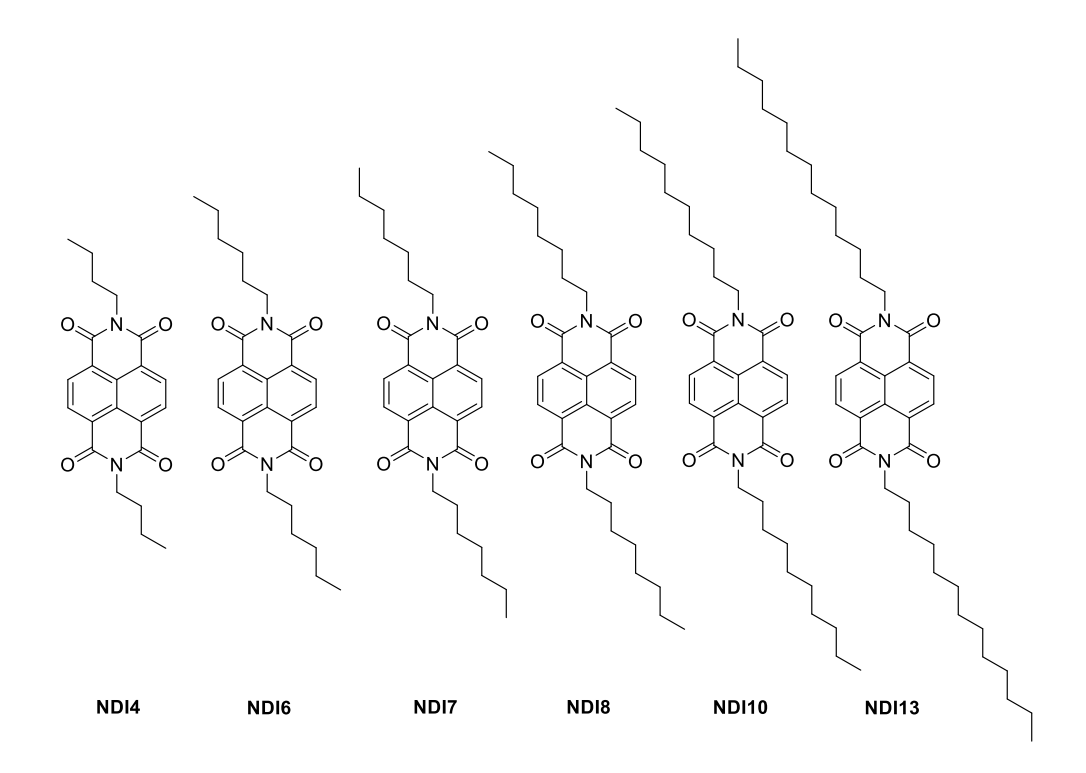


Figure 51: chemical structure of NDIx (x = 4, 6,7, 8, 10 and 13) with x indicating the length if alkyl chain.

Next the phase transitions for compound **10** were analysed. In the first heating cycle seen in Figure 53, there was a melting event with two peak maxima's at 37.3 °C and 38.5 °C respectively. The presence of two peaks could suggest the presence of two separate polymorphs, with a total enthalpy change of 78.5 J g⁻¹. These peaks were not reproducible but interestingly this double melt peak was observed by Insuasty et al. with the DSC data they acquired for 2,7-diheptylpyrene-1,3,6,8(2*H*,7*H*)-tetraone

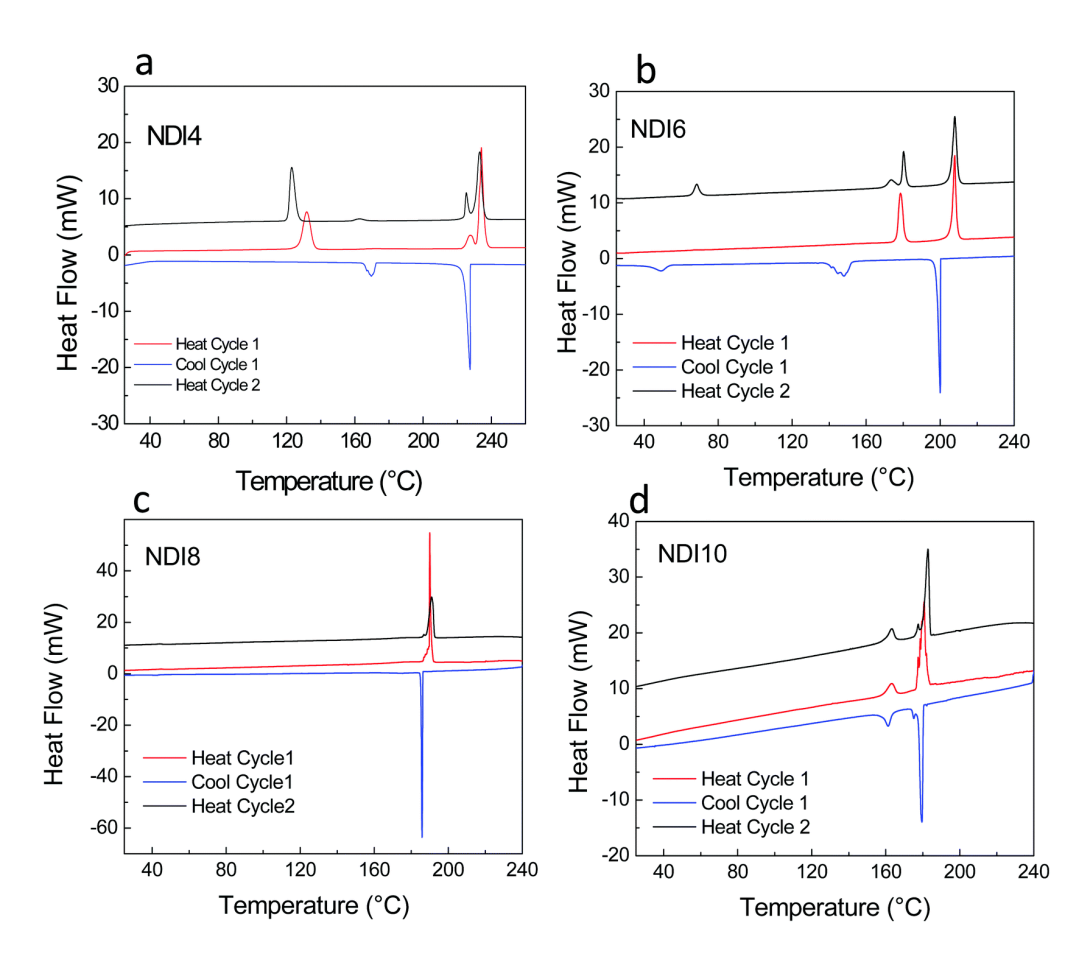


Figure 52: DSC traces measured on the pristine NDIx (x = 4, 6, 8 and 10) powders, upon heating, subsequent cooling and second heating (red, blue and black traces, respectively)¹²⁸.

(**NDI7**, Figure 51)¹⁴⁷. They analysed NDIs with varying alkyl chain lengths from C3 – C8 and did not observe this phenomenon with any of the other NDIs. They did not publish a second scan so limited conclusions can be made but it appears to be significant and currently only seen with chain lengths of seven carbon atoms. In the second heating, there was a single melt peak seen at 37.5°C with a similar enthalpy change of 72.1 J g⁻¹. Additionally, a large cold crystallisation was observed was observed (Tcc = -6.0 °C, ΔHcc = 38.4 J g-1.). This was also observed in compound **9** but to a lesser extent. Compound **10** cold crystallisation has a large change in enthalpy, suggesting that as the glycol chain reduces in length the cold crystallisation enthalpy increases. Similarly as observed with compound **9** the cold crystallisations are specific to the glycol NDIs as no cold crystallisation peak was observed for **NDI-C7**¹⁴⁷.

During the first cooling cycle, there is a crystallisation at 3.0 °C with a change in enthalpy of 10.5 J g⁻¹. This peak was reproducible in the second cooling cycle. It had

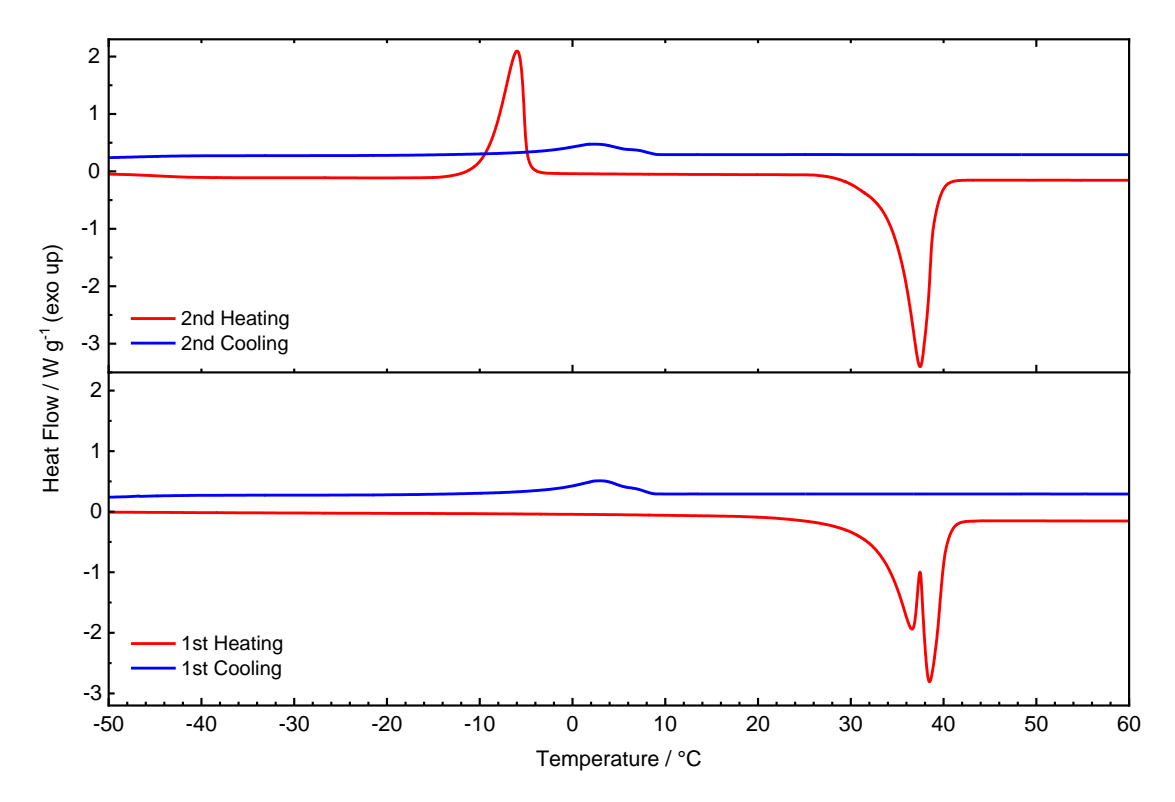


Figure 53: DSC traces measured on a powder of compound **10** with the first heating and cooling cycles below and the second heating and cooling cycles above.

the appearance of a slightly smaller peak followed by and larger peak over a broad area similar to compound **9**. This can be explained as the separation of crystal nucleation and growth. The kinetic rate of nucleus formation is governed by a Boltzmann distribution¹⁴⁸:

$$J_{\text{nucl}} = \frac{N_{\text{v}} k_{\text{B}} T}{3\pi n \lambda^3} \exp\left(-\frac{\Delta G_{\text{c}}}{k_{\text{B}} T}\right) \tag{9}$$

where \mathcal{N} is the number density of molecules in the nucleus, η is the viscosity coefficient, ΔG_c , is the nucleation thermodynamic barrier and λ is the mean free path length (approximated as the molecular diameter). As the temperature approaches the melting point (T_m) , the conditions become less favourable for nucleus formation from a thermodynamic perspective. Consequently, there is a trade-off between nucleation at lower temperatures, which is thermodynamically favoured due to a lower ΔG_c , and nucleation at higher temperatures, which is kinetically favoured due to lower viscosity. Conversely, the kinetic rate for crystal growth is given by 149:

$$J_{\rm gr} = a \frac{\Delta_{\rm m} S}{k_{\rm B} T} \exp\left(-\frac{\Delta_{\rm m} S}{k_{\rm B}}\right) \exp\left(-\frac{\Delta U}{k_{\rm B} T}\right) \Delta T \tag{10}$$

where a is a constant, $\Delta_m S$ is the change in entropy for melting, ΔU is the energy barrier to flow owing to viscosity, and ΔT is the degree of undercooling. ΔT is the difference between the T_m the normal melting point and T the temperature gained from the supercooled melt. Temperature influences the rate of crystallization in two ways. In a highly supercooled melt, a large ΔT leads to an increased crystal growth rate. However, this also means that if T is low, this causes the exponent in the second exponential term to become more negative, which results in a lower rate of crystal growth. Similar to nucleus formation, crystallisation takes place between T_g and T_m . Equations 9 and 10 indicate that the optimal temperature for nucleus formation and the optimal temperature for crystal growth are not necessarily the same.

To observe the phase transitions of compound **11** DSC was performed. The first and second heating cycles both contained a melt at 138 °C with an enthalpy change of 85.5 J g⁻¹ for the first heating cycle and slightly lower 85.9 J g⁻¹ for the second heating cycle as seen in Figure 54. Ichikawa et al. observed three melting peaks during the first heating cycle for 2,7-ditridecylpyrene-1,3,6,8(2*H*,7*H*)-tetraone (**NDI13**, Figure 51) at 109 °C, 144 °C, and 162 °C¹⁵⁰. They attributed these peaks to; the changing of

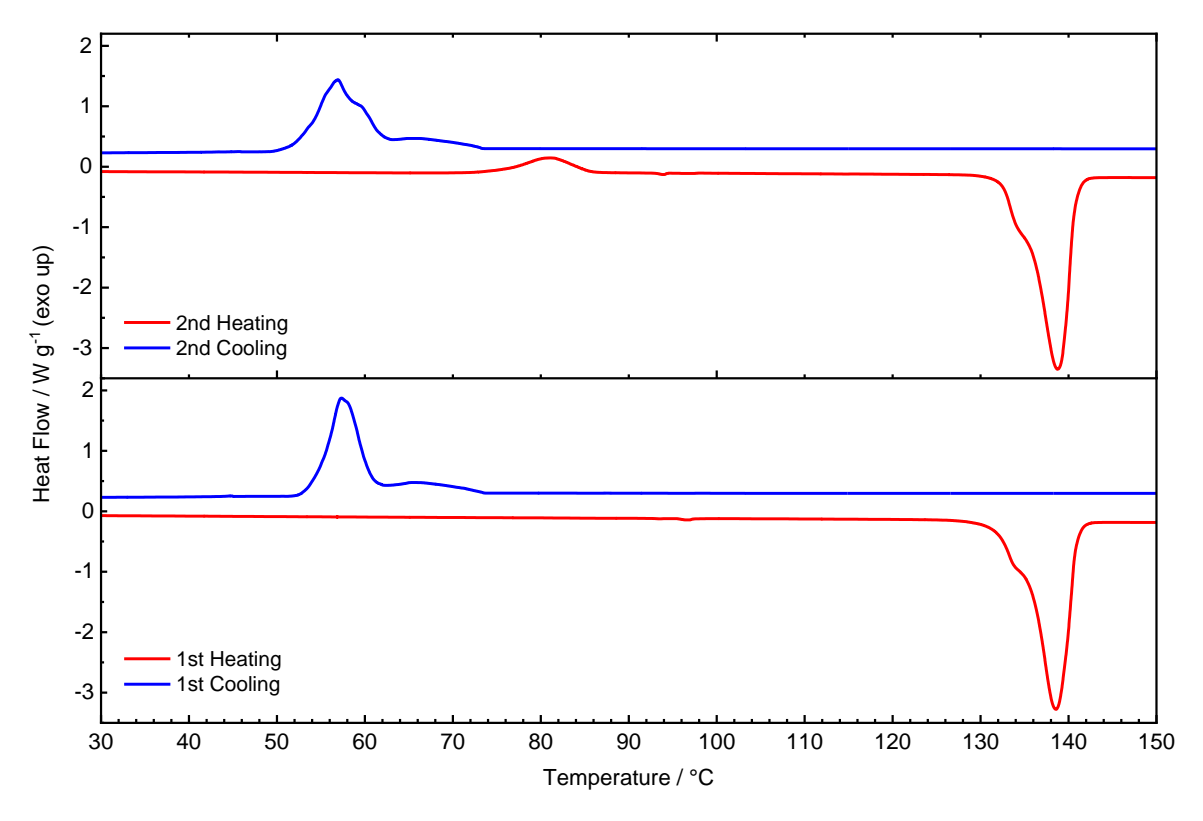


Figure 54: DSC traces measured on a powder of compound **11** with the first heating and cooling cycles below and the second heating and cooling cycles above

crystalline phases, second crystal state to liquid crystal phase and then liquid crystal phase to isotropic liquid respectively. Compound **11** did not show this intricate distinction between polymorphs as seen for **NDI13**. Similarly to compound **10**, compound11 had an initial peak before the larger crystallisation peak. As discussed earlier this may had occurred due to the different rates of crystal nucleation and growth. These crystallisations had a peak at 57 °C with identical enthalpy changes of around 52 J g⁻¹ for both cooling cycles. Also, once again there is a cold crystallisation peak during the second heating cycle at 81 °C with an enthalpy change of 10.2 J g⁻¹.

A comparison of the values gained from the DSC data of compounds **9**, **10** and **11** can be seen in Table 1.4. This table highlights that as there is an increase in repeating glycol units there is an increase in melt and crystallisation temperatures of the NDIs. This opposes what is seen with alkylated NDIs which decrease as the alkyl chain increases^{146, 151}. Each compound has broad endothermic peaks, this may be understood as the nucleation of the initial crystallites, after which a growth phase is observed¹⁴⁸. This causes broader peaks to form as there is an overlap of multiple peaks. Each NDI experiences a cold crystallisation, a phenomenon not seen in alkylated NDIs. The supercooled state that does not crystallise during the cooling cycle then causes a cold crystallisation in the heating cycle; it appears to be specific to NDIs with glycol side chains.

Three water-soluble NDIs have been successfully synthesised and characterised with varying glycol chain lengths, compounds **9**, **10** and **11** with repeating glycol units of three, two and four respectively. Proton NMR confirmed the symmetrical structures and high-resolution mass spectrometry verified the molecular masses. DSC revealed distinct thermal transitions, with heating and cooling peaks increasing as the glycol unit increased. While also showing the unique cold crystallisation properties of compounds (**9**, **10** and **11**). Single crystal X-ray diffraction showed that glycol chain length affects crystal cell parameters and disorder levels. The findings indicate that glycol-substituted NDIs have unique thermal and crystallisation behaviours, especially cold crystallization, influenced by chain length. This work provides a foundation for further studies on these compounds' deposition characteristics and crystal growth

applications.

Compound	1 st Heating	1 st Cooling	2 nd Heating	2 nd Cooling	Cold Crystallisation
9: Peak Temperature (°C)	67.8	15.1	60	15.17	-3.84
Enthalpy Change (J g ⁻¹)	84.6	29.3	48.9	29.3	5
10 : Peak Temperature (°C)	38.5	3	37.5	2.3	-6
Enthalpy Change (Jg^{-1})	78.5	10.5	72.1	9.5	38.4
11: Peak Temperature (°C)	138.6	57.3	138.7	56.9	81
Enthalpy Change (J g ⁻¹)	85.5	51.8	85.9	52.1	10.2

Table 3.3: DSC vales for the first heating, first cooling, second heating, second cooling and cold crystallisation of compound **9,10** and **11**.

3.6.3 Optoelectronic properties of compounds 9 and 11

The following section provides a detailed analysis of the optoelectronic properties of the synthesised glycolated NDIs, examining their UV-visible absorption spectra and electrochemical behaviour. These properties are critical for evaluating the compounds' potential in organic electronic applications, as they directly impact charge transport efficiency, stability, and electronic interactions within devices. Through the study of compounds **9** and **11**, this analysis seeks to elucidate the effects of glycol chain length on electronic properties. However, due to limited remaining material, compound **10** could not be included in this optoelectronic assessment. This limitation notwithstanding, the data obtained from compounds **9** and **11** provide valuable insights into the relationship between molecular structure and optoelectronic function within this class of water-soluble NDIs.

UV-vis spectroscopy provides a valuable method for determining the band gap of materials. In the case of NDIs, a characteristic double peak is typically observed due to π - π * transitions, a signature of their conjugated structure. This spectral feature should appear consistently across both compounds, as the glycol side chains are not anticipated to interact directly with the naphthalene core, thus exerting minimal influence on the band gap. While UV-vis data was collected for both solution and film forms (spin-coated and drop-cast samples), the latter proved insufficient for analysis due to low signal intensity. The solution UV-vis spectra, as illustrated in Figure 55, reveal three distinct absorption peaks for each compound, occurring at 380-381 nm,

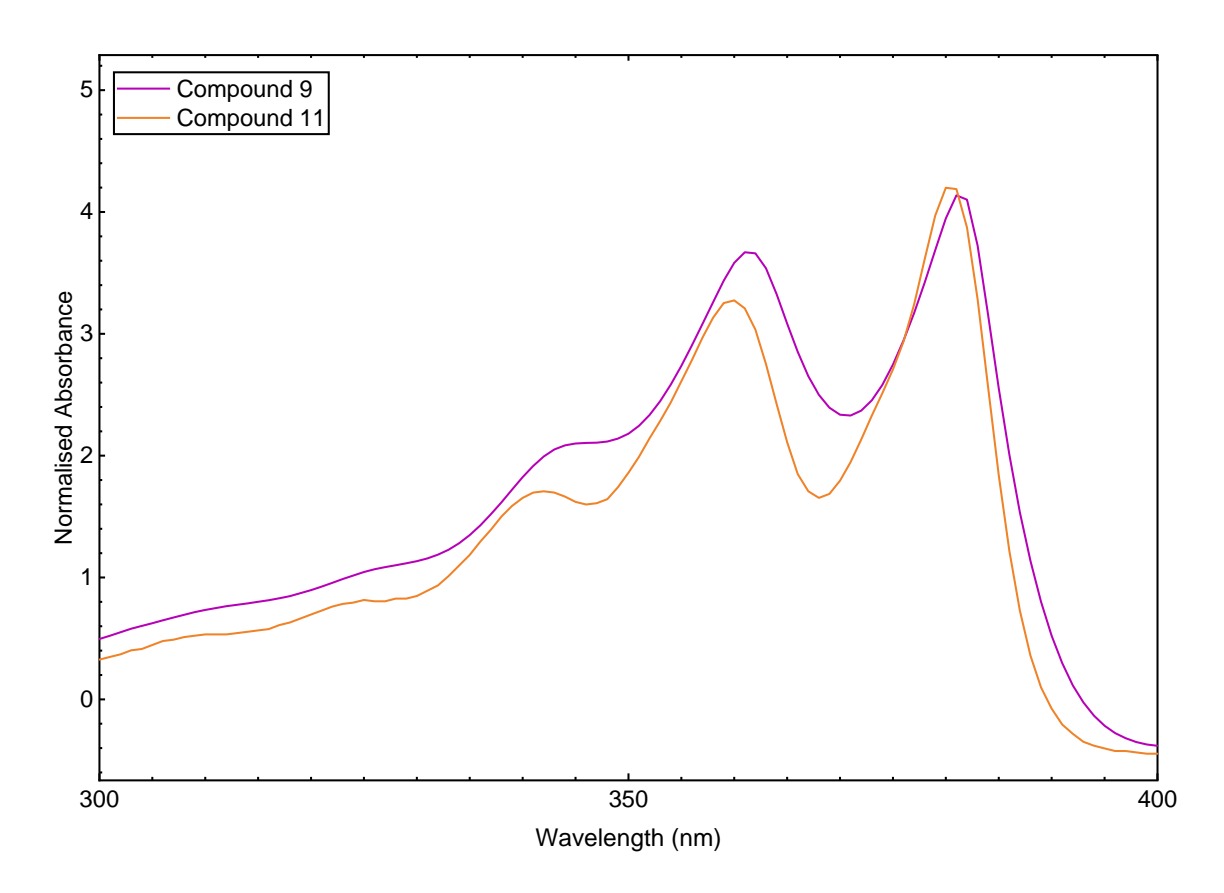


Figure 55: UV-vis. absorption spectrum of compound **9** and compound **11** in chloroform.

362-359 nm, and 345-341 nm. These peaks correspond to the π - π * transitions and the vibrational fine structure of the NDI core, consistent with known spectral features of NDIs.

The electron affinities were established electrochemically. Figure 56 shows the cyclic voltammograms of compound $\bf 9$, and compound $\bf 11$ all in dichloromethane referenced to the potential of an Ag/Ag⁺ electrode. Each compound was scanned five times, with each successive scan reducing in intensity this means the reduction is not fully reversable and could be due to the compound slowly breaking down. Compound $\bf 9$ shows a reversible reduction with an anodic peak potential taken from the first reduction peak maxima was (E_{pa}) = -1.1 V. Compound $\bf 11$ also shows reversibility and an E_{pa} of -1.2 V. Both compounds likely have a reduction proceeded with two consecutive one-electron processes, initially there is a radical-anion generation followed by the transition of this radical-anion into a dianion typically seen for NDIs^{152, 153}. The electron affinity values were estimated from the first onset of reduction (E_{onset}) at 6 -3.92 eV and -3.86 eV for compound $\bf 9$ and compound $\bf 11$. These values were estimated using¹⁵⁴:

$$E_{LUMO} = -4.8 - E_{onset} \tag{11}$$

where 4.8eV is the energy level of ferrocene/ferrocenium below vacuum. From the UV-vis absorption spectrum in Figure 64 the onset of absorption (λ_{onset}) where estimated to be 398 and 397 nm for compound **9** and **11** respectively. From the λ_{onset} the optical band gap can be calculated using¹⁵⁵:

$$E = h \times \frac{C}{\lambda_{onset}} \tag{12}$$

Where E is the band gap energy, h is Planks constant, C is the speed of light, and 1 eV is 1.6 x 10^{-19} Joules (conversion factor). Using this calculation the optical band gaps were 3.12 and 3.13 eV for compound **9**, and compound **11** respectively. Furthermore, the ionisation potentials were calculated by taking the optical band gap away from the electron affinity generating -7.04 eV for compound **9** and -6.99 eV finally for compound **11**. All of the results are summarised in Table 3.4 and the ionisation

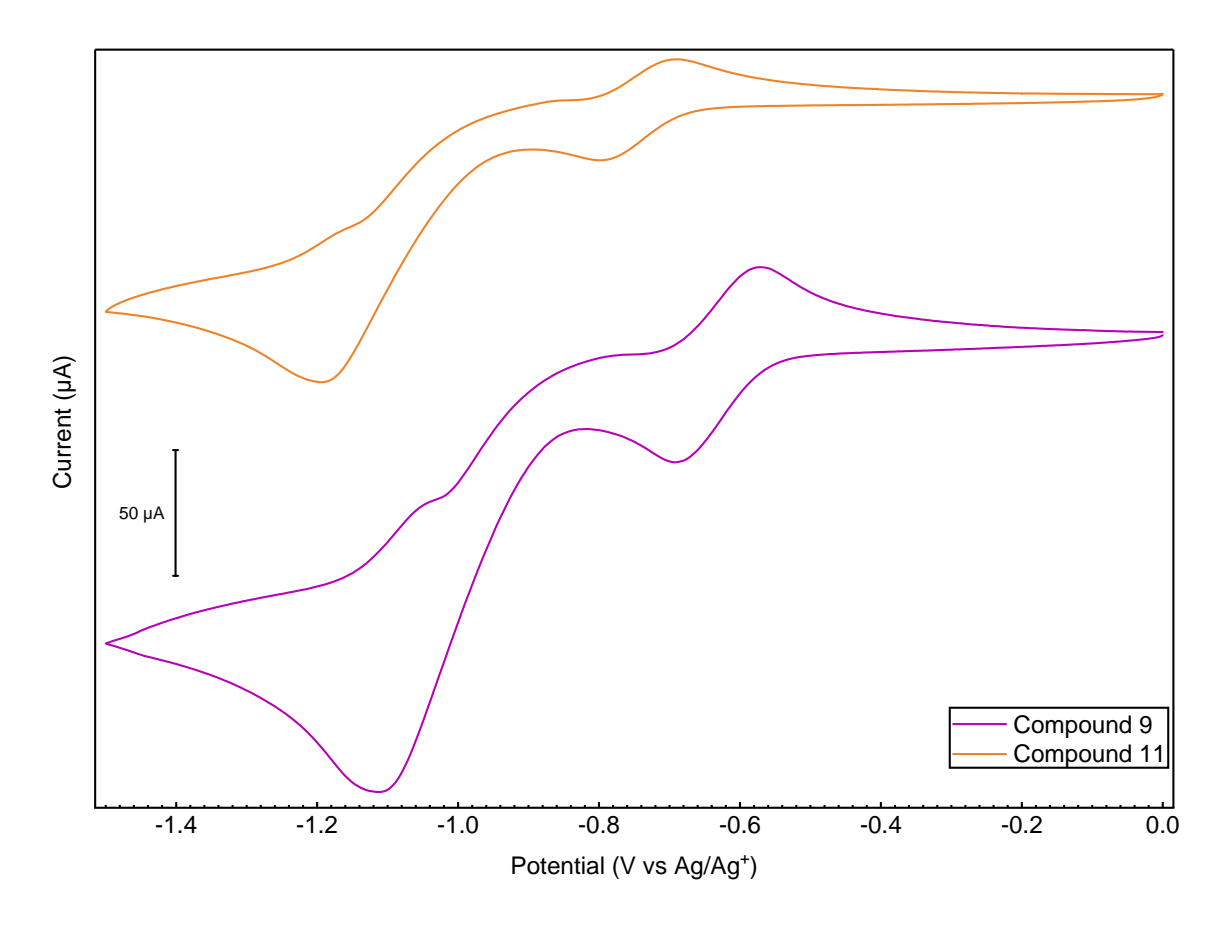


Figure 56: a) Cyclic voltammogram of compound **9** and compound **11** in a solution of dichloromethane solution with 0.1 M TBAPF₆ electrolyte between 0 and -1.5 V. Referenced to Ag/Ag⁺ electrode with a platinum wire counter electrode and glassy carbon working electrode.

potential and electron affinity can be observed in Figure 57. The increasing length of side chain has a measurable impact on the electronic and optical properties of NDI derivatives. While the core electronic structure remains largely consistent, as indicated by the relatively small changes in reduction potentials and band gaps, the increasing side chain length subtly tunes key properties such as electron affinity, ionisation potential, and reduction onset.

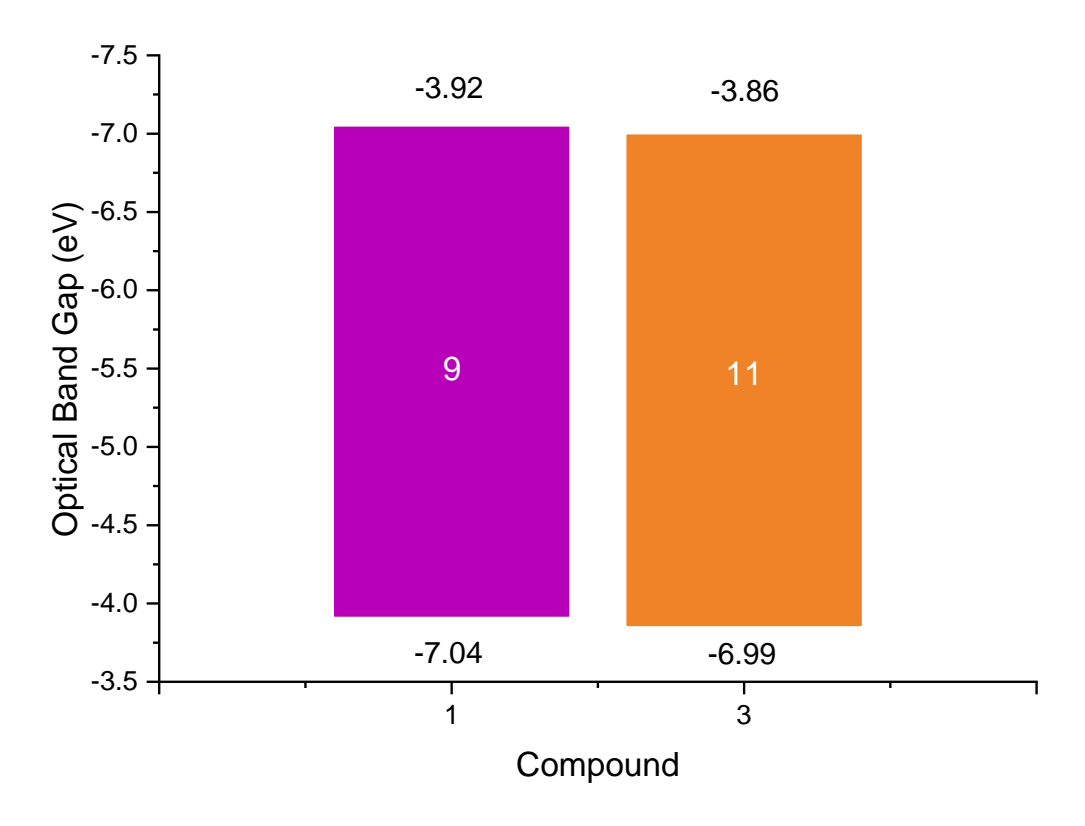


Figure 57: Ionisation potential and electron affinity of compounds **9** and **11** measured by UV-vis and CV.

Table 3.4: Electrochemical and optical properties of compound 9 and compound 11.											
Compound	E _{pa} ^[a] (V)	E _{onset} [a] (V)	λ _{max} ^[b] (nm)	λ _{onset} ^[b] (nm)	Optical band gap [c] (eV)	Electron Affinty ^[d] (eV)	Ionisation potential [e] (eV)				
9	-1.1	-0.88	381	398	3.12	-3.92	-7.04				
11	-1.2	-0.94	380	397	3.13	-3.86	-6.99				

[a] From solution cyclic voltammetry using glassy carbon working electrode, platinum wire counter electrode and Ag/Ag⁺ reference electrode. Values are reported from the 2nd cycle. [b] From solution UV-vis absorption spectroscopy in chloroform. [c] Estimated from λ_{onset} . [d] Estimated from the electrochemical onset of reduction (E_{onset}). [e] Estimated using equation Electron Affinity = Ionisation potential – Optical band gap. [f] calculated from the trendline of the λ_{onset} .

3.7 Droplet Manipulation

This section explores the crystallisation and droplet manipulation techniques employed to study compound **9**. The goal is to use the newly developed novel vapour-guided non-contact method for crystal deposition and to optimise the parameters for crystal growth. Compound **9**, characterised by its high solubility in water and readiness to crystallise from DMF solutions, provides an excellent model for testing these new techniques.

We start by examining the crystallisation behaviour of compound **9**, exploring its solubility limits and conditions that favour crystal formation. Understanding these parameters is crucial for controlling crystal growth and deposition. This section will also cover the methodology used to manipulate droplets to achieve uniform crystal deposition, focusing on factors such as solvent composition, droplet speed, and substrate preparation.

Furthermore, we discuss the challenges faced and solutions developed to standardise the crystallisation process, attempting to ensure reproducibility and consistency. This includes the impact of environmental conditions, substrate cleanliness, and the effects seeding had on crystal nucleation. Once standard conditions are established the vapour-guided non-contact method is tested with additional OSC compounds **10** and **11** synthesised in the previous section. The results from these experiments not only demonstrate the effectiveness of the techniques but also provide insights into the physical and chemical principles governing crystal formation and growth.

Ultimately, this section aims to present a comprehensive overview of the innovative approaches taken to refine droplet-based crystal deposition, laying the groundwork for future research and application in the field of organic semiconductors.

3.7.1 Crystals Nucleation and Growth

The vapor-guided deposition technique is likely to promote crystal growth in water-soluble NDI-based OSCs due to the solubility and supersaturation characteristics of the synthesised compounds, particularly compound **9**, which readily crystallises under ambient conditions. As the droplet moves under the influence of the vapor source, evaporation gradually drives the solute concentration towards supersaturation, a

critical condition for nucleation and crystal growth. Building on Malinowski's preliminary work, this study refines the vapor-guided approach by adjusting parameters such as droplet velocity and solvent composition, which have shown promising results in earlier experiments for achieving reproducible single-crystal formation. Additionally, DSC revealed crystallisation properties of the glycolated NDIs, suggesting that their thermal behaviour aligns well with the controlled supersaturation achievable in vapor-guided deposition. These combined factors indicate that the method holds significant potential for producing single crystals.

Crystallisation is a multifaceted process involving the concurrent nucleation and growth of crystallites. The dynamics of crystal formation are governed primarily by two interdependent parameters: the nucleation rate and the growth rate. Nucleation can either occur spontaneously or be induced through artificial means, both of which present significant challenges in terms of control and reproducibility. Once nucleation is initiated, it is followed by crystal growth, where the newly formed nuclei increase in size. Nucleation can occur through two distinct mechanisms: homogeneous (or primary) nucleation, which proceeds independently of external surfaces or impurities, and heterogeneous (or secondary) nucleation, which occurs in the presence of foreign surfaces that serve as preferential nucleation sites ¹⁵⁶.

Homogeneous nucleation is rarely observed in practice, as foreign phases such as container walls, impurities, or defects typically catalyse the crystallisation process. The driving force behind nucleation is the difference in Gibbs free energy between the liquid and the solid phases. The critical Gibbs free energy, which determines the likelihood of nucleation, is directly influenced by the volume of the nascent nucleus. Thus, any factor that reduces the volume of the nucleus also reduces the critical Gibbs free energy required for its formation, thereby increasing the probability of nucleation 157.

Whereas nucleation represents the initial emergence of a crystal nucleus, crystal growth corresponds to the subsequent enlargement of these nuclei. The interplay between nucleation and growth ultimately dictates the final crystal size distribution. An example of this is seen in solidification processes, where the driving force is the negative Gibbs free energy (ΔG) of solidification:

$$-\Delta G = \frac{L}{T_m} \left(T_m - T \right) \tag{13}$$

where L is the latent heat of solidification, T_m is the melting temperature, and T is the system temperature. The rate of atomic rearrangement across the liquid-solid interface, or the jump frequency, has a temperature-dependent expression given by:

$$f = f_0 exp\left(-\frac{\Delta G_M}{kT}\right) \tag{14}$$

where f_0 is the pre-exponential factor, ΔG_M is the activation energy for movement across the interface, k is the Boltzmann constant, and T is the absolute temperature. Combining these expressions results in the crystal growth rate equation:

Grwoth rate =
$$f_0 exp\left(-\frac{\Delta G_M}{kT}\right)\left(\frac{L}{T_m}\right) (T_m - T)$$
 (15)

This relationship demonstrates that as temperature decreases, the thermodynamic driving force for growth increases, while the atomic jump frequency decreases. These opposing trends result in a maximum growth rate at a specific temperature, highlighting the complex temperature dependence of crystal growth 156.

Supersaturation, a non-equilibrium state in which a solution contains more solute than is permissible under equilibrium conditions, serves as the thermodynamic driving force for both nucleation and growth 158. The relationship between crystal nucleation and growth as a function of supersaturation (Figure 58) is defined by the following equations:

$$G = k_g \Delta C^g \tag{16}$$

$$B = k_b \Delta C^b \tag{17}$$

where G is growth rate, $k_{\rm g}$ is the growth constant g is the growth order, B is nucleation rate, $k_{\rm b}$ is the nucleation constant, b is the nucleation order and ΔC is supersaturation ¹⁵⁶. When these equations are plotted for a hypothetical organic crystallisation process, they illustrate the critical influence of supersaturation. At low supersaturation levels, growth outpaces nucleation, leading to a wider distribution of larger crystals. Conversely, at high supersaturation, nucleation rates exceed growth rates, resulting in a predominance of smaller crystals.

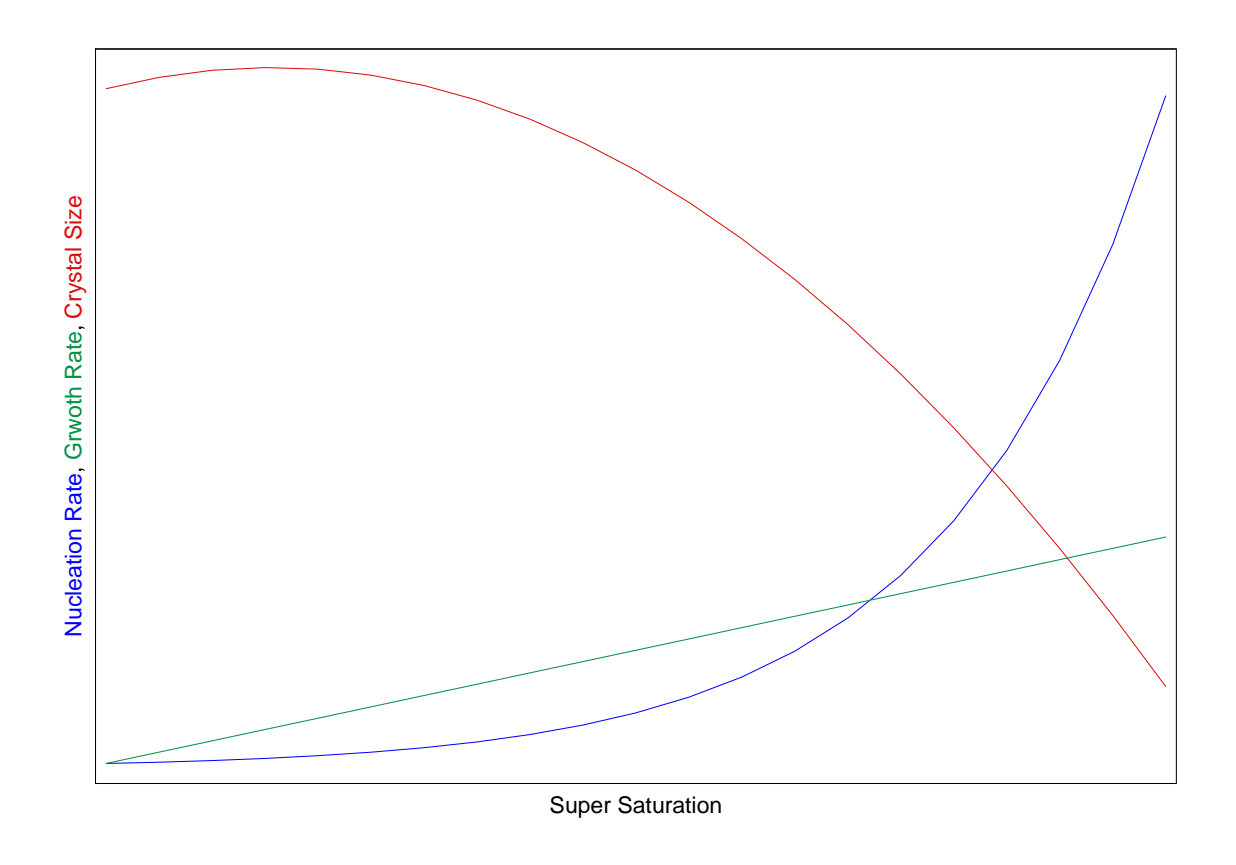


Figure 58: illustration of the relationship between super saturation and crystal growth rate, nucleation and size.

3.7.2 Materials and Setup

Droplets that exhibit negligible contact angle hysteresis are capable of spontaneous motion due to evaporation-induced Marangoni stresses. To achieve such behaviour, the droplet must consist of a binary liquid system, where two miscible solvents are combined to leverage differences in their physical properties. The dynamic behaviour of binary liquids is predominantly governed by two key parameters: the difference in boiling points and the difference in surface tensions between the constituent solvents. Water, for example, has a relatively high surface tension (72 mN m⁻¹ at 21 °C¹⁵⁹) compared to its boiling point (100 °C¹⁰), while many miscible organic solvents possess lower surface tensions and a range of boiling points

In binary liquid systems composed of water and a miscible organic solvent, two scenarios arise depending on the relative volatility of the organic component. In the first scenario, where the organic solvent is more volatile than water, it evaporates more rapidly, leading to an accumulation of water at the droplet's periphery. This differential evaporation creates a surface tension gradient, with higher surface tension at the edges relative to the droplet's apex, effectively "pulling" the droplet outward due to

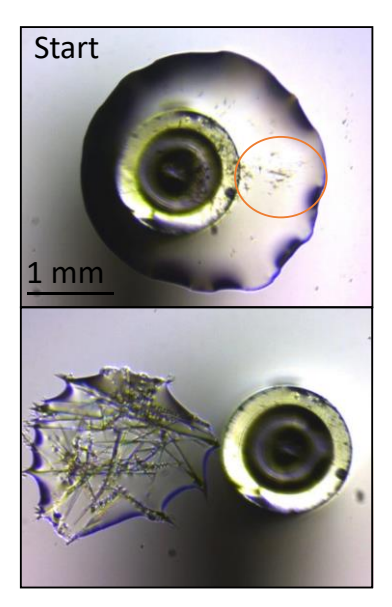
Marangoni flows. Conversely, if the organic solvent is less volatile, water evaporates preferentially at the droplet's edges, resulting in a higher surface tension at the top of the droplet, which causes the droplet to contract and increases the overall contact angle. Consequently, droplets consisting of water and a less volatile, lower surface tension component exhibit minimal contact angle hysteresis and can achieve translational motion.

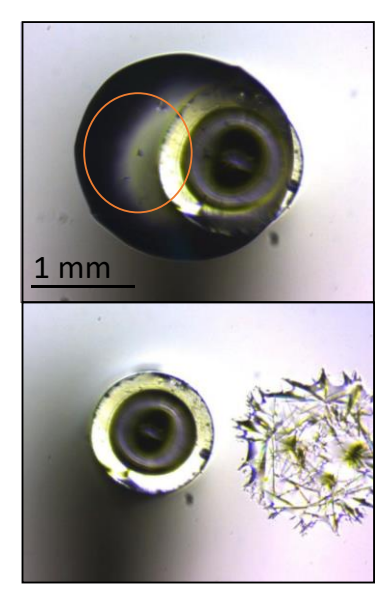
Two binary solvent systems were utilised in the present study to induce droplet motion during deposition experiments. The first system, previously established, consisted of 95 mol% water and 5 mol% propylene glycol (PG). PG has a lower surface tension (40.1 mN m⁻¹ at 25°C¹⁶⁰) than water, but a significantly higher boiling point (187.6°C¹⁶⁰), resulting in preferential water evaporation at the droplet's periphery.

The second system was developed specifically to enhance the dissolution of organic semiconductors, using 95 mol% water and 5 mol% DMF. Similar to PG, DMF has a lower surface tension (36.4 mN m⁻¹ at 25°C¹⁶¹) than water but is less volatile, with a boiling point of 153 °C¹⁶¹.

The solubility of the target compound (**9**) in water was found to be 6 mg mL⁻¹, a concentration achieved through heating at 50°C and sonication for 30 minutes. This concentration was stable for approximately two hours before spontaneous crystallisation began. Within this timeframe, a binary droplet solution was prepared by adding 5 mol% DMF to the aqueous solution of compound 1 at 6 mg mL⁻¹. As compound 1 was already in a supersaturated state in water, the addition of DMF effectively lowered the saturation level, thereby reducing the nucleation rate while serving as the second component of the binary droplet system.

To maintain solution stability, freshly prepared samples were used for each deposition. Initially, batches were prepared and stored for periods ranging from 2 to 7 days, during which very small crystals (<0.1 mm) were observed to form, as shown in Figure 59. This phenomenon was attributed to gradual solvent evaporation, which increased the solution's supersaturation and triggered nucleation. These small crystallites were not visibly detectable until the droplet was placed on the glass substrate, complicating subsequent crystal growth studies. To mitigate this issue, fresh solutions were prepared daily prior to each experiment, ensuring consistency in the initial conditions.





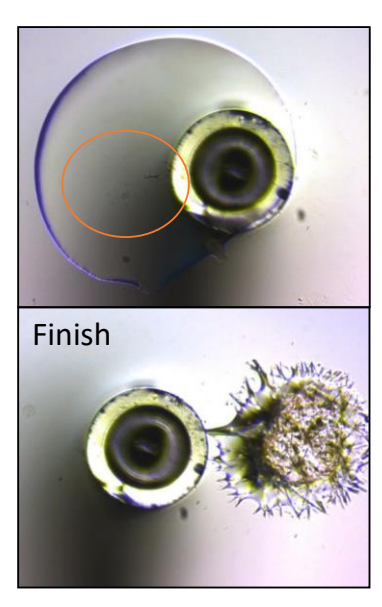


Figure 59: Image of depositions using the same concentration and speed but with starting droplet containing small crystals causing cluster formation as the droplet evaporates. Initial crystals on the top row highlighted, pinned droplet depicts the finish shown on the bottom row.

A critical component in controlling droplet motion is the presence of a vapor source, as detailed in Section 2.3.3, Vapor Source and Droplet Composition. The vapor source disrupts the internal equilibrium of forces within the droplet, thereby inducing motion. The experimental vapor source used a glass capillary with an internal diameter of 1 mm, filled with 1 mL of water, which created a localised vapor field around the droplet. This vapor field reduces the overall evaporation rate of the droplet, and when the droplet is not directly beneath the vapor source, it induces an imbalance in the surface tension gradient. This imbalance generates Marangoni flows, leading to a net shear force on the substrate that propels the droplet 109.

The geometry of the vapor source is a significant determinant of the vapor field it produces and, consequently, the resulting surface tension gradients within the droplet. Larger vapor sources generate higher vapor concentrations, resulting in a shallower concentration gradient and potentially altering the droplet's motion dynamics. To minimise variability, a uniform capillary size (1 mm in diameter) was employed consistently across all experiments to ensure a stable vapor field and reproducible surface tension profiles. This capillary was partially filled with 0.002 mL of water to act as the vapour source. Similarly, the height of the vapor source relative to the substrate can influence the Marangoni flows within the droplet by altering the local humidity

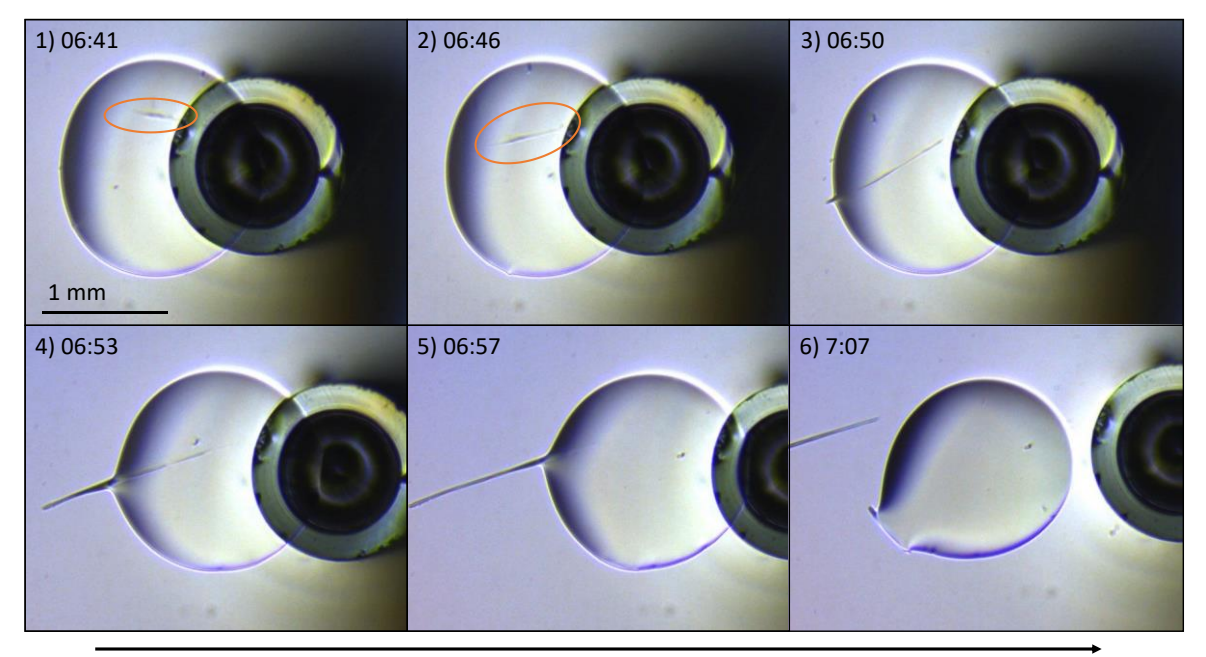
around the droplet. To mitigate this effect, the height of the vapor source was fixed at 0.5 mm from the substrate surface as this showed the best control observed by Malinowski¹¹⁰. This ensured a consistent experimental environment and reducing variability in the induced flows.

Finaly, the laboratories air conditioning system was set to a temperature of 21+/- 2°C with a humidity of 45+/-10 %. Also as mentioned in section 2.2 Optical Microscopy the microscopic set up was surrounded by an acrylic environmental chamber to reduce cross winds produced in the laboratory.

3.7.3 Grown Crystals

The crystals presented in this section were prepared using a standardised set of parameters, which were refined through extensive experimentation to optimise crystal growth conditions. This section focuses exclusively on the most successful outcomes, while subsequent sections will elaborate on the systematic determination of these optimal conditions. Each glass substrate was pre-treated according to the protocol outlined in Section 2.1, *Slide Preparation*. The droplet volumes were set at 0.5 μL, derived from a 5 mol% DMF and 95% water solution, as previously described. The droplet movement speed was adjusted to a range of 0.1-0.2 mm s⁻¹, a velocity that ensures effective tracking of the vapor source. This speed range prevents the vapor source from outpacing the droplet, while also avoiding excessively slow velocities that could destabilise the droplet's movement. This parameter optimisation will be explored in detail in the subsequent section.

Figure 60 provides a visual representation of the crystallisation process within the moving droplet. In Image 1, a single crystal (highlighted by an orange circle in Images 1 and 2) initiates growth and remains mobile due to the internal flows within the droplet as it moves towards the vapor source. Image 2 captures the droplet at a subsequent stage, showing an increase in droplet size concomitant with crystal growth. By Image 3, the crystal has elongated further and is nearing its point of separation from the droplet. At this critical stage, either due to the droplet reaching a maximum size or changes in flow dynamics, the crystal adheres to the substrate. Once deposited on the surface (as depicted in Image 3), the droplet continues its movement, leaving the crystal behind. As long as the crystal remains within the droplet, it continues to grow, as shown in Images 4 and 5.



Direction of droplet movement

Figure 60: One of the first deposition attempts showing a crystal leaving the droplet as it moves from left to right. In images 1 and 2 the crystal is still forming in the droplet, in 3 the crystal breaks out the droplet and pins on the substrate. Images 4 and 5 the crystal is growing as the droplet move until the droplet moves past the end of the crystal in image 6. The droplet stopping moving after 7 minutes and 22 seconds.

The variation in crystal lengths grown under these controlled conditions was assessed across 26 individual experiments. Figure 61 illustrates the length distribution of crystals formed under these conditions. Despite uniform growth conditions, the distribution reveals two primary peaks around 0.6 mm and 1.4 mm, indicating that crystal growth favours these specific size ranges. This bimodal distribution suggests potential underlying factors that influence crystal growth, leading to clustering around two distinct size classes. Additionally, the data range spans from approximately 0.2 mm to 2.0 mm, with relatively few crystals at these extremes. The low counts at both ends suggest that crystals rarely reach these minimal or maximal lengths. This size variability is attributed to the premature detachment of crystals from the droplet, which interrupts the supply of solute material necessary for further growth. This observed distribution pattern diverges from normality and indicates complex growth behaviour that may involve multiple growth phases or stochastic variations in nucleation and crystallisation rates. These findings provide valuable insights into the intrinsic variability of crystal formation and underscore the importance of further investigating the factors that contribute to the emergence of distinct crystal size clusters under

standardised growth protocols. The crystals height and width did not significantly change when compared to the crystals length. This is common with lath-shaped crystals as growth primarily occurs anisotropically due to molecular orientations. These types of crystals have differential growth rates across each crystallographic plane which can lead to pronounced elongation along one axis, producing the needle-like structure observed in these samples. That lead to the focus of the crystal growth measurements beaded on the length as this were generated the most significant change.

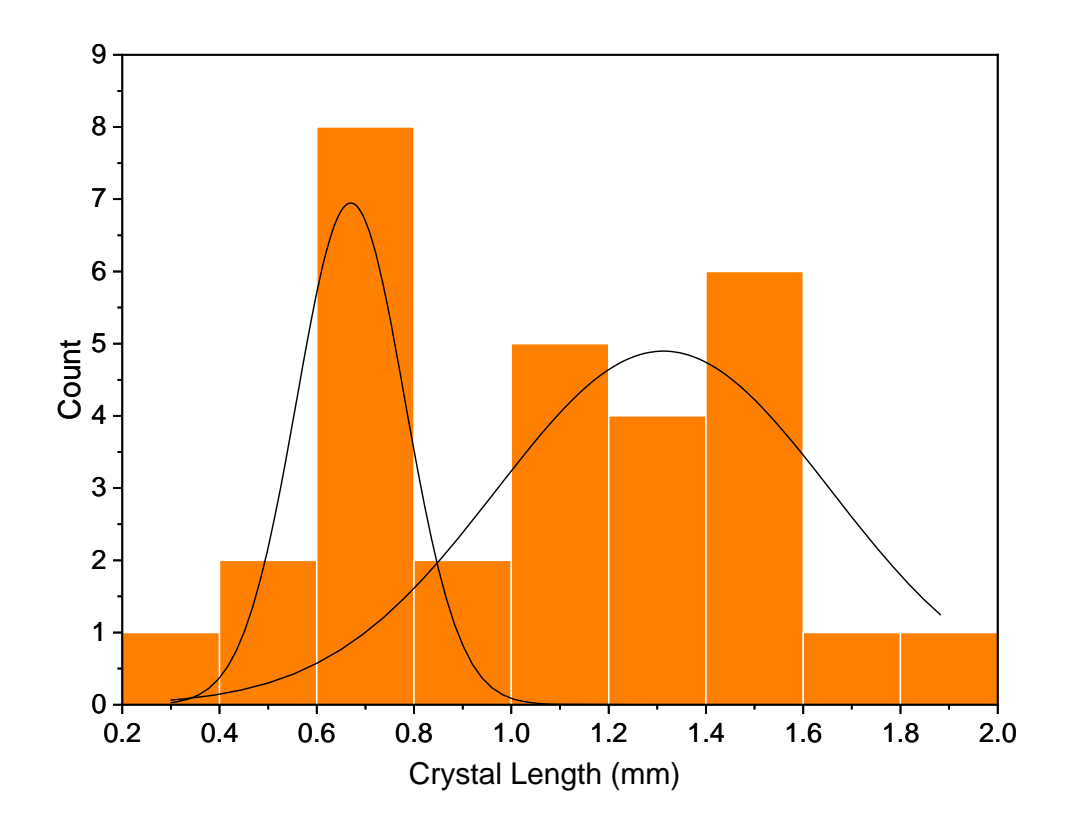


Figure 61: Crystal length of thirty crystals produced from different experimental runs distributed by size with a bimodal distribution curve.

The normal probability plot shown in Figure 62 assesses the distribution of crystal lengths for normality, indicating how closely the observed data adheres to a normal distribution. In this plot, the majority of data points are split between two groups (0.7 and 1.4 mm), suggesting that the distribution of crystal lengths approximates a bimodal distribution. However, there are slight deviations in the lower and upper percentiles, as evidenced by points that deviate marginally from the line at the extremes. This could

suggest minor skewness or the presence of outliers in the crystal length distribution, most likely related to random variations in the growth process. The calculated mean (μ) is 1.06, with a standard deviation (σ) of 0.41, indicating that the crystal lengths are centred around a specific value with moderate variability. The overall linearity of the plot supports the hypothesis that, under the controlled experimental conditions, the crystal lengths follow an approximately normal distribution, reinforcing the suitability of using parametric statistical methods for further analysis.

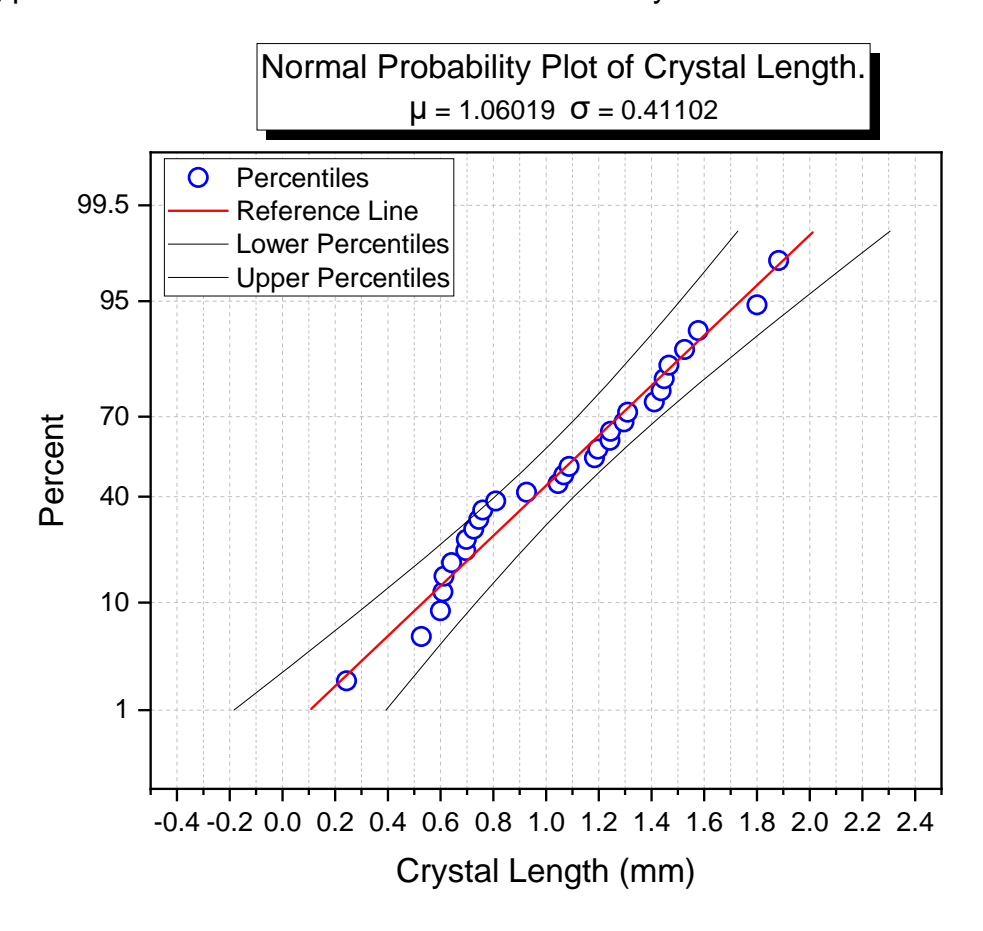


Figure 62: Normal probability plot of crystals lengths with mean of 1.06 and a standard deviation of 0.41.

3.3.3 Crystal Orientation

Figure 61 analyses the relationship between crystal length and the angle at which the crystals emerged from the droplet relative to the direction of droplet movement. These positional and angular variations depend on the saturation point at which the crystal begins to grow and the evaporation point of the droplet. Once a crystal reaches a critical size and the droplet reduces in volume, the crystal may become anchored to the substrate. In such cases, the droplet continues its forward motion without the crystal, leaving it adhered to the surface. This phenomenon can also occur when one

crystal is obstructed by another within the droplet. While hindrance can be disadvantageous for crystal uniformity, it provides an opportunity for isolating individual crystals before a rapid nucleation event leads to mass crystallisation.

The angular distribution of needle-like crystal growth was analysed using the polar plot presented in Figure 63. This plot reveals significant insights into the preferential orientation of crystals within the system. The data demonstrate that crystal growth is highly anisotropic, with growth occurring predominantly at specific angles relative to the droplet's movement direction. Distinct peaks in the polar plot are observed at approximately 30° and 150°, indicating that these directions represent the most favourable orientations for crystal growth under the experimental conditions. Conversely, regions around 90° and 270° show minimal crystal occurrence, suggesting that growth is strongly suppressed in these orthogonal directions.

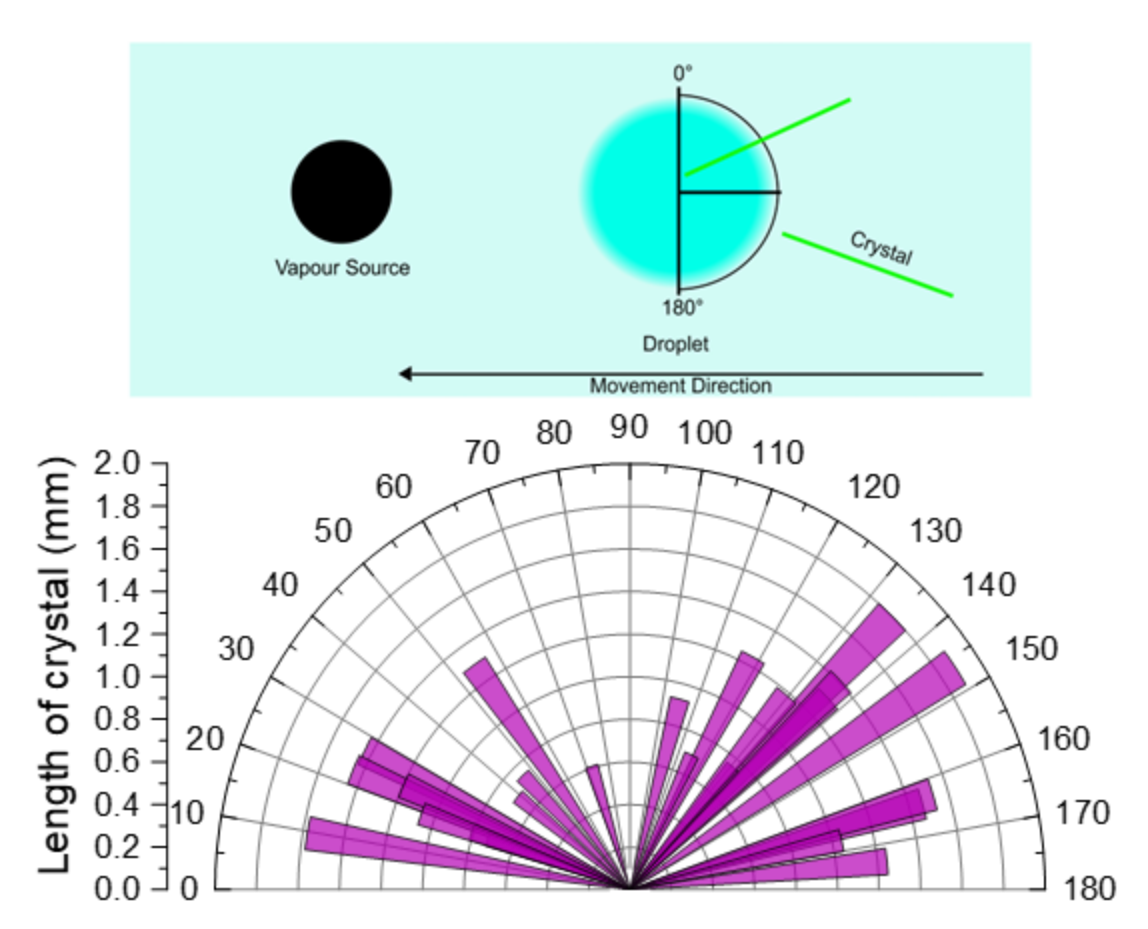


Figure 63: Top left is an illustration of the droplet and its direction of movement with the graphs angles super imposed. The graph shows the angle and length at which crystals left the droplet.

The symmetry of the polar plot about the 0° and 180° axes further emphasizes the directional nature of the growth process. This mirrored distribution suggests that

crystal alignment is influenced by uniform external factors, such as the vapor flux and the movement dynamics of the droplet. The vapor source appears to create a gradient that promotes preferential crystal elongation along the identified angles. The suppression of growth at intermediate angles implies that the growth kinetics or material flux is less favourable in these orientations, leading to the observed anisotropic distribution.

Droplet flows that are induced when Marangoni flows are present indicate that velocity peaks occur symmetrically on either side of the centreline 162, 163, corresponding to the regions of recirculation. This symmetry likely contributes to the observed anisotropic crystal growth, as material fluxes are preferentially directed along these high-flow regions.

Marangoni flows are known to enhance mass transport within droplets, creating directional gradients in precursor concentration. In this system, the high-velocity flows near the droplet's surface may concentrate precursor material along specific axes, promoting crystal nucleation and elongation in those directions. This mechanism aligns with the polar plot analysis, which shows preferential growth at specific angles relative to the droplet's movement direction. The suppression of growth in orthogonal directions may result from reduced material availability in low-flow regions, where precursor transport is less efficient.

Overall, the flow patterns generated by Marangoni effects appear to create anisotropic conditions within the droplet that guide the directional growth of needle-like crystals. These findings suggest that controlling Marangoni flows, through adjustments droplet dynamics, could enable precise control over crystal orientation and growth behaviour.

3.7.4 Evaluation of the Crystal Structures

The crystal structure of two crystals grown via different methods are outlined in this section. The one crystal grown via a solution of DMF as seen previously and the other crystal was grown using the non-contact vapour-guided deposition, crystal **9** (VG). By obtaining a crystal structure from both methods they can be evaluated to observe if both techniques yield the same crystal structure. Both of the crystal packing structures are seen in Figure 64 at the three different cell lengths (a, b and c).

Both crystals **9** and **9**(VG) were single colourless lath-shaped crystals. Both are orthorhombic, where all three axes are unequal at right angles; they have similar call lengths and identical cell angles. Both have similar cell volumes with a 50 Å^3 difference; the crystals have the same space groups. The crystal structures have low R factors (9 = 3.89% and 9(VG) = 3.76%), representing good agreement between the observed amplitude and the calculated amplitudes. We see a small level of disorder towards the end of the pegylated end groups. With a longer chain end, group vacancy rows can form at the chain end if the neighbouring chains remain linear; however, the

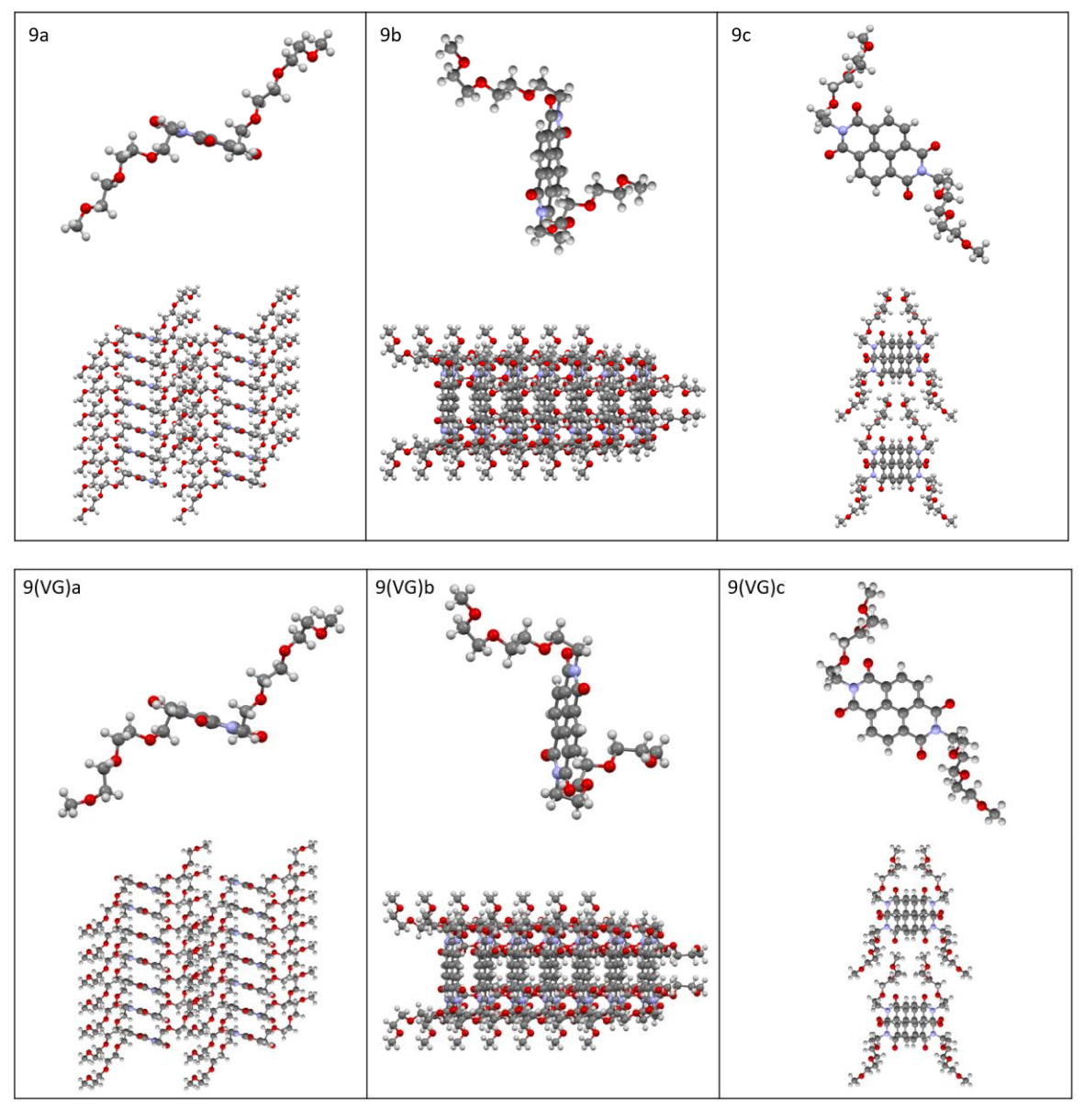


Figure 64: 1a,b,c) illustrations of the molecular geometry of **9** at cell length a, b and c where **9** was dissolved in DMF and left to evaporate over multiple days. **9** vapour guided (VG) a,b,c) illustrations of the molecular geometry of **9** at cell length a, b and c where the crystals where synthesised using our vapour guided deposition technique.

increase in interchain energy can cause this vacancy row to be filled by a neighbour.¹⁴³. Overall, we have discovered that the crystals synthesised using our droplet manipulation techniques are nearly identical to those synthesised using traditional crystallisation techniques.

Crystal Data 9(VG). C₂₈H₃₄N₂O₁₀, M_r = 558.55, orthorhombic, Aea2 (No. 41), a = 26.1317(7) Å, b = 29.2036(8) Å, c = 6.9417(2) Å, $a = b = g = 90^{\circ}$, V = 5297.5(3) Å³, T = 100.00(10) K, Z = 8, Z' = 1, m(Cu K_a) = 0.895 mm⁻¹, 25491 reflections measured, 4376 unique ($R_{int} = 0.0357$) which were used in all calculations. The final wR_2 was 0.1001 (all data) and R_1 was 0.0376 ($I \ge 2$ s(I)).

3.7.5 Parameter Variations

As previously discussed, the droplet motion is influenced by the position of the vapor source, such that as the distance between the droplet and the vapor source increases, the velocity of the droplet also increases¹¹⁰. This variation in velocity results in significant changes in the internal flow dynamics within the droplet. Consequently, the location of maximum surface tension shifts depending on the relative position of the vapor source. For instance, when the vapor source is positioned directly above the droplet, the maximum surface tension is concentrated at the droplet's apex. Conversely, when the vapor source moves laterally relative to the droplet, the maximum surface tension is displaced to an intermediate position between the top and the bottom of the droplet. This shift in surface tension distribution induces complex internal flow patterns, which in turn impact the motion and organisation of crystallisation sites within the droplet.

Crystal growth is predominantly governed by slow nucleation and subsequent growth phases. Accordingly, it was hypothesised that reducing the velocity of the droplet would promote the creation of stable nucleation points, thereby facilitating controlled crystal growth. Given that nucleation occurs naturally as the droplet undergoes evaporation, optimising the subsequent growth phase is crucial for improving crystal yield and uniformity. Slower droplet movement was proposed as a strategy to achieve more consistent internal flows, theoretically enhancing crystal growth outcomes.

Figure 65 shows examples of crystals formed under various droplet velocities. At the slowest tested speed of 0.01 mm s⁻¹, isolated crystals appeared at the conclusion of the droplet's movement, while higher speeds of 0.04 and 0.06 mm s⁻¹ led to the formation of crystal clusters. These clusters indicate reduced system controllability at lower speeds, where the close proximity of multiple nucleation sites impedes the isolation of single crystals.

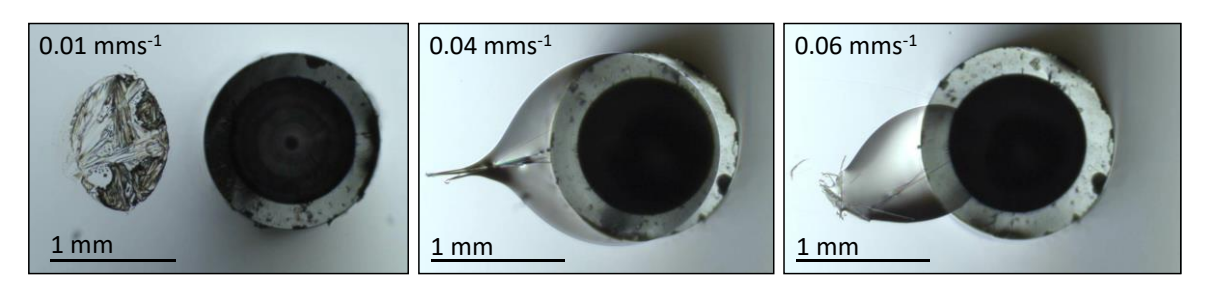


Figure 65: Examples of crystal clusters forming at slower substitute movement speed were multiple cluster form rapidly.

Similarly, Figure 66 demonstrates crystal formation patterns at velocities ranging from 0.02 to 0.1 mm s⁻¹, where the occurrence of crystal clusters is more pronounced at lower speeds. Under these conditions, subsequent crystals tended to use the initial crystal as a secondary nucleation site, leading to spontaneous and rapid crystal development. This phenomenon was found to be difficult to regulate, thus eliminating lower velocities as a viable approach for controlled crystal growth.

The most reproducible results were observed in the intermediate velocity range between 0.1 to 0.2 mm s⁻¹, where crystal growth was more consistent, and the occurrence of rapid, uncontrolled crystallisation was minimized. Nevertheless, the challenge of multiple crystals forming from a single nucleation site persisted at 0.1 mm s⁻¹, as depicted in Figure 66. An optimal velocity of 0.15 mm s⁻¹ was determined to be the most effective, as this speed allowed the droplet to maintain close proximity to the vapor source while lowering the formation of multiple crystals. While this velocity was determined to be the most successful single crystals were observed in twenty-six out of eighty-eight individual droplet experiments using the optimal conditions.

Higher velocities were also explored to determine the upper limits of the system's efficacy. At speeds ranging from 0.2 to 0.3 mm s⁻¹, the droplet was unable to match the movement of the vapor source, leading to a gradual displacement of the droplet outside the observable field of view. This displacement hindered real-time monitoring

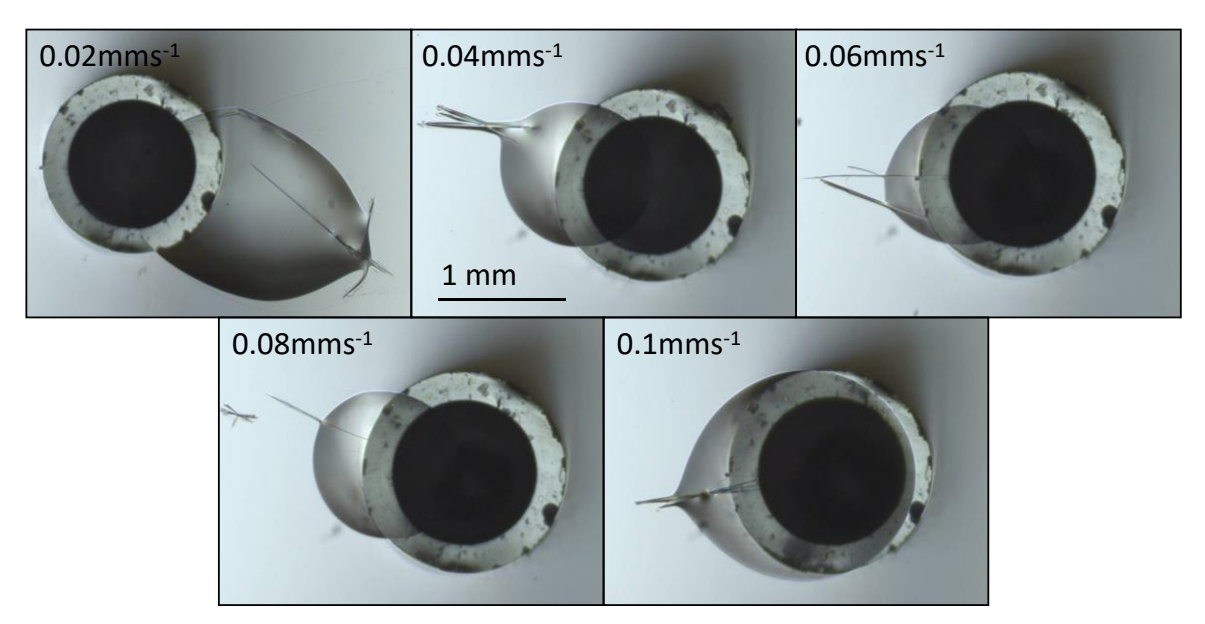


Figure 66: Examples of crystal clusters forming at different substrate movement speeds.

and resulted in incomplete observations of crystal growth. Consequently, these higher velocities were deemed unsuitable for controlled crystallisation due to the lack of visibility and the tendency for droplets to evaporate prematurely, leaving behind disordered crystal clusters similar to those observed at slower speeds.

One of the primary challenges encountered in the early stages of this research was achieving a consistently clean substrate surface. Initial deposition experiments revealed a high degree of surface irregularities, along with the presence of particulates and residual contaminants on the glass substrates. These inconsistencies are inherent to the manufacturing and storage processes of glass, and their presence significantly impacted droplet behaviour, primarily by causing droplet pinning. As the droplet traversed over surface impurities, it would become pinned, leading to either a reduction or complete cessation of its motion, or, in some cases, serving as unintended nucleation sites for crystal growth. Such uncontrolled pinning events compromised the reproducibility of both droplet movement and crystal formation, introducing significant variability into the experimental outcomes. Additionally, the presence of contaminants could induce premature nucleation, further complicating the ability to regulate crystallisation dynamics.

The initial substrate cleaning procedure consisted of multiple sequential steps, including acetone washes, water rinses, and base baths, followed by Marangoni drying. Marangoni drying involves positioning a volatile solvent, such as isopropyl

alcohol (IPA), near the substrate as it is being withdrawn from water. The IPA vapor reduces the surface tension of the water on the substrate, causing the water to migrate toward areas of higher surface tension, thus moving away from the substrate without leaving residues¹⁶⁴. While effective in theory, this method is highly technique-sensitive and prone to inconsistencies, leading to potential human error.

To address these challenges, an ozone cleaning procedure was subsequently implemented to enhance the reproducibility of substrate preparation. The optimized cleaning protocol involved an initial acetone wash, followed by a water wash with Teepol detergent, and concluded with ozone cleaning. The ozone treatment effectively removed organic and particulate contaminants without altering the intrinsic roughness of the glass surface. Additionally, the ozone cleaning treatment rendered the glass substrate more hydrophilic, resulting in a noticeable reduction in the contact angle of the deposited droplets. This approach proved to be significantly more reliable than the initial method, as it provided a more consistent reduction in surface debris, thereby minimizing the frequency of droplet pinning events and improving control over droplet motion and crystallisation processes. This refinement in cleaning methodology substantially mitigated the impact of surface contaminants, establishing a stable and controlled environment for subsequent droplet motion and crystal growth studies.

A commonly used technique for developing crystals is utilising a pre-existing crystal or defect to act as a nucleation point for the growth of new crystals. Multiple types of seeding attempts were used to employ this crystallisation method. Initially, the seed method used was a score across the substrate; to utilise this, a droplet was moved over the line. The hypothesis was that as the droplet was moved over the score, a crystal would nucleate in there, and then as a droplet was moved over, the crystal would grow, creating one long crystal formed in the score of the substrate. As seen in Figure 67, the issue arose because the line acted as many nucleation points as possible rather than one, meaning that not just one long crystal formed. Instead, many crystals formed, which were too many to count accurately due to the small cluster formations. As the droplet moved over the score, the flows caused the smaller crystals to migrate from the trough into the droplet. This means many formed at once rather than one long crystal, causing cluster formation. An alternative method was using single dots from a glass cutter and drilled sections using a rotary tool and a diamond drill bit. Similar issues were apparent where the seeding sections caused too many

smaller crystals to be produced, and this caused the formation of many clusters. The third alternative seeding technique was with the use of seed crystals. The crystals were made using both our deposition technique and the traditional method. This also produced clusters; the clusters originated from the seed crystals. Many seed sections grew new crystals at different orientations to the primary seed. This formed one large cluster with many crystals forming at different rates; this also meant there was a section the droplet pinned on, reducing mobility. Due to the high level of cluster formation, other seeding methods were attempted.

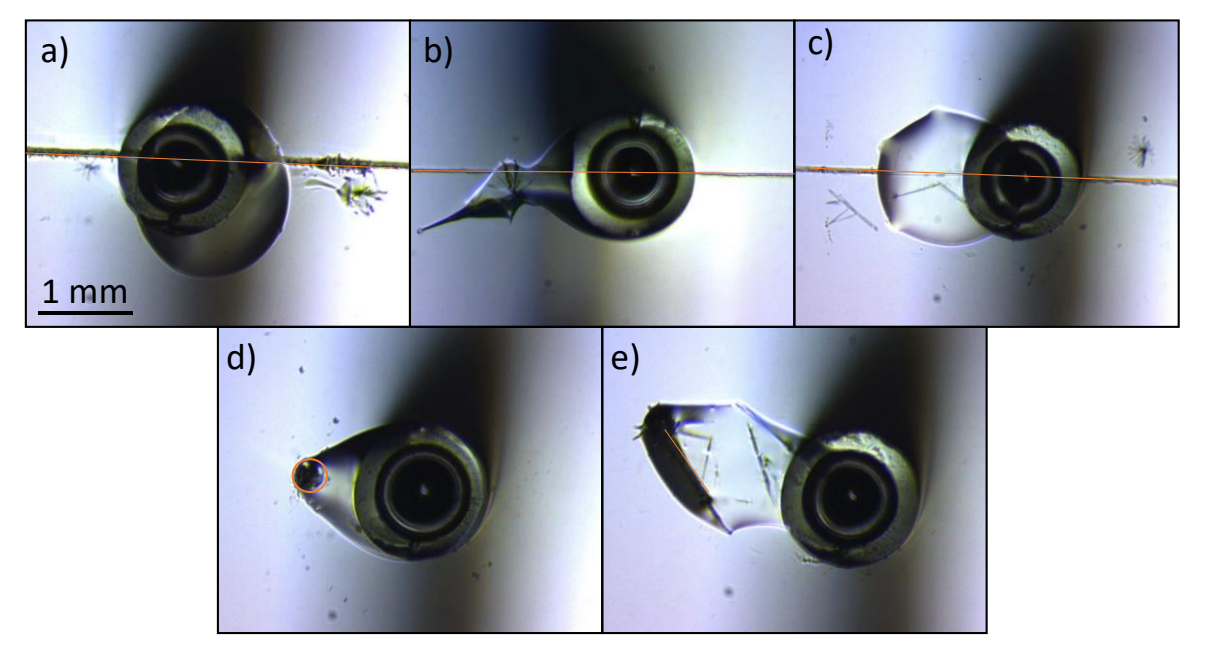


Figure 67: a,b,c) substrates have been scored with a glass cutter forming a line. d) substrate scored with glass cutter forming a dot. e) seed crystals added.

3.7.6 Vapour-Guided Deposition of Compounds 10 and 11

As mentioned before, the reasoning for synthesising additional PEG NDIs was to compare against the crystals formed by compound **9**. After each compound (**10** and **11**) were synthesised and purified with characterisation confirming the structure, they were deposited using the non-contact vapour-guided deposition technique.

Compound **10** did not maintain the same solubility as compound **9** and was considerably less soluble in water. To maintain consistency initially 6 mg of compound **10** was weighed and dissolved in 1 mL of water; similarly, sonication and heat were used to add dissolution. Unfortunately, not all solids dissolved, so this was repeated with 4 mg mL⁻¹ to allow for complete dissolution. The samples were filtered to remove debris, and then DMF was added to make the same concentration of binary droplets.

The deposition was attempted using the same technique as before. The issue with the deposition was the lower concentration of OSC. Due to compound 10 not being as soluble as compound 9, the supersaturation point appeared much later in the droplet lifetime. There were no single crystals isolated in the earlier stages of the droplet's movement. The only crystals produced appeared at the end of the droplet's lifetime. The crystals formed rapidly in a final crystallisation event, creating clusters of crystals, as seen in Figure 68. The droplet would pin, making the nucleation location for crystals; this formed most of the crystals around the edge of the droplet. This result persisted due to the low concentration of 10 in solution.

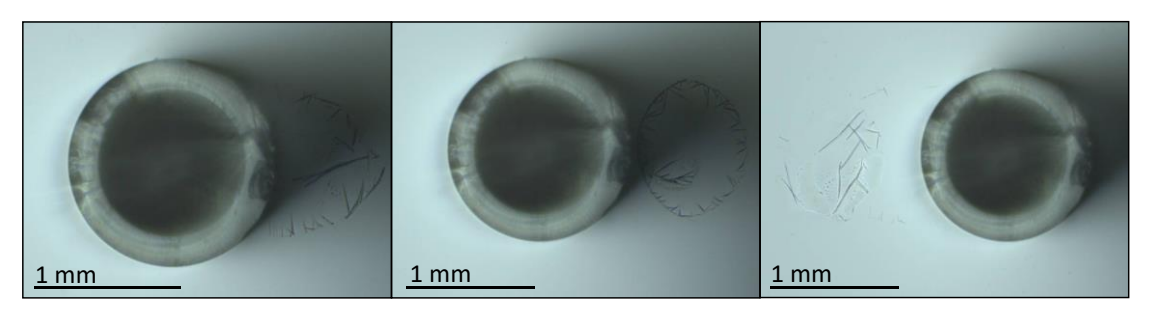


Figure 68: Images of crystals deposited using compound 10 via vapour-guided deposition.

Compound 11 was predicted to be more soluble with the additional length of the glycol chain. The purification process was similar, initially showing increased solubility. Similarly, the samples were made using 6 mgmL-1 as a guide, achieved after sonication and some heating. Once the samples were filtered and DMF was added, there was no tendency to crystalise in solution over an extended period, confirming the increased solubility. The issues arose when the samples were applied to the deposition technique; once the water evaporated, there was still a visible solution. This suggests that the remaining DMF doesn't fully evaporate when the water evaporates, leaving a solution that didn't evaporate after 30 minutes. After 30 minutes, there were no observable solids and no isolated crystals, as shown in Figure 69. These are examples of the thick solution that would always remain after the water evaporated.



Figure 69: Images of the final deposited substance observed when compound **11** was deposited using vapour-guided deposition.

3.7.7 Flexible Crystals

To obtain crystals that exhibit plastic properties, we need compounds that display isotropic interlocking packing compared to traditional anisotropy displayed in plastic deformation. This can allow a structure to be more adaptable to a change in crystal structure under the right conditions. Adding highly polarisable bonds can allow the strained regions to return to their neutral state 165-167. This can also depend on the strength of the interactions with different groups, such as nitro- or iodol-groups, which have formed elastic crystals and produced plastically deforming crystals when substituted for chlorine or bromine (produced plastically deforming crystals¹⁶⁸. It was found that manipulating the bonding groups could change the interactions to make crystals with elastically favourable π -hole orientation. This allowed for orthogonal interactions similar to the halogen-based σ -hole interactions ¹⁶⁹. We hypothesise that these interactions are most likely occurring in these crystals due to the spaced-out ketones in the ethylene glycol structure. Studies have also shown that the presence of π - π interactions can also play a role in the flexibility of crystals¹⁷⁰. Qin and Mei demonstrated elastically flexible crystals inspired by helical proteins where they formed 1D helical hydrogen bonding chains. The neighbouring helices had weaker interlocking interactions between the alkyl chains. These allowed elastic behaviour by absorbing the stress and not becoming permanently deformed in the process¹⁷¹. Krishna et al. developed a range of flexible crystals, including NDI core samples, by carefully selecting supramolecular weak interactions. They introduced active slip planes into the molecular structures using noninterfering van der Waals, π-stacking and hydrogen bonding groups. The van der Waals groups acted like lubricated planes, facilitating flexibility and reducing extended hydrogen bonding¹⁷⁰. These discoveries show that the main factor that affects the crystal flexibility is the presence of a stable core surrounded by weakly bonding end groups that allow the crystal planes to slip and account for varying stresses.

Over multiple successful experiments, many examples of deposited crystals exhibited flexible features once deposited. These features were not always observable during crystal growth, but as crystal growth became more successful, more examples of flexibility were observed. The observed fixability in these crystals may have occurred for various reasons because they all formed at slightly different deposition stages. In Figure 70, we see minor flex in the crystals; this will arise due to the flows produced in

the droplet. As the droplet continues to follow the vapour source, the crystals are slowly getting more significant as the concentration of the semiconductor increases. We then reach a critical length where the crystals will adhere to the substrate. When this phenomenon occurs, the section of the crystal remaining in the droplet will experience the flow without being able to rotate. This means we see elastic features where the exposed section will not move, and the bottom sections will move elastically with the flows produced in the droplet. These crystals exhibit inherent flexibility, but they appear to be limited by the levels of solvation, and the extreme levels of elasticity are only present when they are growing in solution and require the solvent to allow for this to act as a type of plasticiser.

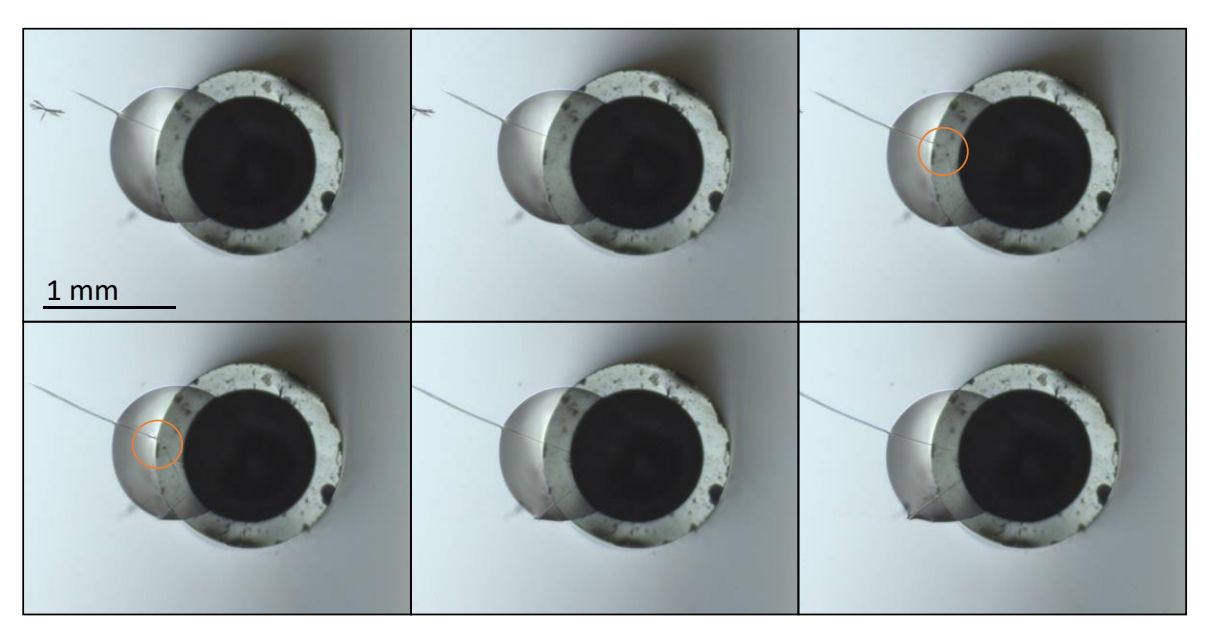


Figure 70: Crystal flexibility observed during deposition of compound 9 at 0.08mm/s.

3.8 Conclusion & Outlook

Initially this chapter looked at the synthesis of water soluble PDIs that where ultimately not pure which lead to a shift in focus which looked at the synthesis of series of glycolterminated NDIs with varying chain lengths. This chapter successfully demonstrated the capability of this technique to produce single crystals comparable with crystals produced using standard evaporation. Characterisation of these compounds using NMR, mass spectrometry, and single-crystal X-ray diffraction confirmed the structures and highlighted the distinct crystallisation behaviours influenced by glycol chain length.

Furthermore, the vapour-guided deposition method enabled control over droplet dynamics, solubility, and crystallisation, facilitating the isolation of single crystals by optimising parameters such as droplet velocity and solvent composition, the technique demonstrated promise for producing high-quality crystals suitable for charge transport studies. This work not only validates the potential of vapour-guided deposition as a viable approach for growing organic single crystals but also lays the groundwork for refining this method to accommodate a broader range of organic semiconductors.

In conclusion, the chapter highlights the importance of addressing the inherent challenges in crystallisation control through innovative deposition strategies. The successful implementation of vapour-guided deposition and the insights gained from the crystallisation behaviour of glycol-terminated NDIs pave the way for further exploration of single-crystal growth techniques. This advancement is a critical step toward realising high-mobility organic semiconductors with improved charge transport characteristics, ultimately contributing to the broader application and understanding of organic electronic materials.

To advance this technique multiple OSC need to be trailed to see if the results are reproducible with a broad range of semiconductor. Furthermore additional solvent system can be explored to verify their effectiveness whist also allowing the possibly of depositing less polar based OSCs. Additionally, the these OSCs may by studied further to understand the underpinning properties that allow for the flexibility observed during crystal growth.

4. Synthesis and Characterisation of Fluorinated Naphthalenediimide

4.1 Introduction

The incorporation of fluorine atoms into organic semiconductor molecules has been a strategic approach to modulate their electronic properties and enhance their performance in electronic devices. Fluorine's high electronegativity and the resultant strong C-F bonds contribute to increased molecular stability¹⁷² and unique solubility¹⁷³. These attributes make perfluorinated compounds particularly interesting for applications in organic field-effect transistors¹⁷⁴⁻¹⁷⁷, organic photovoltaics¹⁷⁸⁻¹⁸⁰, and organic light-emitting diodes^{181, 182}.

Fluorine is the most electronegative element, meaning it has a strong tendency to attract electrons. When fluorine atoms are substituted into the molecular structure of an organic semiconductor, they pull electron density towards themselves. This electron-withdrawing effect stabilises the energy levels, lowering both the ionisation potential and the electron affinity¹⁸³⁻¹⁸⁸. Enhanced electron affinity and stabilisation of the ionisation potential level lead to better injection and transport of electrons. In organic field-effect transistors (OFETs), this can result in higher electron mobilities, which directly translates to better device performance and efficiency. Fluorine's incorporation into organic semiconductors significantly enhances their stability and can influence their crystal structures. Fluorine atoms also contribute to enhanced thermal stability due to their strong C-F bonds¹⁸⁹ at 544 kJ mol⁻¹ (C-H bond enthalpy of ethane 369 kJ mol⁻¹), which are among the strongest in organic chemistry and dramatically increase the thermal stability of the material^{190, 191}.

Due to the uniquely high electronegativity of fluorine, organofluorine derivatives also have unique molecular packing characteristics. Due to these properties' fluorine substitution can significantly alter the crystal packing of organic semiconductors. For instance, the introduction of fluorine atoms into the molecular structure can change the packing motif from π -stacking to herringbone¹⁹². Although herringbone packing is typically considered less favourable for charge transport, fluorinated compounds can still exhibit high electron mobility due to the overall improved molecular alignment and stability. This alteration in packing is primarily due to changes in the electrostatic

potential of the molecule, which modifies the relative orientation of the molecules within the crystal lattice¹⁹³.

This work aims to investigate the influence of fluorinated side chains on the properties of NDI by synthesising two distinct perfluorinated NDI derivatives (Figure 71): one with a linear side chain and another with a branched configuration. The linear fluorinated NDI will be systematically compared to glycol- and alkyl-substituted NDIs to evaluate how the introduction of fluorine affects key properties such as solubility, electronic structure, and ambient stability. These results will be extended to the branched fluorinated NDI to explore how branching influences these same properties, particularly in terms of solubility and molecular packing. This study not only aims to address solubility challenges but also to provide insights into how fluorine incorporation affects crystal packing and the stability of deposited films. Additionally, the unique solubility properties may also be exploited to investigate the solid-state packing through the novel droplet printing. Herein, the synthetic development of novel

Figure 71: Target NDIs to study the effects of fluorinated side chains.

perfluorinated NDIs is reported, along with preliminary characterisation to understand the influence of fluorination on both molecular properties and deposition outcomes.

4.2 Synthesis of Linear Fluorinated Naphthalenediimide

When deciding on a semiconducting core naphthalenediimide was chosen due to my previous synthetic experience whilst also allowing for a comparison with the NDI (Compound 9) seen in Chapter 3. Additionally, there was previous knowledge of the electronic and deposition properties of NDI. This allows for a comparison with newly synthesised samples. Linear alkylated NDIs of varying chain lengths have been successfully synthesised and reviewed generously¹⁹⁴⁻¹⁹⁶. Using the alkylated and the previously synthesised compound 9 there is a framework for modular design for the synthesis of fluorinated NDI (synthetic route can chemical structure shown in Figure 72), followed by molecular comparisons. Using this knowledge a precursor for a linear fluorinated chain was investigated.

Figure 72: Synthetic route to functionalise compound 15.

A readily available inexpensive precursor was found, 3,3,4,4,5,5,6,6,7,7,8,8,8-Tridecafluoro-1-octanol had the desired fluorinated chain terminated with a functional alcohol group. The alcohol group allows for commonly used substitution reactions. Primary alcohols can react to form alkyl halides when under acid conditions via an S_N2 reaction. This reaction commonly uses sulphuric acid and a halide salt in water. Fluorinated compounds are not miscible in water which would dramatically affect the yields. To improve miscibility alternative methods were explored. Jeff Xin Wu et al. synthesised a range of brominated compounds using ionic solvents¹⁹⁷. Using these conditions the alcohol group protonates, causing nucleophilic displacement by the halide anions where the proton is associated with either the halide or the conjugate bases of the Brønsted acid. The authors associated the accelerated reaction with the ability of the ionic solvent to aid in charge separation. In the published work, n-octanol was the closest molecular structure to precursor 3,3,4,4,5,5,6,6,7,7,8,8,8-Tridecafluoro-1-octanol (12) hence those conditions were selected.

To synthesise 8-bromo-1,1,1,2,2,3,3,4,4,5,5,6,6-tridecafluorooctane (13) compound 12 was heated for five hours using concentrated sulphuric acid and the 1-Butyl-3-methylimidazolium bromide under ambient conditions. Unfortunately, 12 was not fully miscible in the chosen ionic liquid, which most likely negatively impacted the yield. To purify compound 13, the liquid mixture was distilled under vacuum at 1 mbar. The target compound evaporated at 68-70 °C with a yield of 32% compared to the literature yield of 95% for 1-Bromooctane¹⁹⁷. The lower yield was attributed mainly to the low miscibility of the precursor in the ionic liquid, but this was not further investigated because sufficient product was recovered, and no further optimisation was attempted.

After successful synthesis of compound **13**, the amination through Gabriel synthesis was attempted (Figure 73)¹⁹⁸. This method useed potassium phthalimide as the amino synthon to prepare primary amines from alkylated halides. After which, the

Figure 73: Synthetic route to compound 14.

3,3,4,4,5,5,6,6,7,7,8,8,8-tridecafluorooctan-1-amine (**14**) was hydrolysed by reacting with a base, leaving a stable cyclic product (sodium phthalate) and a primary amine (**14**). Traditionally, Gabriel synthesis uses polar aprotic solvents which allow the salt to dissolve whilst not interacting significantly with the anion reducing the negative effects on reactivities. In these solvents however the fluorinated reactant would not be miscible. A alternative Gabriel synthesis was found in the literature, which again used an ionic solvent. Qin-Guo Zheng et al. utilised a range of ionic solvents to achieve high yields with different alkyl halides¹⁹⁹. The fluorinated molecule should be more miscible using an ionic solvent due to the highly polarisable carbon-fluorine bond. The authors used two equivalences of 1-bromobutane, potassium hydroxide and one equivalence of phthalimide¹⁹⁹. This was reacted over five hours in 1-Butyl-3-methylimidazolium tetrafluoroborate at 80 °C. This synthesised *N*-butyl phthalimide yielded 94% where the amine would need to be hydrolysed.

These steps were replicated with a phthalimide potassium salt. Compound 13 was reacted for 5 hours with phthalimide potassium salt in 1-Butyl-3-methylimidazolium tetrafluoroborate. Potassium hydroxide was added overnight to hydrolyse the amine. After extraction with chloroform, the product (14) remained as a slightly yellow oil with a yield of 23%. The poor yield was attributed once again to miscibility issues as the fluorinated precursor would not fully mix with the ionic solvent and would separate over time. To reduce this issue the mixture was stirred more vigorously to improve interactions. Despite this low-yielding reaction, sufficient product was recovered to continue to the subsequent step. Further optimisation was not attempted.

To synthesise compound **15**, the NDA was reacted with the **14** at 120 °C in DMF for two days as seen in Figure 74. Compound **7** had poor miscibility in DMF as expected, the reaction time was increased to two days in an attempt to improve the reaction yield.

Initially the column chromatography was 50/50 hexane chloroform based on the polarity of the imide bond, but no pure product was separated. This led to an increase in polarity of the mobile phase (20% acetone, 50% chloroform and 30% hexane) but similar results were observed. It was later understood that the dipoles of the fluorine bonds cancel each other out making the chains behave more like alkyl chains rather than polar ones. Alternatively, the remaining crude product was precipitated from methanol. This produced compound **15** with a yield of 11%.

Figure 74: Synthetic route to compound 15.

NMR was used to confirm the structure of compound **15**. A singlet peak at 8.77 ppm corresponding to the H_a proton in Figure 75. An additional singlet was observed at 8.76 ppm this peak was most likely due to the opening of the imide bond in the presence of trifluoro acetic acid (TFA) which was used to make compound **15** more

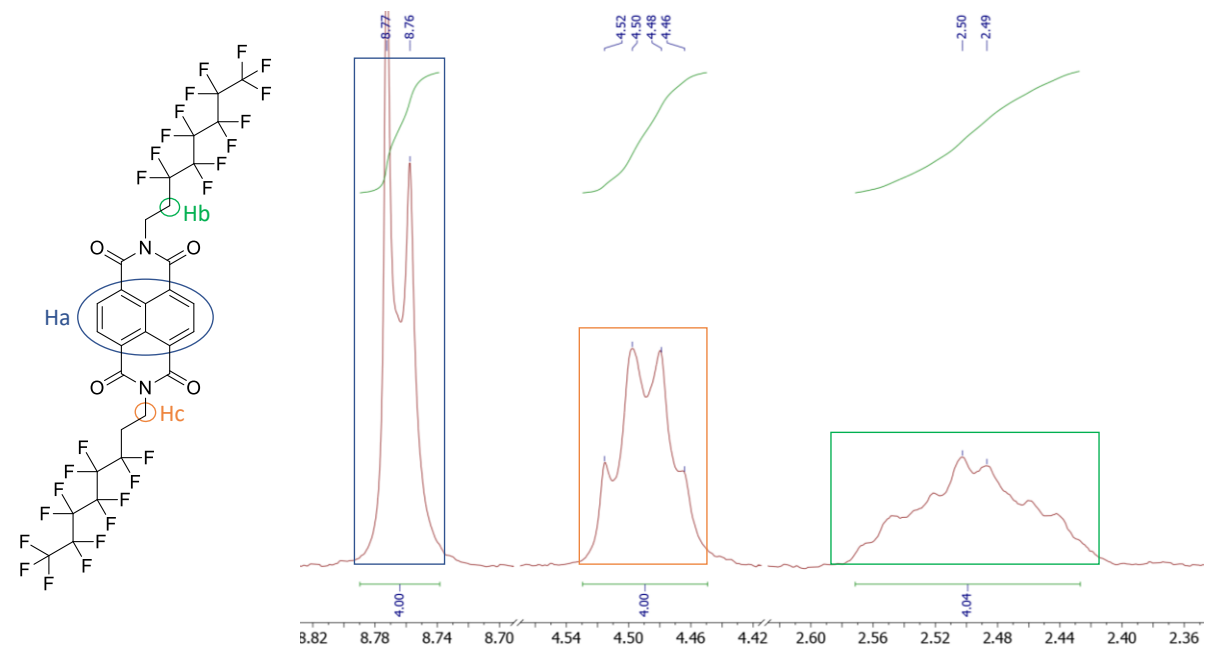


Figure 75: ¹H NMR spectra of compound **15** with deuterated chloroform.

soluble in chloroform. The presence of TFA was also likely to be the reason for alpha carbon H_c protons at 4.50 ppm to be split into a quartet rather hen the expected triplet.

The H_b protons produced a multiplet because of the fluorines on the adjacent carbons. This splitting pattern occurred because the inductive effects effected the protons splitting pattern even with fluorine substituents as far as three carbons away. The inductive effects of fluorine substituents add-up as the number of adjacent fluorine's increases. Where the increase in the number of fluorines that effected the protons environment increased the number of splits. Fluorine's high electronegativity, cause the protons to become more deshielded. The deshielding was more pronounced when the number of fluorine's increased. This will push the peaks further down field. Additionally, the ¹⁹F NMR showed the presence of the fluorine due to the six fluorine environments corresponding to the six different carbon environments.

4.3 Synthesis of Branched Fluorinated Naphthalenediimide

Once decided on the synthesis of compound 20 the first step was to review the best way to synthesise a branched fluorinated amine. To stay consistent with compound 15 the fluorinated chain length would remain the same. This was the basis for the synthesis of the branched perfluorinated amine. Ellen Sletten et al. utilised fluorinated chains to synthesise biocompatible branched fluorous tags more soluble in perfluorocarbon solvents²⁰⁰. 1,1,1,2,2,3,3,4,4,5,5,6,6-tridecafluoro-8-iodooctane was added to ethyl cyanoacetate to provide an ester and a nitrile, transforming them into various practical handles. The initial step, as shown in Figure 76, used ethyl cyanoacetate and 1,1,1,2,2,3,3,4,4,5,5,6,6-tridecafluoro-8-iodooctane with a base to allow for the deprotonation of the alpha carbon. The deprotonated carbon attacked the carbon adjacent to the nitrile in an S_N2 reaction allowing for the initial substitution. The second substitution occured at the now tertiary carbon were the deprotonated carbon again attached the remaining proton forming compound 17. The mixture was evaporated to dryness to remove the DMF and purified via column chromatography using 90% hexane and 10% diethyl ether, producing white needle-like crystals with a 95% yield. Compound 17, The structure and purity were confirmed by NMR.

Figure 76: Proposed synthetic route for the synthesise of compound 20.

The next step was the elimination of the ester via Krapcho decarboxylation. This can was achieved using lithium chloride in the presence of water at 160 °C. The first issue arose when the branched fluorine chain was not soluble even at elevated temperatures. This caused the initial yield to be lower than 20%. To improve the yield, the reaction time was extended to two days. After heating, the reaction mixture was left to cool and compound 18 precipitated out of the solution. The solid was filtered off and washed with water, before being further purified by column chromatography using 90% hexane and 10% ethyl acetate, affording white needle-like crystals with a yield of 95%, confirmed by NMR.

The next step was a nitrile reduction using a potent reducing agent, such as lithium aluminium hydride, to yield the desired amine. After work-up, the recovered oil was

purified by column chromatography using 1% triethyl amine to neutralise the silica and 1-5% methanol in dichloromethane to extract the final product as a yellow oil with a 54% yield confirmed by NMR.

Once the amine had been synthesised, it was condensed with NDA to obtain compound **20** seen in Figure 77. The reaction was heated for 72 hours due to the amine being poorly miscible in DMF, slowing down reaction kinetics. Once the reaction was cooled to room temperature, the DMF was evaporated under vacuum. The resulting solid was then purified via column chromatography; the initial solvent system was DCM, which was changed to 95% DCM and 5% ethyl acetate, after which 90% DCM and 10% ethyl acetate were used to obtain compound **20** (0.63 g, 48%).

Figure 77: Reaction scheme for the synthesis of compound 20.

The ¹H NMR spectrum was obtained in deuterated chloroform. The alpha carbon adjacent to the imide (H_b) was the first peak to be identified. H_b was located in previous samples (**9**, **10**, **11** and **15**) between 4 - 5 ppm. Figure 78 shows this peak at 4.20 ppm as a doublet, the symmetry was confirmed as the peak integrates to four protons. The protons on the aromatic core appear at 8.79 ppm as a singlet and integrate to four protons, further confirming the molecule's symmetry. Due to the overlapping peaks

protons c, d and e were further assigned with COSY (Figure 79), HSQC (appendix) and HMBC (appendix) 2D NMR, respectively.

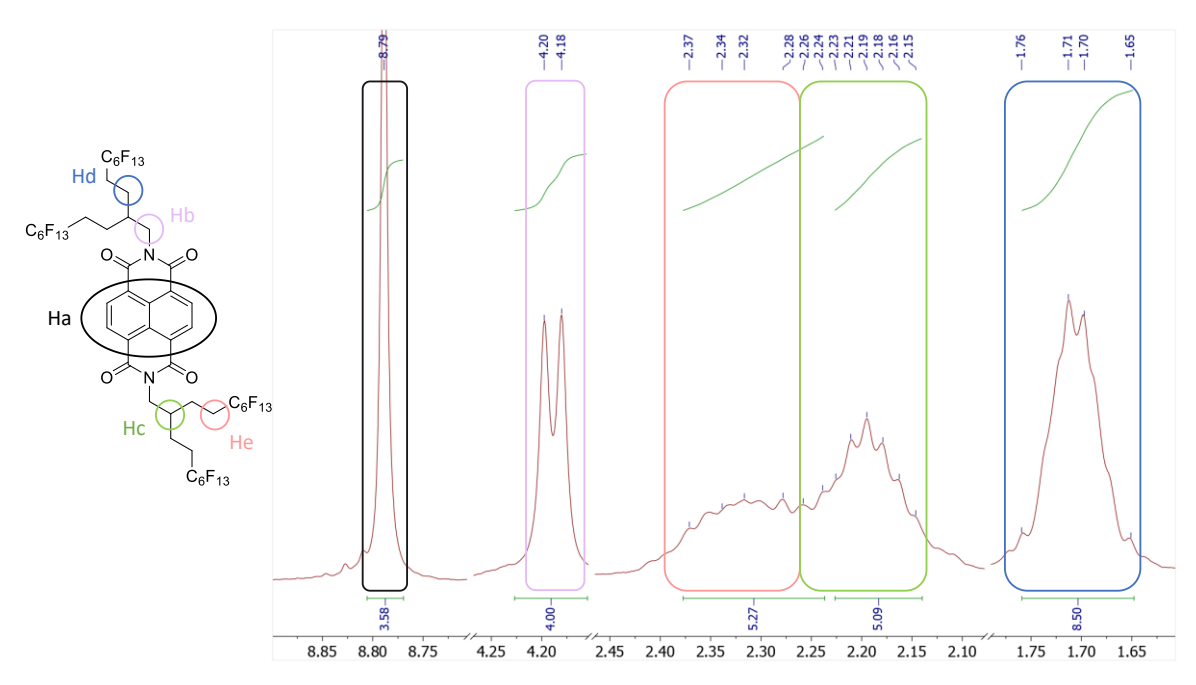


Figure 78: ¹H NMR spectra of compound **20** in deuterated chloroform.

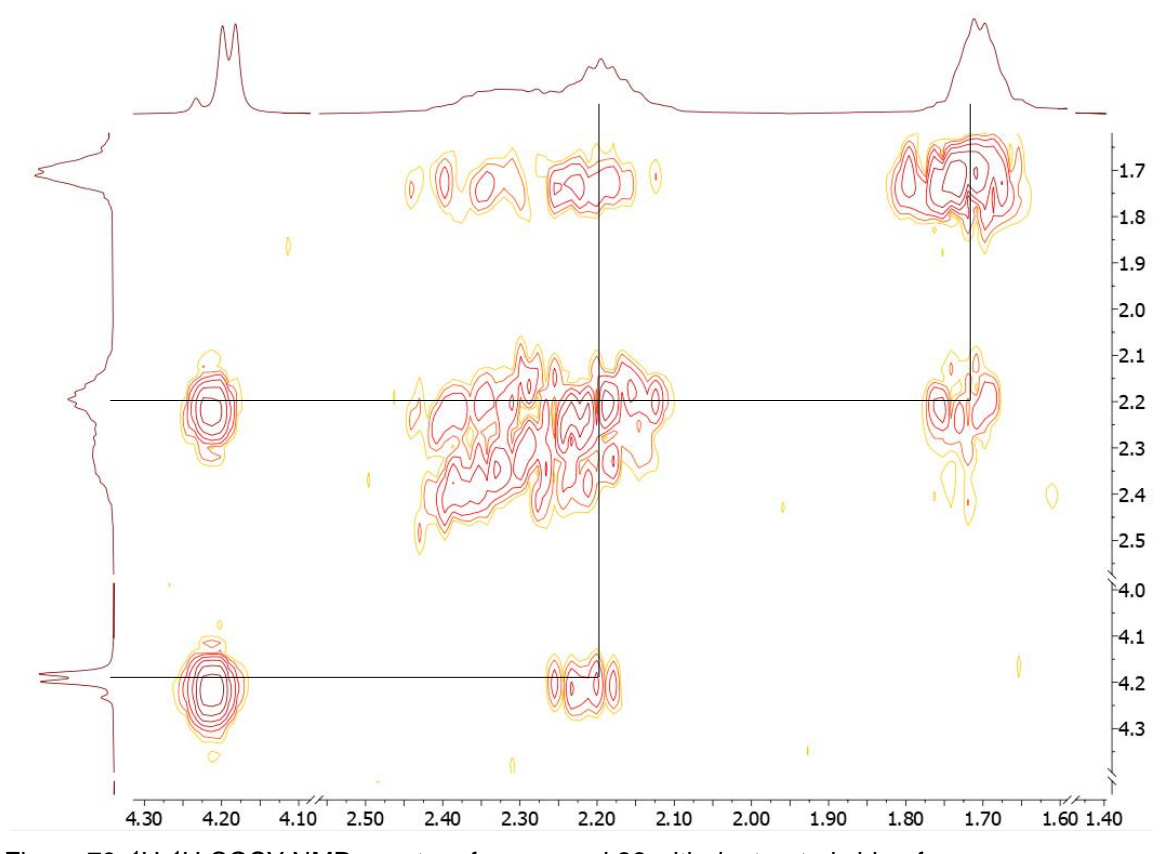


Figure 79: ¹H: ¹H COSY NMR spectra of compound **20** with deuterated chloroform.

First, a COSY NMR spectrum (Figure 79) was obtained to analyse proton-proton coupling. Using the H_b proton as a reference, there was only one neighbouring carbon and thus one proton environment which was the peak at 2.20 ppm making these protons H_c . The peak at 1.70 ppm was assigned to H_d as the COSY showed it neighbouring H_c and H_e . In addition the integration was around eight protons as expected for this peak. H_e is observed at 2.34 ppm, with the COSY confirming that this proton was neighbouring H_c . The proton peaks for H_e and H_c overlapped each other, yet, the total integration of both these peaks added up to ten protons, corresponding to the number of protons expected for H_e and H_c .

In conclusion, the selection of NDI as the semiconducting core was driven by both prior synthetic experience and the opportunity for comparison with previously synthesised NDI derivatives. The synthesis of fluorinated NDIs, following established methodologies, provided insight into the challenges associated with fluorinated chain solubility and yield optimisation. Despite miscibility challenges in ionic solvents, sufficient quantities of the desired intermediates were produced to continue the study. Structural confirmation using NMR and related techniques further validated the identity of the synthesised compounds. Moving forward, further investigation into the electronic properties and performance of these fluorinated compounds will enable a deeper understanding of their potential in organic semiconductor applications.

4.3.1 Optoelectronic properties of Compound 7 and 12

In this section, we will explore the optoelectrical and thermal properties of compounds 15 them with compound and 20. comparing and 2-decvl-7nonylbenzo[lmn][3,8]phenanthroline-1,3,6,8(2H,7H)-tetraone (C8NDI) seen in Figure 80. Compounds 9, 15, and C8NDI exhibit structural similarities, facilitating a direct comparative analysis of the impact of varying end groups on their properties. Additionally, the inclusion of compound **20** provides a basis for evaluating differences between the two perfluorinated derivatives, thereby offering further insights into the influence of fluorination on molecular behaviour. By examining their UV-vis absorption spectra, and electrochemical behaviour, we aim to assess the impact of fluorinated chains on the electronic and structural properties of these NDI derivatives. This comparison will shed light on how fluorination and chain length influence key parameters such as ionisation potential, electron affinity, and aggregation behaviour

in NDI derivatives. The optoelectrical properties of compounds **15** and **20** are outlined in Table 4.1 with compound **9** and **C8NDI** as comparisons.

Figure 80: Structure of Compound 9, C8NDI, 15 and 20.

UV-vis spectroscopy was used to determine the optical absorption properties as well as the optical band gap of the different derivatives. NDIs have a characteristic absorbance band with two maxima due to the presence of π - π * transitions, which should be observed for all four compounds. The side chains are not electronically connected to the naphthalene core and therefore their influence on the bandgap should be minimal. All UV-vis data presented herein was recorded in solution. Any attempts to record data on spin coated and drop cast films were unsuccessful due to unsurmountable film inhomogeneities that made reliable data acquisition impossible. The solution UV-vis spectra of all three compounds are shown in Figure 81. Three distinct absorption peaks can be derived for all four compounds. The peaks at 379-382 nm, 362-359 nm and 345-341 nm appear due to the NDIs π - π * transitions and the vibrational fine structure 133. These values are in accordance with the literature of other similar NDIs^{133, 201, 202}. Compound **15** shows an addition peak at around 400 nm. This peak is most likely due to the presence of aggregates in solutions which may selfassemble into planar conformation²⁰³, this was observed by Insuasty et al where the varying length of alkylated NDIs show a bathochromic shift and a loss of fine features

with the addition of water as an anti-solvent¹⁴⁷. From the UV-vis absorption spectrum in Figure 64 the onset of absorptions (λ_{onset}) where estimated to be 395, 398, 398 and 397 nm for compound **15**, compound **9**, **C8NDI** and compound **20** respectively. From the λ_{onset} the optical band gap can be calculated using equation 12 from section 3.6.3 *Optoelectronic properties of compounds 9 and 11*. Using this calculation the optical band gaps were 3.15, 3.12, 3.12 and 3.13 eV for compound **15**, compound **9**, **C8NDI** and compound **20** respectively.

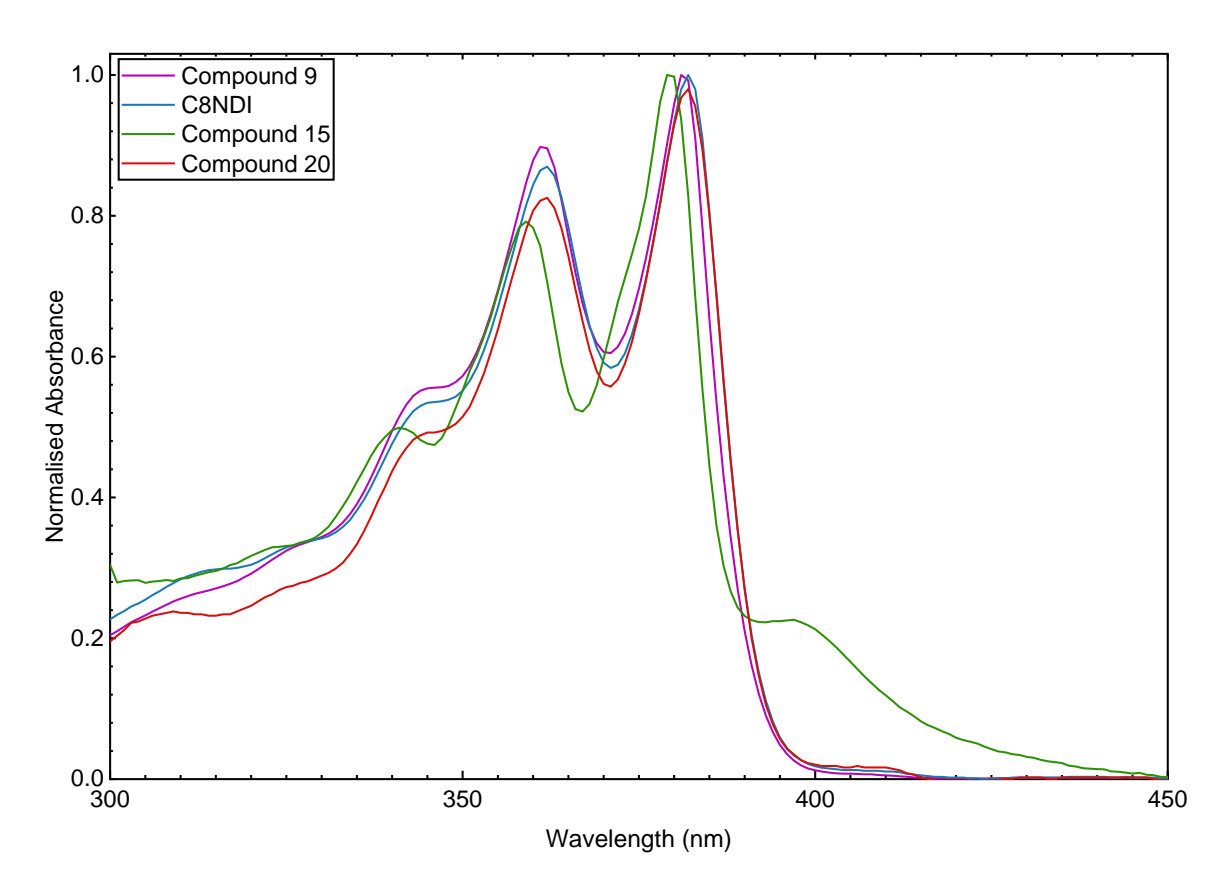


Figure 81: UV-vis. absorption spectrum of compound 15, compound 9 and C8NDI in chloroform.

The electron affinities were established electrochemically. Figure 82 shows the cyclic voltammograms of compound **15**, compound **9**, C8NDI and compound **20** all in dichloromethane referenced to the potential of an Ag/Ag⁺ electrode. Each compound was scanned five times, with each successive scan reducing in intensity most likely related to the compound slowly breaking down in solution. Compound **9**, **C8NDI** and **20** show a fully reversible reduction with an anodic peak potential taken from the first reduction, the peak maxima was $(E_{pa}) = -1.1 \text{ V}$, -1.2 V and -1.1 V respectively. These

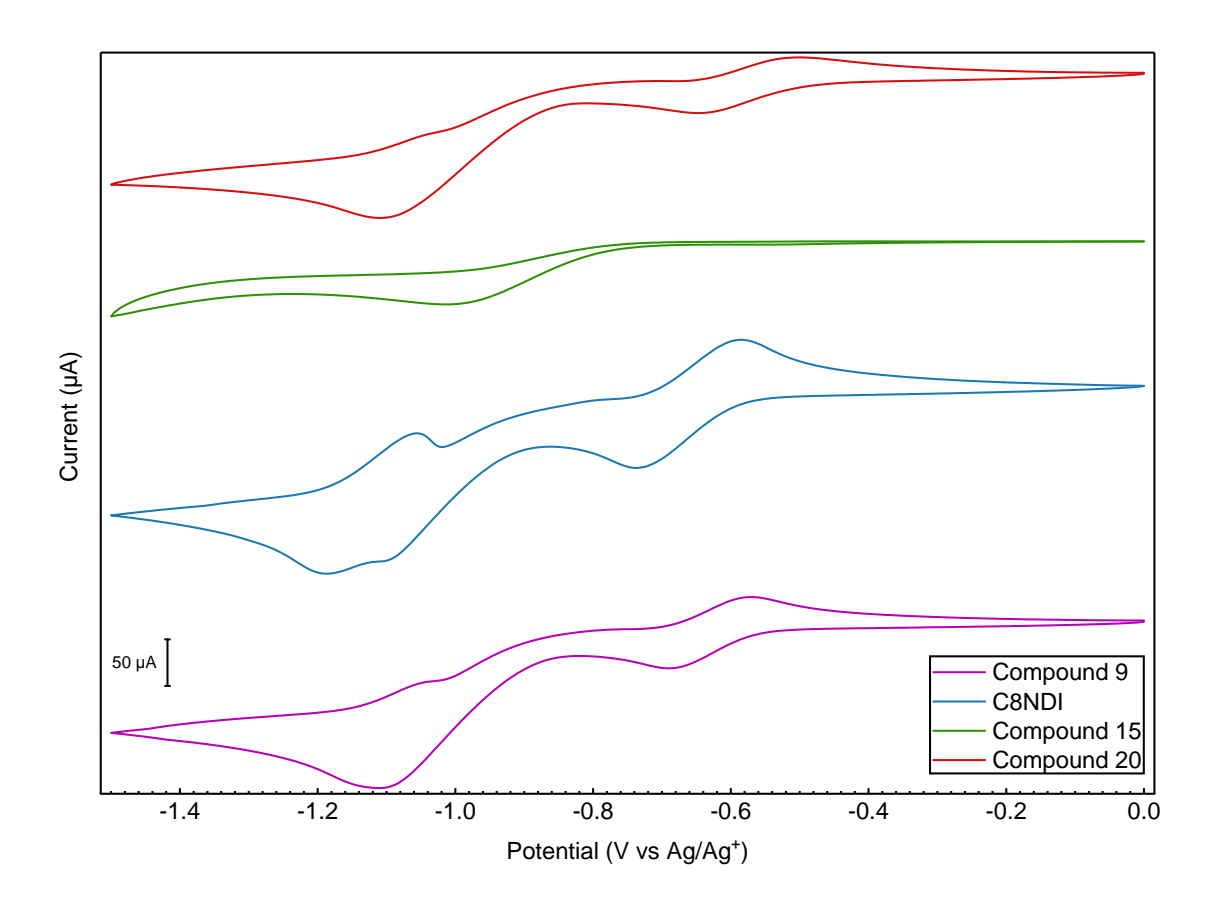


Figure 82: a) Cyclic voltammogram of compound **9**, compound **15**, compound **20** and **C8NDI** in a solution of dichloromethane solution with 0.1 M TBAPF₆ electrolyte between 0 and -1.5 V. Referenced to Ag/Ag⁺ electrode with a platinum wire counter electrode and glassy carbon working electrode.

compounds have a reduction proceeded with two consecutive one-electron processes, initially there is a radical-anion generation followed by the transition of this radical-anion into a dianion typically seen for NDIs^{152, 153}. Compound **15** differs from the others as it has a reduction peak which is irreversible at E_{pa} = -1.0 V. The redox potential for compound **15** appears to be must slower this may be a result aggregation which was seen during the UV-vis spectra. In the UV-vis there is a peak observed around 400 nm due to aggregation of compound **15**²⁰⁴. The tendency for compound **15** to aggregate may be causing either the compound to become absorbed into the electrode, this can then cause the electron transfer rate constant to be much slower leading to an irreversible reduction peak²⁰⁵, or the tight packing reduces the effects of the charges to penetrate aggregate clusters. The electron affinity values were estimated from the first onset of reduction (E_{onset}) at -4.03 eV, -3.92 eV, -3.92 eV and -3.97 eV for compound **15**, compound **9**, **C8NDI** and compound **20** respectively. These

values were estimated using equation 11 from section 3.6.3 Optoelectronic properties of compounds 9 and 11.

Furthermore, the ionisation potentials were calculated by taking the optical band gap away from the electron affinity generating -7.18 eV for compound **15**, -7.04 eV for compound **9**, -7.04 eV for the **C8NDI** and finally -7.10 eV for compound **20**. All of the results are summarised in Table 4.1 and the ionisation potential and electron affinity can be observed in Figure 83. The choice of side chain has a measurable impact on the electronic and optical properties of NDI derivatives. While the core electronic structure remains largely consistent, as indicated by the relatively small changes in

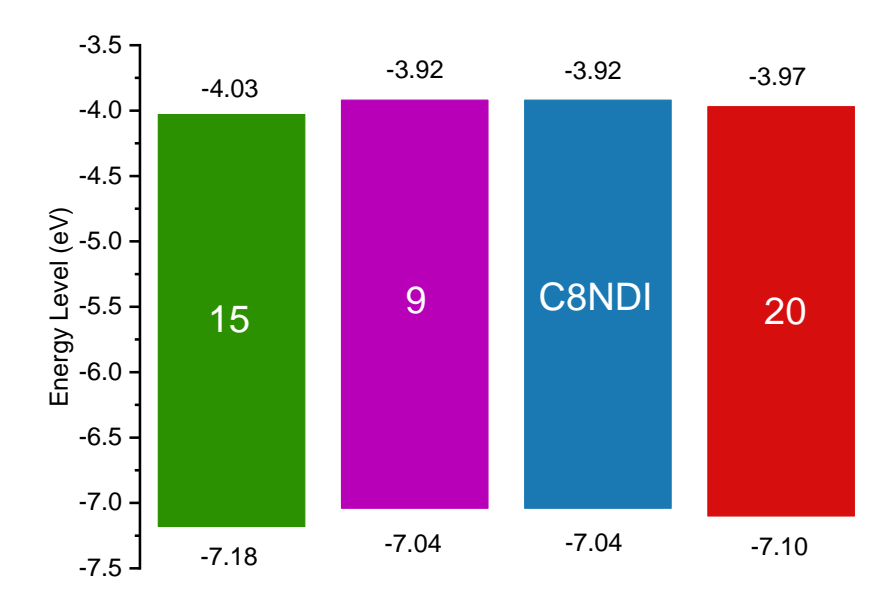


Figure 83: Ionisation potential and electron affinity of compounds **15**, **9**, C8NDI and **20** measured by UV-vis and CV.

Table 4.1. Electrochemical and optical properties of compound 9, C8NDI compound 15 and compound 20.

Compound	E _{pa} ^[a] (V)	E _{onset} ^[a] (V)	λ _{max} ^[b] (nm)	λ _{onset} ^[b] (nm)	Optical band gap ^[c] (eV)	Electron Affinty [d] (eV)	Ionisation potential ^[e] (eV)
9	-1.1	-0.88	381	398	3.12	-3.92	-7.04
C8NDI	-1.2	-0.88	382	398	3.12	-3.92	-7.04
15	-1.0	-0.77	380	395 ^[f]	3.15	-4.03	-7.18
20	-1.1	-0.83	382	397	3.13	-3.97	-7.10

[a] From solution cyclic voltammetry using glassy carbon working electrode, platinum wire counter electrode and Ag/Ag+ reference electrode. Values are reported from the 2nd cycle. [b] From solution UV-vis absorption spectroscopy in chloroform. [c] Estimated from λ_{onset} . [d] Estimated from the electrochemical onset of reduction (E_{onset}). [e] Estimated using equation Electron Affinity = Ionisation potential – Optical band gap. [f] calculated from the trendline of the λ_{onset} .

reduction potentials and band gaps, the introduction of fluorinated and branched side chains subtly tunes key properties such as electron affinity, ionisation potential, and reduction onset. These changes suggest that the fluorinated side chains, in particular, enhance the electron-accepting characteristics of the NDI core, most likely increasing its ambient stability. Overall, the structural modifications via side chain variation offer a valuable means of fine-tuning the properties of NDIs for targeted applications, especially where stability and electron transport are essential.

To evaluate the performance of the NDI derivatives, organic electrochemical transistors (OECTs) were fabricated and tested. Each compound (9, C8NDI, 15, and 20) was spin-coated onto indium tin oxide (ITO) glass slides fitted with polydimethylsiloxane (PDMS) wells. The wells were filled with a sodium chloride solution, with an Ag/AgCI electrode serving as the gate immersed in the solution, while the source and drain contacts were established on the ITO electrodes. However, the resulting data did not exhibit any discernible OECT characteristics, indicating poor device performance. This suboptimal behaviour is most likely attributed to the poor morphology of the NDI films, which appeared cracked and nonuniform upon inspection. Such morphological defects likely led to device shorting, rendering the results inconclusive.

4.3.2 Thermal Properties of Compound 15 and Compound 20

In this section, we explore the thermal properties of compounds **15** and **20**, focusing on their phase transitions and stability as influenced by their fluorinated side chains. Thermogravimetric analysis and DSC were employed to assess the impact of linear versus branched fluorinated chains on the NDI core. By comparing these results with compounds **9** and **C8NDI**, we aim to understand how fluorination affects intermolecular interactions, phase transitions, and overall material stability, providing insights into the structure-property relationships of these semiconducting materials.

The thermogravimetric analysis (TGA) comparing (Figure 84) compound **20** and compound **15** reveals key insights into their thermal stability and degradation behaviour, especially when compared to other compounds such as compound **9** and **C8NDI**. Compound **20** demonstrated higher thermal stability, as it began losing at around 233 °C, while compound **15** started degrading slightly earlier, with mass loss initiating at a lower temperature of 217 °C. When compared to compound **9**, which

degraded around 274 °C, both compound 15 and compound 20 showed similar but slightly different thermal behaviours, with compound 20 being more stable. In contrast, C8NDI, which began degrading at 350 °C, demonstrating the highest thermal stability among all compounds discussed. This trend is in line with data that show an increase in chain length tends to enhance thermal stability, as longer chains often exhibit stronger intermolecular forces and greater resistance to thermal degradation ¹⁵¹. As seen in C8NDI and compound 20, the increased chain length correlates with higher degradation temperatures, making these compounds more stable at high-temperatures compared to compound 9 and compound 15.

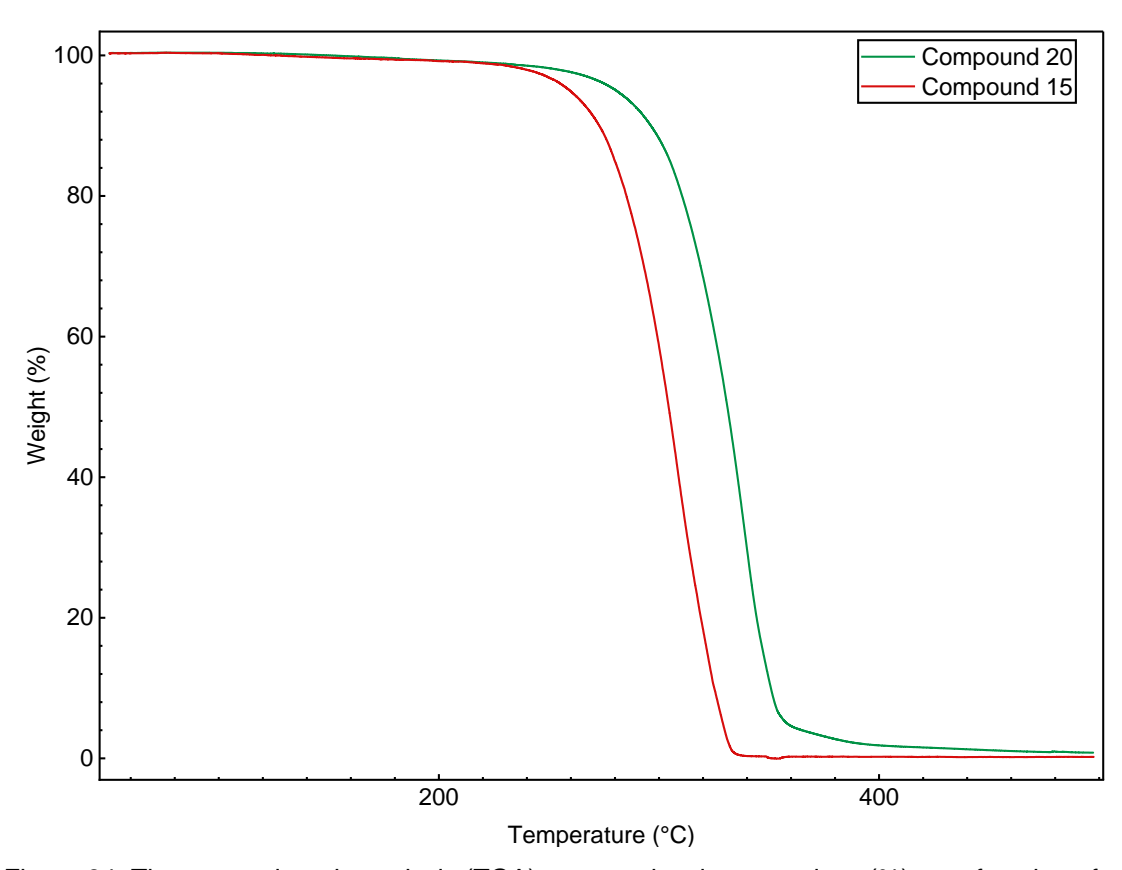


Figure 84: Thermogravimetric analysis (TGA) curves, showing mass loss (%) as a function of temperature for compounds **15** and **20**. TGA was carried out in N_2 at 10 °C min⁻¹ between 50-800 °C for compound **15** and between 50-500 °C for compound **20**. Negligible weight loss is seen past 500 °C for compound **15**.

DSC was employed to understand the effect fluorinated side chains can have on the phase properties of different NDI derivatives. NDIs have shown complex phase behaviours as shown by Milita et al. when analysed alkalising NDIs¹⁴⁶. The second heating and first cooling traces are displayed in Figure 85 for compound **15**. The heating cycle peak at 50.2 °C with an associated enthalpy change of 2.5 J g⁻¹ which

is likely a solid-solid transition due to the low enthalpy, followed by a broad melt at 226 °C with an associated enthalpy change of 45.9 J g⁻¹. Additionally, these traces occur at much higher temperatures when compared to the traces acquired for compound **9** between 59-68 °C with a change in enthalpy of 84.6 J g⁻¹and 48.9 J g⁻¹respectively and traces for **C8NDI** at 183°C a change in enthalpy of 61.2 J g⁻¹ ¹⁵¹. This could be possibly due to the increased interactions that occur between C-F bonds due to the larger dipoles which was observed when Fei et al. substituted hydrogen for fluorine²⁰⁶. Additionally, the repulsion between adjacent fluorine atoms could possibly reduce the associated enthalpy change forming less efficiently ordered crystals when compared to compound **9** and **C8NDI** where the associated enthalpies are higher.

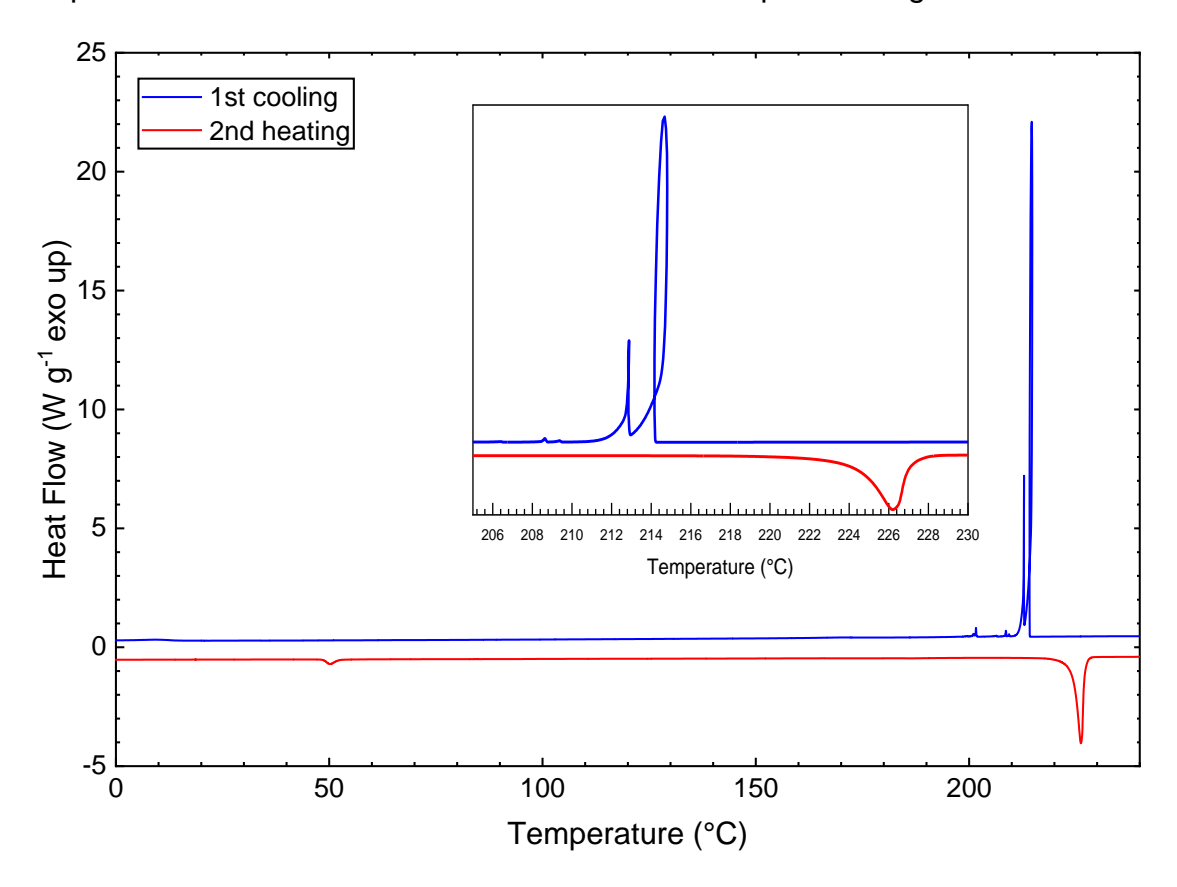


Figure 85: DSC traces measured on **15** powder, upon heating, subsequent cooling (red and blue traces respectively).

During the cooling cycle of compound **15**, the first crystallisation occurs at 214 °C with a change in enthalpy of 32.3 J g⁻¹. As shown in Figure 86 this occurs as a "loop", this can occur when a compound heats as crystallisation occurs causing the temperature to increase. These peaks can arise in compounds that can form supercooled liquids. Supercooled liquids do not solidify immediately after cooling below their melting temperature. The supercooled state is an unstable phase and the results

crystallisation is a rapid energic process resulting in the "self-heating" of the sample²⁰⁷. If the heat flow is plotted against time, then the peak will appear as normal seen in Figure 85. The "loop" can only occur when using TA instruments due to their patented Tzero™ technology. Alternative instruments assume the contributions from the sample and reference sensor total heat flow cancel each other out. The data is then acquired using a thermal equivalent of Ohm's Law relating heat flow to differential temperature:

$$q = \frac{\Delta T}{R} \tag{18}$$

Where q is sample heat flow, ΔT temperature difference between the reference and sample and R is the resistance of the thermoelectric disk. In reality, the resistance and capacitance of each sensor produce imbalances. To account for these imbalances TA instruments have employed their TzeroTM cell design which uses a four-term heat flow expression²⁰⁸:

$$q = -\frac{\Delta T}{R_r} + \Delta T_0 \left(\frac{1}{R_s} - \frac{1}{R_r} \right) + (C_r - C_s) \frac{dT_s}{dt} - C_r \frac{d\Delta T}{dt}$$
(19)

The first term is equivalent to the conventional term seen in equation 18. The following two terms account for the thermal resistance (resistance of sample (R_s), and reference (R_r)) and capacitance imbalances (capacitance of sample (C_s), and reference (C_r)) between the sample and the reference cell. The fourth term accounts for the heating rate differences between the sample and the reference. These loops occur when the compound has a highly energetic fusion. When a highly energic fusion occurs, it can cause the sample to self-heat rapidly. This is expressed by the DSC thermogram as a "loop" because with the four-term heat flow equation the difference between the sample and reference pan is recorded. Hence the instrument can identify the rapid increase in heat of the sample pan as the reference pan will remain the same. The second crystallisation is sharp at 212 °C with a change in enthalpy of 10.3 J g⁻¹ with the same "loop" features.

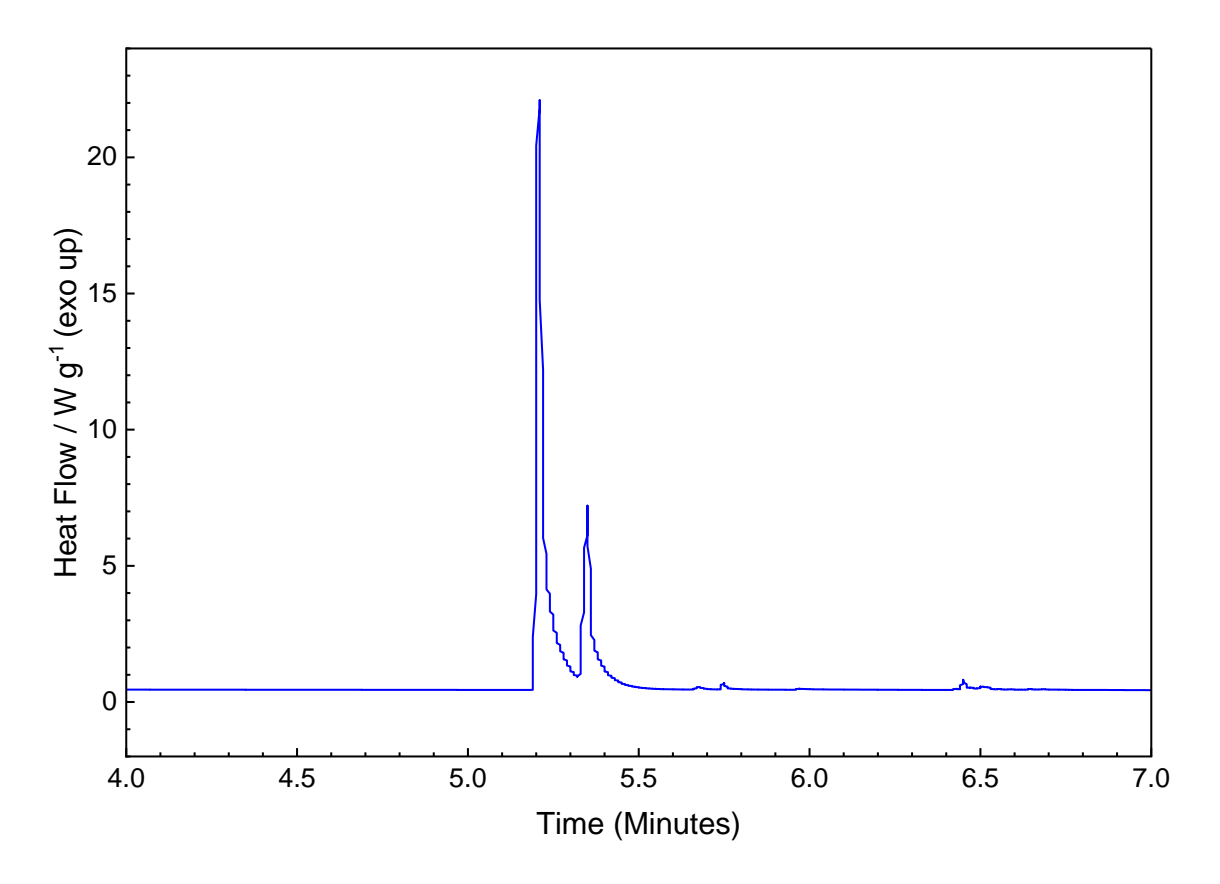


Figure 86: DSC traces measured on **15** powder, during the first cooling cycle. The heat flow to plotted against time where the colling trace of compound 15 no longer expresses the "loop" characteristics

Compound **20**s phase transitions occur at elevated temperatures compared to compound **9** and **C8NDI**. It is probable that this is due to the formation of C-F···F-C solid state interactions that occur between the fluorinated end groups²⁰⁹. Where the compound differs heavily from the other NDIs is the melting and crystallisation traces. Both compound **9** and linear alkylated NDI have sharp melts whereas compound **15** has a broad melt. Comparatively in literature similar melt (227 °C) and crystallisation (217 °C) results are observed with slightly longer fluorinated chains in NDI(C₂H₄C₈F₁₉)¹⁷². Additionally, compound **15** has two sharp crystallisations. These peaks are most likely related to crystallisation events one related to the ordering of the NDI core and the other relating to the ordering of the fluorinated side chains. In literature, a crystal structure has been reported for NDI(CH₂C₇F₁₅) expressing a herring bond motif with no other polymorphs²¹⁰. The enthalpies of compound **15** suggest that the two separate crystallisations are most likely related to the second melt as the first melt enthalpy is much lower than either of the crystallisation enthalpies.

This initial melt peak could be related to a reorganisation of the side chains sometimes expressed as a melting peak in DSC²¹¹.

Compound **20** has a peak at 50 °C with an associated enthalpy change of 1.5 J g⁻¹ and a broad melt at 226 °C similar to compound **15** with an associated enthalpy of fusion 20.8 J g⁻¹ as seen in Figure 87 these peaks are most likely related to a solid-solid phase transition. The first and second crystallisations are also identical to compound **15** at 214 °C and 212.7 °C with a change in enthalpy of 16.8 J g⁻¹ and 2.5

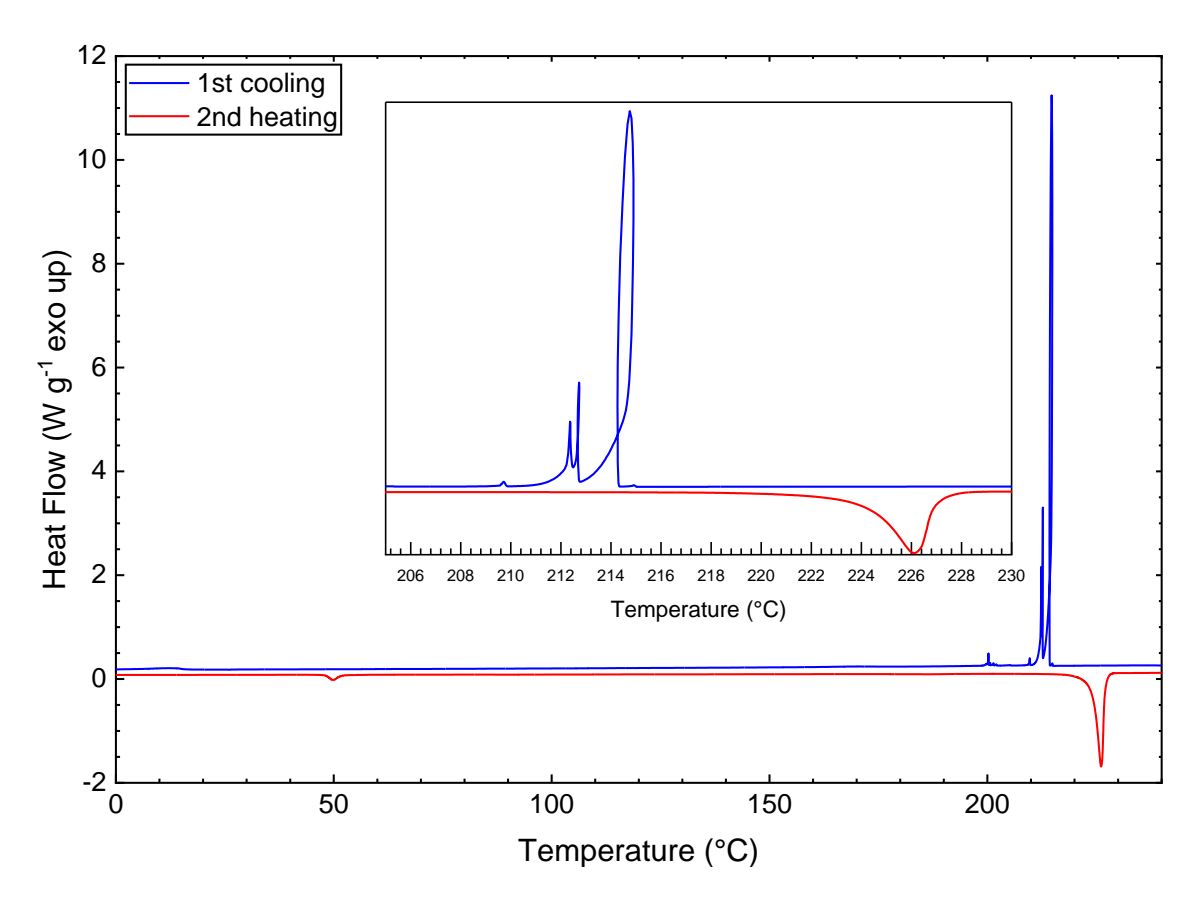


Figure 87: DSC traces measured on **20** powder, upon heating, subsequent cooling (red and blue traces respectively).

J g⁻¹ respectively. The first crystallisation also expresses the same "loop" characteristic seen with compound **15**. The similarities observed between compound **15** and compound **20** suggests that the phase transitions are largely driven by the side chains with Figure 87 displaying a comparison between all the heating a cooling cycles. Compound **15** enthalpy changes are close to double that of compound **20**, where compound **20** requires half the amount of energy required to order the structure.

Compound **20** has a third crystallisation peak as at 212.4 °C with a change in enthalpy of 0.9 J g⁻¹. This could indicate that the first two crystallisations are linked to the ordering of the fluorinated side chains as these are also present for compound **15**. The third crystallisation may be due to the organisation of the alkyl branching point, as this is the main differentiating structural feature of compound **20**. The first melt similar to compound **15** doesn't correlate to the crystallisation peaks as the enthalpies are vastly different suggesting the crystallisations are related to the second melt. As mentioned with compound **15** the initial melt could be related to side-chain reorganisation.

The DSC data reveals that compounds 15 and 20 exhibit intriguing crystallisation behaviours, presenting a promising avenue for further investigation. These crystallisation properties can be systematically manipulated through the application of the non-contact vapour-guided deposition technique detailed in Chapter 3. Future work will focus on transitioning to fluorinated solvents, enabling a more comprehensive exploration of the crystallisation phenomena observed in the DSC analysis. This approach has the potential to enhance our understanding of the interplay between deposition conditions and material properties, advancing the development of tailored crystallisation processes for high-performance organic semiconductors.

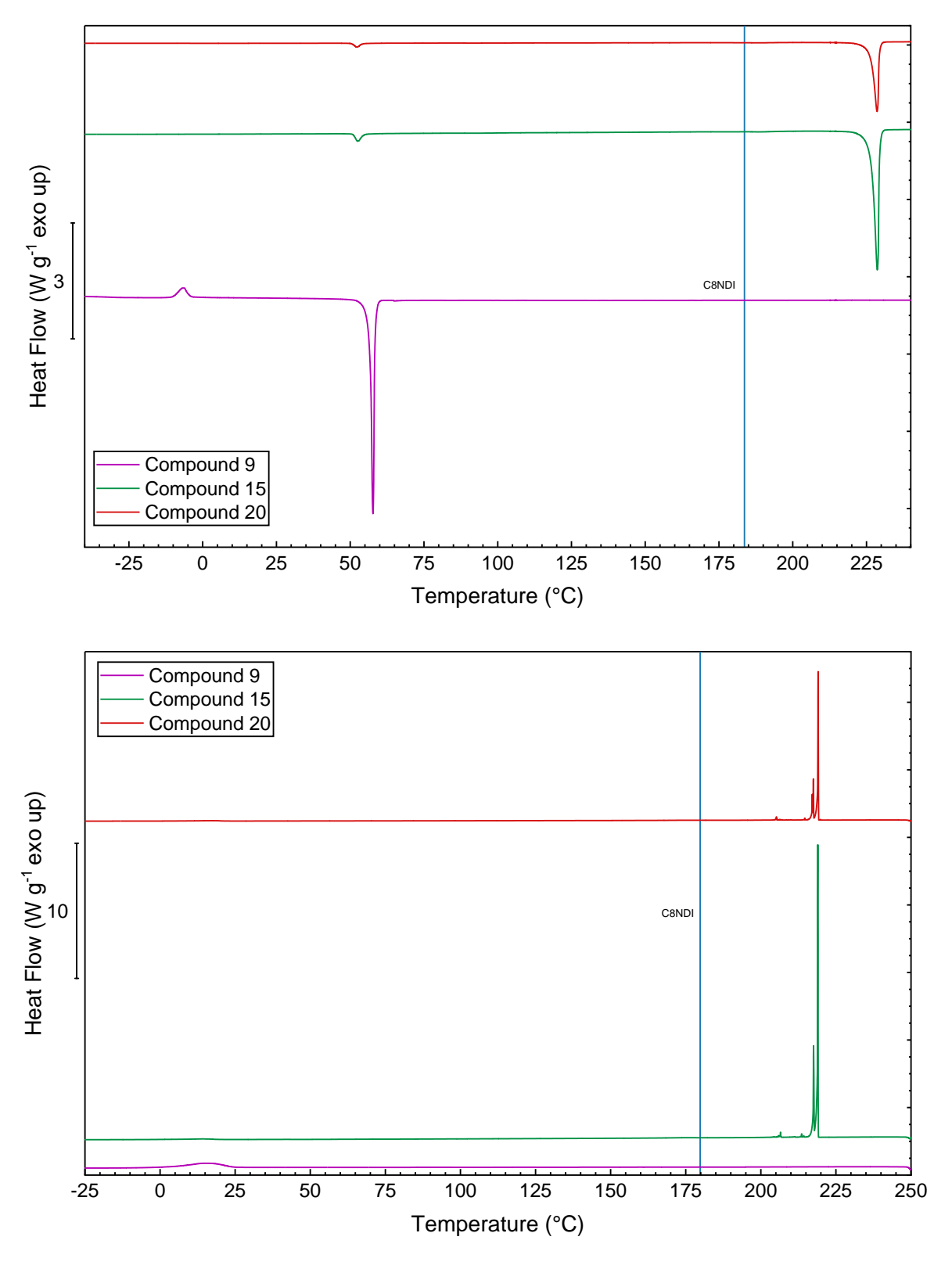


Figure 87: Comparison of DSC traces of Compound 9, 15 and 20. 2nd heating trace (top) with C8NDI melt temperature and 1st cooling traces (bottom) with C8NDI crystallisation temptrure.

4.4 Conclusion & Outlook

This chapter outlines the synthesis, characterisation, and analysis of both linear and branched perfluorinated NDI derivatives. The aim was to evaluate the impact of fluorinated side chains on the phase and optoelectronic properties of NDI compounds, whilst also understanding how side chains affect their deposition and crystallisation.

The phase properties of the synthesised NDIs were analysed using DSC. Compound 15 exhibited a broad melting transition at 226°C and two distinct crystallisation peaks at 214 °C and 212 °C, indicative of the formation of two polymorphs. This behaviour was attributed to the strong dipole interactions between the C-F bonds. In contrast, compound 20 displayed an additional crystallisation peak at 212.4 °C, suggesting the presence of three distinct polymorphs. The change in enthalpy for the melting and crystallisation of compound 20 was approximately half that of compound 7, highlighting the influence of branched fluorinated chains on the crystallisation behaviour.

The optoelectronic properties were examined through UV-Vis spectroscopy and cyclic voltammetry. Both compounds **15** and **20** showed similar absorption peaks corresponding to the π - π * transitions of the NDI core, with no significant shifts due to the fluorinated side chains. However, electrochemical analysis revealed differences in their reduction behaviour. Compound **15** exhibited an irreversible reduction peak, while compound **20** showed two fully reversible reductions, highlighting the impact of molecular structure on electronic properties. The calculated electron affinity and ionisation potential energy levels for both compounds confirmed their suitability for semiconductor applications, with slight variations reflecting the influence of the fluorinated side chains.

The comparison between the linear and branched fluorinated NDIs reveals significant insights into their phase and optoelectronic properties. The presence of fluorinated side chains, whether linear or branched, elevates the phase transition temperatures, attributed to C-F interactions. However, the branched structure introduces additional complexity in crystallization behaviour, as evidenced by the presence of an additional polymorphs and varied enthalpy changes. Optoelectronically, compound **20** exhibited more stable reduction behaviour compared to compound **15**, suggesting that branching may enhance the stability of electronic states.

While this study has successfully synthesised and characterised new perfluorinated NDIs, further work is needed to optimise the synthesis process, particularly to address miscibility issues that affect yields. Additionally, obtaining crystal structures of the new compounds would provide deeper insights into their crystals behaviour. Due to time restraints, the deposition behaviours were never obtained. This also would have been insightful in obtaining more information into the polymorphic nature of these compounds and could have explored ways to obtain different polymorphs.

The fluorinated compound introduced in Chapter 4 will be integrated into the novel non-contact vapour-guided deposition technique elaborated in Chapter 3 to explore the unique properties and applications of fluorinated organic semiconductors. By employing fluorinated solvents during the deposition process, the study aims to investigate how these solvents influence the crystallisation dynamics and molecular alignment of the fluorinated compound. This modified approach is anticipated to yield insights into the interplay between solvent composition and the self-assembly of fluorinated materials, potentially enhancing control over crystal growth and improving the uniformity and electronic properties of the resulting films. This integration underscores the adaptability of the deposition method and its utility in advancing the design of high-performance organic electronic devices.

5. Conclusions and Outlook

This thesis has investigated the design, synthesis, and application of organic semiconductors, with a particular focus on leveraging non-contact vapour-guided deposition as a novel technique for achieving enhanced crystallisation control. Through the systematic exploration of molecular design and deposition strategies, the research has provided critical insights into the relationships between structural modifications, crystallisation behaviour, and electronic properties of organic semiconductors.

Chapter 3 began with the synthesis of water-soluble PDI derivatives; however, challenges with purification impeded their application despite promising preliminary IR data. These challenges highlighted the need for further optimisation of synthesis techniques. Subsequently, the focus shifted to NDIs with smaller aromatic cores to reduce aggregation tendencies. Compound 8 demonstrated some promising deposition results but lacked sufficient water solubility, prompting a transition to glycol-based end groups to improve solubility. This shift led to the successful synthesis of compounds 9, 10, and 11, offering a comparative framework for evaluating the effects of glycol chain length on crystallisation behaviour. Compounds 9 and 10 exhibited needle-like crystal formation, whereas compound 11, with longer glycol chains, failed to produce significant crystals. Differential scanning calorimetry revealed that longer glycol chains increased melting and crystallisation temperatures, while all compounds exhibited cold crystallisation a phenomenon absent in alkyl and fluorinated derivatives. These findings underline the profound impact of subtle molecular modifications on self-assembly and crystallisation behaviour.

The development of the non-contact vapour-guided deposition technique emerged as a cornerstone of this work. Utilising surface tension gradients to guide droplet movement, this method enabled the formation of highly ordered single crystals comparable to those obtained via traditional evaporation techniques. By separating single crystals through directed droplet motion, the technique offers a scalable and reproducible approach to crystallisation control, holding significant potential for high-performance organic semiconductor fabrication.

Chapter 4 shifted focus to the synthesis and characterisation of novel fluorinated NDI derivatives, revealing their distinct crystallisation behaviours as evidenced by DSC

data. Compound **20** exhibited significantly higher solubility than compound **15**, with both compounds displaying unique crystallisation profiles. While compound **15** formed well-ordered crystals with a high enthalpy of fusion exceeding 40 J g⁻¹, compound 20 exhibited a reduced enthalpy of fusion, likely attributable to its fluorinated end groups rather than differences in the NDI core. These findings underscore the influence of fluorinated substituents on crystallisation dynamics and highlight the potential of fluorinated solvents to further refine these properties. This chapter establishes a foundation for future studies to tailor the properties of fluorinated organic semiconductors. Additionally these findings highlight the potential of fluorinated solvents to further refine these properties though the use of the novel non-contact vapour guided deposition technique. This chapter establishes a foundation for future studies to tailor the properties of fluorinated organic semiconductors.

In conclusion, this research contributes both fundamental understanding and practical advancements to the field of organic semiconductors. By addressing critical challenges in crystallisation control and demonstrating the utility of innovative deposition methods, this thesis lays the groundwork for the continued evolution of organic electronics. The methodologies and findings presented here provide a robust platform for future research, fostering innovation in the design and fabrication of next-generation organic electronic materials and devices.

The successful application of the vapour-guided deposition technique across a range of organic semiconductors underscores its versatility and potential for broad adoption in the organic electronics industry. As the field continues to evolve, the approaches and discoveries outlined in this thesis are poised to play a pivotal role in driving the development of more efficient, scalable, and environmentally sustainable electronic technologies. By combining advanced molecular design with cutting-edge deposition techniques, this work establishes a foundation for the future of organic electronic materials and devices.

6. Experimental Procedures

6.1 General Experimental

Reactions were carried out or prepared using standard Schlenk line techniques under a positive flow of N_2 . All chemicals and solvents were purchased from Sigma-Aldrich, Honeywell, Merck, Manchester Organics, Fluorochem, Fisher Scientific or Tokyo Chemical Industry UK Ltd. All glassware was dried in a vacuum over at 120 °C for a minimum of 2 hours. Flash column chromatography was carried out using C60 silica gel and thin layer chromatography (**TLC**) purification analyses performed on C60 silica F254 plates, developed using a UV lamp (λ = 336 nm).

Nuclear magnetic resonance spectroscopy (NMR) - 1 H, 13 C and 19 F NMR experiments were performed using Bruker Avance 400, 500, 600 or 700 MHz spectrometers. Spectra were processed and analysed using MestreNova software, with all chemical shifts (δ) being reported relative to the solvent peak (CDCl₃: δ 7.26, 77.2 ppm; DMSO-d6: δ 2.50, 39.5 ppm; Water (D₂O), δ 3.45).

Fourier transform infrared spectroscopy (FTIR) - carried out using Shimadzu IRTracer-100 FTIR spectrometer on solid samples. The compound in Chapter 4 was drop cast onto low iron glass slides in water and chloroform.

Mass Spectrometry (MS) - Electrospray ionisation (ESI) mass spectrometry experiments were carried out on Waters LCT Premier Q-TOF and Waters UPLC-SQD mass spectrometers by Dr. Kersti Karu.

Thermal gravimetric analysis (TGA) - measurements were performed using TA Waters TGA5500 with platinum bails under a positive flow of N2 (50 mL min⁻¹) at a rate of 10 °C min⁻¹ between 50 and 850 °C

Differential Scanning calorimetry (DSC) - was conducted using DSC2500 (TA Waters) with liquid nitrogen to modulate temperature. The instrument was calibrated against sapphire and indium. Samples were recorded under helium (25 mL min⁻¹) in aluminum Tzero pans at a rate of 10 C min⁻¹. Some reported DSC scans are the second scan, where the first scan involved removal of thermal history, some are the first and second scans. All DSCs display which scans they are and the values reported are the peak maxima.

Surface measurements - were conducted on a DektakXT Surface Profiler.

Elemental Analysis - Samples are weighed using Mettler Toledo high precision scale and analysed using ThermoFlash 2000 by Dr O. McCullough

UV-Visible-NIR Spectroscopy - carried out using a Shimadzu UV-3600i Plus spectrometer for solution and thin film samples between 300 – 1000 nm against a blank reference. Solutions were prepared between 0.001-0.1 mg mL⁻¹ concentration. Drop cats were prepared from 1 mg mL⁻¹ solutions on glass substrates.

Cyclic Voltammetry (CV) - using a Metrohm Autolab Potentiostat (PGSTAT101), electrochemical measurements were conducted using 0.1 M tetrabutylammonium

hexafluorophosphate in dichloromethane (degassed with N2) as the electrolyte. Glassy carbon was used as the working electrode, platinum as the counter electrode and a Ag/AgCl reference electrode.

Thermal gravimetric analysis (TGA) - measurements were performed using TA Waters TGA5500 with platinum HT bails under a positive flow of N2 (50 mL min⁻¹) at a rate of 10 °C min⁻¹ between 50 and ending at either 500 or 850 °C.

Contact Angle Measurements – using a Zelux 1.6-megapixel camera (Thorlabs), images of $0.5~\mu L$ droplets of water were captured. For each surface four images were collected for analysis. The contact angles were measured using ImageJ software.

X-ray Diffraction - Single colourless lath-shaped-shaped crystals of 2022NCS0592_1a were The crystal was chosen from the sample as supplied.. A suitable crystal $0.39 \times 0.04 \times 0.02$ mm3 was selected and mounted on a MITIGEN holder in oil on a Rigaku 007HF equipped with ArcSec VHF Varimax confocal mirrors and a UG2 goniometer and HyPix 6000HE detector. The crystal was kept at a steady T = 100.00(10) K during data collection. The structure was solved with the ShelXT 2018/2²¹² structure solution program using the using dual methods solution method and by using Olex2 1.3^{213} as the graphical interface. The model was refined with version 2018/3 of ShelXL 2018/3²¹⁴ using full matrix least squares minimisation on F2 minimisation.

6.2 Experimental Procedure for Chapter 3

All PDIs were deprotonated using sodium carbonate to a pH of 9-11then went through additional purification via Spectrum™ Spectra/Por™ Biotech Cellulose Ester (CE) Dialysis Membrane Tubing at 0.5 kDa in a 5 L beaker three times over 72 hours. All NMRs are after going through dialysis and thus do not contain carboxylic acids protons.

2,2'-(1,3,8,10-tetraoxo-1,3,8,10-tetrahydroanthra[2,1,9-def:6,5,10-d'e'f']diisoquinoline-2,9-diyl)disuccinic acid (1)

3,4,9,10-Perylene tetracarboxylic acid dianhydride (0.19 g, 0.5 mmol), L-aspartic acid (0.14 g, 1.1 mmol) and imidazole (1 g) were added into a two necked round bottom flask with DMF (50 mL) and heated at 120 °C for 4 hours. The reaction mixture was cooled then quenched with water and filtered. The filtrate was acidified with 2.0 M HCl and the precipitate was filtered and washed with water several times, then with methanol, dried under vacuum to give the final products. 1 H NMR (400 MHz, DMSO) δ 8.47 (s, 8H, Ar*H*), 6.07 (dd, J = 8.6, 4.6 Hz, 2H, CON-C*H*₂), 2.84 (dd, J = 15.9, 4.4 Hz, 2H, HOOC-C*H*₂CH).

2,2'-(1,3,8,10-tetraoxo-1,3,8,10-tetrahydroanthra[2,1,9-def:6,5,10-d'e'f']diisoquinoline-2,9-diyl)bis(3-hydroxybutanoic acid) (2)

3,4,9,10-Perylene tetracarboxylic acid dianhydride (0.2g, 0.5 mmol), L-Threonine (0.1191g, 1 mmol) and imidazole (1 g) were added into a two necked round bottom flask with DMF (50 ml) and heated at 110 °C for 20 h. The reaction mixture was cooled then quenched with water and filtered. The filtrate was acidified with 2.0 M HCl and the precipitate was filtered and washed with water several times, then with methanol, dried under vacuum to give the final products. 1 H NMR (600 MHz, DMF) δ 8.90 (s, 8H, Ar*H*), 5.70 (d, J = 8.8 Hz, 2H, CON-C*H*₂), 4.88 – 4.83 (m, 2H, C*H*CH₃), 1.45 (s, 6H, CHC*H*₃).

2,2'-(1,3,8,10-tetraoxo-1,3,8,10-tetrahydroanthra[2,1,9-def:6,5,10-d'e'f']diisoquinoline-2,9-diyl)bis(3-hydroxypropanoic acid) (3)

3,4,9,10-Perylene tetracarboxylic acid dianhydride (0.1 g, 2.5 mmol), L-Serine (0.54 g, 5.2 mmol) and imidazole (2.5g) were added into a two necked round bottom flask with DMF (100 mL) and heated at 110 °C for 20 h. The reaction mixture was cooled then quenched with water and filtered. The filtrate was acidified with 2.0 M HCl and the precipitate was filtered and washed with 2.0 M HCl several times, then with methanol, dried under vacuum to give the final products. 1 H NMR (600 MHz, DMSO) δ 7.95 (s, 8H, Ar*H*), 5.76 – 5.71 (m, 2H, CON-C*H*₂), 4.17 – 4.12 (m, 4H, OHC*H*₂CH), 1.22 (s, 2H).

3,3'-(1,3,8,10-tetraoxo-1,3,8,10-tetrahydroanthra[2,1,9-def:6,5,10-d'e'f']diisoquinoline-2,9-diyl)dipropionic acid (4)

3,4,9,10-Perylene tetracarboxylic acid dianhydride (1 g, 2.5 mmol), β -alanine (0.47 g, 5.2 mmol) and imidazole (2 g) were added into a two necked round bottom flask with DMF (100 mL) and heated at 110 °C for 20 h. The reaction mixture was cooled then quenched with water and filtered. The filtrate was acidified with 2.0 M HCl and the precipitate was filtered and washed with 2.0 M HCl several times, then with methanol, dried under vacuum to give the final products (1.215 g). ¹H NMR (500 MHz, DMSO) δ 8.55 (s, 8H, Ar*H*), 5.75 – 5.71 (m, 4H, CON-C*H*₂), 2.59 (s, 4H, CH₂CH₂COOH).

2,2'-(1,3,8,10-tetraoxo-1,3,8,10-tetrahydroanthra[2,1,9-def:6,5,10-d'e'f']diisoquinoline-2,9-diyl)bis(3-(4-hydroxyphenyl)propanoic acid) (5)

3,4,9,10-Perylene tetracarboxylic acid dianhydride (1g, 2.5 mmol), L-Tyrosine (0.86 g, 4.7 mmol) and imidazole (2.5 g) were added into a two necked round bottom flask with DMF (100 mL) and heated at 110 °C for 20 h. The reaction mixture was cooled then quenched with water and filtered. The filtrate was acidified with 2.0 M HCl and the precipitate was filtered and washed with 2.0 M HCl several times, then with methanol, dried under vacuum to give the final products. H NMR (600 MHz, DMSO) δ 8.23 (s, 8H, Ar*H*), 7.05 (d, J = 7.4 Hz, 4H, Ar*H*), 6.56 (d, J = 8.6 Hz, 4H), 5.91 (dd, J = 10.2, 5.6 Hz, 2H, CON-CH₂), 3.51 (dd, J = 14.1, 5.3 Hz, 3H, ArCH₂CH).

2,2'-(1,3,8,10-tetraoxo-1,3,8,10-tetrahydroanthra[2,1,9-def:6,5,10-d'e'f']diisoquinoline-2,9-diyl)bis(4-(methylthio)butanoic acid) (6)

3,4,9,10-Perylene tetracarboxylic acid dianhydride (0.48g, 1 mmol), L-Methionine (0.39g, 2.6 mmol) and imidazole (1 g) were added into a two necked round bottom flask with DMF (100 ml) and heated at 110 °C for 20 h. The reaction mixture was cooled then quenched with water and filtered. The filtrate was acidified with 2.0 M HCl and the precipitate was filtered and washed with water several times, then with methanol, dried under vacuum to give the final products. 1 H NMR (500 MHz, DMSO) δ 12.99 (s, 2H), 8.17 (s, 8H, Ar*H*), 5.71 (s, 2H, CON-C*H*₂), 2.66 (s, 3H CHC*H*₂CH₂), 2.33 (dd, J = 14.7, 7.4 Hz, 2H, SC*H*₂CH₂), 2.10 (s, 5H, SC*H*₃).

2,2'-(1,3,8,10-tetraoxo-1,3,8,10-tetrahydroanthra[2,1,9-def:6,5,10-d'e'f']diisoquinoline-2,9-diyl)bis(3-mercaptopropanoic acid) (7)

3,4,9,10-Perylene tetracarboxylic acid dianhydride (1 g, 2.5 mmol), Cysteine (0.63 g, 5.2 mmol) and imidazole (2 g) were added into a two necked round bottom flask with DMF (100 mL) and heated at 110 °C for 20 h. The reaction mixture was cooled then quenched with water and filtered. The filtrate was acidified with 2.0 M HCl and the precipitate was filtered and washed with 2.0 M HCl several times, then with methanol, dried under vacuum to give the final products. ¹H NMR (400 MHz, DMSO)

δ 8.36 (dd, J = 48.3, 8.7 Hz, 7H, Ar*H*), 5.73 (dd, J = 8.5, 4.5 Hz, 2H, CON-C*H*₂), 2.64 (d, J = 2.8 Hz, 4H, SHC*H*₂CH).

3,3'-(1,3,6,8-tetraoxo-1,3,6,8-tetrahydrobenzo[lmn][3,8]phenanthroline-2,7-diyl)dipropionic acid (8)

1,4,5,8-Naphthalenetetracarboxylic dianhydride (2 g, 7.6 mmol) and B-alanine (1.6 g, 18.7 mmol) were dissolved in DMF (250 mL) and heated at 100°C for 4 hours. The black reaction mixture was cooled to room temperature, and the solvent was evaporated under vacuum. Water (150 mL) was added, and the resulting solids were filtered and washed with acetone. 1H NMR (600 MHz, DMSO) δ 8.62 (s, 4H, Ar*H*), 4.26 (t, J = 7.8 Hz, 4H, CON-C*H*₂), 2.63 (t, J = 7.8 Hz, 4H, CH₂CH₂COOH).

2,7-bis(2-(2-(2-methoxyethoxy)ethoxy)ethyl)benzo[lmn][3,8]phenanthroline-1,3,6,8(2H,7H)-tetraone (9)

$$0 \longrightarrow 0$$

1,4,5,8-Naphthalenetetracarboxylic dianhydride (0.5 g, 1.87 mmol) was added to 50 mL of DMF under a nitrogen atmosphere in a single necked round bottom flask. 2-(2-(2-Methoxyethoxy)ethoxy) ethanamine (0.6 g, 4.5 mmol) was then added to the mixture and heated to 100 °C for 20 hours. The brown mixture was then evaporated to dryness under vacuum. The product was then purified via column chromatography using ethyl acetate and 2-8% methanol (0.73g, 70%). MS (ESI) *m/z* calc'd for

C28H34N2O10 [M+H]⁺: 558.22; found 558.22;1H NMR (400 MHz, CDCl3) δ 8.74 (s, 4H, Ar*H*), 4.46 (t, J = 5.9 Hz, 4H, CON-C*H*₂), 3.85 (t, J = 5.9 Hz, 4H, CON-CH₂C*H*₂C), 3.71 (t, J = 4.9 Hz, 4H, CO-C*H*₂CH₂CO), 3.63 – 3.59 (m, 4H, CO-CH₂C*H*₂CO), 3.57 (d, J = 4.8 Hz, 4H, CO-C*H*₂CH₂CO)), 3.48 – 3.44 (m, 4H, CO-CH₂C*H*₂CO), 3.31 (s, 6H, CO-C*H*₃). 13 C NMR (101 MHz, CDCl₃) δ 162.96 (CONH), 131.05 (Ar*C*), 126.84 (Ar*C*), 126.70 (Ar*C*), 71.95 (CON-CH₂), 70.73 (COCH₂-CH₂), 70.60 (COCH₂-CH₂), 70.19(COCH₂-CH₂), 67.87 (COCH₂-CH₂), 59.10 (COCH₂-CH₂), 39.66 (CH₂-CH₃).

2,7-bis(2-(2-methoxyethoxy)ethyl)benzo[lmn][3,8]phenanthroline-1,3,6,8(2H,7H)-tetraone (10)

1,4,5,8-Naphthalenetetracarboxylic dianhydride (0.2 g, 0.75 mmol) and 2-(2-methoxyethoxy)ethan-1-amine (0.2 g, 1.67 mmol) were dissolved in DMF (20ml) and heated at 120 °C for 24 hours. The orange reaction mixture was cooled to room temperature. The solvent was removed under vacuum. The crude product was recrystalised from DMF (0.12 g, 35%) MS (ESI) m/z calc'd for C24H26N2O8 [M+H]⁺: 470.17; found 471.17; ¹H NMR (400 MHz, CDCl₃) δ 8.74 (s, 4H, ArH), 4.46 (t, J = 5.9 Hz, 4H, CON-CH₂), 3.86 (t, J = 5.9 Hz, 4H, CON-CH₂CH₂), 3.71 – 3.67 (m, 4H, CO-CH₂CH₂CO), 3.52 – 3.47 (m, 4H, CO-CH₂CH₂CO), 3.28 (s, 6H, CO-CH₃). ¹³C NMR (101 MHz, CDCl₃) δ 162.97 (CONH), 131.03 (ArC), 126.82 (ArC), 126.71 (ArC), 72.02 (CON-CH₂), 70.06 (COCH₂-CH₂), 67.89 (COCH₂-CH₂), 59.05 (COCH₂-CH₂), 39.60 (CH₂-CH₃).

2,7-di(2,5,8,11-tetraoxatridecan-13-yl)benzo[lmn][3,8]phenanthroline-1,3,6,8(2H,7H)-tetraone (11)

1,4,5,8-Napthalenetetracarboxylic dianhydride (0.5 g, 1.87 mmol) and 2,5,8,11-tetraoxatridecan-13-amine (0.85 g, 4.1 mmol) were dissolved in DMF (25ml) and heated at 120°C for 24 hours. The orange reaction mixture was cooled to room temperature. The solvent was removed under vacuum. The crude product was recrystalised from DMF (0.48g, 40%). MS (ESI) m/z calc'd for C32H42N2O12 [M+H]⁺: 646.27; found 647.28; ¹H NMR (400 MHz, CDCl₃) δ 8.75 (s, 4H, Ar*H*), 4.46 (t, J = 6.0 Hz, 4H, CON-CH₂), 3.85 (t, J = 6.0 Hz, 4H, CON-CH₂CH₂), 3.70 (t, J = 4.8 Hz, 4H, CO-CH₂CH₂CO), 3.60 (p, J = 7.6, 6.8 Hz, 16H, CO-CH₂CH₂CO), 3.51 (t, J = 4.7 Hz, 4H, CO-CH₂CH₂CO), 3.36 (d, J = 1.3 Hz, 6H, CO-CH₃). ¹³C NMR (101 MHz, CDCl₃) δ 162.96 (CONH), 131.07 (Ar*C*), 126.85 (Ar*C*), 126.71 (Ar*C*), 72.00 (CON-CH₂), 70.71 (COCH₂-CH₂), 70.64 (COCH₂-CH₂), 70.59 (COCH₂-CH₂), 70.17 (COCH₂-CH₂), 67.86 (COCH₂-CH₂), 59.12 (COCH₂-CH₂), 39.66 (CH₂-CH₃).

6.3 Experimental Procedure for Chapter 4

8-bromo-1,1,1,2,2,3,3,4,4,5,5,6,6-tridecafluorooctane (13)

1H,1H,2H,2H-Perfluoro-1-octanol (4) (11.5 g, 31.7 mmol) was added to a round bottom flask with 1-Butyl-3-methylimidazolium bromide (7.1 g, 32.3 mmol) the mixture was stirred vigorously. Sulphuric acid (3.1 g, 31.7 mmol) was added to the mixture after which the solution began to turn orange. The reaction was heated to 40° C for 1 hour to ensure a homogenous solution after which the reaction was cooled to R.T and left stirring for 5-6 hours. The of the solids were dissolved leaving a thick orange solution. The product was distilled under vacuum, a slightly yellow liquid (7.63g, 32%) at 68-70°C condenses. ¹H NMR (400 MHz, CDCl₃) δ 4.00 (td, J = 6.4, 1.6 Hz, 2H, CF₂-CH₂CH₂), 2.40 (tt, J = 18.9, 6.2 Hz, 2H, CH₂CH₂-Br). ¹⁹F NMR (376 MHz, CDCl₃) δ -80.82 (CF₃CF2), -113.47 (ddd, J = 34.6, 16.2, 10.0 Hz, CF₂CF2), -121.90 (CF₂CF2), -122.89 (CF₂CF2), -123.73 (CF₂CF2), -126.15 (CF₂CH2).

3,3,4,4,5,5,6,6,7,7,8,8,8-tridecafluorooctan-1-amine (14)

5 (7.63 g, 17 mmol) was added to a round bottom flask containing 1-Butyl-3-methylimidazolium tetrafluoroborate (20 mL) with vigorous stirring. Phthalimide potassium salt (3.97 g, 21 mmol) was added to the mixture which was left stirring for 12 hours at 80°C. The next day potassium hydroxide (3M) in 30ml was added to the mixture and left over another 12 hours. The mixture was cooled and the product was extracted using chloroform (3 x 30mL) producing a slightly yellow oil (1.4734g, 23%). ¹H NMR (400 MHz, CDCl₃) δ 4.01 (q, J = 6.0 Hz, 2H, CF₂-CH₂CH₂), 2.40 (tt, J = 19.1, 6.4 Hz, 2H, CH2CH2-NH2). ¹⁹F NMR (376 MHz, CDCl₃) δ -80.77 (t, J = 10.0 Hz, CF₃CF2), -113.34 – -113.61 (m, CF₂CF2), -121.91 (t, J = 14.7 Hz, CF₂CF2), -122.74 – -123.05 (m), -123.75 (dd, J = 18.9, 11.1 Hz, CF₂CF2), -126.15 (td, J = 14.9, 6.1 Hz, CF₂CH2).

2,7-bis(3,3,4,4,5,5,6,6,7,7,8,8,8-tridecafluorooctyl)benzo[lmn][3,8]phenanthroline-1,3,6,8(2H,7H)-tetraone (15)

1,4,5,8-Naphthalenetetracarboxylic dianhydride (0.036 g, 0.13 mmol) and **6** (0.1003 g, 0.27 mmol) were dissolved in DMF (10ml) and heated at 120 °C for 24 hours. The orange reaction mixture was cooled to room temperature. The solvent was removed under vacuum. The crude product was recrystalised from methanol (0.014 g, 11%) ¹H NMR (400 MHz, CDCl₃) δ 8.91 (s, 4H, Ar*H*), 4.64 (q, 4H, CON-C*H*₂), 2.72 – 2.55 (m, 4H, CON-CH₂C*H*₂). ¹⁹F NMR (376 MHz, CDCl₃) δ -80.73 (t, J = 10.2 Hz, C*F*₃CF2), -114.45 (C*F*₂CH2), -121.85 (C*F*₂CF2), -122.85 (C*F*₂CF2), -123.42 (C*F*₂CF2), -126.12 (C*F*₂CH2). Elemental analyses Found: C, 36.2; H, 0.4; N, 2.58. Calc. for C30H12F26N2O4: C, 37.6; H, 1.3%; N, 2.92.

ethyl 2-cyano-5,5,6,6,7,7,8,8,9,9,10,10,10-tridecafluoro-2-(3,3,4,4,5,5,6,6,7,7,8,8,8-tridecafluorooctyl)decanoate (17)

$$C_{6}$$
 C_{13} C_{6} C_{13} C_{6}

To perfluorohexyl ethyl iodide (9.2 mL) ethyl cyanoacetate (1.88 mL), flame dried K2CO3 (5.38 g), and anhydrous DMF (12.4 mL) was added. The vial was sealed under nitrogen and stirred at rt. After 72 h, the reaction mixture was evaporated to dryness. The crude product was purified by column chromatography (silica gel, 90% hexane/Et2O) to afford a white solid (4.37 g, 95%). 1H NMR (400 MHz, CDCl3) δ 4.37 (q, J = 7.1 Hz, 2H), 2.50 – 2.26 (m, 4H), 2.21 (d, J = 14.6 Hz, 1H), 2.17 – 2.08 (m, 3H), 1.36 (t, J = 7.0 Hz, 3H). ¹⁹F NMR (376 MHz, CDCl₃) δ -80.75 (CF₃CF2), -80.75 (d, J = 20.1 Hz CF₂CF2), -114.07 – -114.39 (m, CF₂CF2), -121.87 CF₂CF2, -122.85 CF₂CF2, -123.16 (t, J = 15.3 Hz, CF₂CF2), -126.11 (td, J = 15.6, 14.7, 6.4 Hz, CF₂CH2).

5,5,6,6,7,7,8,8,9,9,10,10,10-tridecafluoro-2-(3,3,4,4,5,5,6,6,7,7,8,8,8-tridecafluorooctyl)decanenitrile (18)

$$C_6F_{13}$$
 C_6F_{13}

To **9** (5.01 g, 6.2 mmol), was added lithium chloride (0.92 g, 21 mmol), DMSO (50 mL), and H2O (10 mL). The reaction mixture was heated to 160 °C and stirred for 24 h. The reaction mixture was allowed to cool to room temperature, and product crashes out of solution. The crude product was rinsed with water, dissolved in EtOAc, and evaporated to dryness. The crude product was purified by column chromatography (silica gel, 95% hexanes/EtOAc) to afford a white solid (4.373 g, 95%). ¹H NMR (400 MHz, CDCl₃) δ 2.78 (tt, J = 9.8, 5.6 Hz, 1H), 2.34 (dtd, J = 52.1, 16.4, 9.5 Hz, 4H), 2.08 – 1.90 (m, 4H). ¹⁹F NMR (376 MHz, CDCl₃) δ -80.74 (t, J = 9.9 Hz, CF₃CF2), -113.21 (d, J = 15.3 Hz, CF₂CF2), -113.95 (t, J = 14.8 Hz, CF₂CF2), -114.32 (t, J = 14.8 Hz, CF₂CF2), -115.02 (d, J = 14.8 Hz, CF₂CF2), -121.71 – -122.01 (m, CF₂CH2), -122.84 (CF₂CF2), -123.15 – -123.46 (m, CF₂CF2), -126.11 (td, J = 15.4, 14.8, 6.3 Hz, CF₂CH2).

5,5,6,6,7,7,8,8,9,9,10,10,10-tridecafluoro-2-(3,3,4,4,5,5,6,6,7,7,8,8,8-tridecafluorooctyl)decan-1-amine (19)

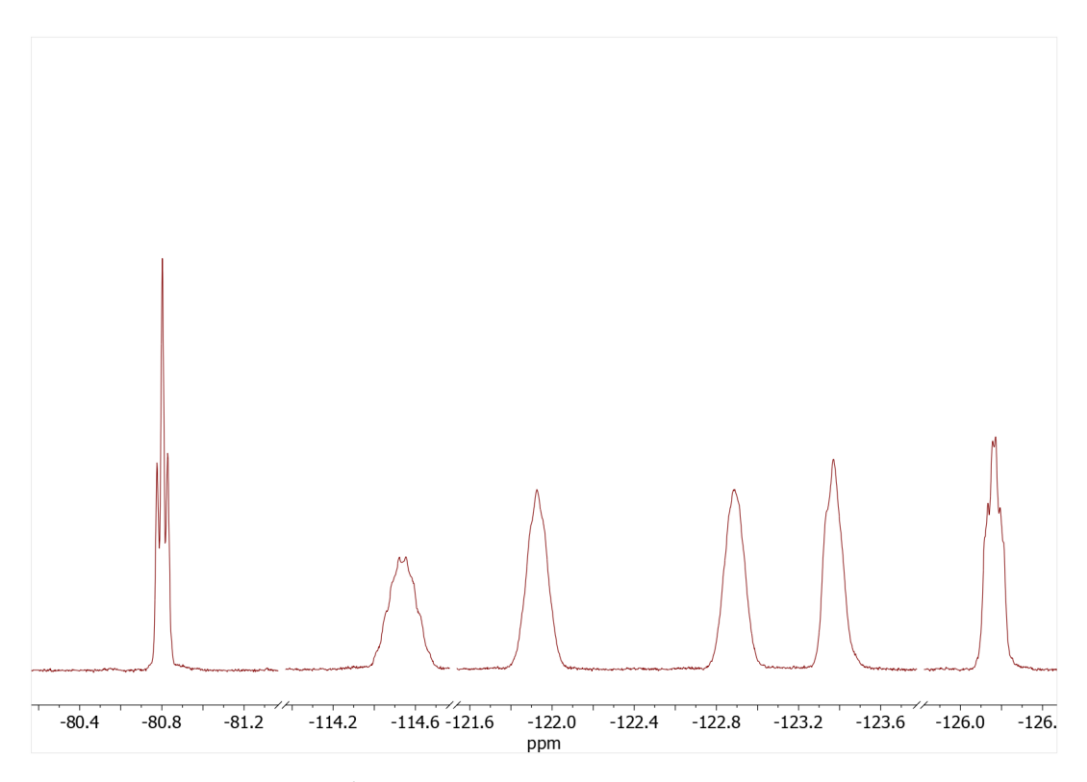
To **10** (3 g, 4 mmol) was added dry Et₂O (60 mL) under nitrogen. Procedure reported from Miller et al.²⁰⁰ Nitrile was stirred until it was fully dissolved, and then cooled to 0 °C. Lithium aluminium hydride (0.31 g, 8 mmol) was added. After 1 h, the reaction was let warm to room temperature and stirred for 5 h. The reaction was quenched by dropwise addition of H₂O with stirring, and then extracted with EtOAc, dried (MgSO4), filtered, and evaporated to dryness. The crude mixture was purified by column chromatography (silica gel, 100% DCM->1% MeOH/DCM-> 5% MeOH/DCM (all with 1% TEA)) to provide the product as a yellow oil (2g, 54%). ¹H NMR (700 MHz, CDCl₃) δ 2.71 (d, J = 5.7 Hz, 2H, H₂NCH₂), 2.16 – 2.04 (m, 4H, CF₂CH₂), 1.74 – 1.56 (m, 5H, CH₂CH₂). Spectra in line with reported literature²⁰⁰.

2-(5,5,6,6,7,7,8,8,9,9,10,10,11,11,11-pentadecafluoro-2-(3,3,4,4,5,5,6,6,7,7,8,8,8-tridecafluorooctyl)undecyl)-7-(5,5,6,6,7,7,8,8,9,9,10,10,10-tridecafluoro-2-(3,3,4,4,5,5,6,6,7,7,8,8,8-

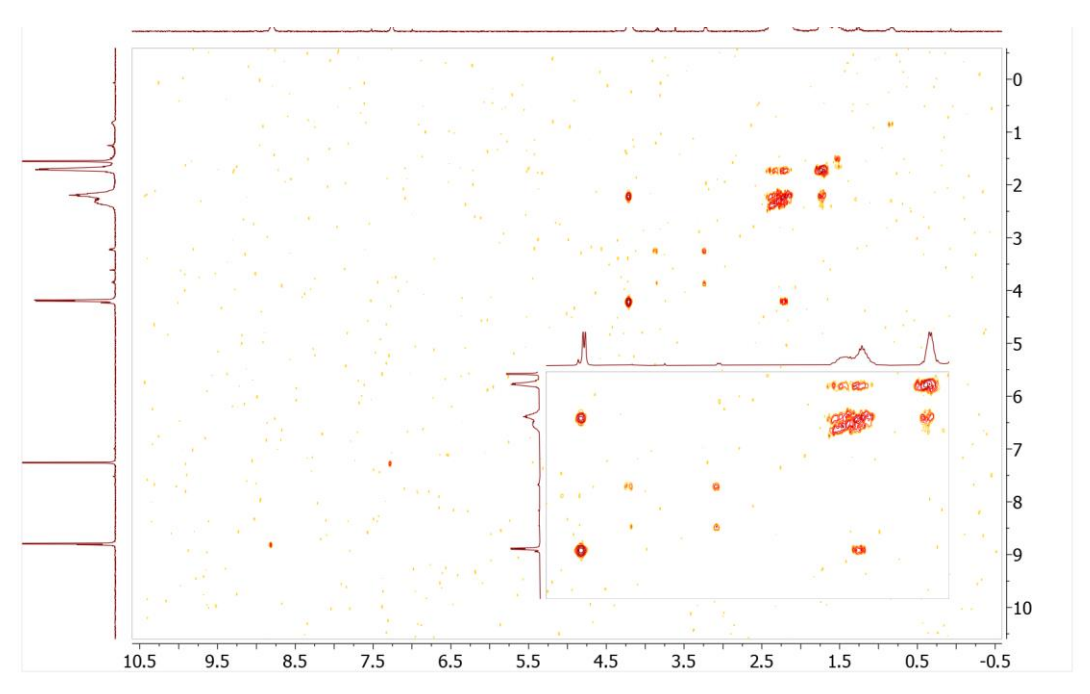
tridecafluorooctyl)decyl)benzo[lmn][3,8]phenanthroline-1,3,6,8(2H,7H)-tetraone (20)

$$C_{6}F_{13}$$
 $C_{6}F_{13}$
 $C_{6}F_{13}$
 $C_{6}F_{13}$

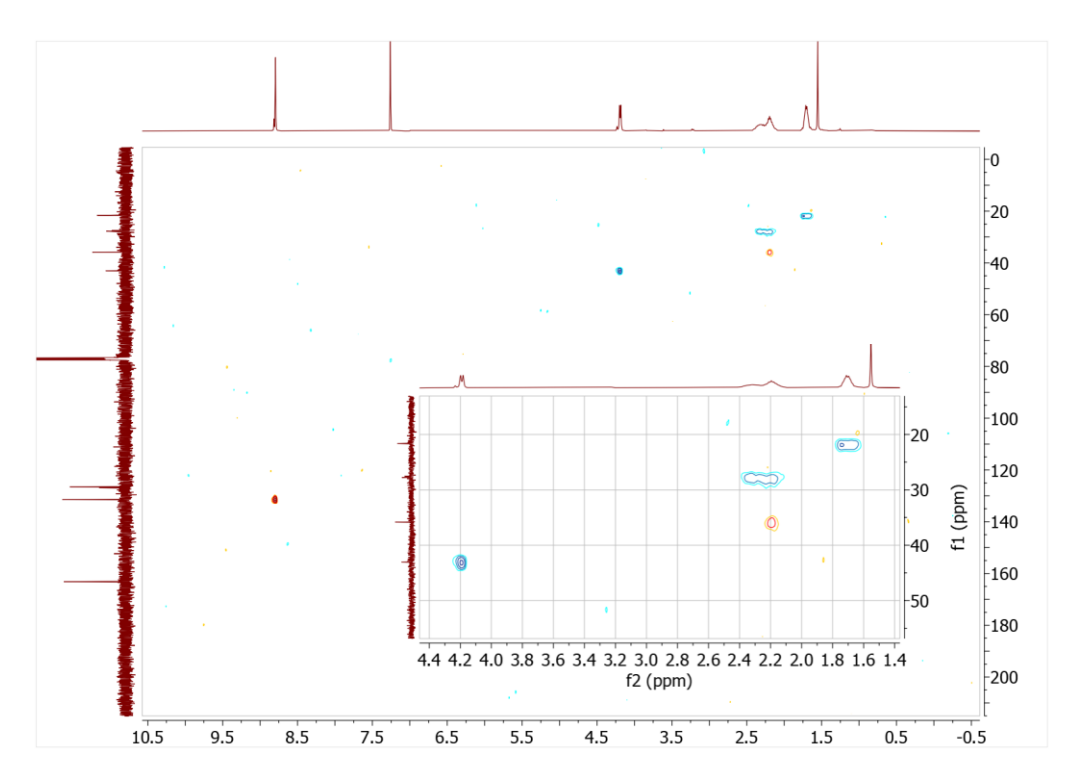
1,4,5,8-Naphthalenetetracarboxylic dianhydride (0.2g, 0.75 mmol) and **11** (1.2g, 1.64 mmol) were dissolved in DMF (30ml) and heated at 120°C for 72 hours. The reaction mixture was cooled to room temperature. The solvent was removed under vacuum. The crude product was purified using column chromatography silica gel, 100% DCM->5% EtOAc/DCM-> 10% EtOAc/DCM (0.63 g, 48%). ¹H NMR (400 MHz, CDCl₃) δ 8.79 (s, 4H, Ar*H*), 4.19 (d, *J* = 6.9 Hz, 4H, CON-C*H*₂), 2.43 – 2.25 (m, 5H), 2.22 – 2.14 (m, 5H), 1.72 (dd, *J* = 10.7, 5.5 Hz, 9H). ¹³C NMR (101 MHz, CDCl₃) δ 163.16 (CONH), 131.48 (Ar*C*), 126.88 (Ar*C*), 126.50 (Ar*C*), 43.06 (CON-CH2), 35.83 (CHCH2), 27.75 (CF₂CH2), 21.63 (CF₂CH2). ¹⁹F NMR (376 MHz, CDCl₃) δ -80.80 (d, *J* = 20.3 Hz, C*F*₃CF2), -114.52 (dp, *J* = 27.1, 14.1, 13.6 Hz, C*F*₂CF2), -121.78 – 122.08 (m, C*F*₂CF2), -122.88 (t, *J* = 10.7 Hz, C*F*₂CF2), -123.35 (d, *J* = 15.7 Hz, C*F*₂CF2), -126.16 (t, *J* = 15.3 Hz, C*F*₂CH2).



Supplementary Figure 6.1: 9F NMR 2-(5,5,6,6,7,7,8,8,9,9,10,10,11,11,11-pentadecafluoro-2-(3,3,4,4,5,5,6,6,7,7,8,8,8-tridecafluorooctyl)undecyl)-7-(5,5,6,6,7,7,8,8,9,9,10,10,10-tridecafluoro-2-(3,3,4,4,5,5,6,6,7,7,8,8,8-tridecafluorooctyl)decyl)benzo[lmn][3,8]phenanthroline-1,3,6,8(2H,7H)-tetraone (20) in CDCl₃



Supplementary Figure 6.2: ${}^{1}\text{H-}{}^{1}\text{H COSY 2-}(5,5,6,6,7,7,8,8,9,9,10,10,11,11,11-pentadecafluoro-2-}(3,3,4,4,5,5,6,6,7,7,8,8,8-tridecafluorooctyl)undecyl)-7-(5,5,6,6,7,7,8,8,9,9,10,10,10-tridecafluoro-2-(3,3,4,4,5,5,6,6,7,7,8,8,8-tridecafluorooctyl)decyl)benzo[lmn][3,8]phenanthroline-1,3,6,8(2H,7H)-tetraone (20) in CDCl₃$



Supplementary Figure 6.3: ${}^{1}\text{H-}{}^{13}\text{C HSQC 2-}(5,5,6,6,7,7,8,8,9,9,10,10,11,11,11-pentadecafluoro-2-}(3,3,4,4,5,5,6,6,7,7,8,8,8-tridecafluorooctyl)undecyl)-7-(5,5,6,6,7,7,8,8,9,9,10,10,10-tridecafluoro-2-(3,3,4,4,5,5,6,6,7,7,8,8,8-tridecafluorooctyl)decyl)benzo[lmn][3,8]phenanthroline-1,3,6,8(2H,7H)-tetraone (20) in CDCl₃$

7.0 References

- 1. Liao, Y.; Weber, J.; Faul, C. F. J., Fluorescent Microporous Polyimides Based on Perylene and Triazine for Highly CO2-Selective Carbon Materials. *Macromolecules* **2015**, *48* (7), 2064-2073.
- 2. Broggi, A.; Tomasi, I.; Bianchi, L.; Marrocchi, A.; Vaccaro, L., Small Molecular Aryl Acetylenes: Chemically Tailoring High-Efficiency Organic Semiconductors for Solar Cells and Field-Effect Transistors. *ChemPlusChem* **2014**, *79* (4), 486-507.
- 3. Lin, Y.; Li, Y.; Zhan, X., Small molecule semiconductors for high-efficiency organic photovoltaics. *Chemical Society Reviews* **2012**, *41* (11), 4245-4272.
- 4. Yang, Y.; Zhang, Z.-G.; Bin, H.; Chen, S.; Gao, L.; Xue, L.; Yang, C.; Li, Y., Side-Chain Isomerization on an n-type Organic Semiconductor ITIC Acceptor Makes 11.77% High Efficiency Polymer Solar Cells. *Journal of the American Chemical Society* **2016**, *138* (45), 15011-15018.
- 5. Lee, S. H.; Park, H.; Kim, S.; Son, W.; Cheong, I. W.; Kim, J. H., Transparent and flexible organic semiconductor nanofilms with enhanced thermoelectric efficiency. *Journal of Materials Chemistry A* **2014**, *2* (20), 7288-7294.
- 6. Duan, Y.; Zhang, B.; Zou, S.; Fang, C.; Wang, Q.; Shi, Y.; Li, Y., Low-power-consumption organic field-effect transistors. *Journal of Physics: Materials* **2020**, *3* (1), 014009.
- 7. Wang, Q.; Jiang, S.; Qian, J.; Song, L.; Zhang, L.; Zhang, Y.; Zhang, Y.; Wang, Y.; Wang, X.; Shi, Y.; Zheng, Y.; Li, Y., Low-voltage, High-performance Organic Field-Effect Transistors Based on 2D Crystalline Molecular Semiconductors. *Scientific Reports* **2017**, *7* (1), 7830.
- 8. Klauk, H.; Zschieschang U Fau Pflaum, J.; Pflaum J Fau Halik, M.; Halik, M., Ultralow-power organic complementary circuits. **2007**, (1476-4687 (Electronic)).
- 9. Clayden, J.; Greeves, N.; Warren, S., Organic Chemistry. OUP Oxford: 2012.
- 10. Lide, D. R., *CRC handbook of chemistry and physics : a ready-reference book of chemical and physical data.* 85th edition. ed.; CRC Press: Boca Raton, Fla.; London, 2004.
- 11. Grozema, F. C.; Siebbeles, L. D. A., Mechanism of charge transport in self-organizing organic materials. *International Reviews in Physical Chemistry* **2008**, *27* (1), 87-138.
- 12. Kokil, A.; Yang, K.; Kumar, J., Techniques for characterization of charge carrier mobility in organic semiconductors. *Journal of Polymer Science Part B: Polymer Physics* **2012**, *50* (15), 1130-1144.
- 13. Rani, V.; Kumar, P.; Sharma, A.; Yadav, S.; Singh, B.; Ray, N.; Ghosh, S., Carrier Induced Hopping to Band Conduction in Pentacene. *Scientific Reports* **2019**, 9 (1), 20193.
- 14. Yavuz, I., Dichotomy between the band and hopping transport in organic crystals: insights from experiments. *Physical Chemistry Chemical Physics* **2017**, *19* (38), 25819-25828.
- 15. Marcus, R. A.; Sutin, N., Electron transfers in chemistry and biology. Biochimica et Biophysica Acta (BBA) - Reviews on Bioenergetics **1985**, 811 (3), 265-322.
- 16. Fratini, S.; Nikolka, M.; Salleo, A.; Schweicher, G.; Sirringhaus, H., Charge transport in high-mobility conjugated polymers and molecular semiconductors. *Nat Mater* **2020**, *19* (5), 491-502.

- 17. Mitsui, C.; Okamoto, T.; Yamagishi, M.; Tsurumi, J.; Yoshimoto, K.; Nakahara, K.; Soeda, J.; Hirose, Y.; Sato, H.; Yamano, A.; Uemura, T.; Takeya, J., High-performance solution-processable N-shaped organic semiconducting materials with stabilized crystal phase. *Adv Mater* **2014**, *26* (26), 4546-51.
- 18. Kubo, T.; Hausermann, R.; Tsurumi, J.; Soeda, J.; Okada, Y.; Yamashita, Y.; Akamatsu, N.; Shishido, A.; Mitsui, C.; Okamoto, T.; Yanagisawa, S.; Matsui, H.; Takeya, J., Suppressing molecular vibrations in organic semiconductors by inducing strain. *Nat Commun* **2016**, *7*, 11156.
- 19. Troisi, A.; Orlandi, G., Charge-Transport Regime of Crystalline Organic Semiconductors: Diffusion Limited by Thermal Off-Diagonal Electronic Disorder. *Physical Review Letters* **2006**, *96* (8), 086601.
- 20. Fratini, S.; Ciuchi, S.; Mayou, D.; de Laissardiere, G. T.; Troisi, A., A map of high-mobility molecular semiconductors. *Nat Mater* **2017**, *16* (10), 998-1002.
- 21. Kunkel, C.; Margraf, J. T.; Chen, K.; Oberhofer, H.; Reuter, K., Active discovery of organic semiconductors. *Nature Communications* **2021**, *12* (1), 2422.
- 22. Uejima, M.; Sato, T.; Tanaka, K.; Kaji, H., Vibronic coupling density analysis for the chain-length dependence of reorganization energies in oligofluorenes: a comparative study with oligothiophenes. *Physical Chemistry Chemical Physics* **2013**, *15* (33), 14006-14016.
- 23. Bronstein, H.; Nielsen, C. B.; Schroeder, B. C.; McCulloch, I., The role of chemical design in the performance of organic semiconductors. *Nature Reviews Chemistry* **2020**, *4* (2), 66-77.
- 24. Holliday, S.; Ashraf, R. S.; Nielsen, C. B.; Kirkus, M.; Röhr, J. A.; Tan, C.-H.; Collado-Fregoso, E.; Knall, A.-C.; Durrant, J. R.; Nelson, J.; McCulloch, I., A Rhodanine Flanked Nonfullerene Acceptor for Solution-Processed Organic Photovoltaics. *Journal of the American Chemical Society* **2015**, *137* (2), 898-904.
- 25. Insuasty, A.; Maniam, S.; Langford, S. J., Recent Advances in the Core-Annulation of Naphthalene Diimides. *Chemistry* **2019**, *25* (29), 7058-7073.
- 26. Kobaisi, M. A.; Bhosale, S. V.; Latham, K.; Raynor, A. M.; Bhosale, S. V., Functional Naphthalene Diimides: Synthesis, Properties, and Applications. *Chem Rev* **2016**, *116* (19), 11685-11796.
- 27. Vener, M. A.-O.; Kharlanov, O. G.; Sosorev, A. A.-O., High-Mobility Naphthalene Diimide Derivatives Revealed by Raman-Based In Silico Screening. LID 10.3390/ijms232113305 [doi] LID 13305. **2022**, (1422-0067 (Electronic)).
- 28. Yan, W.; He, Z.; Jiang, J.; Lu, D.; Gong, Y.; Yang, W.; Xia, R.; Huang, W.; Xin, H., Highly thermal-stable perylene-bisimide small molecules as efficient electron-transport materials for perovskite solar cells. *Journal of Materials Chemistry C* **2020**, *8* (42), 14773-14781.
- 29. Li, Y.; Zhang, X.; Liu, D., Recent developments of perylene diimide (PDI) supramolecular photocatalysts: A review. *Journal of Photochemistry and Photobiology C: Photochemistry Reviews* **2021**, *48*, 100436.
- 30. Markiewicz, G.; Smulders, M. M. J.; Stefankiewicz, A. R., Steering the Self-Assembly Outcome of a Single NDI Monomer into Three Morphologically Distinct Supramolecular Assemblies, with Concomitant Change in Supramolecular Polymerization Mechanism. *Advanced Science* **2019**, *6* (16), 1900577.
- 31. Fu, C.; Lin, H.-p.; Macleod, J. M.; Krayev, A.; Rosei, F.; Perepichka, D. F., Unravelling the Self-Assembly of Hydrogen Bonded NDI Semiconductors in 2D and 3D. *Chemistry of Materials* **2016**, *28* (3), 951-961.
- 32. Wagalgave, S. M.; Padghan, S. D.; Burud, M. D.; Kobaisi, M. A.; La, D. D.; Bhosale, R. S.; Bhosale, S. V.; Bhosale, S. V., Supramolecular super-helix

- formation via self-assembly of naphthalene diimide functionalised with bile acid derivatives. *Scientific Reports* **2019**, *9* (1), 12825.
- 33. Shao, H.; Parquette, J. R., A pi-conjugated hydrogel based on an Fmoc-dipeptide naphthalene diimide semiconductor. *Chem Commun (Camb)* **2010**, *46* (24), 4285-7.
- 34. Shao, H.; Nguyen, T.; Romano, N. C.; Modarelli, D. A.; Parquette, J. R., Self-assembly of 1-D n-type nanostructures based on naphthalene diimide-appended dipeptides. *J Am Chem Soc* **2009**, *131* (45), 16374-6.
- 35. Palma, C.-A.; Bjork, J.; Bonini, M.; Dyer, M. S.; Llanes-Pallas, A.; Bonifazi, D.; Persson, M.; Samorì, P., Tailoring Bicomponent Supramolecular Nanoporous Networks: Phase Segregation, Polymorphism, and Glasses at the Solid-Liquid Interface. *Journal of the American Chemical Society* **2009**, *131* (36), 13062-13071.
- 36. Ruiz-Osés, M.; de Oteyza, D. G.; Fernández-Torrente, I.; Gonzalez-Lakunza, N.; Schmidt-Weber, P. M.; Kampen, T.; Horn, K.; Gourdon, A.; Arnau, A.; Ortega, J. E., Non-covalent interactions in supramolecular assemblies investigated with electron spectroscopies. *Chemphyschem* **2009**, *10* (6), 896-900.
- 37. Pandeeswar, M.; Avinash, M. B.; Govindaraju, T., Chiral Transcription and Retentive Helical Memory: Probing Peptide Auxiliaries Appended with Naphthalenediimides for Their One-Dimensional Molecular Organization. *Chemistry A European Journal* **2012**, *18* (16), 4818-4822.
- 38. Aleshinloye, A. O.; Bodapati, J. B.; Icil, H., Synthesis, characterization, optical and electrochemical properties of a new chiral multichromophoric system based on perylene and naphthalene diimides. *Journal of Photochemistry & Photobiology, A: Chemistry* **2015**, *300* (Complete), 27-37.
- 39. Narayan, B.; Bejagam, K. K.; Balasubramanian, S.; George, S. J., Autoresolution of Segregated and Mixed p-n Stacks by Stereoselective Supramolecular Polymerization in Solution. *Angewandte Chemie International Edition* **2015**, *54* (44), 13053-13057.
- 40. Sun, M.; Müllen, K.; Yin, M., Water-soluble perylenediimides: design concepts and biological applications. *Chemical Society Reviews* **2016**, *45* (6), 1513-1528.
- 41. Türkmen, G.; Erten-Ela, S.; Icli, S., Highly soluble perylene dyes: Synthesis, photophysical and electrochemical characterizations. *Dyes and Pigments* **2009**, 83 (3), 297-303.
- 42. Aivali, S.; Tsimpouki, L.; Anastasopoulos, C.; Kallitsis, J. K., Synthesis and Optoelectronic Characterization of Perylene Diimide-Quinoline Based Small Molecules. LID 10.3390/molecules24234406 [doi] LID 4406. **2019**, (1420-3049 (Electronic)).
- 43. Scheibe, G., Holleman-Wiberg: Lehrbuch der anorganischen Chemie. 37–39. Auflage, XXVIII, 663 S. mit 166 Abb. Walter de Gruyter & Co., Berlin 1956. Ganzleinen DM 28,—. Zeitschrift für Elektrochemie, Berichte der Bunsengesellschaft für physikalische Chemie 1957, 61 (8), 1117-1118.
- 44. Lindner, H. J., K. D. Sen, C. K. Jørgensen (Eds.): Electronegativity, Structure and Bonding, Vol. 66, Springer Verlag, Berlin, Heidelberg, New York, London, Paris, Tokyo 1987. 198 Seiten, Preis: DM 138,—. *Berichte der Bunsengesellschaft für physikalische Chemie* **1989**, *93* (4), 535-536.
- 45. Kirsch, P., *Modern Fluoroorganic Chemistry: Synthesis, Reactivity, Applications.* WILEY-VCH Verlag GmbH & Co.

KGaA, Weinheim: Weinheim, 2004.

- 46. Banks, R. E.; Smart, B. E.; Tatlow, J. C. In *Organofluorine chemistry : principles and commercial applications*, 1994.
- 47. Smart, B. E., Fluorine substituent effects (on bioactivity). *Journal of Fluorine Chemistry* **2001**, *109* (1), 3-11.
- 48. Hayashi, N.; Ujihara, T.; Ikeda, H., Effect of bond orbital interactions on the conformational stabilities of 1,2-difluoroethane and 2,3-difluorobutanes. *Tetrahedron* **2019**, *75* (4), 527-532.
- 49. Allinger, N. L.; Grev, R. S.; Yates, B. F.; Schaefer, H. F., III, The syn rotational barrier in butane. *Journal of the American Chemical Society* **1990**, *112* (1), 114-118.
- 50. Organo-Fluorine Compounds / Methods Index. 4th Edition ed.; Baasner, B.; Hagemann, H.; Tatlow, J. C., Eds. Georg Thieme Verlag KG: Stuttgart, 2000. http://www.thieme-connect.de/products/ebooks/book/10.1055/b-003-111691.
- 51. Hertel, D.; Dr, C.; Meerholz, K., Organische Leuchtdioden. *Chemie in unserer Zeit* **2005**, *39*, 336-347.
- 52. Bao, Z.; Locklin, J., Organic Field-Effect Transistors. CRC Press, Inc.: 2007.
- 53. Facchetti, A., π-Conjugated Polymers for Organic Electronics and Photovoltaic Cell Applications. *Chemistry of Materials* **2011**, *23* (3), 733-758.
- 54. Tang, M. L.; Bao, Z., Halogenated Materials as Organic Semiconductors. *Chemistry of Materials* **2011**, *23* (3), 446-455.
- 55. Ma, H.; Yip, H.-L.; Huang, F.; Jen, A. K. Y., Interface Engineering for Organic Electronics. *Advanced Functional Materials* **2010**, *20* (9), 1371-1388.
- 56. Reichenbächer, K.; Süss, H. I.; Hulliger, J., Fluorine in crystal engineering—"the little atom that could". *Chemical Society Reviews* **2005**, *34* (1), 22-30.
- 57. Cho, D. M.; Parkin, S. R.; Watson, M. D., Partial Fluorination Overcomes Herringbone Crystal Packing in Small Polycyclic Aromatics. *Organic Letters* **2005**, *7* (6), 1067-1068.
- 58. Tsao, H. N.; Cho, D.; Andreasen, J. W.; Rouhanipour, A.; Breiby, D. W.; Pisula, W.; Müllen, K., The Influence of Morphology on High-Performance Polymer Field-Effect Transistors. *Advanced Materials* **2009**, *21* (2), 209-212.
- 59. Jurchescu, O. D.; Subramanian, S.; Kline, R. J.; Hudson, S. D.; Anthony, J. E.; Jackson, T. N.; Gundlach, D. J., Organic Single-Crystal Field-Effect Transistors of a Soluble Anthradithiophene. *Chemistry of Materials* **2008**, *20* (21), 6733-6737.
- 60. Ganguly, P.; Desiraju, G. R., Long-range synthon Aufbau modules (LSAM) in crystal structures: systematic changes in C 6 H 6- n F n ($0 \le n \le 6$) fluorobenzenes. CrystEngComm **2010**, *12* (3), 817-833.
- 61. Berger, R.; Resnati, G.; Metrangolo, P.; Weber, E.; Hulliger, J., Organic fluorine compounds: a great opportunity for enhanced materials properties. *Chemical Society Reviews* **2011**, *40* (7), 3496-3508.
- 62. Diemer, P. J.; Lyle, C. R.; Mei, Y.; Sutton, C.; Payne, M. M.; Anthony, J. E.; Coropceanu, V.; Bredas, J. L.; Jurchescu, O. D., Vibration-assisted crystallization improves organic/dielectric interface in organic thin-film transistors. *Adv Mater* **2013**, 25 (48), 6956-62.
- 63. Goto, O.; Tomiya, S.; Murakami, Y.; Shinozaki, A.; Toda, A.; Kasahara, J.; Hobara, D., Organic single-crystal arrays from solution-phase growth using micropattern with nucleation control region. *Adv Mater* **2012**, *24* (8), 1117-22.
- 64. Chen, J.; Tee, C. K.; Shtein, M.; Martin, D. C.; Anthony, J., Controlled solution deposition and systematic study of charge-transport anisotropy in single crystal and single-crystal textured TIPS pentacene thin films. *Organic Electronics* **2009**, *10* (4), 696-703.

- 65. Kim, D. H.; Han, J. T.; Park, Y. D.; Jang, Y.; Cho, J. H.; Hwang, M.; Cho, K., Single-Crystal Polythiophene Microwires Grown by Self-Assembly. *Advanced Materials* **2006**, *18* (6), 719-723.
- 66. Lee, S. S.; Kim, C. S.; Gomez, E. D.; Purushothaman, B.; Toney, M. F.; Wang, C.; Hexemer, A.; Anthony, J. E.; Loo, Y.-L., Controlling Nucleation and Crystallization in Solution-Processed Organic Semiconductors for Thin-Film Transistors. *Advanced Materials* **2009**, *21* (35), 3605-3609.
- 67. Li, H.; Buesen, D.; Williams, R.; Henig, J.; Stapf, S.; Mukherjee, K.; Freier, E.; Lubitz, W.; Winkler, M.; Happe, T.; Plumere, N., Preventing the coffee-ring effect and aggregate sedimentation by in situ gelation of monodisperse materials. *Chem Sci* **2018**, *9* (39), 7596-7605.
- 68. Shimobayashi, S. F.; Tsudome, M.; Kurimura, T., Suppression of the coffeering effect by sugar-assisted depinning of contact line. *Sci Rep* **2018**, *8* (1), 17769.
- 69. Kotsuki, K.; Tanaka, H.; Obata, S.; Stauss, S.; Terashima, K.; Saiki, K., The importance of spinning speed in fabrication of spin-coated organic thin film transistors: Film morphology and field effect mobility. *Applied Physics Letters* **2014**, *104* (23).
- 70. Kim, N.-K.; Jang, S.-Y.; Pace, G.; Caironi, M.; Park, W.-T.; Khim, D.; Kim, J.; Kim, D.-Y.; Noh, Y.-Y., High-Performance Organic Field-Effect Transistors with Directionally Aligned Conjugated Polymer Film Deposited from Pre-Aggregated Solution. *Chemistry of Materials* **2015**, *27* (24), 8345-8353.
- 71. Yuan, Y.; Giri, G.; Ayzner, A. L.; Zoombelt, A. P.; Mannsfeld, S. C.; Chen, J.; Nordlund, D.; Toney, M. F.; Huang, J.; Bao, Z., Ultra-high mobility transparent organic thin film transistors grown by an off-centre spin-coating method. *Nat Commun* **2014**, *5*, 3005.
- 72. Qiu, L.; Lim, J. A.; Wang, X.; Lee, W. H.; Hwang, M.; Cho, K., Versatile Use of Vertical-Phase-Separation-Induced Bilayer Structures in Organic Thin-Film Transistors. *Advanced Materials* **2008**, *20* (6), 1141-1145.
- 73. Shibata, M.; Sakai, Y.; Yokoyama, D., Advantages and disadvantages of vacuum-deposited and spin-coated amorphous organic semiconductor films for organic light-emitting diodes. *Journal of Materials Chemistry C* **2015**, 3 (42), 11178-11191.
- 74. Kim, G. W.; Kwon, E. H.; Kim, M.; Park, Y. D., Uniform and Reliable Dip-Coated Conjugated Polymers for Organic Transistors as Obtained by Solvent Vapor Annealing. *The Journal of Physical Chemistry C* **2019**, *123* (37), 23255-23263.
- 75. Rogowski, R. Z.; Dzwilewski, A.; Kemerink, M.; Darhuber, A. A., Solution Processing of Semiconducting Organic Molecules for Tailored Charge Transport Properties. *The Journal of Physical Chemistry C* **2011**, *115* (23), 11758-11762.
- 76. Murray, A. R.; Baldrey, J. A.; Mullin, J. B.; Jones, O., A systematic study of zone refining of single crystal indium antimonide. *Journal of Materials Science* **1966**, *1* (1), 14-28.
- 77. Su, Y.; Gao, X.; Liu, J.; Xing, R.; Han, Y., Uniaxial alignment of triisopropylsilylethynyl pentacene via zone-casting technique. *Phys Chem Chem Phys* **2013**, *15* (34), 14396-404.
- 78. Kahng, S.-J.; Cerwyn, C.; Dincau, B. M.; Kim, J.-H.; Novosselov, I. V.; Anantram, M. P.; Chung, J.-H., Nanoink bridge-induced capillary pen printing for chemical sensors. *Nanotechnology* **2018**, *29* (33), 335304.
- 79. Giri, G.; Verploegen, E.; Mannsfeld, S. C.; Atahan-Evrenk, S.; Kim, D. H.; Lee, S. Y.; Becerril, H. A.; Aspuru-Guzik, A.; Toney, M. F.; Bao, Z., Tuning charge

- transport in solution-sheared organic semiconductors using lattice strain. *Nature* **2011**, *480* (7378), 504-8.
- 80. Diao, Y.; Zhou, Y.; Kurosawa, T.; Shaw, L.; Wang, C.; Park, S.; Guo, Y.; Reinspach, J. A.; Gu, K.; Gu, X.; Tee, B. C.; Pang, C.; Yan, H.; Zhao, D.; Toney, M. F.; Mannsfeld, S. C.; Bao, Z., Flow-enhanced solution printing of all-polymer solar cells. *Nat Commun* **2015**, *6*, 7955.
- 81. Molina-Lopez, F.; Wu, H.-C.; Wang, G.-J. N.; Yan, H.; Shaw, L.; Xu, J.; Toney, M. F.; Bao, Z., Enhancing Molecular Alignment and Charge Transport of Solution-Sheared Semiconducting Polymer Films by the Electrical-Blade Effect. *Advanced Electronic Materials* **2018**, *4* (7).
- 82. Minemawari, H.; Yamada, T.; Matsui, H.; Tsutsumi, J. y.; Haas, S.; Chiba, R.; Kumai, R.; Hasegawa, T., Inkjet printing of single-crystal films. *Nature* **2011**, *475* (7356), 364-367.
- 83. Pitsalidis, C.; Pappa, A. M.; Hunter, S.; Laskarakis, A.; Kaimakamis, T.; Payne, M. M.; Anthony, J. E.; Anthopoulos, T. D.; Logothetidis, S., High mobility transistors based on electrospray-printed small-molecule/polymer semiconducting blends. *Journal of Materials Chemistry C* **2016**, *4* (16), 3499-3507.
- 84. Yuan Y., L. T. R., Contact Angle and Wetting Properties. *Springer Series in Surface Sciences* **2013**, *51*.
- 85. Deegan, R. D.; Bakajin, O.; Dupont, T. F.; Huber, G.; Nagel, S. R.; Witten, T. A., Capillary flow as the cause of ring stains from dried liquid drops. *Nature* **1997**, 389 (6653), 827-829.
- 86. Robert D. Deegan, O. B., Todd F. Dupont, Greg Huber, Sidney R. Nagel, and Thomas A. Witten, Contact line deposits in an evaporating drop. *PHYSICAL REVIEW E* **2000**, *62*.
- 87. Soltman, D.; Subramanian, V., Inkjet-Printed Line Morphologies and Temperature Control of the Coffee Ring Effect. *Langmuir* **2008**, *24* (5), 2224-2231.
- 88. Okaiyeto, S. A.; Xiao, H.-W.; Mujumdar, A. S., Understanding the coffee ring effect: how it has led to advanced applications. *Drying Technology* **2023**, *41* (7), 1083-1084.
- 89. Sliz, R.; Czajkowski, J.; Fabritius, T., Taming the Coffee Ring Effect: Enhanced Thermal Control as a Method for Thin-Film Nanopatterning. *Langmuir* **2020**, *36* (32), 9562-9570.
- 90. Majumder, M.; Rendall, C. S.; Eukel, J. A.; Wang, J. Y. L.; Behabtu, N.; Pint, C. L.; Liu, T.-Y.; Orbaek, A. W.; Mirri, F.; Nam, J.; Barron, A. R.; Hauge, R. H.; Schmidt, H. K.; Pasquali, M., Overcoming the "Coffee-Stain" Effect by Compositional Marangoni-Flow-Assisted Drop-Drying. *The Journal of Physical Chemistry B* **2012**, *116* (22), 6536-6542.
- 91. Fabien Girard, M. I. A., *,† Sylvain Faure,‡ and Annie Steinchen*,†, Evaporation and Marangoni Driven Convection in Small Heated

Water Droplets. Langmuir 2006, 22.

- 92. Parsa, M. M. Wetting and Evaporation of Nanosuspension Droplets. 2017.
- 93. Li, Y.; Lv, C.; Li, Z.; Quéré, D.; Zheng, Q., From coffee rings to coffee eyes. *Soft Matter* **2015**, *11* (23), 4669-4673.
- 94. Thokchom, A. K.; Gupta, A.; Jaijus, P. J.; Singh, A., Analysis of fluid flow and particle transport in evaporating droplets exposed to infrared heating. *International Journal of Heat and Mass Transfer* **2014**, *68*, 67-77.
- 95. Ta, V. D.; Carter, R. M.; Esenturk, E.; Connaughton, C.; Wasley, T. J.; Li, J.; Kay, R. W.; Stringer, J.; Smith, P. J.; Shephard, J. D., Dynamically controlled

- deposition of colloidal nanoparticle suspension in evaporating drops using laser radiation. *Soft Matter* **2016**, *12* (20), 4530-4536.
- 96. Li, Y.; Diddens, C.; Segers, T.; Wijshoff, H.; Versluis, M.; Lohse, D., Rayleigh—Taylor instability by segregation in an evaporating multicomponent microdroplet. *Journal of Fluid Mechanics* **2020**, *899*, A22.
- 97. Park, J.; Moon, J., Control of Colloidal Particle Deposit Patterns within Picoliter Droplets Ejected by Ink-Jet Printing. *Langmuir* **2006**, *22* (8), 3506-3513.
- 98. Cui, L.; Li, Y.; Wang, J.; Tian, E.; Zhang, X.; Zhang, Y.; Song, Y.; Jiang, L., Fabrication of large-area patterned photonic crystals by ink-jet printing. *Journal of Materials Chemistry* **2009**, *19* (31), 5499-5502.
- 99. Cheng, J.; Sun, Y.-f.; Zhao, A.; Huang, Z.-h.; Xu, S.-p., Preparation of gradient wettability surface by anodization depositing copper hydroxide on copper surface. *Transactions of Nonferrous Metals Society of China* **2015**, *25* (7), 2301-2307.
- 100. Chaudhury, M. K.; Whitesides, G. M., How to Make Water Run Uphill. *Science* **1992**, *256* (5063), 1539.
- 101. Ichimura, K.; Oh, S.-K.; Nakagawa, M., Light-Driven Motion of Liquids on a Photoresponsive Surface. *Science* **2000**, *288* (5471), 1624.
- 102. Berná, J.; Leigh, D. A.; Lubomska, M.; Mendoza, S. M.; Pérez, E. M.; Rudolf, P.; Teobaldi, G.; Zerbetto, F., Macroscopic transport by synthetic molecular machines. *Nature materials* **2005**, *4* (9), 704-710.
- 103. Yamada, R.; Tada, H., Manipulation of Droplets by Dynamically Controlled Wetting Gradients. *Langmuir* **2005**, *21* (10), 4254-4256.
- 104. Kim, J.-H.; Lee, J.-H.; Mirzaei, A.; Kim, H. W.; Tan, B. T.; Wu, P.; Kim, S. S., Electrowetting-on-dielectric characteristics of ZnO nanorods. *Scientific Reports* **2020**, *10* (1), 14194.
- 105. Brzoska, J. B.; Brochard-Wyart, F.; Rondelez, F., Motions of droplets on hydrophobic model surfaces induced by thermal gradients. *Langmuir* **1993**, *9* (8), 2220-2224.
- 106. Gao, C.; Wang, L.; Lin, Y.; Li, J.; Liu, Y.; Li, X.; Feng, S.; Zheng, Y., Droplets Manipulated on Photothermal Organogel Surfaces. *Advanced Functional Materials* **2018**, *28* (35), 1803072.
- 107. Irajizad, P.; Ray, S.; Farokhnia, N.; Hasnain, M.; Baldelli, S.; Ghasemi, H., Remote Droplet Manipulation on Self-Healing Thermally Activated Magnetic Slippery Surfaces. *Advanced Materials Interfaces* **2017**, *4* (12), 1700009.
- 108. Konvalina, G.; Leshansky, A.; Haick, H., Printing Nanostructures with a Propelled Anti-Pinning Ink Droplet. *Advanced Functional Materials* **2015**, *25* (16), 2411-2419.
- 109. Cira, N. J.; Benusiglio, A.; Prakash, M., Vapour-mediated sensing and motility in two-component droplets. *Nature* **2015**, *519* (7544), 446-450.
- 110. Malinowski, R. A. Dynamic Control of Evaporating Droplets Using a Point Source of Vapour. University College London, 2019.
- 111. Wang, Z.; Wang, S.; Huang, L.; Li, L.; Chi, L., Microstructured Ultrathin Organic Semiconductor Film via Dip-Coating: Precise Assembly and Diverse Applications. *Accounts of Materials Research* **2020**, *1* (3), 201-212.
- 112. Huang, B.; Hua, H.; Lai, P.; Shen, X.; Li, R.; He, Z.; Zhang, P.; Zhao, J., Constructing Ion-Selective Coating Layer with Lithium Ion Conductor LLZO and Binder Li-Nafion for Separator Used in Lithium-Sulfur Batteries. *ChemElectroChem* **2022**, *9* (14), e202200416.

- 113. Zhang, Y.; Liu, Y.; Xu, Z.; Ye, H.; Yang, Z.; You, J.; Liu, M.; He, Y.; Kanatzidis, M. G.; Liu, S., Nucleation-controlled growth of superior lead-free perovskite Cs3Bi2l9 single-crystals for high-performance X-ray detection. *Nature Communications* **2020**, *11* (1), 2304.
- 114. Ma, L.; Yan, Z.; Zhou, X.; Pi, Y.; Du, Y.; Huang, J.; Wang, K.; Wu, K.; Zhuang, C.; Han, X., A polymer controlled nucleation route towards the generalized growth of organic-inorganic perovskite single crystals. *Nature Communications* **2021**, *12* (1), 2023.
- 115. Zhang, T.; Liu, Y.; Du, S.; Wu, S.; Han, D.; Liu, S.; Gong, J., Polymorph Control by Investigating the Effects of Solvent and Supersaturation on Clopidogrel Hydrogen Sulfate in Reactive Crystallization. *Crystal Growth & Design* **2017**, *17* (11), 6123-6131.
- 116. Duffy, D.; Barrett, M.; Glennon, B., Novel, Calibration-Free Strategies for Supersaturation Control in Antisolvent Crystallization Processes. *Crystal Growth & Design* **2013**, *13* (8), 3321-3332.
- 117. Soeda, J.; Okamoto, T.; Mitsui, C.; Takeya, J., Stable growth of large-area single crystalline thin films from an organic semiconductor/polymer blend solution for high-mobility organic field-effect transistors. *Organic Electronics* **2016**, *39*, 127-132.
- 118. Brixi, S.; Melville, O. A.; Mirka, B.; He, Y.; Hendsbee, A. D.; Meng, H.; Li, Y.; Lessard, B. H., Air and temperature sensitivity of n-type polymer materials to meet and exceed the standard of N2200. *Scientific Reports* **2020**, *10* (1), 4014.
- 119. Lahav, M.; Leiserowitz, L., The effect of solvent on crystal growth and morphology. *Chemical Engineering Science* **2001**, *56* (7), 2245-2253.
- 120. Kung, Y.-C.; Hsiao, S.-H., Solution-processable, high-Tg, ambipolar polyimide electrochromics bearing pyrenylamine units. *Journal of Materials Chemistry* **2011**, *21* (6), 1746-1754.
- 121. Draper, E. R.; Walsh, J. J.; McDonald, T. O.; Zwijnenburg, M. A.; Cameron, P. J.; Cowan, A. J.; Adams, D. J., Air-stable photoconductive films formed from perylene bisimide gelators. *Journal of Materials Chemistry C* **2014**, *2* (28), 5570-5575.
- 122. Draper, E. R.; Archibald, L. J.; Nolan, M. C.; Schweins, R.; Zwijnenburg, M. A.; Sproules, S.; Adams, D. J., Controlling Photoconductivity in PBI Films by Supramolecular Assembly. *Chemistry A European Journal* **2018**, *24* (16), 4006-4010.
- 123. Cameron, J.; Adams, D. J.; Skabara, P. J.; Draper, E. R., Amino acid functionalised perylene bisimides for aqueous solution-deposited electron transporting interlayers in organic photovoltaic devices. *Journal of Materials Chemistry C* **2022**, *10* (10), 3944-3950.
- 124. Bürgi, T., Properties of the gold–sulphur interface: from self-assembled monolayers to clusters. *Nanoscale* **2015**, *7* (38), 15553-15567.
- 125. Abubakar, S.; Das, G.; Prakasam, T.; Jrad, A.; Gándara, F.; Varghese, S.; Delclos, T.; Olson, M. A.; Trabolsi, A., Enhanced Removal of Ultratrace Levels of Gold from Wastewater Using Sulfur-Rich Covalent Organic Frameworks. *ACS Applied Materials & Interfaces* **2024**.
- 126. Häkkinen, H., The gold–sulfur interface at the nanoscale. *Nature Chemistry* **2012**, *4* (6), 443-455.
- 127. Siegel, J.; Lyutakov, O.; Rybka, V.; Kolská, Z.; Švorčík, V., Properties of gold nanostructures sputtered on glass. *Nanoscale Research Letters* **2011**, *6* (1), 96.

- 128. Corbierre, M. K.; Lennox, R. B., Preparation of Thiol-Capped Gold Nanoparticles by Chemical Reduction of Soluble Au(I)–Thiolates. *Chemistry of Materials* **2005**, *17* (23), 5691-5696.
- 129. Jakub, S.; Ondřej, K. t.; Zdeňka, K.; Petr, S. k.; Václav, S. v. i. k., Gold Nanostructures Prepared on Solid Surface. In *Metallurgy*, Yogiraj, P., Ed. IntechOpen: Rijeka, 2012; p Ch. 3.
- 130. Abdelsalam, M. E.; Bartlett, P. N.; Kelf, T.; Baumberg, J., Wetting of Regularly Structured Gold Surfaces. *Langmuir* **2005**, *21* (5), 1753-1757.
- 131. Dahan, E.; Sundararajan, P. R., Polymer compatibilized self-assembling perylene derivatives. *European Polymer Journal* **2015**, *65*, 4-14.
- 132. Schill, J.; Milroy, L.-G.; Lugger, J. A. M.; Schenning, A. P. H. J.; Brunsveld, L., Relationship between Side-Chain Polarity and the Self-Assembly Characteristics of Perylene Diimide Derivatives in Aqueous Solution. *ChemistryOpen* **2017**, *6* (2), 266-272.
- 133. Balzer, N.; Lukášek, J.; Valášek, M.; Rai, V.; Sun, Q.; Gerhard, L.; Wulfhekel, W.; Mayor, M., Synthesis and Surface Behaviour of NDI Chromophores Mounted on a Tripodal Scaffold: Towards Self-Decoupled Chromophores for Single-Molecule Electroluminescence. *Chemistry A European Journal* **2021**, *27* (47), 12144-12155.
- 134. Lu, B.; Stolte, M.; Liu, D.; Zhang, X.; Zhao, L.; Tian, L.; Frisbie, C. D.; Würthner, F.; Tao, X.; He, T., High Sensitivity and Ultra-Broad-Range NH3 Sensor Arrays by Precise Control of Step Defects on The Surface of Cl2-Ndi Single Crystals. *Advanced Science* **2024**, *11* (14), 2308036.
- 135. Lv, A.; Li, Y.; Yue, W.; Jiang, L.; Dong, H.; Zhao, G.; Meng, Q.; Jiang, W.; He, Y.; Li, Z.; Wang, Z.; Hu, W., High performance n-type single crystalline transistors of naphthalene bis(dicarboximide) and their anisotropic transport in crystals. *Chemical Communications* **2012**, *48* (42), 5154-5156.
- 136. He, T.; Stolte, M.; Burschka, C.; Hansen, N. H.; Musiol, T.; Kälblein, D.; Pflaum, J.; Tao, X.; Brill, J.; Würthner, F., Single-crystal field-effect transistors of new Cl2-NDI polymorph processed by sublimation in air. *Nature Communications* **2015**, *6* (1), 5954.
- 137. Shao, M.; He, Y.; Hong, K.; Rouleau, C. M.; Geohegan, D. B.; Xiao, K., A water-soluble polythiophene for organic field-effect transistors. *Polymer Chemistry* **2013**, *4* (20), 5270-5274.
- 138. Cong, S.; Creamer, A.; Fei, Z.; Hillman, S. A. J.; Rapley, C.; Nelson, J.; Heeney, M., Tunable Control of the Hydrophilicity and Wettability of Conjugated Polymers by a Postpolymerization Modification Approach. *Macromolecular Bioscience* **2020**, *20* (11), 2000087.
- 139. Cao, P.-L. D.; Wu, Z.; Nalaoh, P.; Lindsey, J. S., Molecular designs with PEG groups for water-solubilization of sparsely substituted porphyrins. *New Journal of Chemistry* **2024**, *48* (24), 11140-11152.
- 140. Ensing, B.; Tiwari, A.; Tros, M.; Hunger, J.; Domingos, S. R.; Pérez, C.; Smits, G.; Bonn, M.; Bonn, D.; Woutersen, S., On the origin of the extremely different solubilities of polyethers in water. *Nature Communications* **2019**, *10* (1), 2893.
- 141. De, S.; Ramakrishnan, S., Folding of a Donor-Containing Ionene by Intercalation with an Acceptor. *Chemistry An Asian Journal* **2011**, *6* (1), 149-156.
- 142. Kumar, M.; George, S. J., Green fluorescent organic nanoparticles by self-assembly induced enhanced emission of a naphthalene diimide bolaamphiphile. *Nanoscale* **2011**, *3* (5), 2130-2133.

- 143. Matsui, M.; Masui, R.; Wada, Y., Defects Caused by Chain Ends in Polymer Crystals and Interpretation of Plastic Deformation and γ-Relaxation in Terms of Them. *Polymer Journal* **1971**, *2* (2), 134-147.
- 144. Ishino, K.; Shingai, H.; Hikita, Y.; Yoshikawa, I.; Houjou, H.; Iwase, K., Cold Crystallization and the Molecular Structure of Imidazolium-Based Ionic Liquid Crystals with a p-Nitroazobenzene Moiety. *ACS Omega* **2021**, *6* (48), 32869-32878.
- 145. Honda, A.; Kakihara, S.; Kawai, M.; Takahashi, T.; Miyamura, K., Cold Crystallization and Polymorphism Triggered by the Mobility of the Phenyl Group in Alkyl Azo Dye Molecules. *Crystal Growth & Design* **2021**, *21* (11), 6223-6229.
- 146. Milita, S.; Liscio, F.; Cowen, L.; Cavallini, M.; Drain, B. A.; Degousée, T.; Luong, S.; Fenwick, O.; Guagliardi, A.; Schroeder, B. C.; Masciocchi, N., Polymorphism in N,N'-dialkyl-naphthalene diimides. *Journal of Materials Chemistry C* **2020**, *8* (9), 3097-3112.
- 147. Insuasty, A.; Carrara, S.; Xuechen, J.; McNeill, C. R.; Hogan, C.; Langford, S. J., Aggregation-Induced Emission of Naphthalene Diimides: Effect of Chain Length on Liquid and Solid-Phase Emissive Properties. *Chemistry An Asian Journal* **2024**, *19* (9), e202400152.
- 148. Moura Ramos, J. J.; Diogo, H. P., Are Crystallization and Melting the Reverse Transformation of Each Other? *Journal of Chemical Education* **2006**, *83* (9), 1389.
- 149. Markov, I. V., Crystal Growth for Beginners: Fundamentals of Nucleation, Crystal Growth and Epitaxy. World Scientific: 2003.
- 150. Ichikawa, M.; Yokota, Y.; Jeon, H.-G.; Banoukepa, G. d. R.; Hirata, N.; Oguma, N., Comparative study of soluble naphthalene diimide derivatives bearing long alkyl chains as n-type organic thin-film transistor materials. *Organic Electronics* **2013**, *14* (2), 516-522.
- 151. Chlebosz, D.; Goldeman, W.; Janus, K.; Szuster, M.; Kiersnowski, A. Synthesis, Solution, and Solid State Properties of Homological Dialkylated Naphthalene Diimides—A Systematic Review of Molecules for Next-Generation Organic Electronics *Molecules* [Online], 2023.
- 152. Pluczyk, S.; Laba, K.; Schab-Balcerzak, E.; Bijak, K.; Kotowicz, S.; Lapkowski, M., Electrochemical and spectroelectrochemical properties of new polymers with diimide subunits. *Journal of Electroanalytical Chemistry* **2017**, *795*, 90-96.
- 153. Karoń, K.; Rode, J. E.; Kaczorek, D.; Kawęcki, R.; Pluczyk-Małek, S.; Łapkowski, M.; Ostrowski, S.; Lyczko, K.; Dobrowolski, J. C., UV–vis and ECD spectroelectrochemistry of atropisomeric naphthalenediimide derivative. *Spectrochimica Acta Part A: Molecular and Biomolecular Spectroscopy* **2023**, 288, 122089.
- 154. Ashraf, R. S.; Shahid, M.; Klemm, E.; Al-Ibrahim, M.; Sensfuss, S., Thienopyrazine-Based Low-Bandgap Poly(heteroaryleneethynylene)s for Photovoltaic Devices. *Macromolecular Rapid Communications* **2006**, *27* (17), 1454-1459.
- 155. Wallace, A. M.; Curiac, C.; Delcamp, J. H.; Fortenberry, R. C., Accurate determination of the onset wavelength (λonset) in optical spectroscopy. *Journal of Quantitative Spectroscopy and Radiative Transfer* **2021**, *265*, 107544.
- 156. Celikbilek Ersundu, M.; Ersundu, A. E.; Aydın, Ş., Crystallization Kinetics of Amorphous Materials. 2012; pp 127-162.
- 157. Ragone, D. V.; John, W.; Sons, *Thermodynamics of materials. Vol. 1.* Wiley: New York, 1995.

- 158. David A. Porter, K. E. E., Kenneth E. Easterling, *Phase Transformations in Metals and Alloys (Revised Reprint)*. CRC Press: Boca Raton, 2009; Vol. 3rd Edition.
- 159. Vargaftik, N. B.; Volkov, B. N.; Voljak, L. D., International Tables of the Surface Tension of Water. *Journal of Physical and Chemical Reference Data* **1983**, *12* (3), 817-820.
- 160. PubChem Annotation Record for , Propylene glycol, Source: Hazardous Substances Data Bank (HSDB). National Center for Biotechnology Information: 2024.
- 161. PubChem Compound Summary for CID 6228, N,N-Dimethylformamide. National Center for Biotechnology Information: 2024.
- 162. Josyula, T.; Mahapatra, P. S.; Pattamatta, A., Internal flow in evaporating water drops: dominance of Marangoni flow. *Experiments in Fluids* **2022**, *63* (2), 49.
- 163. Lama, H.; Mondal, R., *The Physics of Drying of Colloidal Dispersion: Pattern Formation and Desiccation Cracks.* 2020.
- 164. Leenaars, A. F. M.; Huethorst, J. A. M.; Van Oekel, J. J., Marangoni drying: A new extremely clean drying process. *Langmuir* **1990**, *6* (11), 1701-1703.
- 165. Saha, S.; Desiraju, G. R., Crystal Engineering of Hand-Twisted Helical Crystals. *Journal of the American Chemical Society* **2017**, *139* (5), 1975-1983.
- 166. Whittaker, J. J.; Brock, A. J.; Grosjean, A.; Pfrunder, M. C.; McMurtrie, J.
- C.; Clegg, J. K., Comment on "Trimorphs of 4-bromophenyl 4-bromobenzoate. Elastic, brittle, plastic" by S. Saha and G. R. Desiraju, Chem. Commun., 2018, 54, 6348. *Chemical Communications* **2021**, *57* (40), 4974-4975.
- 167. Saha, S.; Desiraju, G. R., Trimorphs of 4-bromophenyl 4-bromobenzoate. Elastic, brittle, plastic. *Chemical Communications* **2018**, *54* (49), 6348-6351.
- 168. Saha, S.; Desiraju, G. R., Using structural modularity in cocrystals to engineer properties: elasticity. *Chemical Communications* **2016**, *52* (49), 7676-7679.
- 169. Saha, S.; Desiraju, G. R., σ -Hole and π -Hole Synthon Mimicry in Third-Generation Crystal Engineering: Design of Elastic Crystals. *Chemistry A European Journal* **2017**, 23 (20), 4936-4943.
- 170. Krishna, G. R.; Devarapalli, R.; Lal, G.; Reddy, C. M., Mechanically Flexible Organic Crystals Achieved by Introducing Weak Interactions in Structure: Supramolecular Shape Synthons. *Journal of the American Chemical Society* **2016**, *138* (41), 13561-13567.
- 171. Wang, J.-R.; Li, M.; Yu, Q.; Zhang, Z.; Zhu, B.; Qin, W.; Mei, X., Anisotropic elasticity and plasticity of an organic crystal. *Chemical Communications* **2019**, *55* (59), 8532-8535.
- 172. Jung, B. J.; Lee, K.; Sun, J.; Andreou, A. G.; Katz, H. E., Air-Operable, High-Mobility Organic Transistors with Semifluorinated Side Chains and Unsubstituted Naphthalenetetracarboxylic Diimide Cores: High Mobility and Environmental and Bias Stress Stability from the Perfluorooctylpropyl Side Chain. *Advanced Functional Materials* **2010**, *20* (17), 2930-2944.
- 173. He, G.; Wan, X.; Li, Z.; Zhang, Q.; Long, G.; Liu, Y.; Hou, Y.; Zhang, M.; Chen, Y., Impact of fluorinated end groups on the properties of acceptor–donor–acceptor type oligothiophenes for solution-processed photovoltaic cells. *Journal of Materials Chemistry C* **2014**, *2* (7), 1337-1345.
- 174. Yuan, Z.; Ma, Y.; Geßner, T.; Li, M.; Chen, L.; Eustachi, M.; Weitz, R. T.; Li, C.; Müllen, K., Core-Fluorinated Naphthalene Diimides: Synthesis, Characterization, and Application in n-Type Organic Field-Effect Transistors. *Organic Letters* **2016**, *18* (3), 456-459.

- 175. Li, H.; Geng, D.; Lei, Y.; Jiao, F.; Li, L.; Ji, D.; Hu, W., Recent Progress in Fluorinated Dielectric-Based Organic Field-Effect Transistors and Applications. *Advanced Sensor Research* **2023**, *2* (10), 2300034.
- 176. Tamayo, A.; Salzillo, T.; Mas-Torrent, M., Organic Field-Effect Transistors Based on Ternary Blends Including a Fluorinated Polymer for Achieving Enhanced Device Stability. *Advanced Materials Interfaces* **2022**, *9* (6), 2101679.
- 177. Xiang, L.; Wang, W.; Xie, W., Achieving high mobility, low-voltage operating organic field-effect transistor nonvolatile memory by an ultraviolet-ozone treating ferroelectric terpolymer. *Scientific Reports* **2016**, *6* (1), 36291.
- 178. Li, D.; Wang, H.; Chen, J.; Wu, Q., Fluorinated Polymer Donors for Nonfullerene Organic Solar Cells. *Chemistry A European Journal* **2024,** *30* (12), e202303155.
- 179. Kim, J.; Yun, M. H.; Kim, G.-H.; Lee, J.; Lee, S. M.; Ko, S.-J.; Kim, Y.; Dutta, G. K.; Moon, M.; Park, S. Y.; Kim, D. S.; Kim, J. Y.; Yang, C., Synthesis of PCDTBT-Based Fluorinated Polymers for High Open-Circuit Voltage in Organic Photovoltaics: Towards an Understanding of Relationships between Polymer Energy Levels Engineering and Ideal Morphology Control. *ACS Applied Materials & Interfaces* **2014**, *6* (10), 7523-7534.
- 180. Fan, Q.; Méndez-Romero, U. A.; Guo, X.; Wang, E.; Zhang, M.; Li, Y., Fluorinated Photovoltaic Materials for High-Performance Organic Solar Cells. *Chemistry An Asian Journal* **2019**, *14* (18), 3085-3095.
- 181. Morse, G. E.; Helander, M. G.; Maka, J. F.; Lu, Z.-H.; Bender, T. P., Fluorinated Phenoxy Boron Subphthalocyanines in Organic Light-Emitting Diodes. *ACS Applied Materials & Interfaces* **2010**, *2* (7), 1934-1944.
- 182. Lozano-Hernández, L. A.; Maldonado, J. L.; Hernández-Cruz, O.; Nicasio-Collazo, J.; Rodríguez, M.; Barbosa-García, O.; Ramos-Ortíz, G.; Zolotukhin, M. G.; Scherf, U., Structurally simple OLEDs based on a new fluorinated poly(oxindolylidenearylene). *Dyes and Pigments* **2020**, *173*, 107989.
- 183. Feng, K.; Zhang, X.; Wu, Z.; Shi, Y.; Su, M.; Yang, K.; Wang, Y.; Sun, H.; Min, J.; Zhang, Y.; Cheng, X.; Woo, H. Y.; Guo, X., Fluorine-Substituted Dithienylbenzodiimide-Based n-Type Polymer Semiconductors for Organic Thin-Film Transistors. *ACS Applied Materials & Interfaces* **2019**, *11* (39), 35924-35934.
- 184. Shin, J.; Kim, M.; Kang, B.; Lee, J.; Kim, H. G.; Cho, K., Impact of side-chain fluorination on photovoltaic properties: fine tuning of the microstructure and energy levels of 2D-conjugated copolymers. *Journal of Materials Chemistry A* **2017**, *5* (32), 16702-16711.
- 185. Lee, S. W.; Hussain, M. D. W.; Shome, S.; Ha, S. R.; Oh, J. T.; Whang, D. R.; Kim, Y.; Kim, D. Y.; Choi, H.; Chang, D. W., Effect of electron-withdrawing fluorine and cyano substituents on photovoltaic properties of two-dimensional quinoxaline-based polymers. **2021**, (2045-2322 (Electronic)).
- 186. Fuhrer, T. J.; Houck, M.; Iacono, S. T., Fluoromaticity: The Molecular Orbital Contributions of Fluorine Substituents to the π -Systems of Aromatic Rings. *ACS Omega* **2021**, *6* (48), 32607-32617.
- 187. Hasegawa, T.; Ashizawa, M.; Kawauchi, S.; Masunaga, H.; Ohta, N.; Matsumoto, H., Fluorination and chlorination effects on quinoxalineimides as an electron-deficient building block for n-channel organic semiconductors. *RSC Advances* **2019**, *9* (19), 10807-10813.
- 188. Lu, Y.; Xiao, Z.; Yuan, Y.; Wu, H.; An, Z.; Hou, Y.; Gao, C.; Huang, J., Fluorine substituted thiophene–quinoxaline copolymer to reduce the HOMO level

- and increase the dielectric constant for high open-circuit voltage organic solar cells. *Journal of Materials Chemistry C* **2013**, *1* (4), 630-637.
- 189. Lemal, D. M., Perspective on Fluorocarbon Chemistry. *The Journal of Organic Chemistry* **2004**, *69* (1), 1-11.
- 190. Nishikawa, D.; Nakajima, T.; Ohzawa, Y.; Koh, M.; Yamauchi, A.; Kagawa, M.; Aoyama, H., Thermal and oxidation stability of organo-fluorine compound-mixed electrolyte solutions for lithium ion batteries. *Journal of Power Sources* **2013**, *243*, 573-580.
- 191. Xin, Y.; Zeng, G.; OuYang, J.; Zhao, X.; Yang, X., Enhancing thermal stability of nonfullerene organic solar cells via fluoro-side-chain engineering. *Journal of Materials Chemistry C* **2019**, *7* (31), 9513-9522.
- 192. Bischof, D.; Tripp, M. W.; Hofmann, P. E.; Ip, C.-H.; Ivlev, S. I.; Gerhard, M.; Koert, U.; Witte, G., Regioselective Fluorination of Acenes: Tailoring of Molecular Electronic Levels and Solid-State Properties. *Chemistry A European Journal* **2022**, *28* (7), e202103653.
- 193. Komissarova, E. A.; Dominskiy, D. I.; Zhulanov, V. E.; Abashev, G. G.; Siddiqui, A.; Singh, S. P.; Sosorev, A. Y.; Paraschuk, D. Y., Unraveling the unusual effect of fluorination on crystal packing in an organic semiconductor. *Physical Chemistry Chemical Physics* **2020**, *22* (3), 1665-1673.
- 194. Chlebosz, D.; Goldeman, W. A.-O.; Janus, K.; Szuster, M.; Kiersnowski, A. A.-O., Synthesis, Solution, and Solid State Properties of Homological Dialkylated Naphthalene Diimides-A Systematic Review of Molecules for Next-Generation Organic Electronics. LID 10.3390/molecules28072940 [doi] LID 2940. (1420-3049 (Electronic)).
- 195. Maniam, S.; Higginbotham, H.; Bell, T.; Langford, S., Naphthalene Diimidebased Photovoltaics. 2017.
- 196. Bhosale, S. V.; Al Kobaisi, M.; Jadhav, R. W.; Morajkar, P. P.; Jones, L. A.; George, S., Naphthalene diimides: perspectives and promise. *Chemical Society Reviews* **2021**, *50* (17), 9845-9998.
- 197. Ren, R. X.; Wu, J. X., Mild Conversion of Alcohols to Alkyl Halides Using Halide-Based Ionic Liquids at Room Temperature. *Organic Letters* **2001**, *3* (23), 3727-3728.
- 198. Gibson, M. S.; Bradshaw, R. W., The Gabriel Synthesis of Primary Amines. *Angewandte Chemie International Edition in English* **1968,** *7* (12), 919-930.
- 199. Le, Z.-G.; Chen, Z.-C.; Hu, Y.; Zheng, Q.-G., Organic Reactions in Ionic liquids: N-Alkylation of Phthalimide and Several Nitrogen Heterocycles. *Synthesis* **2004**, *2004* (02), 208-212.
- 200. Miller, M. A.; Sletten, E. M., A General Approach to Biocompatible Branched Fluorous Tags for Increased Solubility in Perfluorocarbon Solvents. *Organic Letters* **2018**, *20* (21), 6850-6854.
- 201. Würthner, F.; Ahmed, S.; Thalacker, C.; Debaerdemaeker, T., Core-Substituted Naphthalene Bisimides: New Fluorophors with Tunable Emission Wavelength for FRET Studies. *Chemistry A European Journal* **2002**, *8* (20), 4742-4750.
- 202. Yue, W.; Zhen, Y.; Li, Y.; Jiang, W.; Lv, A.; Wang, Z., One-Pot Synthesis of Well-Defined Oligo- Butadiynylene-Naphthalene Diimides. *Organic Letters* **2010**, *12* (15), 3460-3463.
- 203. Lasitha, P., Radical anion formation exhibiting "turn-on" fluorescence sensing of hydrazine using a naphthalene diimide (NDI) derivative with a donor–acceptor–

- donor (D–A–D) molecular structure. *Photochemical & Photobiological Sciences* **2020**, *19* (11), 1603-1612.
- 204. Fang, X.; Ke, H.; Li, L.; Lin, M.-J., Structural insights into the aggregation-induced emission mechanism of naphthalene diimide solids. *Dyes and Pigments* **2017**, *145*, 469-475.
- 205. Elgrishi, N.; Rountree, K. J.; McCarthy, B. D.; Rountree, E. S.; Eisenhart, T. T.; Dempsey, J. L., A Practical Beginner's Guide to Cyclic Voltammetry. *Journal of Chemical Education* **2018**, *95* (2), 197-206.
- 206. Fei, Z.; Boufflet, P.; Wood, S.; Wade, J.; Moriarty, J.; Gann, E.; Ratcliff, E. L.; McNeill, C. R.; Sirringhaus, H.; Kim, J.-S.; Heeney, M., Influence of Backbone Fluorination in Regioregular Poly(3-alkyl-4-fluoro)thiophenes. *Journal of the American Chemical Society* **2015**, *137* (21), 6866-6879.
- 207. Alvey, P. M.; Reczek Jj Fau Lynch, V.; Lynch V Fau Iverson, B. L.; Iverson, B. L., A systematic study of thermochromic aromatic donor-acceptor materials. (1520-6904 (Electronic)).
- 208. Danley, R. L. Differential scanning calorimeter. US6561692B2, May 13, 2003, 2003.
- 209. Baker, R. J.; Colavita, P. E.; Murphy, D. M.; Platts, J. A.; Wallis, J. D., Fluorine–Fluorine Interactions in the Solid State: An Experimental and Theoretical Study. *The Journal of Physical Chemistry A* **2012**, *116* (5), 1435-1444.
- 210. Katz, H. E.; Lovinger, A. J.; Johnson, J.; Kloc, C.; Siegrist, T.; Li, W.; Lin, Y. Y.; Dodabalapur, A., A soluble and air-stable organic semiconductor with high electron mobility. *Nature* **2000**, *404* (6777), 478-481.
- 211. Schulz, M.; Seidlitz, A.; Petzold, A.; Thurn-Albrecht, T., The effect of intracrystalline chain dynamics on melting and reorganization during heating in semicrystalline polymers. *Polymer* **2020**, *196*, 122441.
- 212. Sheldrick, G., SHELXT Integrated space-group and crystal-structure determination. *Acta Crystallographica Section A* **2015**, *71* (1), 3-8.
- 213. Dolomanov, O. V.; Bourhis, L. J.; Gildea, R. J.; Howard, J. A. K.; Puschmann, H., OLEX2: a complete structure solution, refinement and analysis program. *Journal of Applied Crystallography* **2009**, *42* (2), 339-341.
- 214. Sheldrick, G., Crystal structure refinement with SHELXL. *Acta Crystallographica Section C* **2015**, *71* (1), 3-8.